
PEDOT
Development of flexible electrodes and lightweight capacitors
BY MARICRUZ SABORIO GONZALEZ.

UNIVERSITAT POLITÈCNICA DE CATALUNYA BARCELONATECH

Developmet of flexible electrodes and lightweight capacitors

Maricruz Saborío González

School of Engineering, East of Barcelona (EEBE)

Presented by:

Maricruz Saborío González

Supervisors:

Francesc Estrany Coda

Carlos Alemán Llansó

Thesis submitted to obtain the degree Doctor of Philosophy in Polymers and Biopolymers at Universitat Politècnica de Catalunya

Departament d'Enginyeria Química Grup d'Innovació en Materials i Enginyeria Molecular

Barcelona, March 2018

Elogio del vivir (Elogi del viure)

Ama tu oficio,
tu vocación,
tu estrella,
aquello para lo que sirves,
aquello en que realmente,
eres uno entre los hombres,
esfuérzate en tu quehacer
como si de cada detalle que piensas,
de cada palabra que dices,
de cada pieza que colocas,
de cada martillazo que das,
dependiese la salvación de la humanidad.

Porque depende, créeme….

Joan Maragall

Abstract

This Thesis has been divided in different and well-defined parts. The first one presents the hierarchically development of flexible supercapacitors based on poly(3,4-ethylenedioxythiophene/alumina (PEDOT/Al_2O_3) composites loaded into poly(γ-glutamic acid (γPGA) hydrogels, whereas the second is devoted to the utilization of polycations bearing a quaternary ammonium in the backbone (i.e. ionenes) as n-dopant agents of PEDOT.

The Thesis started with the preparation of PEDOT/Al_2O_3 composites by in situ anodic polymerization. For this purpose, the stability of 1:1 and 4:1 monomer:alumina aqueous solutions was examined as a function of the pH (2.3, 4.0, 7.0, 8.8 or 10.8). Results indicated that the monomer behaves as a dispersant that remains stable at the studied basic pHs despite they were close to the isoelectric point of alumina. Although the thermal stability of the composites was considerably affected by the pH of the reaction medium, its influence on the surface morphology was very small. Independently of the synthetic conditions, the electrochemical properties were better for PEDOT/Al_2O_3 than for pure PEDOT, reflecting that alumina particles promote the charge mobility. The highest specific capacitance (141 F/g), which was 55% higher than that obtained for pure PEDOT, was achieved for the composite prepared at pH= 8.8 using a 4:1 monomer:alumina ratio. These conditions favored the participation of OH^- groups as secondary doping agents without degrading the polymer matrix and enhanced the specific surface of the films, facilitating the ionic mobility. On the other hand, application of a multi-step polymerization strategy showed that interfaces originated by consecutive steps enhance the specific capacitance.

After that, flexible and lightweight electrodes were prepared using a two-step process. First, PEDOT microparticles were loaded into γPGA hydrogel matrix, during the reaction of the biopolymer chains with the cross-linker, cystamine. After this, PEDOT particles dispersed inside the hydrogel were used as polymerization nuclei for the chronoamperometric synthesis of poly(hydroxymethyl-3,4-ethylenedioxythiophene) (PHMeDOT) in aqueous solution. After characterization of the resulting electrode composites, electrochemical studies revealed that the capacitive properties drastically depend on the polymerization time used to produce PHMeDOT inside the loaded hydrogel matrix. Specifically, flexible electrodes obtained using a polymerization time of 7 hours exhibited an specific capacitance of 45.4±0.7 mF/cm^2 from cyclic voltammetry and charge-discharge long-term stability. The applicability of these electrodes in lightweight and flexible energy-harvesting systems useful for energy-autonomous, low-power, disposable electronic devices, was proved powering a LED bulb.

This part ended with the fabrication of a flexible symmetric supercapacitor prototype composed of electrodes that were prepared by polymerizing PHMeOH inside a γPGA biohydrogel matrix, already loaded with microparticles of PEDOT and Al_2O_3. The prototype was assembled in a totally solid, compact and lightweight configuration, where the supporting electrolytic medium is a γPGA prepared in presence of $NaHCO_3$. After characterization of the elements involved in the prototype, their dimensions (*i.e.* width of the electrode and the solid electrolyte) were optimized to obtain the highest specific capacitance. The electrochemical performance of the prototype was investigated by cyclic voltammetry, galvanostatic charge-discharge cycles and electrochemical impedance spectroscopy. After 2000 charge-discharge cycles (*i.e.* 60.000 s of continuous operation), the loss of specific capacitance was of only 8%, evidencing an excellent stability. The results are very promising for the development of a compact, flexible, lightweight and biocompatible supercapacitors to be employed like energy-autonomous electronic device.

The second part of the Thesis starts with the reduction of PEDOT films using a cationic 1,4-diazabicyclo[2.2.2]octane-based ionene bearing *N,N'*-(*meta*-phenylene)dibenzamide linkages (*m*PI). Our main goal was to obtain n-doped PEDOT using a polymeric dopant agent rather than small conventional tetramethylammonium (TMA), as is usual. This was achieved using a three-step process, which were individually optimized: (1) preparation of p-doped (oxidized) PEDOT at a constant potential of +1.40 V in acetonitrile with $LiClO_4$ as electrolyte; (2) dedoping of oxidized PEDOT using a fixed potential of –1.30 V in water; and (3) redoping of dedoped PEDOT applying a reduction potential of –1.10 V in water with *m*PI. The resulting films displayed the globular appearance typically observed for PEDOT, *m*PI being structured in separated phases forming nanospheres or ultrathin sheets. This organization, which was supported by atomistic Molecular Dynamics simulations, resembled the nanosegregated phase distribution observed for PEDOT p-doped with poly(styrenesulfonate). Furthermore, the doping level achieved using *m*PI as doping agent was comparable to that reached with TMA, even though the ionene provided distinctive properties to the conducting polymer. For example, films redoped with *m*PI exhibited much more hydrophilicity than the oxidized ones, whereas films redoped with TMA were hydrophobic. Similarly, films redoped *m*PI exhibited the highest thermal stability, while those redoped with TMA showed a thermal stability that was intermediate between the latter and dedoped PEDOT. Overall, the incorporation of *m*PI polycation as n-dopant into PEDOT had important advantages for modulating the properties of this emblematic conducting polymer.

Finally, three isomeric ionene polymers containing DABCO and *N,N*'-(*x*-phenylene)dibezamide (*x*= *ortho*- / *meta*- / *para*-) linkages have been used as dopant agents to produce n-doped PEDOT electrodes by reducing already dedoped conducting polymer films. Our main objective was to study

the influence of the ionene topology in both the properties of n-doped PEDOT:ionene electrodes and the success of the *in situ* thermal gelation of the ionene inside the conducting polymer matrix. The highest doping level was reached for the *para*-isomeric ionene-containing electrode, even though the content of *ortho*- and *meta*-topomers into the corresponding n-doped PEDOT:ionene electrodes was greater. Thus, many of the incorporated ionene units were not directly interacting with conducting polymer chains and, therefore, did not play an active role as n-dopant agent but they were crucial for the *in situ* formation of ionene hydrogels. The effect of the ionene topology was practically inexistent in properties like the specific capacitance and wettability of PEDOT:ionene films, and it is small but non-negligible in the electrochemical and thermal stability. In contrast, the surface morphology, topography, and distribution of dopant molecules significantly depended on the ionene topology. *In situ* thermal gelation was successful in PEDOT films n-doped with the *ortho*- and *para*-topomers PEDOT, even though this assembly process was much faster for the former than for the latter. The gelation considerably improved the mechanical response of electropolymerized PEDOT film, which was practically non-existent before it. Molecular dynamics simulations prove that the strength and abundance of PEDOT⋯ionene specific interactions (*i.e.* π-π stacking, N–H⋯S hydrogen bonds and both N^+⋯O and N^+⋯S interactions) are higher for the *meta*-isomeric ionene, for which the *in situ* gelation was not achieved, than for the *ortho*- and *para*-ones.

Acknowledgements

First and foremost, I want to say thanks to God and Science (for me not an antagonism). Thank you to help me overpass that personal challenge in 2015 and thank you for helping me start an amazing jouney in Science and culture. Thanks also goes to everybody who represents a link to my self-growth and to those who gave me positive energies to continue with my dream of research in better conditions.

I also want to give special thanks to all those who taught, trusted and invested in me; MINECO/FEDER (MAT2015-69367-R) for financial support. M.S.G is grateful to Costa Rica National Commission of Scientific and Technological Research (CONICYT-Support N°FI-172B-14). C.A., Instituto Costarricense de Electricidad (ICE), Departamento de Investigación y Desarrollo en Energías Renovables, my bosses and all my friends that supported me to get to where I am today.

Thanks to the Research Group of Innovation and Materials (IMEM), to director Dr. Carlos Alemán Llansó who always guided me in the best way. Thank you for hearing my ideas and taking them into account and why not, as well, thanks for the scoldings. To my co-director Francesc Estrany, that always was being kind and willing to help me. Teacher, I will never forget your summary sheets with all that amazing electrochemical explanations, but more than this. Finally, I can distinguish clearly among CA and CP.

To the technicians that were always in good disposition to help me with the execution of tests and specially to the Dr. Trifon Trifonov, Dr. Lourdes Franco and Dr. Montse Domínguez and Dr. Lluís Soler. To my colleagues (Ina, Angélica, Ana, Brenda, Iranians, Max, Guillem and to the ones that already finsihed and will continue) who were beside me working hard and enjoying the free times. To Dr. Georgina (first hydrogel project), Dr.Sonia (second hydrogel project and Raman Analysis) and Dr.Neudys (for helping me to disconnect from work). Adding to them, to MSc. Nuria Borrás, Dr. Margarita Sánchez, Bach. Treyci García, Bach. María Cambra and to my twins, Msc. Sjela and Petra for our months of work together and being able to manage my fast Spanish and our daily hard work schedule.

To my best partners Autolabs, who always made me pull my hair while at the same time made go into deep thoughts, once the results came out. Thanks to the night labs in which the silence was my best platform of creation.

And overall in specially, to my family Óscar, Julia, Mauricio, auntie Lety, cousins and to my boyfriend Dr. Shiva Prasad and his family, who always support me and gave me goods times of sharing.

To the technology (Skype), thanks for make me part of my brother's wedding, grandparents farewells (Mima, Abuela Engracia), celebrations of birthdays, relatives meetings, pregnancy news and all. And to my Catalonia best friend Kuka, Dolos Amat, Ana and Albert, Lirio, Tere, Marga, Phio and Jaume, Radio program friends (*una Finestra Oberta al Mon*) and to my Costa Rican friends, who remind me the value of friendship and made me feel warm.

To Barcelona,

Barcelona, represented to me the wave of changes, culture, modernism and ancient times, brave people. Represented to me the tolerance and the ocean, the blue skies and the dark. You gave me the key to open the door of hope and made me value all things before I had. One thousand of thanks wonderful Barcelona, is not a good bye it is a see you later.

Table of Contents

Table of figures

List of symbols and abbreviations

Abbreviation	Description
%	Percentage
°	Grades
α-β	Polymerization alpha-beta linkages
γ	Gamma
β,β'	Beta-beta thiophene ring carbon position interaction
δ	Chemical shift
θ	Time or angle
$\theta^{1/2}$	Square of the electropolimerization time
μ	Micra
μm	Micrometer
σ	Conductivity
Ω	Ohms
π	Pi
π-π	Stacking interactions
°C	Degrees Celsius
1s	Orbital atómico1s
2s	Orbital atómico 2s
2p	Orbital atómico 2p
2D	Second dimension
3D	Third dimension
Δ	Differential
***Δ*t**	Time differential
ΔV	Defferential of potential
ζ-potential	Zeta potential
A	Amp
A	Area
Å	Anstrong
AFM	Atomic Force Microscopy
AISI	American Iron Steel Industry
APMA	N-(3-aminopropyl) methacrylamide hydrochloride
APMA	N-(3-Aminopropyl)methacrylamide hydrochloride
b	Betha
C^o	Celsius
C^*	Molar concentration
CA	Chronoamperometry
C_{dl}	Double Layer Capacitance Element
cm	Centimeter
cm^{-1}	Reciprocal centimeter or wavenumber
cm^2	Centimetre squared

CNT	Carbon Nanotube
CPE	Composite Polymer Electrolyte or Constant Phase Element
CPs	Conductive Polymers
CV	Cyclic Voltammetry
D	Diameter
Da	Dalton
DABCO	1,4-diazabicyclo[2.2.2]octane
$\mathbf{D_{CP}}$	Diameter of the particle
$\boldsymbol{D_{eff}}$	Effective diameter
$\mathbf{dl_{mPI}}$	Doping level *meta* polyionene
DLS	Dynamic Light Scattering
$\mathbf{dl_{TMA}}$	Doping level tetramethylammonium
DMF	Dimethylformamide
$\mathbf{D_{PEDOT}}$	Diameter of the PEDOT particles
DTGA	Differential Thermogravimetric Analysis
E	Energy density
e.g.	Exempli gratia
EAPs	Electroactive polymers
ECH	Electrical Conductive Hydrogels
EDC	1-[3-(dimethylamino)propyl]-3-ethylcarbodiimide methiodide
EDL	Electrochemical Double Layer
EDLC	Electrochemical Double Layer Capacitor
EDOT	3,4-ethylenedioxythiophene
EDOT-OH	Hydroxy (3,4-ethylenedioxythiophene)
EDX	Energy Dispersive X-Ray
EES	Electrical Energy Storage
EEC	Electrical Equivalent Circuit
$\mathbf{E_p^a}$	Anodic Peak Potencial
EIS	Electrochemical Impedance
$\mathbf{E_p^c}$	Cathodic peak potential
eV	Electron volts
F	Faraday or Faraday's constant (96 500 C)
fs	Femtosecond
FTIR	Fourier-Transform Infrared
g	Gram(s)
$\boldsymbol{g_{ar\text{-}ar}}$	Aromatic ring centre of mass interaction
GCD	Galvanostatic Charge Discharge
GW	Giga Watts
h	Hour(s)
HEC	Hybrid Electrochemical Capacitors
Hep-MA/PVA	Heparin methacrylate/poly(vinyl alcohol)
HFP	Hexafluoropropene
$\mathbf{^1H}$**-NMR**	Proton Nuclear Magnetic Resonance

HMeDOT	hydroxymethyl-3,4-ethylenedioxy thiophene
Hz	Hertz
I	Current
i.e.	Id est
ICPs	Intrinsic Conductive Polymer
J	J coupling, indirect dipole–dipole coupling
K	Kelvin
kV	Kilovolts
kWh	Kilo Watthora
Kx	Magnification 1000x
L	Thickness
LED	Light Emitting Diode
Li-ion	Lithium battery
LiTFSA	Lithium bis(trifluoromethanesulfonyl)amide
M	Molar
m	Milli
m1	Model 1
m2	Model 2
m3	Model 3
mA	Miliampere
MD	Computational Molecular Dynamics Simulations
min	Minutes
mm	milimeter
mM	Milimolar
MPa	Megapascals
mPI	1,4-diazabicyclo[2.2.2]octane-based ionene bearing N,N'-(*meta*-phenylene)dibenzamide linkages
m_{pol}	Polymerization mass
mVs^{-1}	Milivolts/second
mW	Miliwatts
M_w	Molecular weight
n	Moles
n	Number of electrons transferred
N_{ClO4-}	Moles of chlorate
N_{EDOT}	Moles of 3,4-ethylenedioxythiophene
nm	Nanometre
N_{mPI}	Moles of *meta* polyionene
N_{TMA}	Moles of tetramethylammonium
n-type doping	Negative doping
O_1	Oxidation peak 1
O_2	Oxidation peak 2
Ocp	Open Circuit
P	Power
P(ECH-co-EO)	Copolymer epichlorohydrin/ ethylene oxide
P(ECH-co-EO)	Copolymer epichlorohydrin/ ethylene oxide

P(MA-co-AHPS):	Poly(methyl acrylate-co-sulfonate allyloxy
PA	Polyacetylene
PAAK	Potassium polyacrylate
PAM	Polyacrylamide
PANI	Polyaniline
PEDOT	Poly(3,4-ethylenedioxythiophene)
PEDOTCOOH	Carboxy-poly(3,4-ethylenedioxythiophene)
PEG	Polyethylene glycol
PEO	Polyethylene oxide
PF	Paper Fibers
γ-PGA	Gamma-polyglutamic acid
pH	Grado de acidez o basicidad de una solución acuosa.
PHMeDOT	Poly(hydroxymethyl-3,4-ethylenedioxythiophene)
PMMA	Poly(methyl methacrylate)
ppm	Parts per million
PPV	Poly(phenylenevinylene)
PPy	Polypyrrole
ps	Picosecond
PS	Polystyrene
PSS	Polystyrene sulfonate
PTh	Polythiophene
p-type doping	Positive doping
PVdF	Poly(vinylidene fluoride
PVdF-HFP	Poly(vinylidene fluoride-co-hexafluoropropene
Q	Charge
$\mathbf{Q_2}$	Second cycle charge
$\mathbf{Q\ cm^{-2}}$	Charge per surface
$\mathbf{Q\ cm^{-3}}$	Charge per volume
$\mathbf{Q\ g^{-1}}$	Charge per grame
$\boldsymbol{Q_{blank}}$	Charge of white
$\boldsymbol{Q_{ddop}}$	Charge of dedopig
$\boldsymbol{Q_i}$	Oxidation-reduction cycle
Q_{rdop}^{neat}	Neat redonping charge
$\boldsymbol{Q_{pol}}$	Polymerization charge
$\boldsymbol{Q_{rdop}}$	Charge of redoping
QPV	Quaternized Poly(Vinylalcohol)
r	Distance in Angstrom in between center of masses
$\mathbf{R_1}$	Reduction peak 1
$\mathbf{R_2}$	Reduction peak 2
$\mathbf{R_C}$ **or** $\mathbf{R_{ct}}$	Charge transfer resistance
Rdf	Partial Radial Distribution Functions
$\mathbf{R_e}$	Solid electrolyte resistance
Resp	Restrained Electrostatic Potential Method
rGO	Reduced Graphene Oxide
$\mathbf{R_{max}}$	Maximum roughness

R_{max}	Maximum roughness
R_q	Root mean square roughness
RT	Room Temperature
S	Seconds
SC	Specific Capacitance
S cm^{-1}	Siemens per centimetre
SEM	Scanning Electron Microscopy
SiNP	Silicon nanoparticles
SR	Swelling Ratio
$T_{50\%}$	Temperature at a 50% weight loss
TEGDA-BA	Triethylene glycol diacetate-2-propenoic acid butyl ester
TEM	Transmission Electron Microscopy
TGA	Thermogravimetry
TMA	Tetramethylammonium
T_{max}	Maximum temperature
t_{son}	Sonication time
V	Volt
Var	Volt-ampere
V_{drop}	Voltage drop
V_{gain}	Voltage gain
VRB	Vanadium Redox Battery
VRES	Variable Electricity Sources
W	Watts
W kg^{-1}	Watt per kilogram
w/w %	Weight/ weight percentage
WE	Working Electrode
Wh kg^{-1}	Watt hour per kilogram
x	*x*-phenylenediamine *(x= ortho-* / *meta-* / *para)*
XPS	X-Ray Photoelectron Spectroscopy
Y_0	Admittance
Z_{CPE}	CPE impedance
ZEBRA	Zeolite Battery Research Africa Project

Chapter I

1.1. General Background

The worldwide energy and climate change circumstances[1] are directing the way towards renewable energy sources at all scales from energy plant generation until electric vehicles, regenerative breaking technologies and cheap solar cells. The development of energy storage devices[2] is indispensable to deal with the efficient usage of clean and variable electricity sources (VRES).[3] IHS Technology affirmed that grid-connected energy storage systems plants got 2 GW by 2016, this improvement being due to many factors, as for example government funding programs, electrical energy storage (EES) devices cost reduction (*i.e.* for residential EES plant, the expected cost reduction of 70% $/kWh by 2030) and utility tenders.[4]

Renewable energy plants, such as eolic (Power worldwide stored: 54 GW)[5] and solar (Power worldwide stored: 75 GW) plants,[6] possess peculiar characteristics depending on the season, weather and stochastic performance along the day, claiming an energy storage system to back up the electricity surplus during day, and making possible to use them as peaking power plant (*e.g.* during night or in imbalanced circumstances due to predicted error).[7,8]

Many countries are developing technologies in this line. For example, energy storage plants based mainly on batteries[9] [lead acid, nickel cadmium (NiCd), sodium sulfide (Na_2S), nickel (II) chloride ($NiCl_2$), lithium ion, Zeolite Battery Research Africa Project (ZEBRA), vanadium oxide (VO)], have been installed in China, India, Alaska (Goldel Valley, Faribanks), Japan, Denmark, Germany, France, Mediterranean islands and United States.[4] Also, capacitors and supercapacitors possess a promising future as high- voltage power systems,[10] even though they should be used as hybrids with batteries, for power factor correction, voltage and volt-ampere (Var) reactive support and harmonic safety.[3,11]

Nowadays, capacitors and supercapacitors are more suitable for medium and low scale on-board and stationary applications, specially, in those that demand a burst of energy. Capacitors and supercapacitors are characterized by a high-power density capability, even thought, the charge storage is lower than in batteries (3-30 times lower). Following, it is shown a Ragone plot comparing the specific energy and power of the different EES devices, which illustrate the characteristics discussed above.

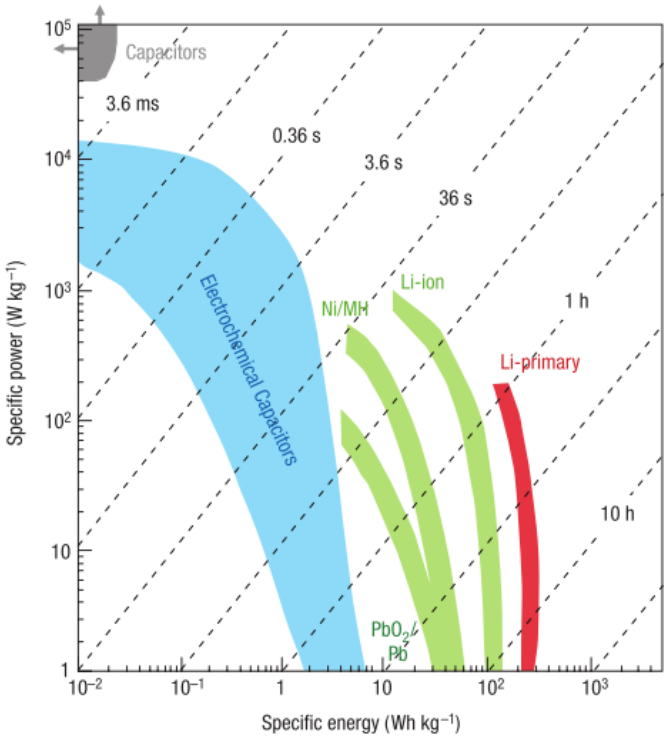

Figure 1.1-1. Ragone plot of power (W kg^{-1}) against specific energy (Wh kg^{-1}) for the most important energy storage systems. Reproduced with permission.[7] Copyright © 2008, Springer Nature

It is relevant to highlight that the specific energy and specific power are key selection criteria for final applications. Batteries have the highest specific energy by mass when compared with capacitors and supercapacitors; however, capacitors exhibit the highest specific power.

Further emphasis should also be given to the charge-discharge criteria. The best option to favor this criterion is provided by capacitors followed by supercapacitors since the formers take less time to charge and discharge, creating an instantaneous energy storage and delivery. Due to these properties, it has been feasible to use capacitors and supercapacitors in electric vehicles, utility load-levelling, heavy-load starting assists for diesel locomotives (supporting the voltage during load increasing),[12] military and medical applications, as well as, low-power demanding equipment, such as camera-flash, lasers, pulsed-light generators and back-up power for computer memory.[13] Finally, the most attractive factor is the cost-effectiveness of the energy storage device, which is determined by long life cycles and excellent cycling capabilities without losing energy storage capacities.[10]

The capacitance of supercapacitors per unit of volume or mass is 20–200 times higher than that of common capacitors.[14] Currently, the attention is focused on supercapacitors because their higher energy (in Wh kg^{-1}), these devices being categorized as is described in Figure 1.1-2.[15]

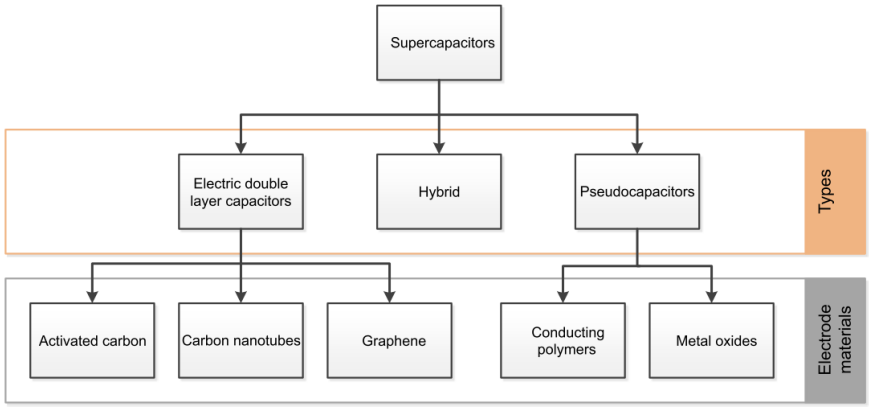

Figure 1.1-2. Supercapacitors classification by type and electrodes material. Reproduced with permission.[16] Copyright © 2016 Elsevier Ltd. All rights reserved.

Supercapacitors are classified as: electrochemical double layer capacitors (EDL), which are characterized by electrostatic interactions at the double layer; pseudo-capacitors, which involve Faradic reactions; and hybrids, a mixture of both. In addition, the formers are usually organized according to the chemical constitution of the electrodes, as is indicated in Figure 1.1-2. For example, pseudocapacitors are classified into devices fabricated with conducting polymers (CPs) and metal oxides. Besides, capacitors can be categorized as symmetrical or asymmetrical when electrodes present the same or different capacitance, respectively.[15]

EDL devices store the energy by electrostatic forces (“charge separation”) along the double layer electrode/electrolyte, whereas pseudo-capacitors do it by charge transfer via Faradaic reactions, such as intercalation or redox processes occurring at the bulk of the solid–electrode surface.[2,13,15]

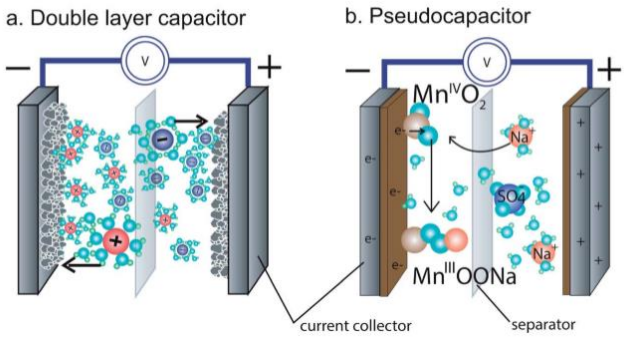

Figure 1.1-3. Basic schematics for (a) an all carbon EDL capacitor, (b) a pseudo-capacitor (MnO_2 depicted in the center). Both devices have an active material (e.g. carbon, MnO_2), a current collector, a separating membrane and an electrolyte (e.g. Na_2SO_4, solutions). Modified and reproduced with permission.[17] Copyright © 2014, Royal Society of Chemistry.

Figure 1.1-3 describes the main components of EDL capacitors and pseudo-capacitors: electrodes, electrolyte, collector and separator.[14,18] Electrodes, are typically constituted by metal oxides, CPs or hybrid organic-inorganics materials. Improvement of the surface area and pore size at the electrodes, as well as of the electrolytes, is very desirable to obtain higher capacitances.[12] Currently, electrolytes can be fabricated using ionic liquids and solid electrolytes, in addition of conventional salts dissolved in aqueous and non-aqueous solvents.[13]

The components of the electrolytes and electrodes developed in this Thesis (*i.e.* CPs, hydrogels, fillers such as Al_2O_3 (alumina), and ionenes will be discussed in the next section *Overview of Key Concepts.*

1.2. Overview

1.2.1. Conducting Polymers (CPs)

The discovery of CPs occurred around 1978 when Shirakawa *et al.*[19] proved that polyacetylene (PA), an insulating organic conjugated polymer, exhibits a dramatic increase in the electrical conductivity upon treatment with oxidizing or reducing agents.[20] Currently, the most usual CPs are polyaniline (PANI), polypyrrole (PPy), poly(phenylenevinylene) (PPV), polythiophene (PTh), and their derivatives.[21] Table 1.2-1 lists the conductivity values of some representative CPs.

Table 1.2-1. Conductivity of common CPs in the doped state.[22]

CPs	Conductivity (S cm^{-1})
PANI	400
PPy	400
PPV	10^4
Poly(3-methylthiophene)	400
(PEDOT)[a]	500

[a] PEDOT: Poly(3,4-ethylenedioxythiophene).

Heterocyclic CPs in neutral state have a large energy gap (or band gap) between the valence and conduction band, which is due to their favorable benzenoid electronic structure (Figure 1.2-1). The reduction of the band gap occurs when charge carriers are incorporated into their conjugated backbone through oxidation (p-type doping) or reduction (n-type doping).[23] These doping processes result in the transformation of the electronic structure from benzenoid to quinoid (Figure 1.2-1).

The oxidation of the neutral polymer, after relaxation, causes the generation of localized electronic states, known as *polarons*. Through the continuation of this oxidation process, another electron can be detached forming *bipolarons*. It is worth noting that the formation of a *bipolaron* is favored with respect to two separated *polarons*.[20] However, the entire CP chain should be saturated with *polarons* before the formation of the *bipolarons*. The charge injection (doping) capacity of CPs leads to interesting phenomena that can be used in several applications.[24]

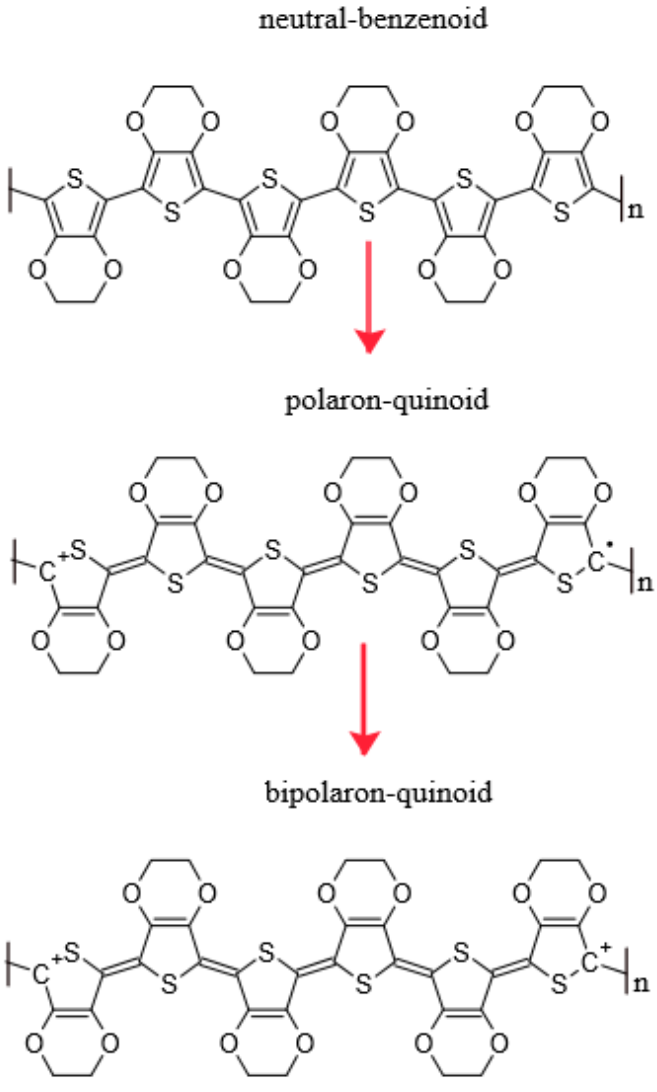

Figure 1.2-1. Chemical structure of PEDOT in different electronic states. The scheme depicts the transformation of PEDOT chains from neutral state to polaron and from polaron to bipolaron during the doping process.[23,25] Own design by ACD Labs Freeware 2016.

As it was mentioned above, the formation of charged CP chains is due to oxidation (p-type doping to form cationic polarons and bipolarons) or reduction (n-type doping to form anionic polarons and bipolarons) processes. The charge neutrality of the whole system is achieved through counter ions arising from the dopant agent, which can move along the charged polymer chain.

Upon doping, the conductivity of CPs can increase several orders of magnitude, becoming near to those of metals. For example, poly(3,4-ethylenedioxythiophene)-tosylate-poly(p-phenylene) (PEDOT–Tos–PPP) films reduced with sodium borohydride ($NaBH_4$) solutions reach an electrical conductivity of 1.5×10^3 S cm^{-1}, whereas the conductivity of neutral PEDOT is $\sim10^{-5}$ S cm^{-1} only.[26]

CPs have softer mechanical interface compared to conventional metallic electrodes and, therefore, efforts are being made to avoid the fragility of the polymer. Some studies suggest that the mechanical properties of CPs can be improved by incorporating inorganic materials, as for example titanium oxides (as anatasa), silica (as montmorillonite), silicon carbide, Al_2O_3, and boron nitride.[27,28,29]

1.2.2. PEDOT

PThs constitute a group of sulfur-containing heterocyclic CPs_{30} with properties superior to PPy and PANI. At present moment, PEDOT is the most studied organic material for energy storage because of its excellent electrical properties, charge–discharge kinetics, low cost, suitable morphology, and fast doping/ dedoping processes (*e.g.* switching properties, optical properties).[21,31] Indeed, PEDOT is considered the most successful PTh derivative due to its electrical conductivity, which is high even when prepared using standard conditions (~500 S cm^{-1}).[32] PEDOT can be obtained in different architectures such as films, nanorod arrays, nanofiber mats.[27,33,34] In this work we will focus on the electrochemical synthesis of PEDOT to produce films.

1.2.3. Electrically conducting hydrogels (ECH)

Hydrogels and CPs are auspicious resources used for new material developments, especially in the field of smart materials for energy storage.[35] Garg *et al*.[36] conceptualized the hydrogels, distinguishing them from gels, as hydrophilic cross-linked materials that can absorb and swell more than 20% of their weight in water while maintaining their 3D-structure with high elasticity.

Some common synthetic hydrogels are derived from polyethylene oxide (PEO), polyvinyl pyrrolidone (PVP), polylactic acid (PLA), polyvinyl alcohol (PVA), polyacrylic acid (PAA), polymethacrylate (PMA), polyacrylamide (PAAm) and polyethylene glycol (PEG). Besides, hydrogels prepared using biopolymers, usually called biohydrogels, are very popular for biomedical applications. Among the biopolymers more frequently employed for the prepared of biohydrogels[37]

are polyglutamic acid (PGA), chitosan, alginate, carrageenan, hyaluronic and carboxymethyl cellulose (CMC).[38,39]

Hydrogels can present, depending on their chemical and physical nature, a variety of properties, as for example mechanical strength, mass transport, dielectric relaxation, biocompatibility, biodegradability and bioadhesion.[40]

The synthesis of hydrogels consists in the construction of cross-links using chemical or physical processes that allow controlling the porous size.[41-43] Besides, the poor mechanical properties and hydrophobicity of CPs, which are in detriment of some applications, can be improved by combining with hydrogels. Thus, the synergies between CPs and some hydrogels sometimes result in advantageous flexible conductive materials.[44]

Hybrid materials resulting from the combination of CPs and hydrogels, which are known as electrically conducting hydrogels (ECH), usually exhibit a high degree of hydration, swell-ability, diffusive capacity, electrical conductivity, ON–OFF electrical ability, optical switching, and electrochemical redox properties.[40]

ECH can be produced using complex chemical processes that involve several steps or, simply, by in situ polymerization. The latter is illustrated in Figure 1.2-2(a), which depicts the electrochemical polymerization of the CP inside a hydrogel while Figure 1.2-2(b) exemplifies the mixture of CPs and hydrogel monomers with initiators or oxidants (a single cocktail) after a step-wise polymerization.[40,42,44]

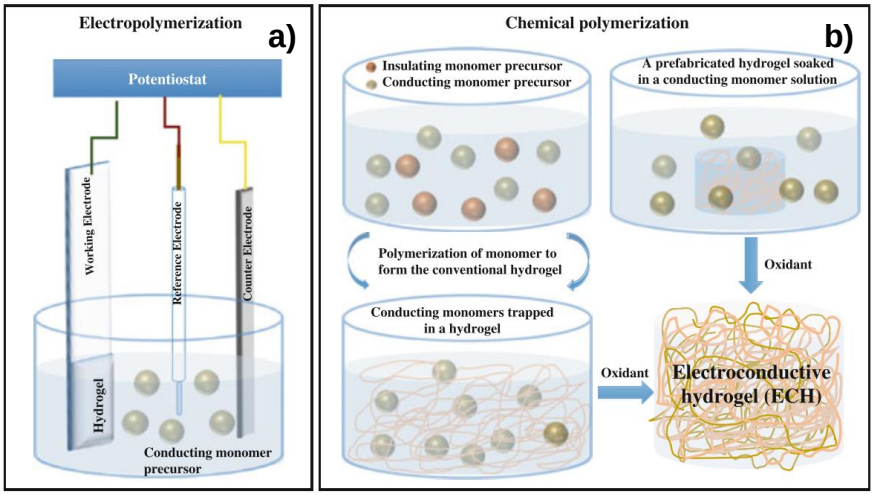

Figure 1.2-2. Schematic representation of approaches developed to fabricate ECHs: a) Electropolymerization and b) chemical polymerization by the monomer precursors of both the hydrogel and the CP. In b) the polymerization occurs either simultaneously or step-wise by the addition of the appropriate initiators/oxidants or by a prefabricated hydrogel soaking in a solution of the monomer precursor of the CP. Reproduced with permission.[44] Copyright © 2016, Springer Nature.

ECH electrodes have been recently developed in parallel to new technologies that demand low scale and elastic devices. Green *et al.*[45] produced hybrid materials by photopolymerizing 18 w/w% poly (vinyl alcohol) (PVA) and 2 w/w% heparin methacrylate (Hep-MA) or 30 w/w% Hep-MA onto platinum disc electrodes, pre-coated with PEDOT, doped with *para*-toluenesulfonate (PEDOT/pTS), and finally electrodepositing PEDOT. The conductivity increased from 0.1 ± 0.01 S cm^{-1} for Hep-MA/PVA without PEDOT to 1.1 ± 0.2 S cm^{-1}, when the CP was incorporated into the matrix.[45]

Ghosh *et al.* prepared an aqueous dispersion of PEDOT in PSS (Polystyrene Sulfonate) using $MgSO_4$ as crosslinker.[46] Others researchers, like Sekine *et al.*, [47] Mawad *et al.*[48] and Ghosh *et al.*,[49] have developed PEDOT-based ECHs.

Table 1.2-2 summarizes some applications of hydrogels to the energy storage field, including their use as solid electrolytes or ECH-based electrodes.

Table 1.2-2. Summary of some advances in capacitors, electrodes and electrolytes based on hydrogels. The method of synthesis, application, electrical conductivity and/or electrochemical capacitance are reported.

	Compound*	Method of synthesis of electrode and electrolyte hydrogel	Application	Conductivity /Aerial or gravimetric capacitance	Ref
Capacitors**	Carbon/PAAK-KOH	Chemical reaction	EDL supercapacitors	150 F g^{-1}	50
	CNT/PANI	Electrochemical reaction	Flexible solid-state supercapacitor	0.185 F cm^{-2}	51
	CNT/PVA	Cast/ Chemical reaction	EDL supercapacitors	100-112 F g^{-1}	52
	Graphene// PVA-H_2SO_4	Chemical reaction	Flexible solid-state supercapacitors	186 F g^{-1}	8
	PAAm-PEDOT/PSS// PAAm-$LiClO_4$	Chemical reaction	Supercapacitor	$8.38x10^{-4}$ F g^{-1}	53
	PEDOT/γ-PGA// γ-PGA-$NaHCO_3$	Chemical/Electrochemical reaction	Supercapacitor	168 F g^{-1}	10
	PF–rGO–PANI//H_2SO_4// PF–rGO	Chemical reaction	Asymmetric capacitor	0.989 F cm^{-2}	54
	PPy-C//PVA–H_2SO_4	Chemical reaction	Supercapacitor	380 F g^{-1}	55
	SiNP-PANi// $LiPF_6$	Electrochemical reaction	Electrodes for Ni batteries	----	56

Continuation.Table 1.2-2.

	Compound*	Method of synthesis of electrode and electrolyte hydrogel	Application	Conductivity/ Aerial or gravimetric capacitance	Ref
ECH electrodes	3D PEDOTCOOH/APMA	Chemical reaction	Sensor for bioelectric signals or tissue engineering	----	48
	PANI/chitosan	Wet Spinning/Electrochemical reaction	Power devices at industrial level	703 F g^{-1}	57
	PEDOT/PSS	Chemical reaction	Electro sensors, supercapacitors, flexible electronics to soft machines	x10^{-2} S cm^{-1}	42
	PEDOT-PSS/PPy	Electrochemical reaction/ Cast	Supercapacitors	65 F g^{-1}	58
	PAAm -PPy	Chemical and electrochemical reaction	Electrodes for batteries and capacitors	----	35
Electrolytes	P(ECH-co-EO) /KOH	Chemical reaction/Cast	Electrolyte for batteries	10^{-3} S cm^{-1} at RT	59
	PEO/KOH–H_2O	Chemical reaction	Electrolytes in thin film energy storage devices	10^{-3} at RT	60
	PVA- H_2SO_4	Chemical reaction	Multiple applications (scalability)	17.3 S cm^{-1} 34.1 F g^{-1}	61
	PVA/Na_2SO_4	Freezing/thawing	Electrolytes for high voltage and safe flexible supercapacitors	135 F g^{-1} at 0.8V	38
	Sulfonated polypropylene /PAAK/KOH	Chemical reaction	Electrolyte in EDL capacitor	110 F g^{-1}	62

* **APMA**: N-(3-Aminopropyl) methacrylamide hydrochloride; **CNT**: Carbon Nanotube; **P(ECH-co-EO):** Copolymer epichlorohydrin/ ethylene oxide; **PAAK**: Potassium polyacrylate; **PEDOTCOOH**: Carboxy-poly(3,4-ethylenedioxythiophene); **PF**: Paper Fiber; **rGO**: Reduced graphene oxide; **SiNP**: Silicon Nanoparticles.
** Configured with a separator in between the electrodes.

In addition of the intrinsic good properties discussed for ECHs, next section is devoted to inorganic compounds that can be incorporated into the ECH matrix to improve the electrical and electrochemical properties.[42,44]

1.2.4. Fillers: Al_2O_3

The term filler, which includes lots of materials, refers to solid particulates immiscible with the polymer but dispersed into it. Fillers can be classified according to their chemical nature, for example: inorganics (oxides, hydroxides, salts, silicates, metals, etc) and organics (carbon, graphite, natural polymers, synthetic polymers, etc.); or by size, shape and aspect ratio (cube, sphere, block, plate, flake, fiber).[63]

Fillers are known as modifiers of mechanical, electrical and magnetic properties, surface, fire retardant capacity, and processing aids. The minerals more commonly used in the polymer industry are talc calcium carbonate, mica, kaolin, wollastonite, feldspar and barite. To dimension their industrial relevance, it is estimated that the demand is higher than 15 million tons of global demand for fillers or reinforcing fillers by year.[27,63]

The homogenously dispersion of fillers maintains the equilibrium necessary between the conduction of the counterions present in solution and the charge storage through the polarons along the CP chains, necessary for the energy storage devices. Some authors determined that particles smaller than 1 µm (nanosized particles) increase the conductivity pathways. Specifically, a decrease in the aspect ratio of the particle size may produce a move away from the percolation zone.[27] Siekierski *et al.*[64] found that the percentage of filler needed to enhance the conductivity in this case, of the composite electrolytes based on LiI/Al_2O_3 and $CuCl/Al_2O_3$ decreases with the size of the particle. For example, the maximum conductivity was obtained with a content of particles lower than 5 w/w% when their size was 3 µm, while for particles of 11 µm at the required content was 23 w/w%. Other properties that may be affected by the filler addition are the dissipation factor, the dielectric constant, the thermal stability and the heat dissipation,[65,66] and the mechanical properties of the composite.[67-70]

In this work, alumina (Al_2O_3) was used as filler to enhance the mechanical strength, volume control and capacitance of electrodes. Al_2O_3 is a widely used material in areas such as catalysis, coatings and microelectronics, due to its excellent properties: hardness, wear resistance, excellent dielectric properties, high strength and stiffness, and resistance to acids and alkali attack at elevated temperatures.[28] In addition, Al_2O_3 increases the thermal stability and produces heat dissipation.

Besides, Al_2O_3 exhibits amphoteric character due to its surface hydroxyl groups.[71] Depending on the pH, the surface will become positively (acid solution) or negatively (basic solution) charged.[72]

Table 1.2-3 presents a compendium of Al_2O_3-based composites used to fabricate rigid and flexible electrodes, electrolytes, or capacitors.

Table 1.2-3. CP-alumina and ECH-alumina composites with a brief description of the synthesis, and the electrical conductivity (κ, in S·cm^{-1}) and mechanical properties (Young modulus, E, and tensile strength, σ, both in MPa).

Composite*	Description of the synthesis	Properties	Ref
PS-*b*-PMMA / Cu-Al_2O_3 **PS / Cu-Al_2O_3**	Dispersion filler/polymer solution (3-21 w/w% Cu-Al_2O_3) and cast. Stirring time: 6h. Solvent: THF.	κ: 5.55×10^{-5} for PS-*b*-PMMA; and 5.0×10^{-6} for PS E: 1122 for PS-*b*-PMMA; 1053.9 for PS σ: 27.998 for PS-*b*-PMMA; 30.585 for PS	73
TEGDA-BA / CPE/ Al_2O_3	Mixing polymer + 0-10 wt.% Al_2O_3 (10-20 nm grain size). Stirring time: 4 h. Heating: 80 °C (30min) for thermal polymerization. Cast on Teflon plate.	κ: 6.02×10^{-3}	74
PVA/P(MA-*co*-AHPS) / Al_2O_3	Composite gel polymer + Al_2O_3 5-50 w/w% (100 nm pore size). Suspension in water. Stirring time: 24 h. Mechanical stirring. Cast.	κ: 1.08×10^{-3}	75

Continuation.Table 1.2-2.

Composite*	Description of the synthesis	Properties	Ref
Chitosan / NH_4SCN / Al_2O_3	Composite gel polymer Al_2O_3 (<50 nm) 3-15 w/w%. Film cast process. Stirring time: 3 h. Solvent: Glacial acetic.	κ: 5.86×10^{-4}	76
PEO / Al_2O_3	Melt, mix (180 °C), 5 min, 32 rpm. Compression molded.	κ: 15×10^{-8} at 100 000 Hz	77
QPV / Al_2O_3	Composite polymer - Al_2O_3 (10-30 nm, 200 $m^2\ g^{-1}$) 0-10 wt. %. Solution cast method. Stirring time: 1st step, 85 °C, 3 h and 2nd step, 65 °C, 4 h. Dry cast film temperature: 60 °C. Solvent: KOH.	κ: 4.79×10^{-11} at 70 °C	78
$PEO_9(MgClO_4)_2/Al_2O_3$	Al_2O_3, 0-18.5 w/w%. Stirring time: 24 h at room temperature. Cast and dry 24 h. Solvent: Anhydrous acetonitrile.	κ: 3.7×10^{-3} at 100 °C	79
PVdF-HFP/PEG/Al_2O_3	Solvent: Acetone. Stir time: 8 h. Cast as film. Dry at 80 °C, 12 h.	κ: 9×10^{-2}	80

* **CPE**: composite polymer electrolyte; **P(MA-*co*-AHPS)**: poly(methyl acrylate-co-sulfonate allyloxy; **PMMA**: poly (methyl methacrylate); **PS**: polystyrene; **PVdF-HFP**: poly(vinylidene fluoride-co-hexafluoropropene; **QPV:** Quaternized poly(vinylalcohol); **TEGDA-BA**: triethylene glycol diacetate-2-propenoic acid butyl ester.

Electrogeneration of CPs, which follows a radical polycondensation mechanism, occurs in combination with the p-type doping process (*i.e.* the formation of positively charged *polarons* and *bipolarons*). The p-type doping is the most frequent in CPs since they exhibit an intrinsic tendency towards oxidation. The quinoid structure obtained in the oxidized state results in a reduction of the band gap, enhancing the electrical conductivity and, therefore, favoring applications related with the fabrication of electronic components. On the other hand, cationic dopants act as reducing agents of CPs.[81] Next sub-section briefly describes the antecedents for the n-type doping of PEDOT.

1.2.5. n-type doping

As a part of CP electrodes, the study of n-type doped PEDOT deserves attention because of the applications of this material in photovoltaic optoelectronic devices and supercapacitors.[82] In spite of

the advantages of this substituted PTh, the amount of studies related with its reduction through either chemical and electrochemical reduction reactions is very scarce.[83-85] The preferences of PEDOT towards oxidation are typically attributed to the electron donor properties of the oxygen atoms at the fused dioxane ring, which reduce the oxidation potential. The low stability of n-doped PEDOT with respect to p-doped was demonstrated by Ahoen *et al.*,[84] who reported a drastic reduction in the Coulombic efficiency of n-doped PEDOT (~50%) after a relatively small number of oxidation-reduction cycles.

The conductivity of n-doped PEDOT is around 1% of the p-doped (*ca.* 0.1 S cm^{-1} at -2.3 V in acetonitrile), which has been attributed to the hampered diffusion of cationic species through the CP matrix and to a higher separation among PEDOT chains neutralized with counterions.[84] Moreover, negative charges are highly localized in n-doped PTh derivatives, which causes a significant reduction of the active conjugation length with respect to the corresponding p-doped materials.[82]

An interesting application of n-doped PEDOT is the fabrication of symmetric supercapacitors, in which the two electrodes are prepared using the same CP.[86]

In this work, an electrochemical methodology has been explicitly developed to produce n-doped PEDOT using ionenes as a potential cationic dopant.[87]

1.2.6. Ionenes

Polyelectrolytes are of fundamental and practical importance since many of them play critical biological functions in nature.[88-90] Within this type of macromolecules, synthetic ionenes represent an important subgroup in which the ionic groups form part of the polymer backbone.[91-92] In general, the term refers to polycations carrying quaternary ammonium as the charged species. From a synthetic point of view, ionenes are typically accessible either by 1)chain or step polymerization of suitable monomers (e.g. Menshutkin reaction between bis-tertiary amines and activated dihalides, self-polyaddition of aminoalkylhalides) or 2)cationic functionalization of reactive precursor polymers.[93,94]

Since the first synthesis of an ionene more than 80 years ago by Marvel and co-workers,[95,96] they have been the subject of intensive investigations in diverse fields including chemistry, biology, physics, medicine and materials science. Such tremendous research activity has culminated with the development of manifold applications of these macromolecular materials in daily life, biosciences and industrial processes (e.g. as antibacterial agents or building blocks for the preparation of chromatography stationary phases, symplexes or functional gels, among other uses).[91]

The unique physical and chemical properties of these polymers are the result of a judicious balance between multiple interactions including hydrophobic, charge transfer and long-ranged electrostatic interactions. As for all polycations, besides the density and charge distribution along the backbone, the nature of the counterion, the molecular weight, flexibility and hydrogen bonding capability of the polymer chain are also critical aspects that may markedly influence the conformation and dynamics of polymer chains. Additionally, their considerable structural versatility (e.g. achievable via counterion exchange, chemical modification of monomers, polymerization method) and key features such as electrostatic stabilization of colloids and tunability of their mechanical properties can be used to induce the formation of stable polyelectrolyte hydrogels for applications in biomedicine, engineering and food science.[97,98]

In this Thesis, we reasoned that using different structural isomers of phenylenediamine-containing ionene polymers as dopant agents for the preparation of n-doped CP would lead to different types of electrodes if cross-linked networks are induced by applying an in situ thermal hydrogelation process.

1.3. Bibliography

(1) Jacobson, M. Z.; Delucchi, M. A.; Bauer, Z. A. F.; Goodman, S. C.; Chapman, W. E.; Cameron, M. A.; Bozonnat, C.; Chobadi, L.; Clonts, H. A.; Enevoldsen, P.; et al. 100% Clean and Renewable Wind, Water, and Sunlight All-Sector Energy Roadmaps for 139 Countries of the World. *Joule.* **2017**, *1* (1) 1–14.

(2) Snook, G. A.; Kao, P.; Best, A. S. Conducting-Polymer-Based Supercapacitor Devices and Electrodes. *J. Power Sources.* **2011**, *196* (1), 1–12.

(3) Beaudin, M.; Zareipour, H.; Schellenberg, A.; Rosehart, W. Energy Storage for Mitigating the Variability of Renewable Electricity Sources. *Energy Storage Smart Grids Plan. Oper. Renew. Var. Energy Resour.* **2014**, *14* (4), 1–33.

(4) Lai, C. S.; Jia, Y.; Lai, L. L.; Xu, Z.; McCulloch, M. D.; Wong, K. P. A Comprehensive Review on Large-Scale Photovoltaic System with Applications of Electrical Energy Storage. *Renew. Sustain. Energy Rev.* **2017**, *78* (32), 439–451.

(5) GWEC. *Global Wind Report 2016*; Mongolia, 2017.

(6) Khetarpal, D. *World Energy Resources: Solar*; 2016.

(7) Simon, P.; Gogotsi, Y. Materials for Electrochemical Capacitors. *Nat. Mater.* **2008**, *7* (11), 845–854.

(8) Xu, Y.; Lin, Z.; Huang, X.; Liu, Y.; Huang, Y.; Duan, X. Flexible Solid-State Supercapacitors Based on Three-Dimensional Graphene Hydrogel Films. *ACS Nano.* **2013**, *7* (5), 4042–4049.

(9) Muruganantham, B.; Gnanadass, R.; Padhy, N. P. Challenges with Renewable Energy Sources and Storage in Practical Distribution Systems. *Renew. Sustain. Energy Rev.* **2017**, *73* (11), 125–134.

(10) Pérez-Madrigal, M. M.; Edo, M. G.; Díaz, A.; Puiggalí, J.; Alemán, C. Poly-γ-glutamic Acid Hydrogels as Electrolyte for Poly(3,4-ethylenedioxythiophene)-Based Supercapacitors. *J. Phys. Chem. C.* **2017**, *121* (6), 3182–3193.

(11) ABB. Static Var Compensator An Insurance for Improved Grid System Stability and Reliability. *Elanders Sverige AB*: Sweden 2015, pp 1–15.

(12) Aricò, A. S.; Bruce, P.; Scrosati, B.; Tarascon, J.; Schalkwijk, W. V. A. N.; Picardie, U. De; Verne, J.; Umr-, C. Nanostructured Materials for Advanced Energy Conversion and Storage Devices. *Nat. Mater.* **2005**, *4* (1), 366–377.

(13) Choudhury, N. A.; Sampath, S.; Shukla, A. K. Hydrogel-Polymer Electrolytes for Electrochemical Capacitors: An Overview. *Energy Environ. Sci.* **2009**, *2* (1), 55–67.

(14) Zhang, Y.; Feng, H.; Wu, X.; Wang, L.; Zhang, A.; Xia, T.; Dong, H.; Li, X.; Zhang, L. Progress of Electrochemical Capacitor Electrode Materials: A Review. *Int. J. Hydrogen Energy.* **2009**, *34* (11), 4889–4899.

(15) Lian, K. Proton-Conducting Polymer Electrolytes and Their Applications in Solid Supercapacitors : A Review RSC Advances. *RSC Adv.* **2014**, *4* (62), 33091–33113.

(16) González, A.; Goikolea, E.; Barrena, J. A.; Mysyk, R. Review on Supercapacitors: Technologies and Materials. *Renew. Sustain. Energy Rev.* **2016**, *58* (1), 1189–1206.

(17) Jost, K.; Dion, G.; Gogotsi, Y. Textile Energy Storage in Perspective. *J. Mater. Chem. A.* **2014**, *2* (28), 10776-10787.

(18) Dubal, D. P.; Ayyad, O.; Ruiz, V.; Gómez-Romero, P. Hybrid Energy Storage: The Merging of Battery and Supercapacitor Chemistries. *Chem. Soc. Rev.* **2015**, *44* (7), 1777–1790.

(19) Shirakawa, H.; Louis, E. J.; Macdiarmid, A. G.; Chiang, N. K.; Heegert, A. J. Synthesis of Electrically Conducting Organic Polymers : Halogen Derivatives of Polyacetylene, (CH). *J. Chem. Soc. Chem. Commun.* **1977**, (16), 578–580.

(20) Bakhshi, A. K.; Bhalla, G. Electrically Conducting Polymers: Materials of the Twentyfirst Century. *J. Sci. Ind. Res.* **2004**, *63* (9), 715–728.

(21) Wallace, G.; Spinks, G.; Kane-Maguire, L.; Teasdale, P. *Conductive Electroactive Polymers. Intelligent Polymer Systems*, 3rd ed.; CRC Press: United Stated, 2008.

(22) Le, T.-H.; Kim, Y.; Yoon, H. Electrical and Electrochemical Properties of Conducting Polymers. *Polymers.* **2017**, *9* (4), 150.

(23) Elschner, A.; Stephan, K.; Lovenich, W.; Merker, U.; Reuter, K. *PEDOT. Principles and Applications of an Intrinsically Conductive Polymer*, 1st ed.; CRC Press: United Stated, 2011.

(24) Lange, U.; Roznyatovskaya, N. V.; Mirsky, V. M. Conducting Polymers in Chemical Sensors and Arrays. *Anal. Chim. Acta.* **2008**, *614* (1), 1–26.

(25) Alemán, C.; Curcó, D.; Casanovas, J. A Density Functional Theory Study of N-Doped 3,4-Ethylenedioxythiophene Oligomers. *Chem. Phys. Lett.* **2004**, *386* (4–6), 408–413.

(26) Wang, J.; Cai, K.; Shen, S. A Facile Chemical Reduction Approach for Effectively Tuning Thermoelectric Properties of PEDOT Films. *Org. Electron.* **2015**, *17* (1), 151–158.

(27) Kaur, G.; Adhikari, R.; Cass, P.; Bown, M.; Gunatillake, P. Electrically Conductive Polymers and Composites for Biomedical Applications. *RSC Adv.* **2015**, *5* (47), 37553–37567.

(28) Elimat, Z.; Zihlif, A.; Schulte, K.; de la Vega, A.; Ragosta, G. Electrical Characterization of Polyethylene Oxide-Alumina Composite. *J. Thermoplast. Compos. Mater.* **2013**, *26* (2), 176–192.

(29) Bandara, T. M. W. J.; Karunathilaka, D. G. N.; Ratnasekera, J. L.; De, L. A. Electrical and Complex Dielectric Behaviour of Composite Polymer Electrolyte Based on PEO , Alumina and Tetrapropylammonium Iodide. *Ionics.* **2017**, *23* (7), 1711–1719.

(30) Nyholm, L.; Nyström, G.; Mihranyan, A.; Strømme, M. Toward Flexible Polymer and Paper-Based Energy Storage Devices. *Adv. Mater.* **2011**, *23* (33), 3751–3769.

(31) Bhat, D. K.; Kumar, M. S. N and P Doped Poly(3,4-Ethylenedioxythiophene) Electrode Materials for Symmetric Redox Supercapacitors. *J. Mater. Sci.* **2007**, *42* (19), 8158–8162.

(32) Wang, J.; Xu, Y.; Sun, X.; Li, X.; Du, X. Electrochemical Capacitance of the Composite of Poly(3,4-ethylenedioxythiophene) and Functionalized Single-Walled Carbon Nanotubes. *J. Solid State Electrochem.* **2008**, *12* (7–8), 947–952.

(33) Aradilla, D.; Azambuja, D.; Estrany, F.; Casas, M. T.; Ferreira, C. A.; Alemán, C.; Alemán, C. Hybrid Polythiophene–Clay Exfoliated Nanocomposites for Ultracapacitor Devices. *J. Mater. Chem.* **2012**, *22* (26), 13110-13122.

(34) Aradilla, D.; Estrany, F.; Alemán, C. Symmetric Supercapacitors Based on Multilayers of Conducting Polymers. *J. Phys. Chem. C.* **2011**, *115* (16), 8430–8438.

(35) Kim, B. C.; Spinks, G. M.; Wallace, G. G.; John, R.; Cho, S. I.; Lee, S. B.; Ghosh, S.; Inganäs, O.; Green, R. A.; Baek, S.; et al. Electroformation of Conducting Polymers in a Hydrogel Support Matrix. *Polymer.* **2000**, *41* (5), 1783–1790.

(36) Gupta, P.; Vermani, K.; Garg, S. Hydrogels: From Controlled Release to pH-Responsive Drug Delivery. *Drug Discov. Today.* **2002**, *7* (10), 569–579.

(37) Armelin, E.; Pérez-Madrigal, M. M.; Alemán, C.; Díaz, D. D. Current Status and Challenges of Biohydrogels for Applications as Supercapacitors and Secondary Batteries. *J. Mater. Chem. A.* **2016**, *4* (23), 8952–8968.

(38) Batisse, N.; Raymundo-Piñero, E. A Self-Standing Hydrogel Neutral Electrolyte for High Voltage and Safe Flexible Supercapacitors. *J. Power Sources.* **2017**, *348* (1), 168–174.

(39) Shi, Z.; Gao, X.; Ullah, M. W.; Li, S.; Wang, Q.; Yang, G. Electroconductive Natural Polymer-Based Hydrogels. *Biomaterials.* **2016**, *111* (1), 40–54.

(40) Guiseppi-Elie, A. Electroconductive Hydrogels: Synthesis, Characterization and Biomedical Applications. *Biomaterials.* **2010**, *31* (10), 2701–2716.

(41) Wu, D.; Xu, F.; Sun, B.; Fu, R.; He, H.; Matyjaszewski, K. Design and Preparation of Porous Polymers. *Chem. Rev.* **2012**, *112* (7), 3959–4015.

(42) Dai, T.; Shi, Z.; Shen, C.; Wang, J.; Lu, Y. Self-Strengthened Conducting Polymer Hydrogels. *Synth. Met.* **2010**, *160* (9–10), 1101–1106.

(43) Green, R. A.; Baek, S.; Poole-Warren, L. A.; Martens, P. J. Conducting Polymer-Hydrogels for Medical Electrode Applications. *Sci. Technol. Adv. Mater. Sci. Technol. Adv. Mater.* **2010**, *11* (11), 14107–14113.

(44) Mawad, D.; Lauto, A.; Wallace, G. G. Conductive Polymer Hydrogels. In *Polymeric Hydrogels as*

Smart Biomaterials; Springer International: Switzerland, 2016; pp 19–45.

(45) Green, R. A.; Hassarati, R. T.; Goding, J. A.; Baek, S.; Lovell, N. H.; Martens, P. J.; Poole-warren, L. A. Conductive Hydrogels : Mechanically Robust Hybrids for Use as Biomaterials. *Macromol. Biosci.* **2012**, *12* (4), 22–24.

(46) Ghosh, S.; Inganäs, O. Conducting Polymer Hydrogels as 3D Electrodes: Applications for Supercapacitors. *Adv. Mater.* **1999**, *11* (14), 1214–1218.

(47) Sekine, S.; Ido, Y.; Miyake, T.; Nagamine, K.; Nishizawa, M. Conducting Polymer Electrodes Printed on Hydrogel. *J. Am. Chem. Soc.* **2010**, *132* (38), 13174–13175.

(48) Mawad, D.; Artzy-schnirman, A.; Tonkin, J.; Ramos, J.; Inal, S.; Mahat, M. M.; Darwish, N.; Zwidantsis, L.; Malliaras, G. G.; Gooding, J. J.; et al. Electroconductive Hydrogel Based on Functional Poly(ethylenedioxythiophene). *Chem. Mater.* **2016**, *28* (17), 6080–6088.

(49) Ghosh, S.; Inganas, O. Electrochemical Characterization of Poly(3,4-ethylenedioxythiophene) Based Conducting Hydrogel Networks. *J. Electrochem. Soc.* **2000**, *147* (5), 1872–1877.

(50) Nohara, S.; Wada, H.; Furukawa, N.; Inoue, H.; Morita, M.; Iwakura, C. Electrochemical Characterization of New Electric Double Layer Capacitor with Polymer Hydrogel Electrolyte. *Electrochim. Acta.* **2003**, *48* (6), 749–753.

(51) Zeng, S.; Chen, H.; Cai, F.; Kang, Y.; Chen, M.; Li, Q. Electrochemical Fabrication of Carbon Nanotube/Polyaniline Hydrogel Film for All-Solid-State Flexible Supercapacitor with High Areal Capacitance. *J. Mater. Chem. A*, **2015**, *3* (47), 23864–23870.

(52) Yang, C. C.; Hsu, S. T.; Chien, W. C. All Solid-State Electric Double-Layer Capacitors Based on Alkaline Polyvinyl Alcohol Polymer Electrolytes. *J. Power Sources.* **2005**, *152* (1–2), 303–310.

(53) Aouada, F. A.; Guilherme, M. R.; Campese, G. M.; Girotto, E. M.; Rubira, A. F.; Muniz, E. C. Electrochemical and Mechanical Properties of Hydrogels Based on Conductive Poly(3,4-ethylenedioxythiophene)/Poly(styrenesulfonate) and PAAm. *Polym. Test.* **2006**, *25* (2), 158–165.

(54) Su, H.; Zhu, P.; Zhang, L.; Zeng, W.; Zhou, F.; li, G.; Li, T.; Wang, Q.; Sun, R.; Wong, C. Low Cost, High Performance Flexible Asymmetric Supercapacitor Based on Modified Filter Paper and an Ultra-Fast Packaging Technique. *RSC Adv.* **2016**, *6* (87), 83564–83572.

(55) Shi, Y.; Pan, L.; Liu, B.; Wang, Y.; Cui, Y.; Bao, Z.; Yu, G. Nanostructured Conductive Polypyrrole Hydrogels as High-Performance, Flexible Supercapacitor Electrodes. *J. Mater. Chem. A.* **2014**, *2* (17), 6086–6091.

(56) Wu, H.; Yu, G.; Pan, L.; Liu, N.; McDowell, M. T.; Bao, Z.; Cui, Y. Stable Li-Ion Battery Anodes by in-Situ Polymerization of Conducting Hydrogel to Conformally Coat Silicon Nanoparticles. *Nat. Commun.* **2013**, *4* (1), 1943–1946.

(57) Ismail, Y. A.; Chang, J.; Shin, S. R.; Mane, R. S.; Han, S.-H.; Kim, S. J. Hydrogel-Assisted Polyaniline Microfiber as Controllable Electrochemical Actuatable Supercapacitor. *J. Electrochem. Soc.* **2009**, *156* (4), A313-A317.

(58) Ghosh, S.; Inganas, O. Conducting Polymer Hydrogels as 3D Electrodes : Applications for Supercapacitors. *Adv. Mater.* **1999**, *11* (14), 1214–1218.

(59) Vassal, N.; Salmon, E.; Fauvarque, J. F. Electrochemical Properties of an Alkaline Solid Polymer

Electrolyte Based on P(ECH-Co-EO). *Electrochim. Acta*. **2000**, *45* (8–9), 1527–1532.

(60) Salmon, E.; Guinot, S.; Godet, M.; Fauvarque, J. F. Structural Characterization of New Poly (Ethylene Oxide). *J. Appl. Polym. Sci.* **1997**, *65* (3), 601–607.

(61) Meng, C.; Liu, C.; Chen, L.; Hu, C.; Fan, S. Highly Flexible and All-Solid-State Paperlike Polymer Supercapacitors. *Nano Lett.* **2010**, *10* (10), 4025–4031.

(62) Yoon, C. S.; Ko, J. M.; Latifatu, M.; Lee, H. S.; Lee, Y.-G.; Kim, K. M.; Won, J. H.; Jo, J.; Jang, Y.; Kim, J. H. Electrochemical Properties of Activated Carbon Supecapacitor Containing Sulfonated Polypropylene Separator Coated with a Hydrogel Polymer Electrolyte. *Korean Chem. Eng. Res.* **2014**, *52* (5), 553–557.

(63) Xanthos, M. Polymers and Fillers Functional. In *Functional Fillers for Plastics*; Xanthos, M., Ed.; Wiley VCH, 2005; pp 1–15.

(64) Siekierski, M.; Rzeszotarski, P.; Nadara, K. Conductivity Studies of Composite Polymeric Electrolytes — from Experiment to Computer Modeling. *Solid State Ionics.* **2005**, *176* (25–28), 2129–2136.

(65) Li, Z.; Ju, D.; Han, L.; Dong, L. Formation of More Efficient Thermally Conductive Pathways due to the Synergistic Effect of Boron Nitride and Alumina in Poly(3-hydroxylbutyrate). *Thermochim. Acta*. **2017**, *652*, 9–16.

(66) Jayathilaka, P. A. R. D.; Dissanayake, M. A. K. L.; Albinsson, I.; Mellander, B. E. Effect of Nano-Porous Al_2O_3 on Thermal, Dielectric and Transport Properties of the $(PEO)_9LiTFSI$ Polymer Electrolyte System. *Electrochim. Acta.* **2002**, *47* (20), 3257–3268.

(67) Luo, J.-J.; Daniel, I. M.; Mccormick, R. R. Characterization and Modeling of Mechanical Behavior of Polymer/clay Nanocomposites. *Compos. Sci. Technol.* **2003**, *63* (11), 1607–1616.

(68) Yang, C.-C.; Chiu, S.-J.; Chien, W.-C.; Chiu, S.-S. Quaternized Poly(vinyl alcohol)/Alumina Composite Polymer Membranes for Alkaline Direct Methanol Fuel Cells. *J. Power Sources.* **2010**, *195* (8), 2212–2219.

(69) Dissanayake, M. a. K. L.; Jayathilaka, P. a. R. D.; Bokalawala, R. S. P.; Albinsson, I.; Mellander, B. E. Effect of Concentration and Grain Size of Alumina Filler on the Ionic Conductivity Enhancement of the $(PEO)_9LiCF_3SO_3$:Al_2O_3 Composite Polymer Electrolyte. *J. Power Sources.* **2003**, *119–121*, 409–414.

(70) Khia, M.; Joshi, G. M.; Deshmukh, K.; Pandey, M. Preparation of Modified Polymer Blend and Electrical Performance. *Compos. Interfaces.* **2015**, *22* (3), 167–178.

(71) Egashira, M.; Utsunomiya, Y.; Yoshimoto, N.; Morita, M. Effects of the Surface Treatment of the Al_2 O_3 Filler on the Lithium Electrode / Solid Polymer Electrolyte Interface Properties. *Electrochim. Acta.* **2006**, *52* (3), 1082–1086.

(72) Pham, T. D.; Kobayashi, M.; Adachi, Y. Interfacial Characterization of α-Alumina with Small Surface Area by Streaming Potential and Chromatography. *Colloids Surfaces A Physicochem. Eng. Asp.* **2013**, *436* (5), 148–157.

(73) Nadeem, Q.; Rizwan, M.; Gill, R.; Rafique, M.; Shahid, M. Fabrication of Alumina Based Electrically Conductive Polymer Composites. *J. Appl. Polym. Sci.* **2016**, *133* (5), 1-12

(74) Wang, Q.; Song, W.; Fan, L.; Shi, Q. Effect of Alumina on Triethylene Glycol Diacetate-2-Propenoic Acid Butyl Ester Composite Polymer Electrolytes for Fl Exible Lithium Ion Batteries. *J. Power Sources.* **2015**,

279 (1), 405–412.

(75) Mallakpour, S.; Khadem, E. Recent Development in the Synthesis of Polymer Nanocomposites Based on Nano-Alumina. *Prog. Polym. Sci.* **2015**, *51* (1), 74–93.

(76) Tominaga, Y.; Endo, M. Ion-Conductive Properties of Polyether-Based Composite Electrolytes Filled with Mesoporous Silica, Alumina and Titania. *Electrochim. Acta.* **2013**, *113* (1), 361–365.

(77) Wu, H.; Cummings, O. T.; Wick, C. D. Computational Investigation on the Effect of Alumina Hydration on Lithium Ion Mobility in Poly(ethylene oxide) $LiClO_4$ Electrolytes. *J. Phys. Chem. B.* **2012**, *116* (51), 14922–14932.

(78) Aziz, N. A.; Majid, S. R.; Yahya, R.; Arof, A. K. Conductivity , Structure , and Thermal Properties of Chitosan-Based Polymer Electrolytes with Nanofillers. *Polym. Adv. Technol.* **2011**, *22* (9), 1345–1348.

(79) Ekanayake, P.; Dissanayake, M. A. K. L. Effect of Nanoporous Alumina Filler on Conductivity Enhancement in $PEO_9(MgClO_4)_2$ Polymer Electrolyte : A 1 H NMR Study. *J. Solid State Electrochem.* **2009**, *13* (12), 1825–1829.

(80) Kumar, G. G.; Kim, P.; Elizabeth, R. N. Structural Characterization of PVdF-HFP / PEG / Al_2O_3 Proton Conducting Membranes for Fuel Cells. *J. Memb. Sci.* **2007**, *303* (1–2), 126–131.

(81) Khomenko, V. G.; Barsukov, V. Z.; Katashinskii, A. S. The Catalytic Activity of Conducting Polymers toward Oxygen Reduction. *Electrochim. Acta.* **2005**, *50* (7–8), 1675–1683.

(82) Neugebauer, H. Infrared Signatures of Positive and Negative Charge Carriers in Conjugated Polymers with Low Band Gaps. *J. Electroanal. Chem.* **2004**, *563* (1), 153–159.

(83) Martinez, J. G.; Berrueco, B.; Otero, T. F. Deep Reduced PEDOT Films Support Electrochemical Applications : Biomimetic Color Front. *Front. Bioeng. Biotechnol.* **2015**, *3* (2), 1–6.

(84) Ahonen, H. J.; Lukkari, J.; Kankare, J. N- and P-Doped Poly(3,4-Ethylenedioxythiophene): Two Electronically Conducting States of the Polymer. *Macromolecules.* **2000**, *33* (18), 6787–6793.

(85) Hillman, A. R.; Daisley, S. J.; Bruckenstein, S. Ion and Solvent Transfers and Trapping Phenomena during N-Doping of PEDOT Films. *Electrochim. Acta.* **2008**, *53* (11), 3763–3771.

(86) Kurra, N.; Wang, R.; Alshareef, H. N. All Conducting Polymer Electrodes for Asymmetric Solid-State Supercapacitors. *J. Mater. Chem. A.* **2015**, *3* (14), 7368–7374.

(87) Bachl, J.; Zanuy, D.; López-Pérez, D. E.; Revilla-lópez, G.; Cativiela, C.; Alemán, C.; Díaz, D. D. Synergistic Computational-Experimental Approach to Improve Ionene Polymer-Based Functional Hydrogels. *Adv. Funct. Mater.* **2014**, *24* (31), 4893–4904.

(88) Netz, R. R.; Andelman, D. Neutral and Charged Polymers at Interfaces. *Phys. Rep.* **2003**, *380* (1–2), 1–95.

(89) Grosberg, A. Y.; Nguyen, T. T.; Shklovskii, B. I. Low Temperature Physics at Room Temperature in Water: Charge Inversion in Chemical and Biological Systems. *Int. J. High Speed Electron. Syst.* **2002**, *12* (2), 235–265.

(90) Poinsignon, C. Polymer Electrolytes. *Mat. Sci. Eng., B.* **1989**, *B3* (1-2), 31 – 37.

(91) Jaeger, W.; Bohrisch, J.; Laschewsky, A. Synthetic Polymers with Quaternary Nitrogen Atoms-Synthesis and Structure of the Most Used Type of Cationic Polyelectrolytes. *Prog. Polym. Sci.* **2010**, *35* (5), 511–577.

(92) Noguchi, H. *Ionene Polymers. In Polymeric Materials Encyclopedia*, J. C. Salo.; CRC Press: Boca Raton, London, New York, Tokyo, 1996.

(93) Laschewsky, A. Recent Trends in the Synthesis of Polyelectrolytes. *Curr. Opin. Colloid Interface Sci.* **2012**, *17* (2), 56–63.

(94) Williams, S. R.; Long, T. E. Recent Advances in the Synthesis and Structure-Property Relationships of Ammonium Ionenes. *Prog. Polym. Sci.* **2009**, *34* (8), 762–782.

(95) Littmann, E. R.; Marvel, C. S. Cyclic Quaternary Ammonium Salts from Halogenated Aliphatic Tertiary Amines. *J. Am. Chem. Soc.* **1930**, *52* (1), 287–294.

(96) Gibbs, C. F.; Littmann, E. R.; Marvel, C. S. Quaternary Ammonium Salts from Halogenated Alkyl Dimethylamines. II. The Polymerization of Gamma-Halogenopropyldimethylamines. *J. Am. Chem. Soc.* **1933**, *55* (2), 753–757.

(97) Friedman, M. Chemistry, Biochemistry, and Safety of Acrylamide. A Review. *J. Agric. Food Chem.* **2003**, *51* (16), 4504–4526.

(98) Oh, J. K.; Drumright, R.; Siegwart, D. J.; Matyjaszewski, K. The Development of Microgels/nanogels for Drug Delivery Applications. *Prog. Polym. Sci.* **2008**, *33* (4), 448–477.

Chapter II

2.1. Objectives

The first part of the Results (Chapter III) presents three consecutive studies in which we hierarchically develop flexible supercapacitors based on PEDOT/Al_2O_3 composites loaded into hydrogels prepared using PGA from biosynthesis. The general and specific objectives of each of studies can be summarized as follows:

1) Evaluation of the properties of in situ polymerized PEDOT/Al_2O_3 composites for energy storage applications,

1a) Analysis of the influence of the Al_2O_3 content and the pH of the generation medium in the properties of PEDOT/ Al_2O_3 composites.

1b) Evaluation of the continuous and multi-step *in situ* polymerization strategies for the preparation of PEDOT/ Al_2O_3 composites.

1c) Comparison of the electrochemical properties for energy storage of PEDOT/Al_2O_3 composites and pure PEDOT.

2) Preparation of flexible electrodes for supercapacitors based on the supramolecular assembly of biohydrogel and PEDOT,

2a) Synthesis in aqueous environment of poly-γ-glutamic acid (γ-PGA) biohydrogel loaded with PEDOT particles.

2b) Design of a strategy to increase the electrosensitivity of the γ-PGA biohydrogel loaded with PEDOT particles. This strategy has been focused on the use of the latter particles as nucleation sites for the *in situ* electropolymerization of poly(hydroxymethyl-3,4-ethylenedioxythiophene) (PHMeDOT), a PEDOT derivative with an exocyclic hydroxyl group that facilitates its preparation in aqueous media.

2c) Characterization of the loaded γ-PGA biohydrogels before and after the *in situ* electropolymerization of PHMeDOT.

2d) Evaluation of the performance of these composites as flexible electrodes for electrochemical supercapacitors.

3) Combine the results obtained in 1) and 2) to develop a new solid organic symmetric supercapacitor prototype.

3a) Synthesis and characterization of electrodes made of γ-PGA, PEDOT microparticles, PHMeDOT polymerized around PEDOT particles, and Al_2O_3.

3b) Fabrication of a flexible, lightweight and compact prototype combining two self-supported p-doped electrodes prepared as in 3a) and a solid supporting electrolyte composed by γ-PGA biohydrogel doped with $NaHCO_3$.

3c) Evaluation of the electrochemical performance the fabricated prototype as a flexible, lightweight and compact energy storage device.

The utilization of polycations bearing a quaternary ammonium in the backbone as n-dopant agents of PEDOT is the focus of second part of the Results (Chapter IV), in which two consecutive studies are reported. In the first one, we develop a synthetic protocol to produce n-doped PEDOT using macromolecular dopant agents, while the second accounts for the influence of the ionene topology on the properties of n-doped PEDOT by comparing three isomeric topomers. The general and specific objectives of each of studies can be summarized as follows:

1) Preparation of n-doped PEDOT using a macromolecular dopant agent for its incorporation into pristine oxidized PEDOT films.

1a) Optimization of the preparation process to achieve the highest n-doping level using a 1,4-diazabicyclo[2.2.2]octane (DABCO)-based ionene bearing *N,N'*-(*meta*-phenylene)dibenzamide linkages as dopant agent.

1b) Evaluation of the properties of the material derived from 1a) and comparison with those of n-doped PEDOT obtained using conventional tetramethylammonium as dopant agent.

2) Preparation of capacitive n-doped electrodes using three different isomeric DABCO-containing ionenes, which differ in the topology of the *N,N*'-(phenylene)dibenzamide linkage (*i.e. ortho*, *meta* and *para*), as polycationic dopants of PEDOT.

2a) Investigation of the influence of the ionene topology in the preparation of PEDOT:ionene electrodes.

2b) Characterization of the chemical and physical properties of PEDOT:ionene electrodes and analysis of the influence of the ionene topology.

2c) Hydrogelation of the ionenes once they have incorporated into the PEDOT matrix by thermally-induced aggregation in acidic conditions.

2d) Investigation of the effects of the *in situ* hydrogelation mentioned in 2c) in the properties of n-doped PEDOT and analysis of the influence of the gelator-topology.

Chapter III

3.1. Properties of in situ polymerized PEDOT/Al_2O_3 composites for energy storage devices

3.1.1. Abstract

Composites formed by PEDOT/Al_2O_3 have been prepared by in situ anodic polymerization. For this purpose, the stability of 1:1 and 4:1 monomer: Al_2O_3 aqueous solutions has been examined as a function of the pH (2.3, 4.0, 7.0, 8.8 or 10.8). Results indicate that the monomer behaves as a dispersant that remains stable at the studied basic pHs despite they are close to the isoelectric point of Al_2O_3. Although the thermal stability of the composites is considerably affected by the pH of the reaction medium, its influence on the surface morphology is very small. Independently of the synthetic conditions, the electrochemical properties were better for PEDOT/Al_2O_3 than for pure PEDOT, reflecting that Al_2O_3 particles promote the charge mobility. The highest specific capacitance (SC), 141 F g^{-1}, which was 55% higher than that obtained for pure PEDOT, was achieved for the composite prepared at pH= 8.8 using a 4:1 monomer: Al_2O_3 ratio. These conditions favor the participation of OH^- groups as secondary doping agents without degrading the polymer matrix and enhance the specific surface of the films, facilitating the ionic mobility. On the other hand, application of a multi-step polymerization strategy has shown that interfaces originated by consecutive steps enhance the *SC*.

TOC graphic

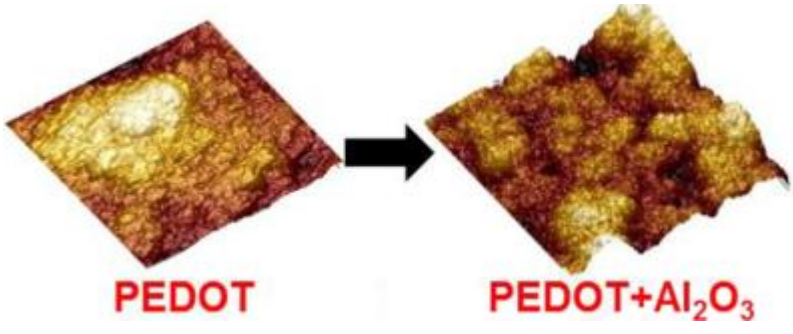

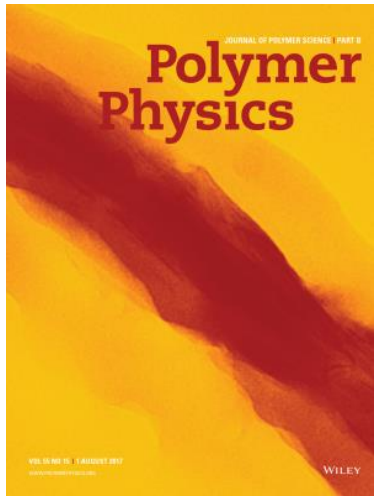

Figure 3.1-1. Cover Image, Volume 55, Issue 15 (pages i–ii) based on the article TEM images of PEDOT containing Al_2O_3 particles.

3.1.2. Introduction

Due to their large capacitance, good electric conductivity, ease of synthesis and low cost, intrinsic conducing polymers (ICPs) are currently considered as mature industrial products for the fabrication of energy storage devices with parallel development activities at the research laboratory level.[1-6] The most commonly used ICPs are PANI, PPy, and PEDOT and their derivatives. Through chemical or electrochemical processes, most ICPs can be synthesized by oxidization of the corresponding monomer in solution.[7] The conductivity and capacitance of these ICPs can be tuned through the dopant, the level of doping and/or the fabrication of a nanocomposite by adding another electroactive material.

Among ICPs, PEDOT has been widely used for the fabrication of energy storage devices because of its outstanding capacitive performance, fast doping-undoping process, stable charge-discharge response, high conductivity, good environmental stability in its doped state, relative ease of preparation, and advantages in cost.[8-13] Furthermore, the capacitive and electrochemical properties of PEDOT have been enhanced forming hybrid nanocomposites through its combination with other materials, as for example with clays,[10] graphene,[14,15] carbon nanotubes,[16] inorganic oxides,[17,18] and even biopolymers.[19,20]

Al_2O_3, commonly named Al_2O_3, represents an attractive material to be used for the fabrication of PEDOT-based electrodes with enhanced electrochemical properties. This ceramic material exhibits noticeable features, as for example, low-cost, availability, non-toxicity and, most importantly, its surface properties in suspensions can be tuned with the pH. Thus, surface hydroxyl groups of Al_2O_3 may react with acid and base at low and high pH, respectively, to form positive and negative charges, respectively, while the Al_2O_3 surface sites are neutral when the isoelectric point is reached at pH=9.2.[21] Thus, the pH-induced interfacial charging properties of Al_2O_3 are expected to be a powerful tool to regulate the characteristics of the PEDOT/Al_2O_3 containing composites

In absence of dispersant, aqueous suspensions of Al_2O_3 particles exhibit colloidal stability at pHs ranging from 3 and 7.8, in which the potential repulsion produced by charged particles preclude aggregation phenomena (*i.e.* van der Waals attraction is overwhelmed).[22] In contrast, van der Waals attraction dominates the total particle–particle interaction when the charge decreases or disappears at the isoelectric point, leading to coagulation of particles in the suspension. Accordingly, the sign and magnitude of the charge onto the Al_2O_3 particle surface will control, at least partially, the interaction of the Al_2O_3 with polymer chains. On the other hand, it has been reported that acidification affects the oxidative polymerization of PEDOT. More specifically, protic and Lewis acids were found to catalyse an equilibrium reaction of 3,4-ethylenedioxythiophene (EDOT) monomers to the corresponding dimeric and trimeric species without further oxidation reaction.[23]

Porous Al_2O_3 membranes with a pore diameter of ~200 nm and a thickness of ~6 μm have been used as a template for the electrochemical synthesis of PEDOT nanotubes[24-27] using an approach based on the pioneering procedure proposed by Martin and co-workers two decades ago.[28-30] Indeed, Al_2O_3 membranes offer advantages as a template over conventional polycarbonate track-etched membranes, such as higher pore density and well-ordered pore structure.[31] However, in spite of their enormous potential for energy storage applications, the electrochemical synthesis of PEDOT/Al_2O_3 in acidic or basic conditions have not explored yet and the properties of the resulting composites are unknown.

On the other hand, in recent studies we investigated the properties of multi-layered systems formed by alternated layers of PEDOT and other ICPs.[8,32-35] We found that such multi-layered composites, which were prepared using the layer-by-layer electrodeposition technique, present higher electrochemical activity and SC than each of the individual ICPs. This improvement was attributed to the synergistic effects produced by both the favorable interactions and the porosity increment at the interfaces of consecutive layers. Such synergistic effects were corroborated by comparing the electrochemical properties of PEDOT films derived from single and multiple polymerization steps

(*i.e.* 1-layered and multi-layered PEDOT films, respectively).[36] Again, both the ability to store charge and electrochemical stability were higher for multi-layered films than for 1-layered ones.

In this work we present a multi-optimization process for preparing PEDOT/Al_2O_3 composites with high *SC* using a simple *in situ* anodic polymerization technique. For this purpose, the influence of the Al_2O_3 content, the pH of the generation medium and the presence of the synergistic effects associated to multi-layered systems, on the electrochemical properties of the composites have been investigated. Besides, the influence of such parameters in the surface morphology, the surface topography and the wettability has been also examined.

3.1.3. Experimental Section

Materials.

EDOT monomer from Aldrich and Al_2O_3 from Panreac were used as received. Anhydrous $LiClO_4$, analytical reagent grade from Aldrich, was stored in an oven at 70 ºC before use in electrochemical experiments. Acetonitrile solvent, hydrochloric acid and sodium hydroxide were purchased from Sigma Aldrich. Milli-Q water grade (0.055 μS cm^{-1}) was used in all synthetic processes.

Inorganic particles diameter and zeta- (ζ-) potential.

The diameter of Al_2O_3 particles in EDOT aqueous solutions was determined by dynamic light scattering (DLS). Measurements were performed at room temperature with a NanoBrook Omni Zeta Potential Analyzer from Brookheaven Instruments Corporation using 10 and 40mM Al_2O_3 aqueous suspensions at all the investigated pHs. The ζ-potential was determined by performing 30 consecutive measurements of 1:1 and 4:1 EDOT: Al_2O_3 samples at each investigated pH.

Synthesis of PEDOT and PEDOT/Al_2O_3.

Both anodic polymerization and electrochemical assays were performed with a potentiostat-galvanostat Autolab PGSTAT101 equipped with the ECD module (Ecochimie, The Netherlands) using a three-electrode compartment cell under nitrogen atmosphere (99.995% pure) at room

temperature. Steel AISI 316 sheets of 2×2 and 2×1cm^2 in area were used as working and counter electrodes, respectively. To prevent interferences during the electrochemical assays, the working and counter electrodes were cleaned with acetone and ethanol before each trial. The reference electrode was an Ag|AgCl electrode containing a KCl saturated aqueous solution (offset potential versus the standard hydrogen electrode, E^0= 0.222V at 25ºC), which was connected to the working compartment through a salt bridge containing the electrolyte solution.

PEDOT films were prepared by chronoamperometry (CA) under a constant potential of 1.10V. The cell was filled with 50mL of a 10mM EDOT aqueous solution at pH of 2.3, 4.0, 7.0, 8.8 or 10.8 containing 0.1M $LiClO_4$ as supporting electrolyte. Before conducting the anodic polymerization of EDOT to produce PEDOT films, the overall solution was stirred at 500rpm for 40min and purged with nitrogen. PEDOT/Al_2O_3 films were obtained using identical conditions with exception of the Al_2O_3 particles, which were added to the generation medium following a 1:1 or 4:1 EDOT: Al_2O_3 ratio. Although the final content of Al_2O_3 is expected to be low, the diffusion of the particles is much smaller than that of monomer. This explains the two 1:1 or 4:1 EDOT: Al_2O_3 ratios selected for this work, which both present a very high content of mineral, especially the 4:1. The polymerization time, θ, was kept fixed at 180 s for PEDOT and PEDOT/Al_2O_3.

The electrochemical properties of conventional 1-layered (1L) films were compared with those of 3-layered (3L) systems, which were obtained applying the layer-by-layer electropolymerization technique. More specifically, 3L-PEDOT/Al_2O_3 were produced using the experimental conditions described for 1L-PEDOT/Al_2O_3 but applying three polymerization steps of θ= 60 s each one (*i.e.* the total polymerization time was identical for 3L-films, 3×60 s= 180 s, than for 1L-ones).

Electrochemical characterization.

All electrochemical assays were performed in acetonitrile with 0.1 M $LiClO_4$ as supporting electrolyte. Cyclic voltammetry (CV) assays were performed to evaluate the *SC* and the electrochemical stability of the composites. The initial and final potentials were -0.5 V, and the reversal potential was 1.6 V. A scan rate of 100 mV s^{-1} was used. In this work the electrochemical stability was evaluated by conducting 50 consecutive cycles.

The *SC* (in F g^{-1}) was determined from the registered voltammograms using the following Eq:

$$SC = \frac{Q}{\Delta V \cdot m} \quad (1)$$

where Q is the voltammetric charge, ΔV is the potential window (in V), and m is the mass of polymer on the surface of the working electrode (in g).

Galvanostatic charge/discharge (GCD) curves between 0.2 and 0.8 V were run. The cycling stability was determined by repeating the GCD test during 100 consecutive cycles. The current was adjusted to provide charge and discharge times in the range between 5 and 30 s.[37] The charge to 0.8 V was performed at 5 mA during 20 s and the discharge to 0.2 V at 1mA during 10 s.

Moreover, GCD profiles were also used as alternative method to measure the *SC*:

$$SC = \frac{i\Delta t}{\Delta V} \quad (2)$$

where i is the current intensity and Δt is the time interval required for the change in voltage ΔV.

The films thickness (L) was derived from the mass of polymer deposited in the electrode (m_{pol}) using the procedure reported by Schirmeisen and Beck.[38] Accordingly, m_{pol} was determined with the following relation:

$$m_{pol} = Q_{pol} \quad \frac{m}{Q} \quad (3)$$

where Q_{pol} is the polymerization charge consumed in the generation of each layer (in mC cm^{-2}) and $m\,Q^{-1}$ is the current productivity (with values in between 0.45±0.02 and 0.70±0.06 mg C^{-1}, depending on the composition). The volume of polymer deposited in the electrode (V_{pol}) was derived from the

values of m_{pol} and the density of PEDOT and PEDOT/Al_2O_3, which was determined using the flotation method.

Morphological and topographical characterization.

Scanning electron microscopy (SEM) studies were performed to examine the surface morphology of PEDOT and PEDOT/Al_2O_3 films. Dried samples were placed in a Focussed Ion Beam Zeis Neon 40 scanning electron microscope operating at 3 kV, equipped with an energy dispersive X-ray (EDX) spectroscopy system. EDX analyses were performed to identify the presence of Al_2O_3 at the surface of PEDOT/Al_2O_3 films.

Atomic force microscopy (AFM) images were obtained with a Molecular Imaging PicoSPM using a NanoScope IV controller under ambient conditions. The tapping mode AFM was operated at constant deflection. The row scanning frequency was set to 1 Hz. AFM measurements were performed on various parts of the films, which provided reproducible images similar to those displayed in this work. The scan window sizes used in this work were 5×5 μm^2. The statistical application of the NanoScope Analysis software was used to determine the root mean square roughness (R_q), which is the average height deviation taken from the mean data plane.

The distribution of Al_2O_3 in composites was examined by transmission electron microscopy (TEM) using a Phillips TECNAI 10 transmission electron microscope at an accelerating voltage of 100kV. For this purpose, small trips of composites were removed from the electrodes with a razor blade and, according the manufacturer protocol, embedded in a low viscosity modified Spurr epoxy resin and curing at 60 ºC for 24 h. Ultra-thin sections (less than 100nm) of these samples were cut at room temperature using a Sorvall Porter-Blum microtome. Finally, the sections were placed on carbon coated cooper grids. Bright field micrographs were taken with a SIS Mega View II digital camera.

Wettability.

Contact angle measurements were performed to examine the influence of Al_2O_3 in the wettability of PEDOT. Measurements were carried out using sessile water drop method at room temperature and controlled humidity. Images of 0.1µL distillate water drops on film surfaces were recorded after stabilization (~10 s) with the equipment OCA 20 (DataPhysics Instruments GmbH, Filderstadt). The software SCA20 was used to analyse the images and acquire the contact angle value. Contact angle values were obtained as the average of 15 independent measures for each sample.

Thermal stability.

The thermal stability of the prepared samples was studied by thermogravimetry (TGA) at a heating rate of 20 ºC min^{-1} (sample weight *ca.* 5 mg) with a Q50 thermogravimetric analyser of TA Instruments and under a flow of dry nitrogen. Test temperatures ranged from 30 to 600 ºC.

3.1.4. Results and discussion

Preparation of Al_2O_3 aqueous dispersions

The solubility of aluminum oxides, hydroxides and oxyhydroxides in aqueous solutions depends on the pH because of the aggregation phenomena induced by the surface charges.[21,22] However, the characteristic pH intervals that typically define the physical properties of aqueous Al_2O_3 dispersions[22] (*e.g.* particle size distribution, surface charge and sedimentation) are expected to be altered by the presence of EDOT monomer during the *in situ* anodic polymerization. Moreover, such properties will have a deep impact in the interfacial interaction between the Al_2O_3 and the polymer matrix in PEDOT/Al_2O_3 composites, as has been observed for other systems involving insulating and electrochemical inactive polymers.[39]

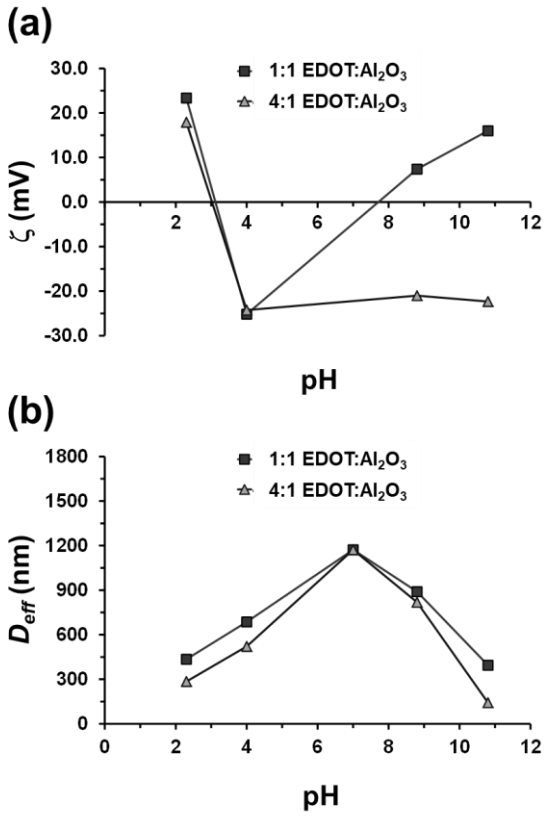

Figure 3.1-2.Variation of (a) the ζ potential and (b) the effective particle diameter as a function of the pH for 1:1 and 4:1 EDOT: Al_2O_3 aqueous dispersions.

Considering the amphoteric behaviour of Al_2O_3, 1:1 and 4:1 EDOT: Al_2O_3 aqueous dispersions were prepared at pH= 2.3, 4.0, 7.0, 8.8 or 10.8. Thus, the oxide groups at the water/ Al_2O_3 interface are expected to protonate or deprotonate depending on the contacting solution pH,[40,41] even though EDOT monomers may interfere causing some deviations with respect to reported behaviour. Figure 3.1-2(a) presents the dependence of ζ-potential of Al_2O_3 as a function of the pH and the EDOT: Al_2O_3 ratio. The ζ-potential indicates the stability of the colloidal dispersion (*i.e.* resistance towards aggregation), reflecting the degree of electrostatic repulsion between adjacent particles in the dispersion. The physical stability of an aqueous dispersion is considered good when the ζ-potential is around +25 or -25 mV.[42] The highest stability of the 1:1 EDOT: Al_2O_3 dispersion is obtained in acidic conditions, the ζ-potential values measured at pH= 2.3 and 4.0 being +23 and -25 mV, respectively.

The ζ-potential obtained at pH= 8.8 (7 mV), which is the closest to the isoelectric point of Al_2O_3 (pH= 9.2), reflects the tendency towards aggregation due to van der Waals inter-particle attraction. Interestingly, when the concentration of Al_2O_3 decreases, the dispersion becomes stable in the whole examined pH interval. Thus, for the 4:1 EDOT:Al_2O_3 ratio, the ζ-potential is +18 mV for pH= 2.3 and lower than -21 mV for pH≥ 4. According to these results, the 4:1 EDOT: Al_2O_3 ratio provides the most favorable polymerization conditions in terms of stability. Besides, the sedimentation of the 4:1 dispersion is also affected by the pH. More specifically, the sedimentation time increases by ~7min at acid or basic pHs with respect to the neutral one, the slowest sedimentation being obtained at the extremes pH values (2.3 and 10.8).

The variation of the average effective diameter (D_{eff}) of Al_2O_3 aggregates, as determined by DLS, with the pH is displayed in Figure 3.1-2(b) for both 1:1 and 4:1 EDOT: Al_2O_3 ratios. As it can be seen, average D_{eff} values are fully consistent with the ζ-potential measures represented in Figure 3.1-2(a). Thus, D_{eff} increases with the van der Waals inter-particle attraction and the reduction of the electrostatic repulsions, the maximum value (1.2µm) being reached at neutral pH. Besides, although the similarity of the two profiles reflects similar aggregation behaviour, at a given pH D_{eff} is systematically higher for the 1:1 dispersion than for the 4:1 one. This effect has been attributed to the fact that collisions among particles, which are followed by aggregation rather than by increasing dispersion, increase with the Al_2O_3 concentration.

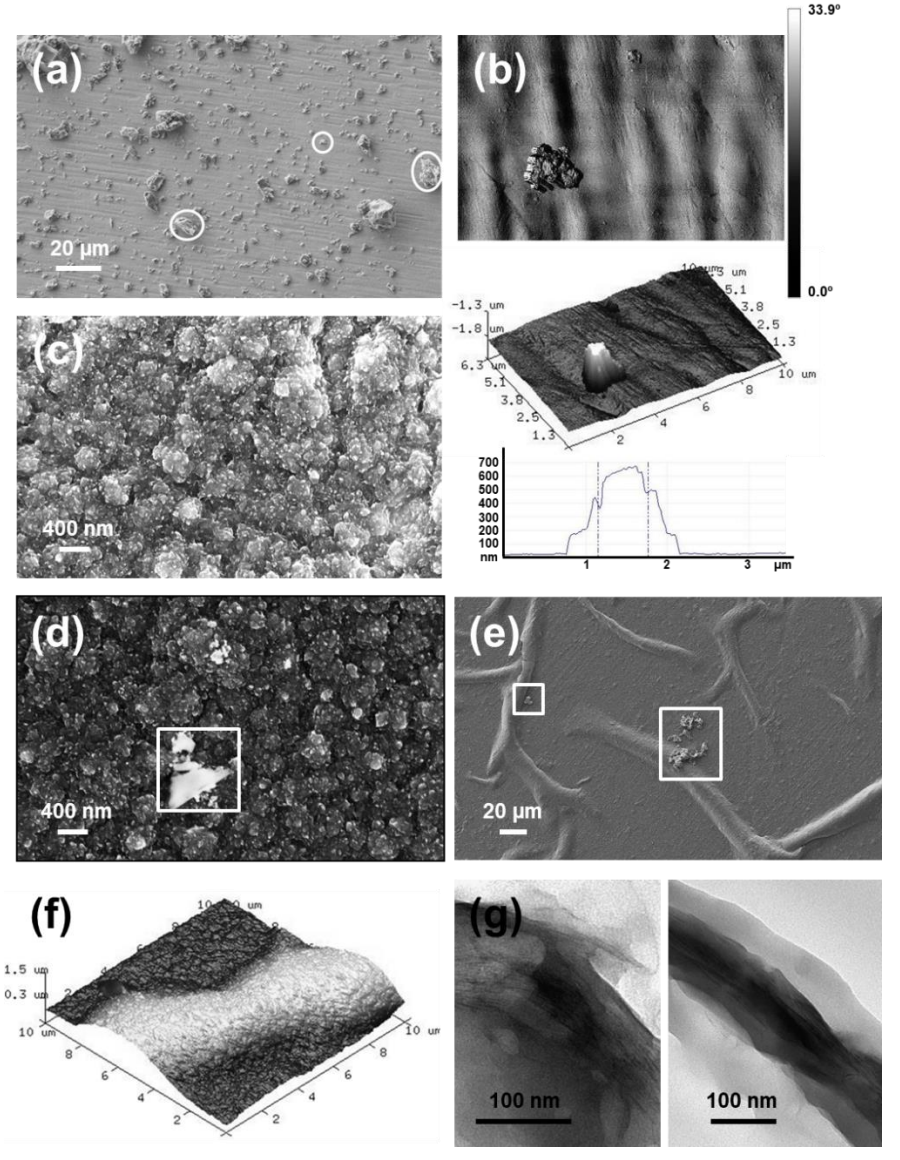

Figure 3.1-3. (a) SEM micrograph and (b) 10× 6.3µm² AFM images (phase, 3D topography and cross-sectional profile at the top, middle and bottom part, respectively) of Al_2O_3 deposited onto steel AISI 316 from an aqueous dispersion at pH= 7. Al_2O_3 particles of very different diameters (0.8 µm, 100 nm and 9 µm from left to right) are marked with white circles in (a). (c) SEM micrograph of PEDOT obtained by anodic polymerization in neutral water (pH= 7) using a polymerization time of 180 s. (d-e) SEM micrographs and (f) 10×10 µm² 3D topographic image of PEDOT/Al_2O_3 obtained using a 1:1 EDOT: Al_2O_3 ratio at pH= 10.8. The infrequent Al_2O_3 particles localized at the surface are inside the white squares. (g) TEM micrographs of PEDOT/Al_2O_3 obtained using the same conditions that in (d-f).

Figure 3.1-3(a) displays a representative SEM micrograph of Al_2O_3 particles deposited onto an AISI 316 sheet from an aqueous dispersion at pH= 7. As it can be seen, irregular particles are widely and randomly distributed onto the steel surface, their size being extremely variable (from more than 10 µm to 50 nm). For example, the diameter of particles marked with a white circle in the micrograph is 0.8 µm, 100 nm and 9 µm (from left to right). Figure 3.1-3(b) displays AFM images of an Al_2O_3 particle deposited onto steel, which is perfectly identifiable by the phase contrast. The 3D topographic image reflects the irregular shape of the particle, which exhibits a length and a height of ~2.3 µm and ~650 nm, respectively.

Overall, results evidence that EDOT behaves as a dispersant, especially when its concentration is higher than that of Al_2O_3. Thus, in absence of dispersants Al_2O_3 forms stable colloidal solutions at pH < 7.8, and The stability decreases on approaching the isoelectric point with maximum instability at pH= 9.1.[22] However, 4:1 EDOT:Al_2O_3 solutions are very stable at pH= 8.8 and 10.8, the average D_{eff} estimated for Al_2O_3 particles at such basic media being similar to that obtained at pH= 4.0 and 2.3, respectively.

Composition of PEDOT/Al_2O_3 films

Densities were measured considering all the tested pHs (five samples per system). The average values were 1.664 ± 0.009, 1.679 ± 0.007 and 1.667 ± 0.009 g cm^{-3} for PEDOT, 1:1 PEDOT/Al_2O_3 and 4:1 PEDOT/Al_2O_3, respectively. The small standard deviations indicate that the influence of pH in the composition is very small. Thus, the maximum difference between the highest and lowest density obtained for PEDOT, 1:1 PEDOT/Al_2O_3 and 4:1 PEDOT/Al_2O_3 was lower than 1.2 %, 1.0 % and 1.1 %, respectively.

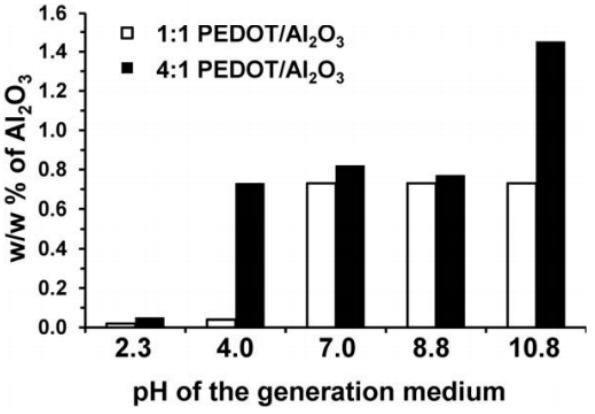

Figure 3.1-4. Variation in the amount of Al_2O_3 (w/w%) in 4:1 and 1:1 PEDOT/Al_2O_3 composites as a function of the pH

Figure 3.1-4 represents the variation of the composition, expressed as Al_2O_3 w/w%, as a function of the pH for 1:1 and 4:1 PEDOT: Al_2O_3. As it can be seen, the incorporation of Al_2O_3 is very low at pH= 2.3 (≤ 0.05 w/w%), while the maximum inorganic loading is achieved at the most basic pH (i.e. 0.73 and 1.45 w/w% for 4:1 and 1:1 nanocomposites, respectively). In spite of its low amount, inorganic particles provide a very remarkable benefit (*e.g.* the *SC* of PEDOT increases more than twice), as will be shown in next sub-sections.

Morphological and thermal characterization of PEDOT/Al_2O_3 films

Comparison of representative SEM micrographs recorded for PEDOT and PEDOT/Al_2O_3 films reveals that the compact globular morphology of the polymer matrix is not influenced by the Al_2O_3 particles [Figure 3.1-3(c-d)]. This feature suggests that Al_2O_3 is homogeneously distributed inside the polymer matrix, without alter the general aspect of the surface morphology. Indeed, the micrograph recorded for PEDOT/Al_2O_3 [Figure 3.1-3(d)] shows a single Al_2O_3 particle (diameter: 0.9µm) at the displayed surface, which reflects that such superficial distribution is relatively infrequent. This is corroborated in Figure 3.1-3(e), which shows a representative SEM micrograph with low magnification.

On the other hand, low magnification micrographs indicate that PEDOT/Al_2O_3 films display well-localized and prominent folds (height:1.4µm according to the topographic AFM image displayed in Figure 3.1-3(f) homogeneously distributed. The folds on the surface of these films, which are not observed for pure PEDOT films, have been attributed to the Al_2O_3 particles embedded into the polymeric matrix. These particles act as crystallization nuclei of polymeric and oligomeric chains, promoting the formation of elongated folds. This hypothesis is supported by TEM images, which enables the identification of Al_2O_3 particles inside the polymeric matrix [Figure 3.1-3(g)]. Furthermore, the particles size is fully consistent with those determined in the previous sub-section [Figure 3.1-2(b)].

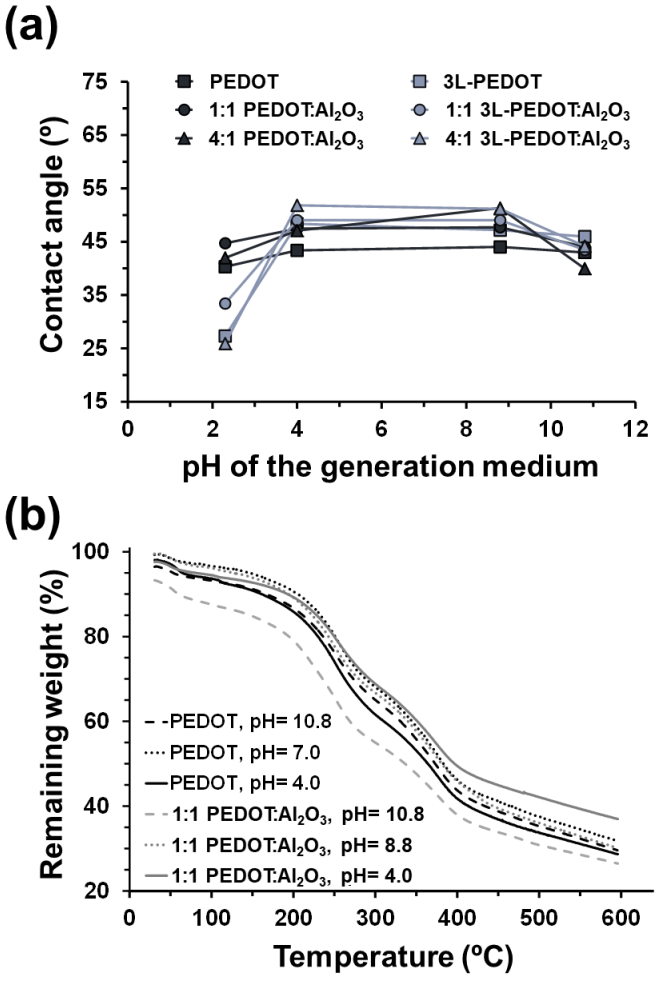

Figure 3.1-5. (a) Variation of the contact angle as function of the pH of the generation medium for PEDOT, 1:1 and 4:1 PEDOT/Al_2O_3. In all cases error bars are smaller than the size of the symbols. (b) Thermogravimetric curves of PEDOT and 1:1 PEDOT/Al_2O_3 prepared at the most representative pHs.

Figure 3.1-5(a) represents the variation of the contact angle for PEDOT and PEDOT/Al_2O_3 against the pH of the generation medium. As it can be seen, the influence of the pH in the wettability is relatively small in all cases, contact angle values being comprised between 40º and 51º. Thus, inorganic particles do not cause important changes in the hydrophilicity of PEDOT, which is consistent with the fact that Al_2O_3 is mainly embedded into the polymeric matrix.

Although details on the thermal decomposition mechanism of PEDOT were already described,[10] the influence of generation conditions (*i.e.* pH and EDOT: Al_2O_3 ratio) in the thermal stability was

examined by TGA. Figure 3.1-5(b) displays the thermogravimetric profiles recorded for PEDOT and 1:1 PEDOT/Al_2O_3 produced at representative pHs. For pristine PEDOT, the thermal decomposition shifts towards lower temperatures when the pH becomes basic and, especially, acid. The onset of the thermal decomposition of Al_2O_3-containing composites depends considerably on the pH of the generation medium. Interestingly, the thermal stability of the composite is lower than that of pure PEDOT at basic pH, whereas it is higher at acid pH. Moreover, the thermal stability of pristine PEDOT and PEDOT/Al_2O_3 obtained at pH= 7.0 and 8.8, respectively, are practically identical. This result represents an important advantage since composites prepared at pH= 8.8 display the best electrochemical performance, as is described in the next sub-section. All these features are illustrated by comparing temperatures at a 50 % weight loss ($T_{50\%}$) at different pHs: *(i)* pH= 4.0, $T_{50\%}$= 364 ºC and 396 ºC for PEDOT and 1:1 PEDOT/Al_2O_3, respectively; *(ii)* pH= 7.0, $T_{50\%}$= 383 ºC for PEDOT and pH= 8.8, $T_{50\%}$= 374 ºC for 1:1 PEDOT/Al_2O_3; and *(iii)* pH= 10.8, $T_{50\%}$= 373ºC and 336 ºC for PEDOT and 1:1 PEDOT/Al_2O_3, respectively.

Electrochemical characterization of PEDOT/Al_2O_3 films

The *SC* of Al_2O_3, which was determined as a control, was low, increasing from 13 to 21F g^{-1} with the pH. compares the SC values determined by GCD (Eq 3) and CV (Eq 2) for pure 1:1 and 4:1 PEDOT/Al_2O_3 with those pure PEDOT at the investigated pHs. As it was expected, tendencies displayed by galvanostatic and potentiostatic *SC* values, which were obtained using the 5th GCD cycle and the 2nd voltammogram, respectively, are fully consistent. Thus, the *SC* is higher for PEDOT/Al_2O_3 than for pure PEDOT and Al_2O_3, independently of the pH and the EDOT:Al_2O_3 ratio, evidencing that Al_2O_3 particles improve considerably (in some cases more than twice) the electrochemical performance of such ICP. Based on previous studies devoted to examine the conductivity enhancement of electrolytic media upon the addition of Al_2O_3,[43] we propose that the surface groups of the Al_2O_3 particles provide additional sites for the migration of charges, favouring the mobility of the dopant agents during the charge-discharge and oxidation-reduction processes. Moreover, the enhancement of the *SC* increases with the concentration of Al_2O_3 in all cases with exception of the composites prepared at pH= 8.8. For the latter, the *SC* of 4:1 composite is ~7% higher than that of 1:1.

The distinctive behaviour of composites prepared at pH= 8.8 has been attributed to the combination of two different phenomena. First, the *SC* is significantly higher at pH= 8.8 than at the rest of the examined pHs, which indicates that such moderately basic environment promotes the

electrochemical performance of PEDOT. This is probably due to the fact that at pH= 8.8 the concentration of OH^- groups is high enough to promote their participations as secondary doping agents but too low for degrading the polymeric matrix (as probably occurs at pH= 10.8). Second, the R_q is different for films yielded using 1:1 and 4:1 EDOT: Al_2O_3 ratios, as it is proved by the AFM images compared in Figure 3.1-6.

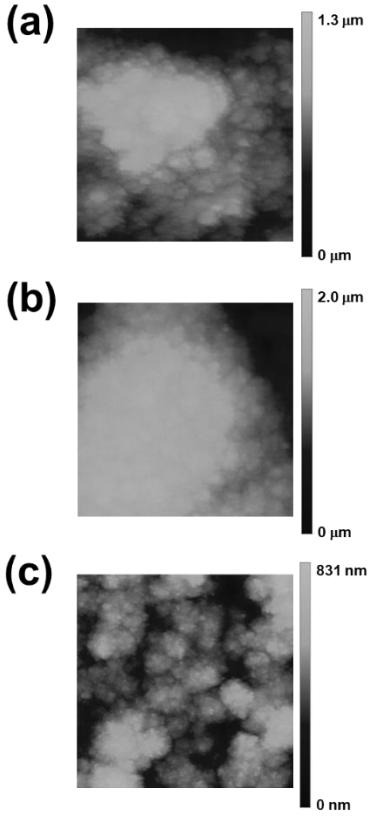

Figure 3.1-6. Representative height AFM images (5×5 μm^2) of PEDOT, 1:1 and 4:1 PEDOT/Al_2O_3 obtained at pH= 8.8

More specifically, R_q= 77 ± 3, 80 ± 5 and 91 ± 3nm for PEDOT, 1:1 and 4:1 PEDOT/Al_2O_3, respectively. The topography of 4:1 films can be described as a uniform distribution of sub-micrometric protuberances with well-defined separations (*i.e.* dissemination of mountains separated by narrow valleys), while the AFM image of the 1:1 film displays a single protuberance of micrometric dimensions in terms of length, width and height. This observation, which is fully consistent with the stability of 1:1 and 4:1 EDOT: Al_2O_3 dispersions discussed above [Figure 3.1-2(a)], explains that R_q is higher for the 4:1 film, even though the maximum roughness (R_{max}) is

higher for the 1:1 film (R_{max}= 623 and 539nm for 1:1 and 4:1 films, respectively). Although these differences do not affect the general aspect of the surface morphology (Figure 3.1-3), they have a notable effect in the capacity of the capacity of the films to exchange ions. Thus, the *SC* increases with the specific surface of the films and, therefore, with R_q.

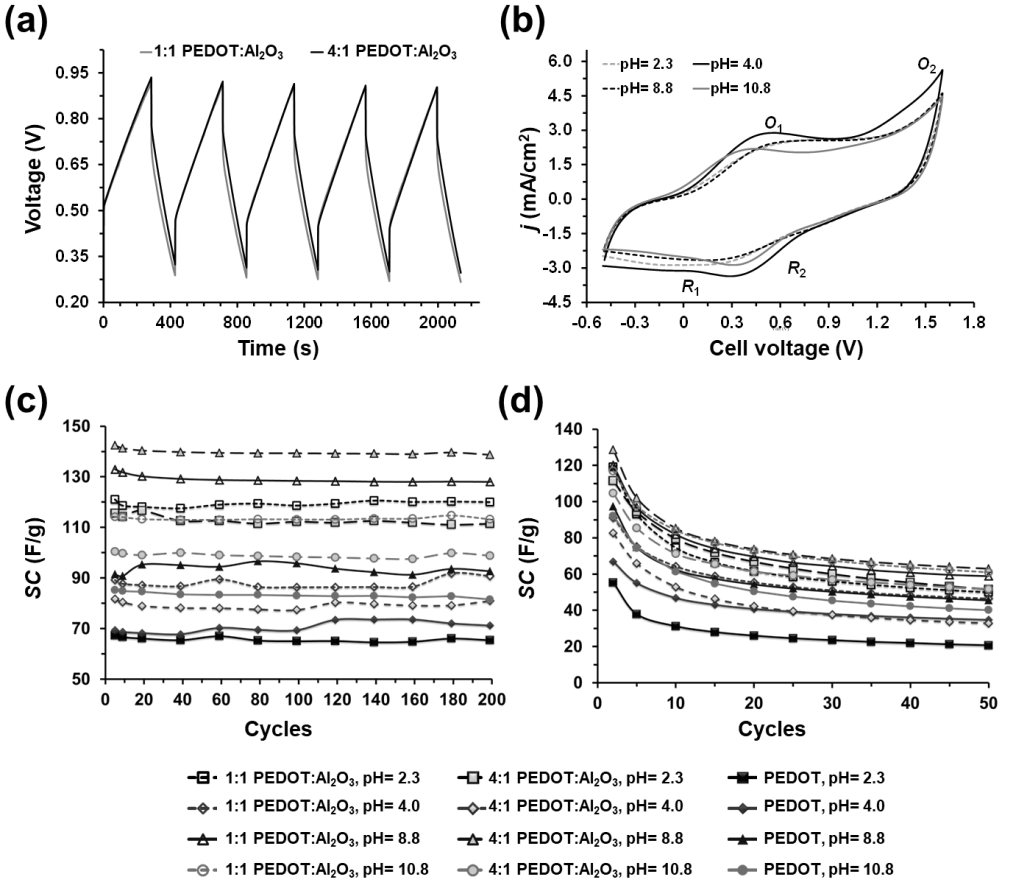

Figure 3.1-7. (a) Five GCD cycles recorded from 0.2 to 0.8V for 1:1 and 4:1 PEDOT/Al_2O_3 prepared at pH= 8.8. (b) Cyclic voltammogram (2th cycle) recorded from -0.5 to 1.6 V at a scan rates of 100 mVs^{-1} for 4:1 PEDOT/Al_2O_3 prepared at pH= 2.3, 4.0, 8.8 and 10.8. (c-d) Variation of the SC with the number of (c) GCD and (d) CV cycles for PEDOT, 1:1 and 4:1 PEDOT/Al_2O_3 prepared at pH= 2.3, 4.0, 8.8 and 10.8. All electrochemical assays were performed using a 0.1 M $LiClO_4$ acetonitrile solution as electrolytic medium.

Figure 3.1-7(a) compares the first five GCD cycles recorded at 1.53 A g^{-1} y 1.67 A g^{-1} of 1:1 and 4:1 PEDOT/Al_2O_3, respectively, prepared at pH= 8.8 using a 0.1M $LiClO_4$ acetonitrile solution as electrolytic medium. The GCD curves present some distortions with respect to the typical triangular shape, which are caused by the voltage drop (V_{drop}) and the voltage gain (V_{gain}) at the beginning of

the discharging and charging process, respectively. Although the curves are very similar for the two PEDOT/Al_2O_3 composites, the V_{drop} is slightly higher for the 1:1 than for the 4:1, which agrees with the *SC* values listed in Table 3.1-1.

Table 3.1-1. The SC (in F g^{-1}) determined by GCD (using the 5th cycle) / CV (using the 2nd voltammogram) for pure PEDOT and PEDOT/Al_2O_3 prepared using both 1:1 and 4:1 EDOT: Al_2O_3 ratios at different pHs.

		PEDOT/Al_2O_3	
pH	**PEDOT**	1:1	4:1
2.3	58 / 55	121 /119	115 / 111
4.0	73 / 67	89 / 91	77 / 82
7.0	58 / 68	- / -	- / -
8.8	91 / 97	132 / 120	141 / 129
10.8	81 / 92	114 / 117	98 / 105

Figure 3.1-7(b) shows the 2nd cyclic voltammogram in 0.1 M $LiClO_4$ acetonitrile recorded for 4:1 PEDOT/Al_2O_3 samples prepared at different pHs. As it can be seen, the first oxidation peak of PEDOT chains, O_1, occurs between 0.3 and 0.5V, depending on the pH, while the second peak, O_2, overlaps with the oxidation potential of the medium. In addition, two reduction peaks, R_1 and R_2, are detected in the cathodic scans, indicating the presence of redox pairs in the recorded potential range. These redox processes, which are well-defined for all the pHs employed during the generation of the films, should be attributed to the formation of polarons in the polymer chains.

Figure 3.1-7(c) indicates that, after 200 GCD of cycles, the *SC* remains practically constant for all PEDOT and PEDOT/Al_2O_3 electrodes, independently of their preparation conditions, indicating that very small changes are expected for a larger number of cycles. The *SC*s determined by CV before and after 50 consecutive oxidation-reduction cycles reflect a decrease of around 50 %-60% for both PEDOT and PEDOT/Al_2O_3 [Figure 3.1-7(d)]. Apparently, these drastic reductions, which occur in the first 20 redox cycles, are in contradiction with the results displayed in Figure 3.1-7(c) for the galvanostatic *SC* values. However, it should be emphasized that application of consecutive oxidation–reduction cycles is the most aggressive electrochemical method to determine the electrochemical stability of polymeric films. This was proved in previous studies, in which potentiostatic redox cycles were found to reduce drastically the porosity and roughness of PEDOT

films, affecting their surface topography and morphology.[8,45] Besides, it should be noted that, after the reduction occurred during the first 20 redox cycles, the order of the potentiostatic *SC* values remains identical to that obtained after the 2nd redox cycle. Accordingly, in spite of all films are affected by the potentiostatically-induced degradation, the electrochemical stability is higher for PEDOT/Al_2O_3 than for PEDOT at all the examined pHs.

Table 3.1-2 compares the thickness of PEDOT and PEDOT/Al_2O_3 films, which was estimated considering the polymerization charge, the current productivity and the density for each generation condition. As it was expected, the thickness is lower for pure PEDOT than for PEDOT/Al_2O_3 in all cases. This should be attributed to the steric hindrance caused by the inorganic particles, which increases with the content of Al_2O_3 in the film (*i.e.* the thickness of 1:1 composite is the highest). On the other hand, the thickness increases with the polymerization charge, reflecting again that the influence of the pH in the amphoteric behaviour of Al_2O_3.

Table 3.1-2. Thickness (L) and polymerization charge (Q_{pol}) consumed in the preparation of PEDOT and PEDOT/Al_2O_3 films at different pHs: L (in μm) / Q_{pol} (in C)

		PEDOT/Al_2O_3	
pH	**PEDOT**	1:1	4:1
2.3	1.180 / 0.430	1.524 / 0.519	1.262 / 0.456
4.0	1.932 / 0.527	2.038 / 0.527	1.957 /0.470
8.8	1.221 / 0.455	1.487 / 0.515	1.249 / 0.535
10.8	1.841 / 0.590	2.074 / 0.627	1.564 / 0.547

Electrochemical advantages of multilayered PEDOT/Al_2O_3 films

Firstly, the potential advantages of multilayered films with respect single-layered ones were analyzed for pure PEDOT films.

Figure 3.1-8 compares the results obtained for 3L-PEDOT films, which were yielded using three polymerization steps of 60 s each one, with those reached for the single layered (1L) PEDOT systems described above (*i.e.* obtained using a continuous electropolymerization process of 180 s). As it can be seen, both the galvanostatic and potentiostatic *SC*s are higher for 3L-films than for 1L-films, independently of the pH. Moreover, this ranking does not change with increasing number of cycles,

the electrochemical stability being higher for the former than for the latter in all cases. Accordingly, observations for PEDOT films prepared in water are fully consistent with our previous results on films prepared in acetonitrile.[36] This behaviour has been attributed to the interfaces created at the interlayer regions during the multi-step polymerization. Thus, such interfaces, which are not present in films prepared using a continuous electropolymerization process, act as dielectric layers, enhancing the ability to store charge.

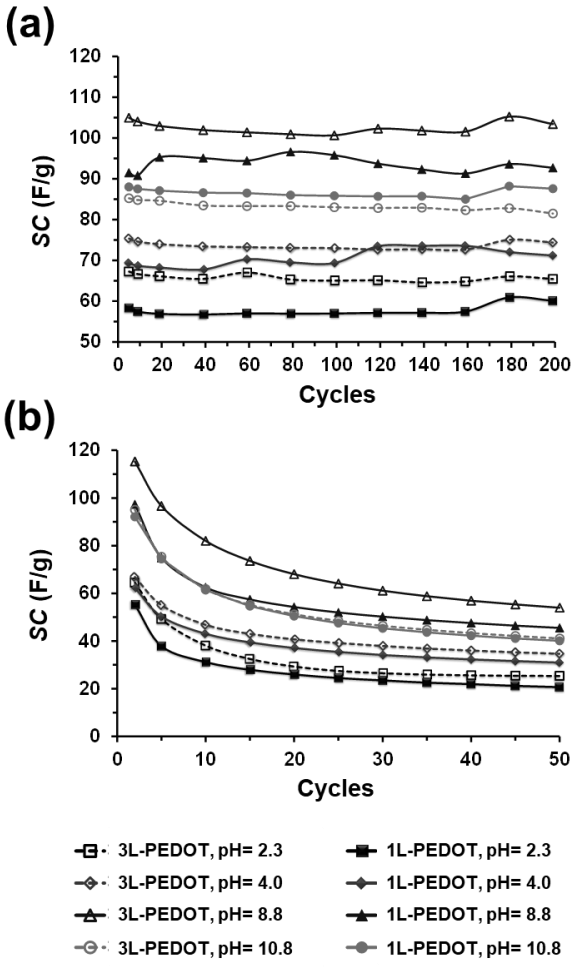

Figure 3.1-8. Variation of the SC with the number of (a) GCD and (b) CV cycles for 1L-PEDOT and 3L-PEDOT prepared at pH= 2.3, 4.0, 8.8 and 10.8. All electrochemical assays were performed using a 0.1 M $LiClO_4$ acetonitrile solution as electrolytic medium.

Besides, the galvanostatic / potentiostatic *SC* of yielded at pH= 8.8 increases from 91 / 97 F g^{-1} to 105 / 115 F g^{-1}, respectively, when the number of layers increases, which represents an enhancement

of 15% / 18%. These remarkable increments corroborate that the application of multiple polymerization steps at pH= 8.8 result in the combination of two favourable effects: *i)* the creation of dielectric layers inside the PEDOT films; and *ii)* the activation of PEDOT chains through the OH^- groups arising from the basic generation medium, as discussed in the previous sub-section.

The galvanostatic and potentiostatic *SCs* values determined for 3L-PEDOT/Al_2O_3 films are compared with those obtained using a single polymerization step in Figure 3.1-8(a,b), respectively. As it can be seen, for a given experimental conditions, 3L-films exhibit higher the ability to store charge than 1L-films. The increment induced by the interfaces formed between composite layers ranges from 2% to 13%, depending on the pH, the EDOT: Al_2O_3 ratio and the methodology used to determine the *SC* (*i.e.* GCD or CV). This interval of variation is in good agreement with that obtained from the comparison of pure 1L- and 3L-PEDOT films prepared in acetonitrile (*i.e.* the average increment of the ability to store charge was 9%), reflecting the synergistic effects induced by the interfaces.[36]

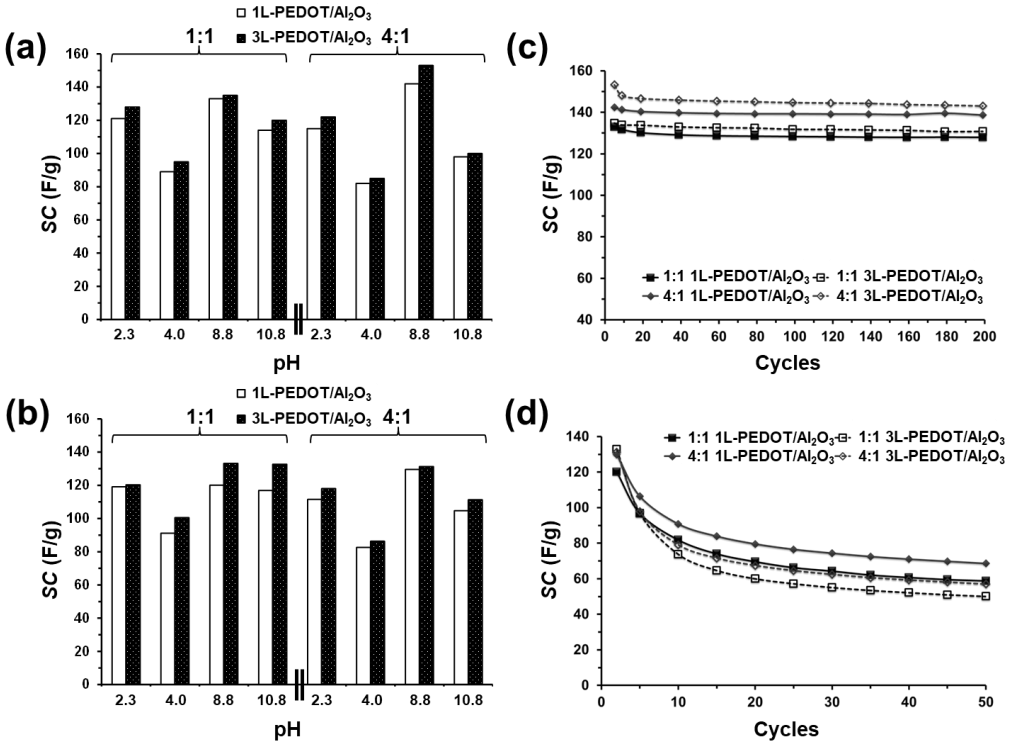

Figure 3.1-9. Variation of the SC with the number of (c) GCD and (d) CV cycles for 1L-PEDOT and 3L-PEDOT prepared at pH= 2.3, 4.0, 8.8 and 10.8. All electrochemical assays were performed using a 0.1 M $LiClO_4$ acetonitrile solution as electrolytic medium.

The galvanostatic *SC* of 3L-PEDOT/Al_2O_3 films remains practically unaltered after 200 GCD cycles, independently of the pH and the feeding ratio, as is illustrated in Figure 3.1-9(c) for 1:1 and 4:1 3L-films obtained at pH= 8.8. In opposition, the potentiostatic *SC* values determined for 3L-films decreases around 45%-55% after 50 consecutive redox cycles [Figure 3.1-9(d)]. This behaviour, which is independent of the pH (not shown) is similar to that displayed in Figure 3.1-7(d) for single layered films

3.1.5. Conclusions

We successfully synthesized PEDOT/Al_2O_3 composites in aqueous medium by CA considering different monomer: Al_2O_3 ratios in the reaction medium, pHs ranging from 2.3 to 10.8, and both continuous and multi-step *in situ* polymerization strategies. Independently of the selected synthetic

conditions, the electrochemical properties for energy storage of PEDOT/Al_2O_3 are better than those of pure PEDOT, which has been attributed to the additional sites for the migration of charges provided by the Al_2O_3 particles. Analyses of the properties of the initial EDOT: Al_2O_3 suspensions and synthesized composites show that the best properties are obtained applying a multi-step polymerization strategy, a 4:1 EDOT:Al_2O_3 ratio and a pH of 8.8. The success of these conditions results from the combination of four different factors: (*i*) 4:1 EDOT:Al_2O_3 suspensions are stable at such basic pH despite it is very close to the isoelectric point of Al_2O_3; (*ii*) the OH^- groups participate as dopant agents giving an extra activation to the PEDOT; (*iii*) the basic pH is still too moderate to promote the degradation of the polymeric matrix; and (*iv*) the interfaces generated by the multi-step polymerization strategy, which act as a dielectric placed between two polymeric layers, are compatible with incorporation of Al_2O_3 particles inside the polymer matrix. The PEDOT/Al_2O_3 composites presented here will be further investigated for their incorporation into solid-state organic supercapacitors based on the combination of PEDOT electrodes and biohydrogels as electrolytic medium. Thus, the replacement of PEDOT by PEDOT/Al_2O_3 prepared at the above-mentioned conditions may lead to improve the performance of these electrochemical energy storage devices introducing a very small amount of non-toxic inorganic material.

3.1.6. References

(1). Huang, Y.; Li, H.; Wang, Z.; Zhu, M.; Pei, Z.; Xue, Q.; Huang, Y.; Zhi, C. Nanostructured Polypyrrole as a Flexible Electrode Material of Supercapacitor. *Nano Energy.* **2016**, *22* (1), 422–438.

(2). Janaky, C.; Rajeshwar, K. The Role of (Photo)Electrochemistry in the Rational Design of Hybrid Conducting Polymer/Semiconductor Assemblies: From Fundamental Concepts to Practical Applications. *Prog. Polym. Sci.* **2015**, *43* (1), 93–135.

(3). Kim, B. C.; Hong, J. Y.; Wallace, G. G.; Park. H. S. Recent Progress in Flexible Electrochemical Capacitors: Electrode Materials, Device Configuration, and Functions. *Adv. Funct. Mater.* **2015**, *5* (22), 1500959.

(4). Wang. K.; Wu, H.; Meng, Y. Conducting Polymer Nanowire Arrays for High Performance Supercapacitors. *Small* **2014**, *10* (1), 14–31.

(5). Chauan, N. P. S.; Mozafari, M.; Chundawat, N. S.; Meghwal, K.; Ameta, R.; Ameta, S.C. High-Performance Supercapacitors Based on Polyaniline–Graphene Nanocomposites: Some Approaches, Challenges and Opportunities. *J. Ind. Eng. Chem.* **2016**, *36* (1), 13–29.

(6). Heeger, A. J. Semiconducting and Metallic Polymers: The Fourth Generation of Polymeric Materials. *Angew. Chem. Int. Ed*. **2001**, *40* (14), 2591–2611.

(7). Aradilla, D.; Estrany, F.; Alemán, C. Symmetric Supercapacitors Based on Multilayers of Conducting Polymers. *J. Phys. Chem. C.*, **2011**, *115* (16), 8430–8438.

(8). Wang, J.; Wu, Z.; Yin, H.; Li, W.; Jiang, Y. Poly(3,4-ethylenedioxythiophene)/MoS_2 Nanocomposites with Enhanced Electrochemical Capacitance Performance. *RSC Adv*. **2014**, *4* (100), 56926–56932.

(9). Aradilla, D.; Azambuja, D.; Estrany, F.; Casas, M. T.; Ferreira, C. A.; Alemán, C. Hybrid Polythiophene–Clay Exfoliated Nanocomposites for Ultracapacitor Devices. *J. Mater. Chem.* **2012**, *22* (26), 13110–13122.

(10). Bai, X.; Hu, X.; Zhou, S. Flexible Supercapacitors Based on 3D Conductive Network Electrodes of Poly(3,4-ethylenedioxythiophene)/Non-Woven Fabric Composites. *RSC Adv.* **2015**, *5* (55), 43941–43948.

(11). Shi, Y.; Peng, L.; Yu, G. Nanostructured Conducting Polymer Hydrogels for Energy Storage Applications. *Nanoscale* **2015**, *7* (30), 12796–12806.

(12). Pérez-Madrigal, M. M.; Estrany, F.; Armelin, E.; Díaz-Díaz, D.; Alemán, C. Towards Sustainable Solid-State Supercapacitors: Electroactive Conducting Polymers Combined with Biohydrogels. *J. Mater. Chem. A* **2016**, *4* (5), 1792–1805.

(13). Guo, W. B.; Zhang, X. D.; Yu, X.; Wang, S.; Qiu, J.; Tang, W.; Li, L.; Liu, H.; Wang, Z. L. Self-Powered Electrical Stimulation for Enhancing Neural Differentiation of Mesenchymal Stem Cells on Graphene–Poly(3,4-ethylenedioxythiophene) Hybrid Microfibers. *ACS Nano* **2016**, *10* (5), 5086–5095.

(14). Chen, C.; Zhang, T.; Zhang, Q.; Chen, X.; Zhu, C.; Xu, Y.; Yang, J.; Liu, J.; Sun, D. Biointerface by Cell Growth on Graphene Oxide Doped Bacterial Cellulose/Poly(3,4-ethylenedioxythiophene) Nanofibers. *ACS Appl. Mater. Interfaces* **2016**, *8* (16), 10183–10192.

(15). Lee, W.; Kang, Y. H.; Lee, J. Y.; Jang, K-S.; Cho, S. Y. Improving the Thermoelectric Power Factor of CNT/PEDOT:PSS Nanocomposite Films by Ethylene Glycol Ttreatment. *RSC Adv* **2016**, *6* (58), 53339–53344.

(16). Ramakrishnan, R.; Devaki, S. J.; Thomas, S.; Varma, M. R.; Naajiya, K. P. P. Nanostructured Semiconducting PEDOT–TiO_2/ZnO Hybrid Composites for Nanodevice Applications. *J. Phys. Chem. C.* **2016**, *120* (8), 4199–4210.

(17). Guo, C. X.; Yilmaz, G.; Chen, S.; Chen, S.; Lu, X. Hierarchical Nanocomposite Composed of Layered V_2O_5/PEDOT/MnO_2 Nanosheets for High-Performance Asymmetric Supercapacitors. *Nano Energy* **2015**, *12* (1), 76–87.

(18). Wang, Z. H.; Tammela, P.; Huo, J.; Zhang, P.; Strømme, M.; Nyholm, L. Solution-Processed Poly(3,4-ethylenedioxythiophene) Nanocomposite Paper Electrodes for High-Capacitance Flexible Supercapacitors. *J. Mater. Chem. A*. **2016**, *4* (5), 1714–1722.

(19). López-Pérez, D.; Aradilla, D.; Del Valle, L. J.; Alemán, C. Capacitive Composites Made of Conducting Polymer and Lysozyme: Toward the Biocondenser. *J. Phys. Chem. C.* **2013**, *117* (13), 6607−6619.

(20). Franks, G.V.; Meagher, L. The Isoelectric Points of Sapphire Crystals and Alpha-Alumina Powder. *Colloids Surf. A* **2003**, *214* (1-3), 99–110.

(21). Singh, B. P.; Menchavez, R.; Takai, C.; Fuji, M.; Takahashi, M. *J.* Stability of Dispersions of Colloidal Alumina Particles in Aqueous Suspensions. *J. Colloid Interface Sci.* **2005**, *291* (1), 181–186.

(22). Kirchmeyer, S.; Reuter, K. Scientific Importance, Properties and Growing Applications of Poly(3,4-ethylenedioxythiophene). *J. Mater. Chem.* **2005**, *15* (21), 2077–2088.

(23). Xiao, R.; Cho, S. Il.; Liu, R.; Lee, S. B. Controlled Electrochemical Synthesis of Conductive Polymer Nanotube Structures. *J. Am. Chem. Soc.* **2007**, *129* (14), 4483–4489.

(24). Liu, R.; Lee, S. B. MnO2/Poly(3,4-ethylenedioxythiophene) Coaxial Nanowires by One-Step Coelectrodeposition for Electrochemical Energy Storage. *J. Am. Chem. Soc.* **2008**, *130* (10), 2942–2943.

(25). Shirai, Y.; Takami, S.; Lasmono, S.; Iwai, H.; Chikyow, T.; Wakayama, Y. Improvement in Carrier Mobility of Poly(3,4-ethylenedioxythiophene) Nanowires Synthesized in Porous Alumina Templates. *J. Polym. Sci., Part B: Polym. Phys.* **2011**, *49* (24), 1762–1768.

(26). Liu, R.; Cho, S. Il.; Lee, S. B. Poly(3,4-ethylenedioxythiophene) Nanotubes as Electrode Materials for a High-Powered Supercapacitor. *Nanotechnology.* **2008**, *19* (21), 215710.

(27). Martin, C. R. Nanomaterials: a Membrane-Based Synthetic Approach. *Science.* **1994**, *266* (5193), 1961–1966.

(28). Parthasarathy, R. V.; Martin, C. R. Template-Synthesized Polyaniline Microtubules. *Chem. Mater.* **1994**, *6* (10), 1627–1632.

(29). Martin, C. R. Template Synthesis of Electronically Conductive Polymer Nanostructures. *Acc. Chem. Res.* **1995**, *28* (2), 61–68.

(30). Steinhart, M.; Wendorff, J. H.; Greiner, A.; Wehrspohn, R. B.; Nielsch, K.; Schilling, J.; Choi, J.; Gosele, U. Polymer Nanotubes by Wetting of Ordered Porous Templates. *Science* **2002**, *296* (5575), 1997–1997

(31). Aradilla, D.; Estrany, F.; Oliver, R.; Alemán, C. Properties of Nanometric and Micrometric Multilayered Films Made of Three Conducting Polymers. *Eur. Polym. J.* **2010**, *46* (12), 2222−2228.

(32). Estrany, F.; Aradilla, D.; Oliver, R.; Armelin, E.; Alemán, C. Properties of Nanometric and Submicrometric Multilayered Films of Poly(3,4-ethylenedioxythiophene) and Poly(N-methylpyrrole). *Eur. Polym. J.* **2008**, *44* (5), 1323−1330.

(33). Aradilla, D.; Estrany, F.; Armelin, E.; Alemán, C. Morphology and Growing of Nanometric Multilayered Films Formed by Alternated Layers of Poly(3,4-ethylenedioxythiophene) and Poly(N-methylpyrrole). *Thin Solid Films.* 2010, *518* (15), 4203−4210.

(34). Aradilla, D.; Pérez-Madrigal, M. M.; Estrany, F.; Azambuja, D.; Iribarren, J. I.; Alemán, C. Nanometric Ultracapacitors Fabricated Using Multilayer of Conducting Polymers on Self-assembled Octanethiol Monolayers. *Org. Electron.* **2013**, *14* (6), 1483−1495.

(35). Aradilla, D.; Estrany, F.; Alemán, C. Different Properties for Poly(3,4-ethylenedioxythiophene) Films Derived from Single or Multiple Polymerization Steps. *J. Appl. Polym. Sci.* **2011**, *121* (4), 1982−1991.

(36). Ramasahayam, S. K.; Clark, A. L.; Hicks, Z.; Viswanathan, T. Spent Coffee Grounds Derived P, N Co-doped C as Electrocatalyst for Supercapacitor Applications. *Electrochim. Acta* **2015**, *168* (1), 414−422.

(37). Schirmeisen, M.; Beck, F. J. Electrocoating of Iron and Other Metals with Polypyrrole. *J. Appl. Electrochem.* **1989**, *19* (3), 401−409.

(38). Mallakpour, S.; Khadem, E. Recent Development in the Synthesis of Polymer Nanocomposites based on Nano-alumina. *Prog. Polym. Sci.* **2015**, *51* (&&), 74−93.

(39). Sung, J.; Zhang, L.; Tian, C.; Shen, Y. R.; Waychunas, G. A. Effect of pH on the Water/α-Al_2O_3 ($1\bar{1}02$) Interface Structure Studied by Sum-Frequency Vibrational Spectroscopy. *J. Phys. Chem. C* **2011**, *115* (28), 13887−13893.

(40). Fitts, J. P.; Shang, X.; Flynn, G. W.; Heinz, T. F.; Eisenthal, K. B. Electrostatic Surface Charge at Aqueous/α-Al_2O_3 Single-Crystal Interfaces as Probed by Optical Second-Harmonic Generation. *J. Phys. Chem. B* **2005**, *109* (16), 7981−7986.

(41). Mandzya, N.; Grulke, E. Breakage of TiO2 Agglomerates in Electrostatically Stabilized Aqueous Dispersions. *Powder Technol.* **2005**, *160* (2), 121–126.

(42). Jayathilaka, P.; Dissanayake, M.; Albinsson, I.; Mellander, B-E. Effect of Nano-porous Al_2O_3 on Thermal, Dielectric and Transport Properties of the $(PEO)_9$LiTFSI Polymer Electrolyte System. *Electrochim. Acta.* **2002**, *47* (20), 3257−3268.

(43). Wang, Z.; Huang, X.; Chen, L. Understanding of Effects of Nano- Al_2O_3 Particles on Ionic Conductivity of Composite Polymer Electrolytes. *Electrochem. Solid-State Lett.* **2003**, *6* (11), E40−E44.

3.2. Flexible Electrodes for Supercapacitorr Based on the Supramolecular Assembly of Biohydrogel and Conducting Polymer.

3.2.1. Abstract

Flexible and lightweight electrodes are prepared using a two-step process. First, PEDOT microparticles are loaded into γ-PGA hydrogel matrix, during the reaction of the biopolymer chains with the cross-linker, cystamine. After this, PEDOT particles dispersed inside the hydrogel are used as polymerization nuclei for the chronoamperometric synthesis of poly(hydroxymethyl-3,4-ethylenedioxythiophene) (PHMeDOT) in aqueous solution. After characterization of the resulting electrode composites, electrochemical studies revealed that the capacitive properties drastically depend on the polymerization time used to produce PHMeDOT inside the loaded hydrogel matrix. Specifically, flexible electrodes obtained using a polymerization time of 7h exhibit a SC of 45.4±0.7mF cm^{-2} from cyclic voltammetry and charge-discharge long-term stability. The applicability of these electrodes in lightweight and flexible energy-harvesting systems useful for energy-autonomous, low-power, disposable electronic devices, has been proved powering a LED bulb.

TOC graphic

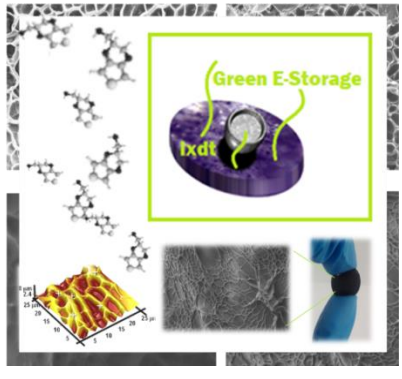

3.2.2. Introduction

A great interest in thin, flexible, safe energy storage devices has been shown by the scientific community over the last decades.[1,2] Fully pliable and robust devices, conceivably and preferably composed of eco-friendly materials, are the new benchmark of modern society.[1] These devices have a large variety of applications from motor vehicles[3-5] to laptops[6,7] or autonomous medical sensors.[8,9] Energy can be stored in batteries or in capacitors; the main difference is the charge storage mechanism, which is based on faradic and non-faradic processes, respectively. In the former devices, an electron transfer that produces a redox reaction takes place, whereas the second type is based on electrostatic processes that occur in absence of electron transfer across the electrode interface.[10] Conventional capacitors share important similarities with another class of devices known as electrochemical capacitors, which rely on charge separation at electrode/electrolyte interfaces to store energy.

Electrochemical capacitors have superb specific power compared to batteries, but modest specific energy. Batteries are characterized by high energy density values of 10−100Wh/kg, whereas capacitors are able to release the stored energy much faster however the energy density is < 0.1Wh kg^{-1}.[11] Recently, electrochemical supercapacitors (ESCs) have emerged displaying higher energy values (*i.e.* 1−10 Wh kg^{-1}) compared to capacitors.[12] ESCs present an interface between an electronic conductor and an ionic conductor (*i.e.* the electrolyte).[13] The simplest ESC is composed of two non-reactive porous electrodes immersed into an electrolytic medium and electrically isolated by a membrane to allow the migration of ions. From a technological point of view, ESCs are characterized by a good acceleration, robustness and excellent life cycle, which can improve the effectiveness of battery-based systems by shrinking the volume of the batteries and reducing the frequency of their replacement.[10]

In spite of the advantages reported for ESCs, the quality of these devices has to be improved by using more environmentally friendly materials (*e.g.* renewable materials) and electrolytes (*e.g.* non-organic, aqueous solvents), and by improving properties such as capacitance, flexibility and durability. These improvements could be obtained through:

- Construction of 3D devices incorporating micro- and/or nanometric conductive components arranged in interpenetrating networks, with the aim to create short diffusional paths and, thus, very high currents.

- Replacement of organic solvents by water-containing gel-biopolymer electrolytes, characterized by ease of processability, large exposed area for electrochemical activity, good resistance to strain and, in addition, significant reduction of costs.

Within this context, we have developed the supra-molecular assembly of a biohydrogel with a conducting polymer (CP), producing and characterizing a new flexible, lightweight and efficient organic electrode for application in ESCs. More specifically, we have prepared an electrode composed by γ-PGA as 3D-gelated network and a PEDOT derivative, as CP.

Selected polymers are characterized by high relevance in research and industrial environments. γ-PGA is an anionic homopolypeptide linked by the peptide bond between the α-amino and the γ-carboxyl groups of glutamic acid,[14] that exhibits good biocompatibility due to its biodegradability, water-solubility and non-toxicity towards humans.[15] This compound is naturally synthetized as a slime layer by a variety of members of the genus *Bacillus.*[16] γ-PGA and its derivatives have been used in different fields such as food industry,[17,18] medicine,[19,20] cosmetic,[21,22] agriculture,[23] and wastewater treatment.[24] Due to their robustness, γ-PGA gels were recently employed as solid electrolyte media for organic ESCs.[25] Armelin *et al.*[26] recently reviewed the utilization and the advantages of biohydrogels for ESCs, highlighting the sustainability of devices composed by materials that can be naturally produced, as γ-PGA from biosynthesis, or directly extracted from biomass.

Among CPs, PEDOT is one of the most widely used for energy storage devices due to its excellent properties: low band gap, easiness to stabilize the oxidized state, high electrical conductivity, stable charge-discharge response, excellent environmental stability and fast doping-dedoping process.[27-30] The unique characteristics of PEDOT are due to the oxygen atoms attached at the β,β'-positions of the thiophene ring, which induce strong electron-donating effects and prevent the formation of parasitic α-β linkages during the polymerization of the EDOT monomers.[31] Moreover, the electrochemical performance of PEDOT can be improved if properly combined with other materials such as graphene,[23,32-34] carbon nanotubes,[35] inorganic oxides,[36,37] and even biomolecules.[26,38-41]

The present work represents a step ahead with respect to the setup of ESCs composed of PEDOT electrodes and γ-PGA solid electrolytic medium. More specifically, γ-PGA biohydrogel has been synthesized and analyzed in presence of PEDOT and PHMeDOT, a PEDOT derivative with an exocyclic hydroxyl group that facilitates its preparation in aqueous environments. Accordingly, the novelty of this work is related with the loading of PEDOT particles into the hydrogel, which are subsequently used as nucleation sites for the *in situ* electropolymerization of PHMeDOT inside the

hydrated γ-PGA matrix. The excellent properties of the resulting electrode composite, the contribution of its different components (*i.e.* γ-PGA, PEDOT particles and PHMeDOT), and its potential applicability are discussed in the next sections.

3.2.3. Experimental Section

Materials

Free-acid γ-PGA (from Bacillus subtilis), with average molecular weight Mw= 350000, was purchased from Wako Chemicals GmbH (Neuss, Germany). Cystamine dihydrochloride (≥98.0%), 1-[3-(dimethylamino)propyl]-3-ethylcarbodiimide methiodide (EDC), EDOT (95%) and hydroxymethyl-3,4-ethylenedioxythiophene (HMeDOT, 95%) were purchased from Sigma-Aldrich. Acetonitrile (Reagent European Pharmacopoeia for analysis, ACS) and $NaHCO_3$ were obtained from Panreac. Anhydrous lithium perchlorate ($LiClO_4$), analytical reagent grade from Aldrich, was stored in an oven at 70 ºC before use in electrochemical experiments. Milli-Q water grade (0.055 S cm^{-1}) was used in all synthetic processes.

Synthesis of PEDOT particles

Both anodic polymerization and electrochemical assays were performed with a potentiostat-galvanostat Autolab PGSTAT101 equipped with the ECD module (Ecochimie, The Netherlands) using a three-electrode compartment cell under nitrogen atmosphere (99.995% pure) at room temperature. Steel AISI 316 sheets of 6 cm^2 in area were used as working and counter electrodes, respectively. To prevent interferences during the electrochemical assays, the working and counter electrodes were cleaned with acetone, ethanol and distillated water before each trial. The reference electrode was an Ag|AgCl electrode containing a KCl saturated aqueous solution (offset potential versus the standard hydrogen electrode, E_0= 0.222 V at 25 ºC).

PEDOT films were prepared by chronoamperometry (CA) applying a constant potential of 1.40 V during 600 s and using a 10 mM monomer solution in acetonitrile with 0.1 M $LiClO_4$ as reaction medium. The resulting films were processed into particles by sonication (Bandelin Sonopuls sonicator) in 0.5M $NaHCO_3$ solution during 25 min in steps of 5 min at low frequency (0.01% frequency). The diameter of the resulting PEDOT particles was determined at room temperature by

dynamic light scattering (DLS) in Milli-Q water dispersions (0.3 v/v %) using a NanoBrook Omni Zeta Potential Analyzer from Brookheaven Instruments Corporation. Finally, the basic aqueous (0.5 M $NaHCO_3$) dispersion with 20 w/w% of the resulting PEDOT particles was directly used for the synthesis of CP-loaded γ-PGA hydrogels (see below).

Synthesis of the γ-PGA hydrogel

γ-PGA hydrogels were prepared adapting the procedure described by Matsusaki *et al.*[42] γ-PGA and EDC were dissolved in 0.75 mL of 0.5 M $NaHCO_3$ at 4 ºC under magnetic stirring. Then, cystamine dihydrochloride, previously dissolved in 0.25 mL sodium hydrogen carbonate solution (0.5 M), was added to the solution and mixed during 2-3 min. The γ-PGA / EDC / Cystamine molar ratio was 5 / 4 / 2. The final solution was removed with a magnetic stirrer, and the reaction solution was poured into glass molds of 2.5 × 1.5 × 0.1 cm. The solution was let to gel at room temperature for one hour. To remove any compound in excess, the resulting hydrogel was washed with distillate water three times.

CP-loaded γ-PGA hydrogels: PEDOT/γ-PGA

The procedure described in the section before*: Synthesis of the γ-PGA hydrogel*, this was also used to prepare γ-PGA hydrogels loaded with PEDOT particles, hereafter denoted PEDOT/γ-PGA. More specifically, the only difference with respect to the preparation of pure γ-PGA hydrogel is that the 0.5 M $NaHCO_3$ solution used to dissolve the biopolymer already contained the PEDOT particles (20 w/w% of PEDOT particles with respect to the weight of γ-PGA).

Preparation of [PEDOT/γ-PGA]PHMeDOT electrodes through polymerization inside PEDOT/γ-PGA

Steel AISI 316 sheets of 0.5×0.5 cm^2 were coated with PEDOT/γ-PGA hydrogel and subsequently kept into the reaction medium overnight whilst stirring (65 rpm). The PEDOT/γ-PGA coated sheets were then used as working electrodes for the anodic polymerization of PHMeDOT by CA. The reaction medium was a 10mM HMeDOT aqueous solution with 0.1 M $LiClO_4$ as supporting electrolyte. The anodic polymerization was conducted under a constant potential of 1.10 V using a polymerization time, θ, of 6 min or 7 h. The experimental setup used for the in situ modification of the PEDOT/γ-PGA hydrogel was identical to that described in the first section: *Synthesis of PEDOT particles*. Hereafter, the loaded PEDOT/γ-PGA hydrogel electrochemically modified with PHMeDOT is denoted [PEDOT/γ-PGA]PHMeDOT

Morphological and topographical characterization

SEM studies were performed to examine the surface morphology of PEDOT, PEDOT/γ-PGA and [PEDOT/γ-PGA]PHMeDOT electrodes. Dried samples were placed in a Focussed Ion Beam Zeis Neon 40 scanning electron microscope operating at 3 kV, equipped with an EDX spectroscopy system. EDX analyses were performed to identify the presence of PEDOT particles and the success of the in situ PHMeDOT polymerization.

The AFM images were obtained with a Molecular Imaging PicoSPM using a NanoScope IV controller under ambient conditions. The tapping mode AFM was operated at constant deflection. The row scanning frequency was set to 1Hz. AFM measurements were performed on various parts of the films, which provided reproducible images similar to those displayed in this work. The scan window sizes used in this work were 5×5 μm^2. The statistical application of the NanoScope Analysis software was used to determine the R_q, which is the average height deviation taken from the mean data plane.

Electrochemical characterization.

All electrochemical experiments were run in triplicate using water with 0.1M $LiClO_4$ as supporting electrolyte. Cyclic voltammetry (CV) was carried out to evaluate the electroactivity, areal SC and the electrochemical stability of the prepared electrodes. The initial and final potentials were –0.50 V, and the reversal potential was 1.10 V. A scan rate of 100 mV s^{-1} was used in all cases.

The areal *SC* (in mF cm^{-2}) was determined using the following expression:

$$SC = \frac{Q}{\Delta V \cdot A} \tag{1}$$

where *Q* is voltammetric charge determined by integrating the oxidative or the reductive parts of the cyclic voltammogram curve, ΔV is the potential window (in V), and *A* is the area of the electrode (in cm^2). The exposed area of the different electrodes for CV analyses was 0.02 cm^2. The electrochemical stability was examined by evaluating the loss of electroactivity (LEA, in %) against the number of oxidation-reduction cycles:

$$LEA = \frac{\Delta Q}{Q_2} = \frac{Q_i \quad Q_2}{Q_2} \tag{2}$$

where ΔQ is the difference between the oxidation charge (in C) of the second (Q_2) and the evaluated oxidation-reduction cycle (Q_i).

Electrochemical impedance spectroscopy (EIS) diagrams were taken at open circuit (OCP) over the frequency range of 100 kHz to 10 mHz with a potential amplitude of 0.05 V using an AUTOLAB-302N potentiostat/galvanostat. All experiments were performed at room temperature in water with 0.1M $LiClO_4$.

Galvanostatic charge-discharge (GCD) cycles were run between -0.50 and 0.40 V using a current of 0.1 mA. GCD curves were also employed to evaluate the areal *SC* according to:

$$SC = \frac{\int I \cdot \Delta t}{\Delta V \cdot A} \quad (3)$$

where I is the applied current, Δt is the time of discharge (in s), ΔV is the difference between the potential at the beginning and at the end of the discharge (in V) and A is the area of the electrode (in cm^2).

Thermal stability, swelling and spectroscopic characterization

The thermal stability of the prepared samples was studied by TGA at a heating rate of 20 ºC min^{-1} (sample weight ca. 5 mg) with a Q50 thermogravimetric analyzer of TA Instruments and under a flow of dry nitrogen. Test temperatures ranged from 30 to 600 ºC.

The swelling ratio (*SR*, %) of the hydrogels was determined according to:

$$SR = \frac{w_W - w_D}{w_D} \quad (4)$$

where w_W is the weight of the hydrogels after 30 min in milli-Q water and w_D is the weight of the hydrogel dried at room temperature during 30 min after preparation.

Samples were characterized by micro-Raman spectroscopy using a commercial Renishaw inVia Qontor confocal Raman microscope. The Raman setup consisted of a laser (at 785nm with a nominal 300mW output power) directed through a microscope (specially adapted Leica DM2700 M

microscope) to the sample after which the scattered light is collected and directed to a spectrometer with a 1200 lines·mm^{-1} grating. The exposure time was 10s, the laser power was adjusted to 1% of its nominal output power and each spectrum was collected with 3 accumulations.

Conductivity measurements under mechanical stretching.

The conductivity of the prepared stretchable electrodes was determined under extreme conditions, which were applied using a universal testing machine (Zwick GmbH & Co., model Z2.5/TN1S) with integrated testing software (testXpert, Zwick). Electrical conductivities (σ) were determined for the stretched specimens using the sheet-resistance method following a previously described procedure.[43]

3.2.4. Results and Discussion

Preparation of PEDOT/γ-PGA and [PEDOT/γ-PGA]PHMeDOT electrodes

In this work, the synthesis of PEDOT/γ-PGA and [PEDOT/γ-PGA]PHMeDOT electrodes to be applied in energy storage devices are reported for the first time. PEDOT particles were obtained by applying a sonication treatment to electropolymerized PEDOT films. The influence of the sonication time (t_{son}) in the diameter of the resulting particles (D_{CP}) was evaluated by DLS in 0.5 M $NaHCO_3$ [Figure 3.2-1(a)] Results indicate that D_{PEDOT} decrease with increasing t_{son}, becoming stable at D_{PEDOT}= 0.85 ± 0.03 μm after 25 min.

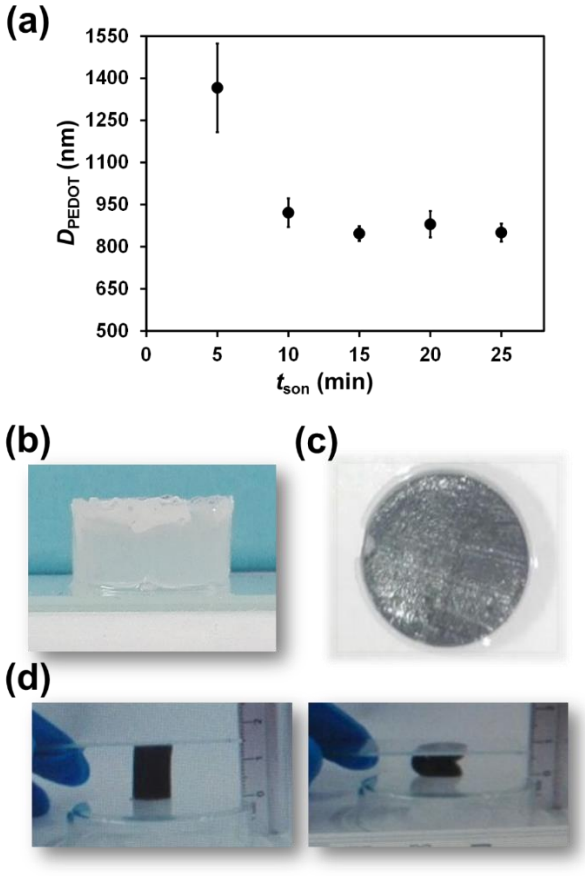

Figure 3.2-1. (a) Variation of the average diameter of PEDOT particles (D_{PEDOT}) against the sonication time (t_{son}) as revealed by DSL measurements in 0.5 M $NaHCO_3$. Optical images of (b) the unloaded γ-PGA and (c) the PEDOT/γ-PGA hydrogels. (d) Optical images illustrating the consistency and compression behaviour of PEDOT/γ-PGA.

On the other hand, the influence of the loaded CP particles in the conductivity of the hydrogel was examined by performing EIS measurements on γ-PGA and PEDOT/γ-PGA using a cell with a geometry explicitly constructed for the analysis of these polymeric systems.[44] The diameter of the semicircle in the recorded Nyquist plots (not shown) corresponded to the charge-transfer resistance, R_C, the conductivity (σ, in S cm^{-1}) being determined through the following expression:

$$\sigma = \frac{L}{R_C A} \quad (5)$$

where L is the thickness of the coating (0.02 cm), A is the area of the coated electrode (1.77 cm^2), and R_C is the hydrogel resistance. As expected, the incorporation of 20 w/w% PEDOT particles significantly affects the electrical conductivity, which increases from $\sigma = 6.84 \cdot 10^{-6}$ S cm^{-1} for γ-PGA to $\sigma = 1.77 \cdot 10^{-3}$ S cm^{-1} for PEDOT/γ-PGA. The latter value is within the typical range attributed to semiconducting materials.

In order to enhance the electrochemical behaviour of the electrode, HMeDOT monomers in aqueous solution were anodically polymerized directly inside the loaded PEDOT/γ-PGA hydrogel. PHMeDOT was chosen for the electrochemical modification of PEDOT/γ-PGA because of the following two reasons: [45, 46] *(i)* the solubility in water of HMeDOT is high, especially when compared with the EDOT monomer, due to the exocyclic hydroxymethyl group; and *(ii)* the capacitance and electrochemical activity of PEDOT and PHMeDOT are very similar.

Accordingly, the exocyclic hydroxymethyl group of HMeDOT allowed us to ensure the success of the polymerization process in water without cause detriment in the electrochemical characteristics of the final [PEDOT/γ-PGA]PHMeDOT electrode. It should be emphasized that PEDOT/γ-PGA was kept under stirring in the reaction medium overnight (see Methods section). This simple procedure guarantees the penetration of the HMeDOT monomers into the hydrogel matrix ensuring the success of the polymerization process.

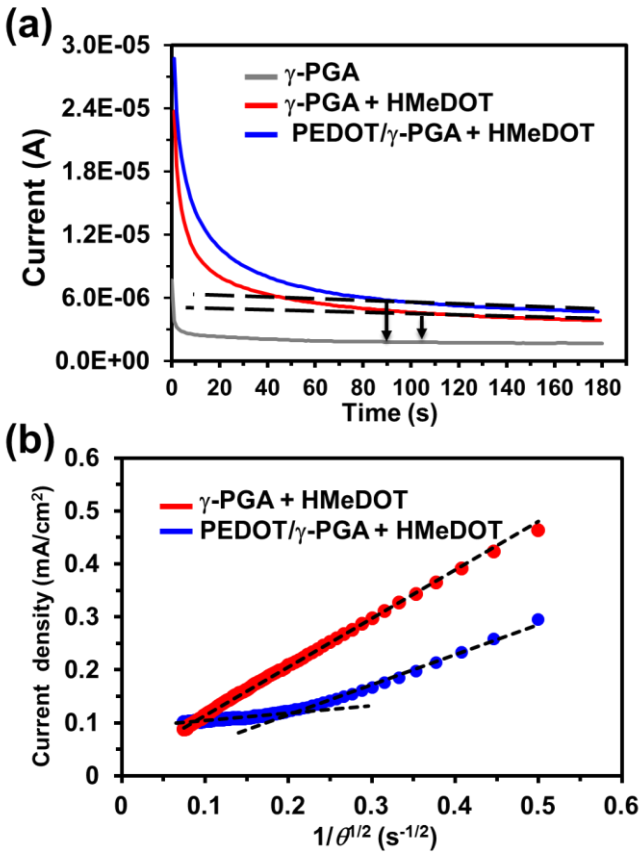

Figure 3.2-2. (a) Chronoamperograms recorded in 0.1 M LiClO4 aqueous solution for unloaded γ-PGA, unloaded γ-PGA with 10 mM of HMeDOT monomer, and PEDOT/γ-PGA with 10 mM of EDOT-OH monomer. (b) Cottrell plots for unloaded γ-PGA and PEDOT/γ-PGA with 10 mM of HMeDOT monomer.

Figure 3.2-2 represents the chronoamperograms obtained after the electropolymerization of a 10 mM HMeDOT aqueous solution with 0.1 M $LiClO_4$ as supporting electrolyte on a steel electrode coated with PEDOT/γ-PGA and unloaded γ-PGA hydrogels. For the sake of comparison, the chronoamperometric curve obtained in aqueous solution with 0.1M $LiClO_4$ (*i.e.* without HMeDOT monomer) for a steel electrode coated with unloaded γ-PGA (blank sample) is also reported. As it can be seen, the electropolymerization charge was 25 % higher in the presence of PEDOT particles (*i.e.* 0.128 and 0.160 C for unloaded γ-PGA and PEDOT/γ-PGA, respectively). This is a very remarkable difference considering that the γ-PGA hydrogel tends to behave as a dielectric material. Therefore, the presence of PEDOT particles inside the γ-PGA matrix presumably provides additional nucleation sites that enhance the HMeDOT polymerization.

To better understand the polymerization reaction when the hydrogel is part of the reaction medium, a detailed study of the kinetics was conducted. The evolution of current with time during the anodic polymerization of PEDOT, and by extrapolation of PHMeDOT, was explained through three main steps:[47] *(i)* the initial spike, which is due to the charging of the double layer; *(ii)* the region that exhibits a slow variation of the current, which is associated to the CP nucleation; and *(iii)* the zone in which the current keeps constant over time because of the growth of the polymer chains. However, chronoamperograms displayed in

Figure 3.2-2(a) reflects a different current decay during the second step, independently of the absence or presence of PEDOT particles. Specifically, this step ends at ~85s and ~105s for the polymerization inside PEDOT/γ-PGA and unloaded γ-PGA, respectively. Accordingly, the nucleation of PHMeDOT is most probably affected by the presence of PEDOT microparticles embedded into the hydrogel, which provide charges and radicals able to bind HMeDOT monomers.

The Cottrell equation was applied using the data shown in

Figure 3.2-2(a) to study the diffusion of the HMeDOT molecules in the solution.

Figure 3.2-2(b) represents the variation of the anodic current density against the inverse of the square of electropolymerization time ($\theta^{1/2}$). The diffusion coefficient (D) was derived from:

$$I = \frac{n \cdot F \cdot A \cdot C^{*} \cdot D^{1/2}}{(\pi \cdot \theta)^{1/2}} \quad (6)$$

where, I is the anodic current, C^{*} is the molar concentration (10 mM), F is the Faraday constant, A is the area of the electrode and n is the number of electrons transferred. The value of the current obtained for the blank sample (i.e. electrode coated with unloaded γ-PGA and without monomer in the reaction medium), which is related to the electron transfer at the steel electrode when ClO_4^- the molecules reach the surface, was subtracted from the currents recorded during the experiments with PEDOT/γ-PGA and unloaded γ-PGA hydrogels in presence of monomer.

Although

Figure 3.2-2(b) shows the current decay, a steady state is detected at long times in presence of PEDOT particles. From that, it can be inferred a “transition time” after which the current profile behaves linearly until the end of the experiment. The transition time is defined by the intersection of the two straight lines in

Figure 3.2-2(b), representing ideal transient and steady-state conditions, respectively. According to the Nernst–Planck equation, the flux of species is due to the concentration gradient and the electric field.

However, since the y-intercept of Cottrell plots is very low (i.e. 0.0013 and 0.022 mA cm^2 for PEDOT/γ-PGA and unloaded γ-PGA, respectively), it can be considered that the influence of the electric field can be roughly disregarded in both cases. Based on this, the results indicate that the transport of molecules inside the swelled γ-PGA hydrogel is driven by the concentration gradient of the charge on the infinite-diffusion system. According to the Cottrell equation (Eq 6), the diffusion coefficients were estimated as 4.525×10^{-9} and 1.739×10^{-9} cm^2 s-1 for unloaded γ-PGA and PEDOT/γ-PGA hydrogels, respectively. These values, which are significantly higher than those typically expected for substances in solution. Thus, the difficulties in the mobility of HMeDOT molecules inside the hydrogel limit the electrogeneration process. However, the differences between the two systems confirm that PEDOT particles dispersed in the hydrogel matrix act as reaction nuclei, decreasing the diffusion coefficient of the intercepted HMeDOT monomer molecules that bind to PEDOT particles before reaching the steel surface.

On the other hand, the electropolymerization times used in this work were θ= 6 min and 7h. Considering the current productivity of PHMeDOT in water and the charge consumed during the electropolymerization process inside PEDOT/γ-PGA hydrogel (*i.e.* 1.80 and 33.5 mC for θ= 6 min and 7 h, respectively), the mass of PHMeDOT produced per 1 mm^3 of loaded hydrogel is estimated to be around $5\cdot10^{-5}$ and $1\cdot10^{-3}$ mg for θ= 6min and 7 h.

Morphological and topographical analysis

Figure 3.2-3 compares SEM micrographs of γ-PGA and PEDOT/γ-PGA hydrogels before [Figure 3.2-3(a-b) and Figure 3.2-3(c-f)], respectively and after [Figure 3.2-3(e) and Figure 3.2-3 (f)], respectively CV analyses. As one of the most important objectives of this work is to promote the movement of ions through the flexible electrode, the hydrogel should present an open porous

structure and mechanical integrity. Figure 3.2-3(a-b) show the porous structure of the γ-PGA hydrogel, which exhibits irregularly shaped pores with diameter typically comprised between 2 and 12μm [Figure 3.2-3(b)]. A similar structure is observed for PEDOT/γ-PGA [Figure 3.2-3(c-d)], even though in this case aggregates of PEDOT microparticles dispersed into the biopolymeric matrix are observed [Figure 3.2-3(d)]. The dispersion of the PEDOT particles in biopolymeric matrix is reflected in the cross section SEM images of PEDOT/γ-PGA [Figure 3.2-3(e-f)], which prove that such particles are not only located at the surface of the γ-PGA hydrogel but also embedded inside.

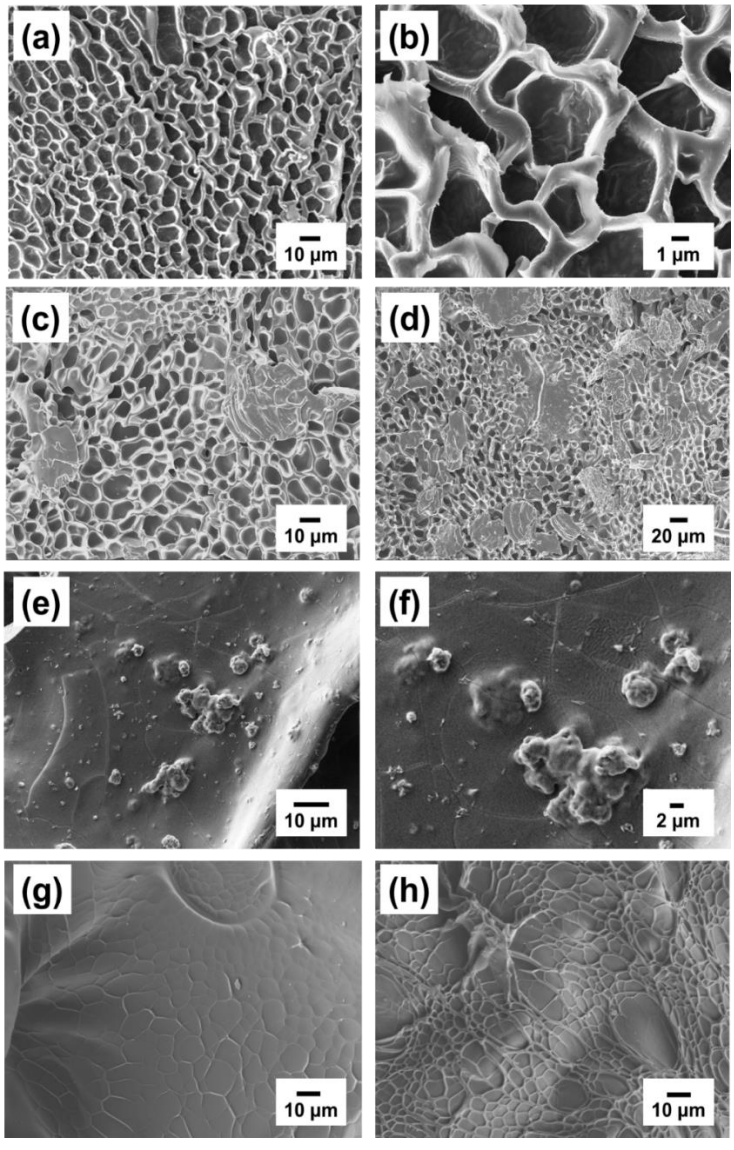

Figure 3.2-3. SEM micrographs of (a, b, e) unloaded γ-PGA and (c, d, e, f, h) PEDOT/γ-PGA hydrogels. Images (e, f) correspond to the cross section of the PEDOT/γ-PGA hydrogel. Images before (a-f) and after

(g, h) analysis by CV in acetonitrile with 0.1 M of $LiClO_4$ are displayed. Additionally, (b), (d) and (f) display high magnification images of (a), (c) and (e), respectively.

After electrochemical analyses, which were performed in water with 0.1 M of $LiClO_4$ as supporting electrolyte, the surface morphology of both γ-PGA and PEDOT/γ-PGA electrodes experienced significant changes [Figure 3.2-3(g) and Figure 3.2-3(h)], respectively. More specifically, the porous hydrogel matrix transforms into a closed structure, while PEDOT particles becomes more compact. These morphological alterations are due to the effects of voltammetric processes on the γ-PGA and PEDOT chains. More specifically, fast rearrangements of the γ-PGA chains after the ions transport are possible because of the chemical nature of the crosslinked polymer network. Thus, cystamine offers relatively flexible crosslinks due to the presence of a bridge with four methylene units, providing mobility to the γ-PGA chains. It should be noted that chain rearrangements are necessary to obtain both a high diffusion rate of the water molecules and a good distribution of the ions inside the matrix. Besides, electrostatic repulsions among the carboxylate groups in the dehydrated structures used for SEM analyses are expected to be significantly mitigated by the presence of Li^+ ions inside the matrix, which chelate with such negatively charges groups.[48]

In addition, for the PEDOT/γ-PGA electrode, at potentials higher than the oxidation potential of the CP, the repulsive forces between emerging positive charges on closer PEDOT chains (*i.e.* formed polarons) induce conformational movements that generate free volume, facilitating the entrance of counterions and solvent molecules from the solution. In opposition, during the voltammetric reduction, the CP polymer shrinks since counterions and solvent molecules are expelled towards the solution and the structure becomes closed (*i.e.* interchain distances are shorter than counterion diameters). The influence of the voltammetric oxidation and reduction on PEDOT was studied in detail by Otero and co-workers.[49]

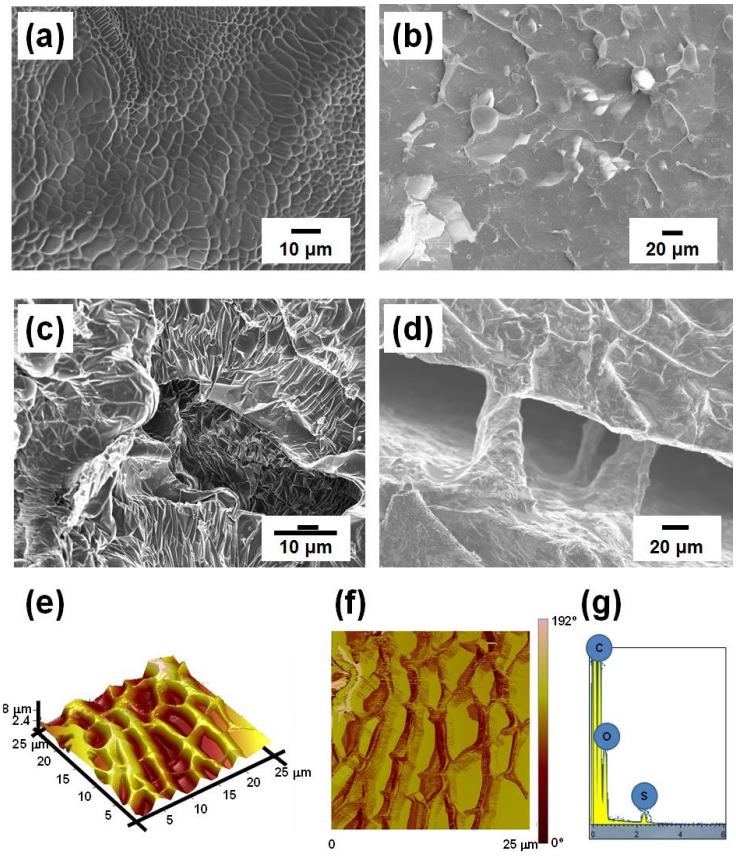

Figure 3.2-4. Surface SEM micrographs of (a) [γ-PGA]PHMeDOT (θ= 6 min), (b) [PEDOT/γ-PGA]PHMeDOT (θ= 6 min), and (c) [PEDOT/γ-PGA]PHMeDOT (θ= 7 h). (d) Cross section SEM image of [PEDOT/γ-PGA]PHMeDOT (θ= 7 h). (e) 3D topographic and (f) 2 D phase AFM images of [PEDOT/γ-PGA]PHMeDOT (θ= 7 h). (g) EDX analysis of the sample displayed in (c).

The Figure 3.2-4 compares SEM micrographs of γ-PGA after electropolymerization of PHMeDOT during 6min [Figure 3.2-4(a)], denoted [γ-PGA]PHMeDOT (θ= 6 min), and [PEDOT/γ-PGA]PHMeDOT considering electropolymerization times of θ= 6 min and 7 h [Figure 3.2-4(b) and Figure 3.2-4(c)], respectively. In absence of PEDOT particles, at low electropolymerization time, no evidence of PHMeDOT is detected on the surface of γ-PGA, the morphology of [γ-PGA]PHMeDOT (θ= 6 min) [Figure 3.2-4(a)] being practically identical to that obtained for pure γ-PGA after apply a voltammetric cycle [Figure 3.2-4(g)]. In contrast, the surface of [PEDOT/γ-PGA]PHMeDOT (θ= 6 min) is covered by a layer [Figure 3.2-4(b)], which has been attributed to PHMeDOT. Moreover, PEDOT particles are surrounded by ramifications. This feature indicates

that the electropolymerization of PHMeDOT starts at the CP particles, corroborating the role of PEDOT particles as nuclei for the electropolymerization process. However, the morphology of PHMeDOT experiences drastic changes when the electropolymerization time increases to θ= 7 h. More specifically, Figure 3.2-4(c) displays a quite uniform and well-distributed 3D microstructure that densely covers the γ-PGA surface. As observed, apparently such microstructure results from the assembly of lamellar architectures, suggesting that PHMeDOT organizes according to a folded-chain model.[50] Moreover, SEM cross section images [Figure 3.2-4(d)]demonstrate that the conductive PHMeDOT networks extends inside the hydrogel matrix.

Representative 3D topographic and 2D phase AFM images of [PEDOT/γ-PGA]PHMeDOT(θ= 7h), which are displayed in Figure 3.2-4 (e,f), respectively, are fully consistent with the conclusions extracted from SEM micrographs [Figure 3.2-4(c)]. Moreover, AFM images indicate that the observed 3D microstructure presents a very high roughness with R_q= 783 nm. Besides, EDX analyses from the sample displayed in Figure 3.2-4(g) confirm the presence of PHMeDOT, as is evidenced by the well-defined sulfur peak.

Chemical characterization, thermal stability and swelling

Figure 3.2-5 shows the FTIR spectra of γ-PGA, PEDOT/γ-PGA and [PEDOT/γ-PGA]PHMeDOT(θ= 6 min and 7 h). The typical absorption bands of the γ-PGA hydrogel, as identified by Pérez-Madrigal *et al.*,[25] are detected for all samples.

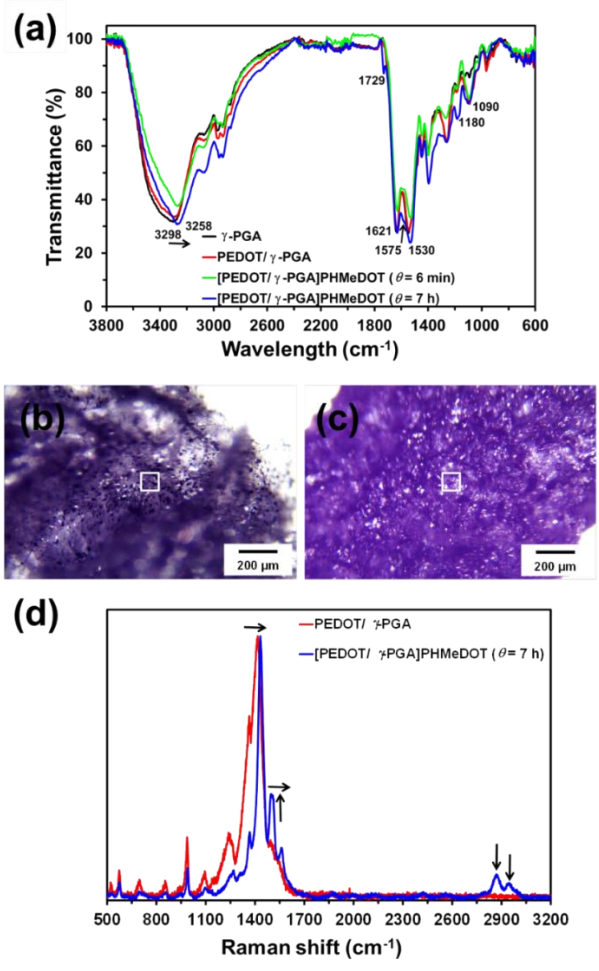

Figure 3.2-5. (a) FTIR spectra for pure γ-PGA, PEDOT/γ-PGA, and [PEDOT/γ-PGA]PHMeDOT (θ= 6 min and 7 h). Images obtained using a confocal Raman microscope for (b) PEDOT/γ-PGA and (c) [PEDOT/γ-PGA]PHMeDOT (θ= 7 h). White squares define the areas used to record de Raman spectra. (d) Raman spectra of PEDOT/γ-PGA and [PEDOT/γ-PGA]PHMeDOT (θ= 7 h). Excitation wavelength: 785 nm.

The success of the cross-linking process was proved by comparing with the FTIR spectrum of the biopolymer acquired before the reaction with the cystamine (not shown). Thus, the formation of –CONH– bonds due to the reaction between the biopolymer and the cross-linker was evidenced by the disappearance of the free carboxylic acid (1718 cm^{-1}) and asymmetric COO^- bands (1595 cm^{-1}), and by the enhancement of the amide I (1621 cm^{-1}) and amide II (1530 cm^{-1}), as compared with non-crosslinked γ-PGA.

Besides, the presence of PEDOT particles in PEDOT/γ-PGA is disclosed by the appearance of the C–O–C stretching vibration (1090 cm^{-1}) and ethylendioxy stretching (1180 cm^{-1}) bands. Electropolymerization of PHMeDOT results in the enhancement of such peaks. Further, the broad peak at around 3298 cm^{-1}, which is due to the overlap of N–H and O–H stretching vibrations from γ-PGA, experiences a shift towards 3258 cm^{-1} for the [PEDOT/γ-PGA]PHMeDOT(θ= 7 h) sample. Both the blue shift and the narrowing of such peak have been attributed to the high amount of hydroxyl groups arising from PHMeDOT. Moreover, peaks at 1530, 1575 and 1729 cm^{-1}, which appear using θ= 7 h, have been associated to enhanced oxidation processes.

Furthermore, Raman spectra and microscopy images were taken from the cross section of transversely cut PEDOT/γ-PGA and [PEDOT/γ-PGA]PHMeDOT(θ= 7 h) samples using confocal Raman microscope. Spectra were taken inside the areas marked in images displayed in Figure 3.2-5(b) and Figure 3.2-5(c). As it can be seen, black spots ascribable to the PEDOT particles are clearly identified in Figure 3.2-5(b), whereas these spots are much less evident in Figure 3.2-5(c) due to the great amount of PHMeDOT covering PEDOT particles.

The spectra reported in Figure 3.2-5(d) exhibit the characteristics peaks of PEDOT: 983cm^{-1} (vibration mode of the thiophene C–S bond), 1085cm^{-1} (stretching of the ethylendioxy group), 1255 cm^{-1} (C–C inter-ring stretching), 1365 cm^{-1} (C–C stretching), 1430 cm^{-1} (C=C symmetrical stretching) and 1485cm^{-1} (C=C asymmetrical stretching). In presence of PHMeDOT, the peaks at 1430 and 1485 cm^{-1} shift to 1433 and 1496 cm^{-1}, respectively, and, in addition, the intensity of the latter experiences a significant increment. However, the most important feature is the appearance of two new peaks at 2878 and 2960 cm^{-1}, which have been associated to the exocyclic hydroxyl group. Therefore, we conclude that both the loaded PEDOT particles and the PHMeDOT electropolymerized on PEDOT/γ-PGA are well and homogenously distributed inside the hydrogel matrix.

The thermal stability is an essential parameter for the potential application of conducting polymers. Unfortunately, the decomposition temperature of these materials is usually low, as is reflected in the literature.[51-53] Figure 3.2-6, which compares the thermogravimetric curves for γ-PGA, PEDOT/γ-PGA and [PEDOT/γ-PGA]PHMeDOT (θ= 7 h), shows a small weight loss (*i.e.* 10 %) at about 100°C for γ-PGA and PEDOT/γ-PGA. This loss corresponds to the evaporation of absorbed traces of water. A similar weight loss is detected for [PEDOT/γ-PGA]PHMeDOT (θ= 7 h) although the evaporation process takes place in a wider temperature interval (*i.e.* the DTGA peak moves to 122 ºC), suggesting that the hydrogel network becomes more compact as expected from the performed polymerization.

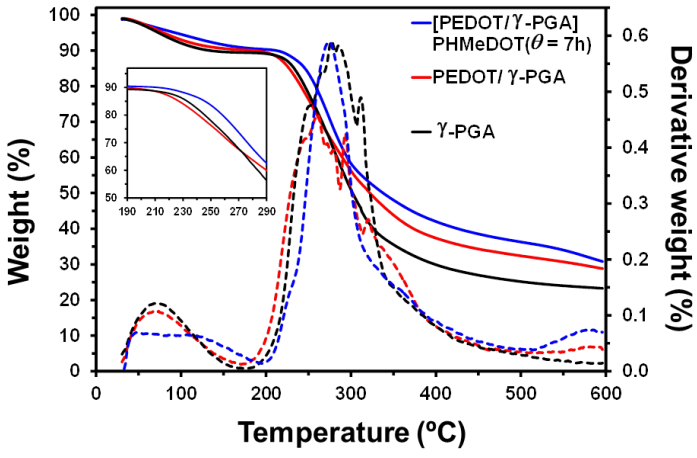

Figure 3.2-6. Thermogravimetric (solid lines) and derivative thermogravimetric curves (dashed lines) for γ-PGA, PEDOT/γ-PGA and [PEDOT/γ-PGA]PHMeDOT (θ= 7 h). Details of the region associated to the main decomposition process are provided in the inset.

Figure 3.2-6 also indicates that the thermal degradation process is roughly similar for the three samples considering that the predominant decomposition step took place around 275 ºC. However, detailed analyses reveal some important differences among the three samples. Thus, γ-PGA shows a multistep degradation that could be justified by the complex molecular architecture that involves different units (*e.g.* γ-PGA and the cystamine crosslinker) and also to a non-highly homogeneous matrix. The degradation process becomes more complex for PEDOT/γ-PGA in the 240-327 ºC interval as evidenced by the higher number of peaks surrounding the one associated to the maximal decomposition. This feature suggests a hindered diffusion of degradation products caused by the presence of PEDOT particles. Small shoulders at 225ºC and 350ºC could also be detected in the DTGA curve as well as a peak at 585 ºC. Interestingly, analysis of the DTGA curve obtained for [PEDOT/γ-PGA]PHMeDOT (θ= 7 h) indicates that the polymerization of PHMeDOT inside the hydrogel matrix gives rise to a highly uniform matrix that causes a similar diffusion of degraded molecules and therefore a single predominant peak. Shoulders detected in the PEDOT/γ-PGA sample are logically still observed as well as a high temperature peak at 582 ºC.

The swelling behaviour of the different systems, which was determined by gravimetric measurements, is displayed in Table 3.2-1 as it can be seen, the swelling ratio of the hydrogels increases with the content of CP, growing from SR= 54% for the pristine γ-PGA hydrogel to SR=

289% [PEDOT/γ-PGA]PHMeDOT (θ= 7 h). This effect has been attributed to the hydrophilicity of PEDOT and, specially, of PHMeDOT.

Table 3.2-1. Properties of the studied systems: Swelling ratio (SR), voltammetric stored charge per surface unit (C cm^{-2}), and the areal SC in (mF cm^{-2}) as determined by cyclic voltammetry.

System	SR (%)	Q (C cm^{-2})	SC (mF cm^{-2})
γ-PGA	54	8.298×10^{-3}	2.4 ± 0.3
PEDOT/γ-PGA	115	7.277×10^{-3}	2.6 ± 0.4
[PEDOT/γ-PGA]PHMeDOT(θ= 6 min)	206	7.981×10^{-3}	2.7 ± 0.5
[PEDOT/γ-PGA]PHMeDOT (θ= 7 h)	289	0.1454	45.4 ± 0.7

Electrochemical properties

The electroactivity, *SC* and electrochemical stability of the prepared electrodes were determined by CVs in water with 0.1 M $LiClO_4$ Figure 3.2-7(a) compares the control voltammograms recorded for γ-PGA, PEDOT/γ-PGA and [PEDOT/γ-PGA]PHMeDOT(*θ*= 6 min and 7 h).

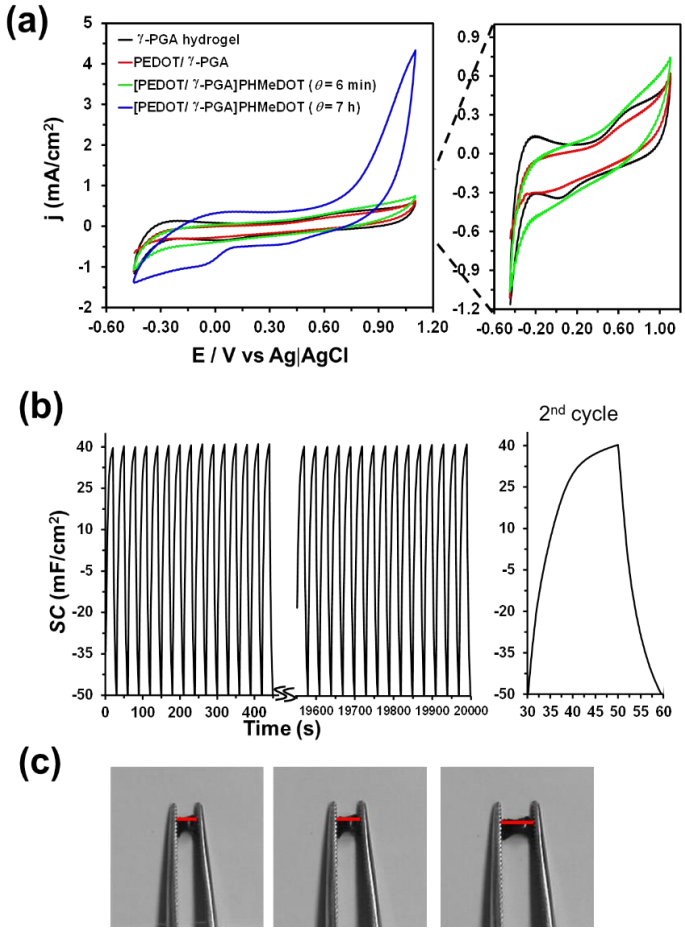

Figure 3.2-7. (a) Control voltammograms (2nd cycle) for γ-PGA, PEDOT/γ-PGA, [PEDOT/γ-PGA]PHMeDOT (θ= 6min) and [PEDOT/γ-PGA]PHMeDOT (θ= 7 h). Initial and final potential: -0.50; reversal potential: 1.10 V; scan rate of 100mVs^{-1}. (b) Galvanostatic charge-discharge (GCD) curves recorded at 0.1 mA (charging and discharging times of 30 s) for [PEDOT/γ-PGA]PHMeDOT (θ= 7 h). The second cycle is displayed at the right. (c) Photographs reflecting the mechanical robustness and compression behaviour of [PEDOT/γ-PGA]PHMeDOT (θ= 7 h) after 1000 GCD cycles.

The response of the γ-PGA hydrogel is more pronounced than that expected for a dielectric. However, previous studies devoted to investigate the electrochemical response of nanomembranes prepared by spin-coating mixtures of polythiophene and insulating thermoplastics,[54, 55] proved the electrochemical response of control nanomembranes made with the latter. In spite of this, voltammograms recorded for insulating thermoplastics did not show well-defined oxidation and

reduction peaks in water with $LiClO_4$, which was consistent with the formation of charged species at unspecific positions.[54, 55]

This represents a significant difference with respect to the voltammogram obtained for the γ-PGA hydrogel [Figure 3.2-7(a)]. In this case, the oxidation peaks with anodic peak potentials of –0.2 and 0.7 V have been attributed to the formation of irreversible polarons and bipolarons, respectively, at preferred positions. Furthermore, the cathodic scan shows a reduction peak with cathodic peak potential of 0.08 V, which has been attributed to the electrochemical reduction of the amide bond to secondary amine (*i.e.* electrochemical deoxygenation process).[56] On the other hand, the electrochemical activity of the γ-PGA hydrogel is higher than that observed for insulating thermoplastics.[54, 55] This has been attributed to the pores (Figure 3.2-7) formed by cross-linked polymer chains, which facilitate considerably the access of the electrolyte ions to the surface of the steel substrate.

On the other hand, the electrochemical response obtained for PEDOT/γ-PGA and [PEDOT/γ-PGA]PHMeDOT(θ= 6 min) is apparently similar to that observed for the pristine hydrogel [Figure 3.2-7(a)], inset. Thus, the incorporation of CP inside the dielectric hydrogel matrix does not cause an increment in the electrochemical activity, even though the oxidation and reduction of PEDOT and PHMeDOT are typically detected.[37] The first oxidation peak of chains occurs at 0.5 V, while the second peak overlaps with the oxidation potential of the medium. In addition, two reduction peaks are detected in the cathodic scans, indicating the presence of redox pairs in the recorded potential range. These redox processes, which are clearly identified for both PEDOT/γ-PGA and [PEDOT/γ-PGA]PHMeDOT(θ= 6 min), should be attributed to the formation of polarons in the CP chains.

The electroactivities, which were quantified as the voltammetric stored charge per surface unit (Q), and the areal *SC*, Eq 1) of γ-PGA, PEDOT/γ-PGA and [PEDOT/γ-PGA]PHMeDOT (θ= 6min), are listed in Table 3.2-1. Consistently with the voltammograms displayed in Figure 3.2-7(a), the electrochemical properties of the three systems were lower than those typically obtained for CPs.[53,57] More specifically, the values of Q and SC determined for PEDOT films prepared using identical experimental conditions are 4.25×10^{-2}C cm^{-2} and 27mF cm^{-2}, respectively.

Enlargement of the PHMeDOT polymerization time from θ= 6 min to t= 7 h causes a remarkable improvement of the electrochemical properties, which is reflected by the gain in both the cathodic and anodic areas of the recorded voltammogram [Figure 3.2-7(a)]. The electroactivity is one order f

magnitude higher for [PEDOT/γ-PGA]PHMeDOT(θ= 7h) than for the other three systems (Table 3.2-1). The well-defined oxidation peak, with anodic peak potencial Epa ≈ 1.35 V and the reduction shoulder, with cathodic peak potential Epc= -0.02 V, are consistent with the very high content of PHMeDOT at the electrode and reflect a remarkable redox charge storage capacity.

The *SC* of [PEDOT/γ-PGA]PHMeDOT (*θ*= 7 h), 45.4 mF cm^{-2}, is almost 20 times higher than the areal capacitance of PEDOT/γ-PGA (2.3 mF cm^{-2}), and several times higher than those recently reported for other flexible PEDOT-based organic electrodes, as for example: four-layered PEDOT: PSS films (4 mF cm^{-2}),[58] graphene oxide/PEDOT and reduced graphene oxide/PEDOT composites electropolymerized onto flexible substrates (16 and 25mF cm^{-2}, respectively),[59] and PEDOT electrochemically deposited on PEDOT: PSS/cellulose substrates (from 11 to 32mF cm^{-2}).[60] Moreover, the *SC* of [PEDOT/γ-PGA]PHMeDOT (*θ*= 7 h) experienced a slight increment after a few consecutive oxidation-reduction cycles (*i.e.* from 45.4 to 46.1 mF cm^{-2} after ten cycles), suggesting that such electrochemical processes induce small structural rearrangements that favor the interactions between different chemical components. This synergistic interaction was not observed for PEDOT/γ-PGA and [PEDOT/γ-PGA]PHMeDOT (*θ*= 6 min).

The lifetime stability of [PEDOT/γ-PGA]PHMeDOT (*θ*= 7 h) was examined by submitting this electrode to one-thousand consecutive GCD cycles from -0.50 to 0.40 V at a current of 0.1 mA [Figure 3.2-7 (b)]. GCD curves exhibited slight distortions with somewhat non-symmetrical curves since the discharge time was imposed to be lower than the charge time. The areal *SC* of the [PEDOT/γ-PGA]PHMeDOT (*θ*= 7 h) electrode, as derived from Eq 3 (47.2 mF cm^{-2}), showed an outstanding retention of 87.5% after 1000 cycles (41.3 mF cm^{-2}). Besides, the mechanical characteristics of the [PEDOT/γ-PGA]PHMeDOT (*θ*= 7 h) electrode remains practically unaltered after multiple charge-discharge cycles. This is demonstrated in Figure 3.2-7(c), which shows the robustness and compression behaviour of the electrode after the 1000 GCD cycles. Specifically, the electrode can be compressed by more than 50% without signs of damages.

Practical application: Powering a LED bulb

The [PEDOT/γ-PGA]PHMeDOT (*θ*= 7 h) electrode retains the flexibility and compression behaviour of the γ-PGA hydrogel. In recent years the importance of organic flexible and stretchable electrodes has been reviewed different authors.[61-64] Important advances have been also described for PEDOT-based electrodes. For example, Cheng *et al.*[65] reported flexible transparent electrodes with

very good electrochemical and optoelectronic performance by combining Ag grids with PEDOT: PSS layers on polyethylene terephthalate substrates using an inkjet printing methodology. The electromechanical properties of these electrodes were superior to those achieved for flexible electrodes constructed embedding Ag nanowires into poly(dimethylsiloxane).[68] Kurungot and co-workers[66] prepared highly conducting and robust PEDOT-paper electrodes using a surfactant-free interfacial polymerization at the interface of two immiscible liquids. This procedure resulted in flexible PEDOT films with highly ordered polymer chains and enhanced doping level. Liu *et al*. obtained highly flexible, bendable and conductive graphene-PEDOT: PSS films using a simple bar-coating method. The assembled device using rGO-PEDOT/ PSS electrode could be bent and rolled up without any decrease in electrochemical performance.[67]

Measurements of conductivity changes have been made in flexible [PEDOT/γ-PGA]PHMeDOT (θ= 7h) electrode when subjected to a uniaxial strain of up to 10 % [Figure 3.2-8(a)]. For this purpose, the prepared specimens, which consisted of rectangular sheets of 30 mm (length) × 5 mm (width) × 0.8mm (thickness), were stretched at a rate of 2mm min^{-1}. Figure 3.2-8(b) displays the change in resistance under tensile deformation. Although the conductivity decreases linearly with increasing uniaxial strain, changes are relatively small (37% for the maximum tensile deformation). These results indicate that embedded CP regions remain relatively associated among them and, therefore, the electrode's electrical properties experience relatively small variations. Unfortunately, the situation changes when the uniaxial strain is ≥ 15%. In that case, the electrical resistivity increases drastically, indicating the irreversible dissociation of conductive regions inside the hydrogel. This should not be attributed to the rupture of the hydrogel but to the very poor mechanical properties of PHMeDOT and PEDOT particles, which are not able to follow the elastic movements of γ-PGA chains without damage.

Finally, the [PEDOT/γ-PGA]PHMeDOT(θ= 7 h) electrode displayed in Figure 3.2-8(c) was used in a simple demonstration of an energy harvesting system by powering a red LED bulb. For this purpose, a Teflon holder with a stainless steel (AISI 304) disk was assembled with the [PEDOT/γ-PGA]PHMeDOT (θ= 7 h) electrode, as is illustrated in Figure 3.2-8(d). The assembled system was charged by coupling a power supply of 24 V and a resistance of 20 kΩ [Figure 3.2-8(e)]. Such two elements were retired after complete the recharge, employing about 60 s. As the voltage required to power a LED bulb is about 1.5 V, the system was connected in series [Figure 3.2-8(f)] with the LED bulb to get an open circuit voltage of 2.2 V. The LED bulb was powered during intervals of time of ~125s, the discharge through the powering of the red LED being displayed in Figure 3.2-8. This result corroborates that the [PEDOT/γ-PGA]PHMeDOT electrode composite is able to supply

enough current instantaneously, evidencing its applicability in flexible energy-harvesting systems (this work is currently in progress).

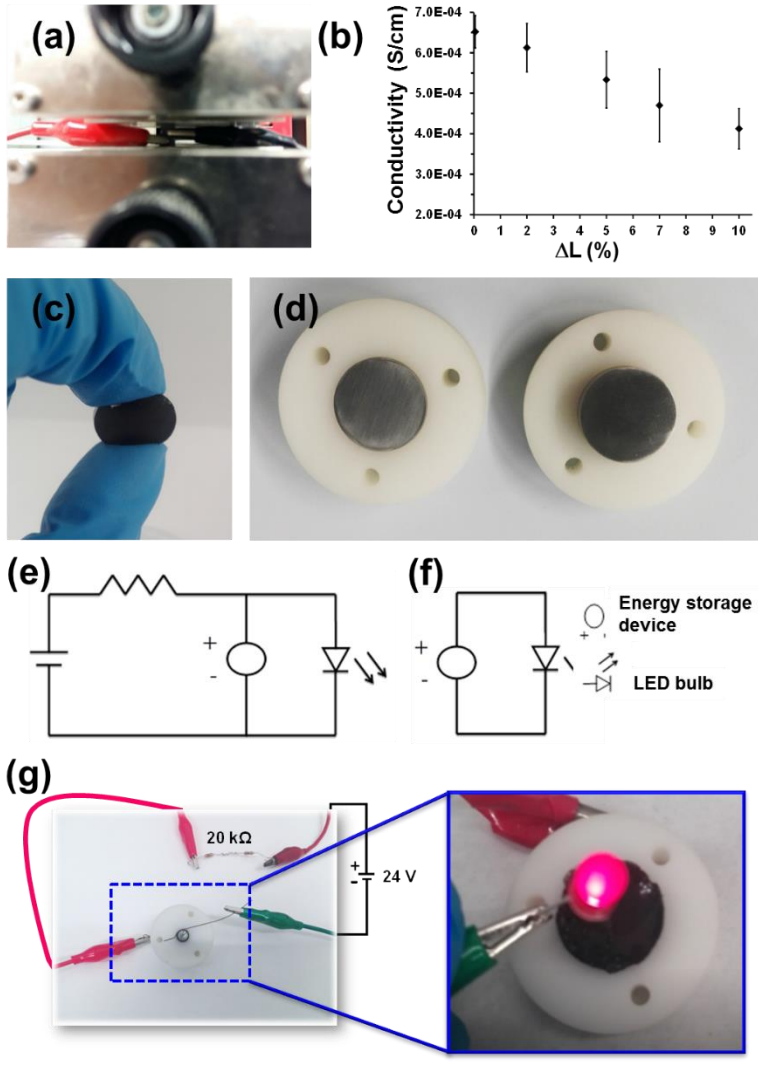

Figure 3.2-8. (a) Photographs showing the electrical conductivity measurement under stretching conditions of the flexible [PEDOT/γ-PGA]PHMeDOT (θ= 7 h) electrode. (b) Variation of the electrical conductivity with the strain for flexible [PEDOT/γ-PGA]PHMeDOT (θ= 7 h) electrodes. Error bars display standard deviations calculated considering five independent samples. (c) Flexible [PEDOT/γ-PGA]PHMeDOT (θ= 7 h) electrode used power the LED bulb. (d) Energy harvesting system constructed using a Teflon holder with a stainless steel (AISI 304) disk and the [PEDOT/θ-PGA]PHMeDOT (θ= 7 h) electrode. Schematic diagram of the circuits used to (e) charge and to (f) power the LED using the energy-harvesting device displayed in (d). (g) Photographs of the device used to power the LED bulb.

3.2.5. Conclusions

Highly flexible and lightweight free-standing electrodes have been synthesized by functionalizing γ-PGA hydrogels with PEDOT particles, which were subsequently used as polymerization nuclei for the anodic polymerization of PHMeDOT. The γ-PGA hydrogel provides a support with consistency, robustness and open internal structure, which is crucial to permit the ion diffusion process. PEDOT particles play a key role in the electropolymerization of HMeDOT monomer, favoring the homogeneous distribution of PHMeDOT chains across the hydrogel. The resulting [PEDOT/γ-PGA]PHMeDOT(θ= 7h) composite presents a great potential in supercapacitors with a *SC* hitting 45-47 mF cm^{-2}, as obtained by CV and GCD, and excellent cycle durability. The effectiveness of this electrode has been proved through a simple application based on power a red LED. The as-made [PEDOT/γ-PGA]PHMeDOT (θ= 7 h) electrodes can be potentially used in various fields, as for example textiles (*e.g.* wearable electronics) and biomedic, where robustness and flexibility is required.

3.2.6. References

(1) Wang, X.; Lu, X.; Liu, B.; Chen, D.; Tong, Y.; Shen, G. Flexible Energy-Storage Devices: Design Consideration and Recent Progress. *Adv. Mater.* **2014**, *26* (28), 4763–4782.

(2) Kim, J.; Lee, J.; You, J.; Park, M. S.; Al Hossain, M. S.; Yamauchi, Y.; Kim, J. H. Conductive Polymers for Next-Generation Energy Storage Systems: Recent Progress and New Functions. *Mater. Horiz.* **2016**, *3* (6), 517–535.

(3) Rezzak, D.; Boudjerda, N. Management and Control Strategy of a Hybrid Energy Source Fuel Cell/Supercapacitor in Electric Vehicles. *Int. Trans. Electr. Energ. Syst.* **2017**, *27* (6), e2308.

(4) Kim, M.-J.; Peng, H. Power Management and Design Optimization of Fuel Cell/Battery Hybrid Vehicles. *J. Power Sources.* **2007**, *165* (2), 819–832.

(5) Bruce, P. G.; Freunberger, S. A.; Hardwick, L. J.; Tarascon, J.-M. Li–O_2 and Li–S Batteries with High Energy Storage. *Nature Mater.* **2012**, *11*, 19–29.

(6) Harfman-Todorovic, M.; Palma, L.; Enjeti, P. Power Electronics Specialists Conference, **2006**. PESC '06. 37th IEEE. 10.1109/pesc.2006.1712101.

(7) Gao, W.; Singh, N.; Song, L.; Liu, Z.; Mohana-Reddy, A. L.; Ci, L.; Vajtai, R.; Zhang, Q.; Wei, B.; Ajayan, P. M. Direct Laser Writing of Micro-Supercapacitors on Hydrated Graphite Oxide Films. *Nature Nanotech.* **2011**, *6*, 496–500.

(8) Guo, H.; Yeh, M.-H.; Zi, Y.; Wen, Z.; Chen, J.; Liu, G.; Hu, C.; Wang, Z. L. Ultralight Cut-Paper-Based Self-Charging Power Unit for Self-Powered Portable Electronic and Medical Systems. *ACS Nano.* **2017**, *11* (5), 4475–4482.

(9) Shao, Y.; El-Kady, M. F.; Lin, C.-W.; Zhu, G.; Marsh, K. L.; Hwang, J. Y.; Zhang, Q.; Li, Y.; Wang, H.; Kane, R. B. 3D Freeze-Casting of Cellular Graphene Films for Ultrahigh-Power-Density Supercapacitors. *Adv. Mater.* **2016**, *28* (31), 6719–6726.

(10) B. E. Conway, *Electrochemical Supercapacitors: Scientific Fundamentals and Technological Applications*, Kluwer academic/Plenum Publishing, New York, 1999.

(11) Pandolfo, A. G.; Hollenkamp, A. F. Carbon Properties and Their Role in Supercapacitors. *J. Power Sources.* **2006**, *157* (1), 11–27.

(12) González, A.; Goikolea, E.; Barrena, J. A.; Mysyk, R. Review on Supercapacitors: Technologies and Materials. *Renew. Sustainable Energy Rev.* **2016**, *58*, 1189–1206.

(13) Wu, X.-L.; Xu, A.-W. Carbonaceous Hydrogels and Aerogels for Supercapacitors. *J. Mater. Chem. A.* **2014**, *2* (14), 4852–4864.

(14) Bajaj, I.; Singhal, R. Poly (glutamic acid)--an Emerging Biopolymer of Commercial Interest. *Bioresour. Technol.* **2011**, *102* (10), 5551–5561.

(15) Shih, I.; Wu, P.; Shieh, C. Microbial Production of a Poly(γ-glutamic acid) Derivative by *Bacillus Subtilis*. *Process Biochem.* **2005**, *40* (8), 2827–2832.

(16) Thome, C. B.; Gómez, C. G.; Noyes, H. E.; Housewright, R. D. Production of Glutamyl Polypeptide by *Bacillus Subtilis*. *J. Bacteriol.* **1954**, *68* (3), 307–315.

(17) Bhat, A. R.; Irorere, V. U.; Bartlett, T.; Hill, D.; Kedia, G.; Morris, M. R. ; Charalampopoulos, D.; Radecka, I. Bacillus Subtilis Natto: A Non-Toxic Source of Poly-γ-Glutamic Acid that Could be Used as a Cryoprotectant for Probiotic Bacteria. *AMB Express.* **2013**, *3*, 36.

(18) Bhat, A. R.; Irorere, V. U.; Bartlett, T.; Hill, D.; Kedia, G.; Charalampopoulos, D.; Nualkaekul, S.; Radecka, I. Improving Survival of Probiotic Bacteria Using Bacterial Poly-γ-glutamic Acid. *Int. J. Food Microbiol.* **2015**, *196*, 24–31.

(19) Akao, T.; Kimura, T.; Hirofuji, Y.; Matsunaga, K.; Imayoshi, R.; Nagao, J.; Cho, T.; Matsumoto, H.; Ohtono, S.; Ohno, J.; et al. Poly(gamma-glutamic acid)-Amphiphile Complex as a Novel Nanovehicle for Drug Delivery System. *J. Drug Targeting.* **2010**, *18* (7), 550–556.

(20) Mi, F. L.; Wu, Y. Y.; Lin, Y. H.; Sonaje, K.; Ho, Y. C.; Chen, C. T.; Juang, J. H.; Sung, H. W. Oral Delivery of Peptide Drugs Using Nanoparticles Self-Assembled by Poly(γ-glutamic acid) and a Chitosan Derivative Functionalized by Trimethylation. *Bioconjugate Chem.* **2008**, *19* (6), 1248–1255.

(21) Zhang, R.; Lin, L.; Xu, S.; Zhang, C.; Liu, X.; Luo, J. Liquid–Liquid Interfacial Behaviour of Dopamine Modified Poly(γ-glutamic acid) Polymer. *Colloids Surf. A.* **2015**, *470*, 218–223.

(22) Poo, H.; Park, C.; Kwak, M.; Choi, D.; Hong, S.; Lee, I.; Lim, Y. T.; Choi, Y. K.; Bae, S.; Uyama, H.; et al. New Biological Functions and Applications of High-Molecular-Mass Poly-γ-glutamic Acid. *Chem. Biodiversity.* **2010**, *7* (6), 1555–1562.

(23) Yu, X.; Wang, M.; Wang, Q.; Wang, X. Biosynthesis of Polyglutamic Acid and Its Application on Agriculture. *Adv. Mat. Res.* **2011**, *183–185*, 1219–1223.

(24) Tsao, C. T.; Chang, C. H.; Lin, Y. Y.; Wu, M. F.; Wang, J. L.; Han, J. L.; Hsieh, K. H. Antibacterial Activity and Biocompatibility of a Chitosan-Gamma-Poly(glutamic acid) Polyelectrolyte Complex Hydrogel. *Carbohydr. Res.* **2010**, *345* (12), 1774–1780.

(25) Pérez-Madrigal, M. M.; Edo, M. G.; Díaz, A.; Puiggalí, J.; Alemán, C. Poly-γ-glutamic Acid Hydrogels as Electrolyte for Poly(3,4-ethylenedioxythiophene)-Based Supercapacitors. *J. Phys. Chem. C.* **2017**, *121*(6), 3182–3193.

(26) Armelin, E.; Perez-Madrigal, M. M.; Alemán, C.; Díaz-Díaz, D. Current Status and Challenges of Biohydrogels for Applications as Supercapacitors and Secondary Batteries. *J. Mater. Chem. A*. **2016**, *4*, 8952–8968.

(27) Kirchmeyer, S.; Reuter, R. Scientific Importance, Properties and Growing Applications of Poly(3,4-ethylenedioxythiophene). *J. Mater. Chem.* **2005**, *15* (21), 2077–2088.

(28) Grenier, C. R. G.; Pisula, W.; Joncheray, T. J.; Müllen, K.; Reynolds, J. R. Regiosymmetric Poly(dialkylphenylenedioxythiophene)s: Electron-Rich, Stackable π-Conjugated Nanoribbons. *Angew. Chem. Int. Ed.* **2007**, *46* (5), 714–717.

(29) Mantione, D.; del Agua, I.; Sanchez-Sanchez, A.; Mecerreyes, D. Poly(3,4-ethylenedioxythiophene) (PEDOT) Derivatives: Innovative Conductive Polymers for Bioelectronics. *Polymers.* **2017**, *9* (8), 354.

(30) Elschner, A.; Kirchmeyer, S.; Lovenich, W.; Merker, U.; Reuter, K. PEDOT: Principles and Applications of an Intrinsically Conductive Polymer, CRC Press, **2010**.

(31) Poater, J.; Casanovas, J.; Solà, M.; Alemán, C. Examining the Planarity of Poly(3,4-ethylenedioxythiophene): Consideration of Self-Rigidification, Electronic, and Geometric Effects. *J. Phys. Chem. A* **2010**, *114* (2), 1023–1028.

(32) Lee, D.-Y.; Na, S.-I.; Kim, S.-S. Graphene Oxide/PEDOT:PSS Composite Hole Transport Layer for Efficient and Stable Planar Heterojunction Perovskite Solar Cells. *Nanoscale.* **2016**, *8* (3), 1513–1523.

(33) Wu, X.-L.; Xu, A.-W. Carbonaceous Hydrogels and Aerogels for Supercapacitors. *J. Mater. Chem. A.* **2014**, *2* (14), 4852–4864.

(34) Nabilah Azman, N. H.; Lim, H. N.; Sulaiman, Y. Effect of Electropolymerization Potential on the Preparation of PEDOT/ Graphene Oxide Hybrid Material for Supercapacitor Application. *Electrochim. Acta*. **2016**, *188*, 785–792.

(35) Dettlaff, A.; Wilamowska, M. Electrochemical Synthesis and Characterization of Nanocomposites Based on Poly(3,4-ethylenedioxythiophene) and Functionalized Carbon Nanotubes. *Synth. Met.* **2016**, *212*, 31–43.

(36) Yan, L.; Rui, X.; Chen, G.; Xu, W.; Zou, G.; Luo, H. Recent Advances in Nanostructured Nb Based Oxides for Electrochemical Energy Storage *Nanoscale.* **2016**, *8* (16), 8443–8465.

(37) Saborío, M. C. G.; Estrany, F.; Alemán, C. Properties of In Situ Polymerized Poly(3,4-ethylenedioxythiophene)/Alumina Composites for Energy Storage Applications. *J. Polym. Sci., Part B: Polym. Phys.* **2017**, *55* (15), 1131–1141.

(38) Pan, L.; Yu, G.; Zhai, D.; Lee, H. R.; Zhao, W.; Liu, N.; Wang, H.; Tee, B. C.-K.; Shi, Y.; Cui, Y.; et al. Hierarchical Nanostructured Conducting Polymer Hydrogel with High Electrochemical Activity. *Proc. Natl. Acad. Sci. U. S. A.* **2012**, *109* (24), 9287–9292.

(39) Ajjan, F. N.; Casado, N.; Rębis, T.; Elfwing, A.; Solin, N.; Mecerreyes, D.; Inganäs, O. Performance PEDOT/Lignin Biopolymer Composites for Electrochemical Supercapacitors. *J. Mater. Chem. A.* **2016**, *4*, 1838–1847.

(40) Fabregat, G.; Teixeira-Dias, B.; del Valle, L. J.; Armelin, E.; Estrany, F.; Alemán, C. Incorporation of a Clot-Binding Peptide into Polythiophene: Properties of Composites for Biomedical Applications. *ACS Appl. Mater. Interfaces.* **2014**, *6* (15), 11940–11954.

(41) López-Pérez, D.; Aradilla, D.; del Valle, L. J.; Alemán, C. Capacitive Composites Made of Conducting Polymer and Lysozyme: Toward the Biocondenser. *J. Phys. Chem. C.* **2013**, *117* (13), 6607–6619.

(42) Matsusaki, M.; Yoshida, H.; Akashi, M. The Construction of 3D-Engineered Tissues Composed of Cells and Extracellular Matrices by Hydrogel Template Approach. *Biomaterials*. **2007**, *28* (17), 2729–2737.

(43) Brillas, E.; Carrasco, J.; Oliver, R.; Estrany, F.; Vilar, J.; Morlans, J. M. Electropolymerization of 2,5-Di-(-2-thienyl)-pyrrole in Ethanolic Medium. Effect of Solution Stirring on Doping with Perchlorate and Chloride Ions. *Electrochim. Acta.* **2000**, *45* (24), 4049–4057.

(44) Müller, F.; Ferreira, C. A.; Azambuja, D.; Alemán, C.; Armelin, E. New Sulfonated Polystyrene and Styrene–Ethylene/Butylene–Styrene Block Copolymers for Applications in Electrodialysis. *J. Phys. Chem. B* **2014**, *118* (38), 1102–1112.

(45) Fabregat, G.; Casanovas, J.; Redondo, E.; Armelin, E.; Alemán, C. A Rational Design for the Selective Detection of Dopamine Using Conducting Polymers. *Phys. Chem. Chem. Phys.* **2014**, *16* (17), 7850–7861.

(46) Hocevar, M. A.; Fabregat, G.; Armelin, E.; Ferreira, C. A.; Alemán, C. Nanometric Polythiophene Films with Electrocatalytic Activity for Non-Enzymatic Detection of Glucose. *Eur. Polym. J.* **2016**, *79*, 132–139.

(47) Patra, S.; Barai, K.; Munichandraiah, N. Scanning Electron Microscopy Studies of PEDOT Prepared by Various Electrochemical Routes. *Synth. Metals.* **2008**, *158 (10)*, 430–435.

(48) Li, Z.; He, G.; Hua, J.; Wu, M.; Guo, W.; Gong, J.; Zhang, J.; Qiao, C. Preparation of γ-PGA Hydrogels and Swelling Behaviours in Salt Solutions with Different Ionic Valence Numbers. *RSC Adv.* **2017**, *7*, 11085–11093.

(49) Otero, T. F.; Caballero Romero, M. Conformational Energy from the Oxidation Kinetics of Poly(3,4-ethylenedioxythiophene) Films. *Polym. Int.* **2010**, *59* (3), 329–336.

(50) Lattach, Y.; Coletta, C.; Ghosh, S.; Remita, S. Radiation-Induced Synthesis of Nanostructured Conjugated Polymers in Aqueous Solution: Fundamental Effect of Oxidizing Species. *Chem.Phys.Chem.* **2014**, *15* (1), 208–218.

(51) Hu, D.; Lu, B.; Duan, X.; Xu, J.; Zhang, L.; Zhang, K.; Zhang, S.; Zhen, S. Synthesis of Novel Chiral L-Leucine Grafted PEDOT Derivatives with Excellent Electrochromic Performances. *RSC Adv.* **2014**, *4* (67), 35597–35608.

(52) Sivula, K.; Luscombe, C. K.; Thompson, B. C.; Frechet, J. M. J. Enhancing the Thermal Stability of Polythiophene: Fullerene Solar Cells by Decreasing Effective Polymer Regioregularity. *J. Am. Chem. Soc.* **2006**, *128* (43), 13988–13989.

(53) Aradilla, D.; Azambuja, D.; Estrany, F.; Casas, M. T.; Ferreira, C. A.; Alemán, C. Hybrid Polythiophene–Clay Exfoliated Nanocomposites for Ultracapacitor Devices. *J. Mater. Chem.* **2012**, *22* (26), 13110–13122.

(54) Pérez Madrigal, M. M.; Armelin, E.; del Valle, L. J.; Estrany, F.; Alemán, C. Bioactive and Electroactive Response of Flexible Polythiophene:Polyester Nanomembranes for Tissue Engineering. *Polym. Chem.* **2012**, *3* (4), 979–991.

(55) Pérez-Madrigal, M. M.; Giannotti, M. I.; del Valle, L. J.; Franco, L.; Armelin, E.; Puiggalí, J.; Sanz, F.; Alemán, C. Thermoplastic Polyurethane:Polythiophene Nanomembranes for Biomedical and Biotechnological Applications. *ACS Appl. Mater. Interfaces.* **2014**, *6* (12), 9719–9732.

(56) Grimshaw, J. In Electrochemical Reactions and Mechanisms in Organic Chemistry, Elsevier, 2000, pp 330–370.

(57) Sánchez-Jiménez, M.; Estrany, F.; Alemán, C. Improving the Fabrication of All-Polythiophene Supercapacitors. *Polym. Sci. Series B.* **2017**, *59* (2), 194–201.

(58) Cheng, T.; Zhang, Y.-Z.; Zhang, J.-D.; Lai, W.-Y.; Huang, W. High-Performance Free-Standing PEDOT:PSS Electrodes for Flexible and Transparent All-Solid-State Supercapacitors. *J. Mater. Chem. A.* **2016**, *4* (27), 10493–10499.

(59) Lehtimäki, S.; Suominen, M.; Damlin, P.; Tuukkanen, S.; Kvarnström, C.; Lupo, D. Preparation of Supercapacitors on Flexible Substrates with Electrodeposited PEDOT/Graphene Composites. *ACS Appl. Mater. Interfaces.* **2015**, *7* (40), 22137–22147.

(60) Kurra, N.; Park, J.; Alshareef, H. N. A Conducting Polymer Nucleation Scheme for Efficient Solid-State Supercapacitors on Paper. *J. Mater. Chem. A.* **2014**, *2* (40), 17058–17065.

(61) Cheng, T.; Zhang, Y.; Lai, W.-Y.; Huang, W. Stretchable Thin-Film Electrodes for Flexible Electronics with High Deformability and Stretchability. *Adv. Mater.* **2015**, *27* (22), 3349–3376.

(62) Zhang, Y.-Z.; Wang, Y.; Cheng, T.; Lai, W.-Y.; Pang, H.; Huang, W. Flexible Supercapacitors Based on Paper Substrates: A New Paradigm for Low-Cost Energy Storage. *Chem. Soc. Rev.* **2015**, *44* (15)**,** 5181–5199.

(63) Pérez-Madrigal, M. M.; Edo, M. G.; Alemán, C. Powering the Future: Application of Cellulose-Based Materials for Supercapacitors. *Green Chem.* **2016**, *18* (22)**,** 5930–5956.

(64) Xiao, Y.; Hwang, J.-Y.; Sun, Y.-K. Transition Metal Carbide-Based Materials: Synthesis and Applications in Electrochemical Energy Storage. *J. Mater. Chem. A.* **2016**, *4* (27), 10379–10393.

(65) Cheng, T.; Zhang, Y.-Z.; Yi, J.-P.; Yang, L.; Zhang, J.-D.; Lai, W.-Y.; Huang, W. Inkjet-Printed Flexible, Transparent and Aesthetic. *J. Mater. Chem. A.* **2016**, *4* (36), 13754–13763.

(66) Anothumakkool, B.; Soni, R.; Bhange, S. N.; Kurungot, S. Novel scalable synthesis of highly conducting and robust PEDOT paper for a high performance flexible solid supercapacitor. *Energy Environ. Sci.* **2015**, *8* (4), 1339–1347.

(67) Liu, Y.; Weng, B.; Razal, J. M.; Xu, Q.; Zhao, C.; Hou, Y.; Seyedin, S.; Jalili, R.; Wallace, G. G.; Chen, J. High-Performance Flexible All-Solid-State Supercapacitor from Large Free-Standing Graphene-PEDOT/PSS Films. *Sci. Rep.* **2015**, *5*, 17045.

(68) Cheng, T.; Zhang, Y.-Z.; Lai, W.-Y.; Chen, Y.; Zeng, W.-J.; Huang, W. High-Performance Stretchable Transparent Electrodes Based on Silver Nanowires Synthesized *via* an Eco-Friendly Halogen-Free Method. *J. Mater. Chem. C.* **2014**, *2* (48)**,** 10369–10376.

3.3. Prototype Flexible Supercapacitor based on Biohydrogel

3.3.1. Abstract

A flexible symmetric supercapacitor prototype composed of electrodes that were prepared by polymerizing poly(hydroxymethyl-3,4-ethylenedioxythiophene) inside a γPGA biohydrogel matrix, already loaded with microparticles of PEDOT and alumina (Al_2O_3), has been fabricated and characterized. The prototype has been assembled in a totally solid, compact and lightweight configuration, where the supporting electrolytic medium is a γPGA prepared in presence of $NaHCO_3$. After characterization of the elements involved in the prototype, their dimensions (*i.e.* width of the electrode and the solid electrolyte) have been optimized to obtain the highest specific capacitance. The electrochemical performances of the prototype have been investigated by cyclic voltammetry, galvanostatic charge-discharge cycles and electrochemical impedance spectroscopy. After 2000 charge-discharge cycles (*i.e.* 60.000 s of continuous operation), the loss of specific capacitance is of only 8%, evidencing an excellent stability. The results are very promising for the development of a compact, flexible, lightweight and biocompatible supercapacitors to be employed like energy-autonomous electronic device.

3.3.2. Introduction

New energy storage devices based on electroactive polymers (EAPs) and produced using novel accessible techniques are currently emerging as a response to recent requirements of sustainable, non-hazardous, light-weight, flexible, and compact (nano and microscale) electronic apparatus. These materials can be used in different fields, which include wearable technologies,[1] flexible mobile phone,[2] conductive adhesives,[3] active electrodes for capacitors or supercapacitors[3-6] and hybrid lithium-ion batteries.[7] Due to their excellent biocompatibility, some of these electroactive materials[8] find applications in biomedicine, such as biosensors,[9-11] transducers,[12] regenerative tissues,[13-15] drug release devices,[10,11,16,17] neural and recording devices.[18-20]

Nowadays, new supercapacitors based on flexible materials like electroactive hydrogels, which fundamentally involve co-networks of EAPs and hydrated hydrogels, constitute an appealing research subject of many investigations.[19-21] EAPs-hydrogels composites have lots of benefits, as for

example, unique energy storage capacity, which is reached through their large surface area (40-100 $m^2 \cdot g^{-1}$), structural adaptability, and 3D hierarchical porosity.[4] These materials are characterized by rapid and short charge transport pathways, obtained as a combination of hydrogel matrix with different porosity, low characteristic interfacial impedance and the intrinsic properties of the EAPs.[5,22]

Some EAPs used in electroactive hydrogels are polyacetylene, poly(*p*-phenylene), polyaniline, polypyrrole, poly(phenylenevinylene), poly(ethyleneimine), and polythiophene.[11,13,22] These materials exhibit high electrical conductivity (from a few to 1000 S cm^{-1} in the doped state) and low band-gap (1–3 eV) as fundamental properties.[7] These inherent and distinctive peculiarities are attributed to the combination of a characteristic electronic structure (*i.e.* EAPs show a conjugated structure with alternating single and double bonds) and the doping process (*i.e.* chemical and electrochemical reactions to form polarons and bipolarons that act as charge carriers).[4,13] Thus, EAPs can be p-doped or n-doped EAPs through oxidation (anions as counter-ions) or reduction (cations as counter-ions), respectively. In the case of EAP-hydrogel composites, the general equations for these two charging processes are:[7]

$$\text{EAP-Hydrogel} \rightarrow \text{EAP}^{n+}(X^-)_n\text{-hydrogel} + n \cdot e^- \ (\textit{p-doping}) \qquad (1)$$

$$\text{EAP-Hydrogel} + ne^- \rightarrow (X^+)_n\,\text{EAP}^{n-}\text{-hydrogel} \ (\textit{n-doping}) \qquad (2)$$

where X^- and X^+ refer to the counter-anion and counter-cation, respectively.

The preparation of electroactive hydrogels has been achieved using different procedures, as for example, by crosslinking the own EAP chains, by chemical coupling of EAP chains to a dielectric hydrogel matrix, by printing the EAP on the hydrogel substrate, and by polymerizing the whole composite using the same compound as gelator and dopant in a one-step process.[22-27]

Currently, one of the most employed EAPs is the PEDOT, which can be easily obtained by anodic polymerization in different conditions. In a pioneering work, Sasaki *et al.*[14] reported the first hydrogel-based device that maintains highly electrically conductive under substantial stretch and bending conditions. Specifically, chemical and anodic polymerizations were combined to obtain a

tight bonding of a composite of PEDOT and polyurethane to an elastic double-network acrylamide hydrogel. The resulting hybrid disclosed excellent electrical conductivity (~120 S cm^{-1}), which was maintained after six months.[14]

In recent studies we developed γPGA biohydrogels for energy storage applications.[28,29] γPGA is anionic homopolypeptide linked by the peptide bond between the α-amino and the γ-carboxyl groups of glutamic acid,[30] that exhibits good biocompatibility due to its biodegradability, water-solubility and non-toxicity towards humans.[31] This compound is produced from biosynthesis as a slime layer by a variety of members of the genus *Bacillus*.[32] Due to their robustness, γPGA biohydogels were used as solid electrolyte media for organic supercapacitors,[28] fulfilling the sustainability requirements of devices composed by naturally produced devices.[33] More recently, we combined γPGA biohydogels with PEDOT microparticles using a new polymerization approach to fabricate flexible electrodes.[29] Besides, we proved that incorporation of Al_2O_3 to PEDOT through in situ polymerization at pH 8.8 significantly enhances the electrochemical activity of such EAP.[34]

In this work we combine our previous experience on γPGA biohydogels and Al_2O_3 composites to develop a solid organic symmetric supercapacitor prototype containing the following elements: 1) two self-supported p-doped electrodes made of γPGA, PEDOT microparticles, PHMeDOT, which is a PEDOT derivative with an exocyclic hydroxyl group that facilitates its preparation in aqueous environments, and Al_2O_3; and 2) a solid supporting electrolyte composed by γPGA biohydrogel doped with $NaHCO_3$. The elements of the prototype, which is flexible, lightweight and compact, have been synthesized and subsequently assembled using simple and low-cost techniques.

3.3.3. Experimental Section

Materials.

Free γPGA from *Bacillus subtilis* (M_w= 350000) was purchased from Wako Chemicals GmbH (Neuss, Germany). EDC, cystamine dihydrochloride (Cys; ≥98%), HMeDOT, 95% were purchased from Sigma-Aldrich. EDOT and HMeDOT monomers were used as received. $NaHCO_3$ and alumina were obtained from Panreac. Anhydrous $LiClO_4$, analytical reagent grade from Aldrich, was stored in an oven at 70 ºC before use in electrochemical experiments. Acetonitrile solvent was purchased from Sigma Aldrich. Milli-Q water grade (0.055 S cm^{-1}) was used in all synthetic processes.

Alumina microparticles.

Al_2O_3 particles were prepared introducing the properly mass quantity into a vial containing magnetic stirrers, which was placed in a vortex at maximum power during 2h. After that, particles were homogenized using a mortar was applied to end the homogenization of the particles.

PEDOT microparticles.

PEDOT films were prepared by chronoamperometry at 1.40 V in an acetonitrile solution with 10 mM EDOT and 0.1 M $LiClO_4$ as supporting electrolyte. The experimental set-up for this anodic polymerization was described in previous work.[35] PEDOT films were processed into particles by ball milling during 2 h. Basic aqueous (0.5 M $NaHCO_3$) dispersions with 20% w/w of the resulting PEDOT particles were employed for the synthesis of loaded γPGA hydrogels.

Preparation of PEDOT/Al2O3/γPGA solid electrode.

Flexible electrodes were prepared by *in situ* loading of PEDOT and Al_2O_3 particles into γPGA biohydrogel (hereafter denoted PEDOT/Al_2O_3/γPGA).[29] In brief, γPGA and EDC were dissolved at 4 ºC under magnetic stirring in 0.75 mL of 0.5 M $NaHCO_3$ containing 20% w/w and 2% w/w of PEDOT and Al_2O_3 particles, respectively, relative to the weight of γPGA. After this, Cys was dissolved in 0.25 mL sodium hydrogen carbonate solution (0.5 M) and, subsequently, added to the solution and mixed during 2-3 minutes. The γPGA / EDC / cystamine molar ratio was 5 / 4 / 2. The final solution was removed with a magnetic stirrer, and the reaction solution was poured into glass molds. The solution was let to gel at room temperature for one hour. To remove any compound in excess, the resulting loaded hydrogel was softly washed during 20 min with distillate water.

Improvement of the PEDOT/Al_2O_3/γPGA electrodes by in situ polymerization of PHMeDOT.

Steel AISI 316 sheets of were coated with PEDOT/Al_2O_3/γPGA electrodes and subsequently kept for 24 h into a 10 mM HMeDOT aqueous solution with 0.1 M $LiClO_4$ at pH 8 under stirring. After

this, PEDOT/Al_2O_3/γPGA coated sheets were used as working electrodes for the anodic polymerization of PHMeDOT by chronoamperometry using the same aqueous solution as reaction medium. Thus, in a previous study we demonstrated that PEDOT particles loaded into γPGA biohydrogel act as reaction nuclei for the electropolymerization of PHMeDOT.[29] The anodic polymerization of HMeDOT monomers was conducted under a constant potential of 1.10 V using a polymerization time, θ, of 2 h, the resulting electrodes being denoted [PEDOT/Al_2O_3/γPGA]PHMeDOT.

The drastic reduction of θ with respect to our previous work,[29] from 7 to 2 h, is because the flexibility of the electrodes, which decreases with the content of PHMeDOT, has been prioritized with respect to the maximization of the electrochemical properties. Accordingly, the equilibrium between the loss in electrochemical properties and the gain in elastic behavior has been modulated with the electropolymeriztion time. In the specific case of [PEDOT/Al_2O_3/γPGA]PHMeDOT electrodes, we observed PEDOT microparticles join through grown PHMeDOT when θ= 2 h and, therefore, the supercapacitor reaches a high performance without detriment in the flexibility. [PEDOT/Al_2O_3/γPGA]PHMeDOT electrodes were used to construct symmetric solid supercapacitors, as described below, using unloaded γPGA biohydrogel as electrolytic medium.

Preparation of γPGA hydrogel as solid electrolyte and assembly of the symmetric cell.

Pure γPGA hydrogel for utilization as solid electrolyte was obtained using the procedure described for [PEDOT/Al_2O_3/γPGA]PHMeDOT electrodes. The only difference with respect to the preparation of the electrodes is that the 0.5 M $NaHCO_3$ solution used to dissolve the biopolymer was free of PEDOT and Al_2O_3 particles. Furthermore, in this case the reaction solution was poured in a cylindrical container (1.2 cm length) that already contained a previously prepared [PEDOT/Al_2O_3/γPGA]PHMeDOT electrode (cathode) of radius 0.45 cm. to glass molds. After five minutes, during the gelling process of the γPGA electrolyte, the second [PEDOT/Al_2O_3/γPGA]PHMeDOT electrode (anode) was added. This approach ensured the complete integration of the three elements of the cell through the electrolyte gelling reaction. Once the symmetric capacitor was assembled, it was soaked in milli-Q water during 2 h to remove any compound in excess coming from the electrolyte gelation.

Chemical and physical characterization.

Spectroscopic characterization of lyophilized hydrogels was conducted using FTIR spectroscopy. Morphological characterization of the electrodes was performed using SEM. The diameter of the particles was determined from the SEM images. The thermal stability was studied by TGA.

The swelling ratio (SR, %) of unloaded and loaded γPGA hydrogels was determined according to:

$$SR = \frac{w_W \quad w_D}{w_D} \tag{1}$$

where w_W is the weight of the as prepared hydrogels after 30 min in milli-Q water and w_D is the weight of the hydrogels dried at room temperature during 30 min after preparation.

Electrochemical characterization.

All electrochemical experiments were run in triplicate using γPGA as solid supporting electrolyte. CV was carried out to evaluate the electroactivity, volumetric capacitance (*VC*) and specific capacitance (*SC*) of the capacitor and the electrochemical stability. Voltammograms were recorded considering different operational conditions: (a) Initial and final potential: 0.00 V; reversal potential: 0.80 V; scan rate: 50 mVs^{-1}; and (b) Initial and final potential: -0.50 V; reversal potential: 0.50 V; scan rate: 50, 100, 200 or 500 mVs^{-1}.

The *SC* (in mF cm^{-2}) and the *VC* (in mF cm^{-3}) were determined using the following expression:

$$SC = \frac{Q}{\Delta V \cdot m} \tag{2}$$

$$VC = \frac{Q}{\Delta V \cdot v} \tag{3}$$

where Q is voltammetric charge determined by integrating the oxidative (anodic charge) or the reductive parts (cathodic charge) of the cyclic voltammogram curve, ΔV is the potential window (in V), and is the area of the electrode (in cm^2), and *v is* the total volume of the prototype.

The electrochemical stability was examined by evaluating the loss of electroactivity (LEA, in %) against the number of oxidation-reduction cycles:

$$LEA = \frac{\Delta Q}{Q_2} = \frac{Q_i \quad Q_2}{Q_2} \tag{4}$$

where ΔQ is the difference between the oxidation charge (in C) of the second (Q_2) and the evaluated oxidation-reduction cycle (Q_i).

GCD cycles were run using a current of 0.0035 mA. GCD curves were also employed to evaluate the *SC* and *VC* according to:

$$SC = \frac{\int I \cdot \Delta t}{\Delta V \cdot m} \tag{5}$$

$$SC = \frac{\int I \cdot \Delta t}{\Delta V \cdot v} \tag{6}$$

where I is the applied current, Δt is the time of discharge (in s), ΔV is the difference between the potential at the beginning and at the end of the discharge (in V), m is the mass of the EAP (in g) and v is the volume of the symmetric capacitor (in cm^3).

The energy and power density were calculated applying the following equations:

$$E = \frac{SCV^2}{2m} \tag{7}$$

$$P = \Delta V \frac{I}{m} \tag{8}$$

where *SC* is the specific capacitance (in mFg^{-1}), V is the voltage at the beginning of the discharge (1 V), m is the mass of EAP (*i.e.* PEDOT and PHMeOH), ΔV is the difference between the potential at the beginning and at the end of the discharge, I is the applied current (0.0035 mA).

Electrochemical impedance spectroscopy (EIS) diagrams were taken at open circuit (OCP) over the frequency range of 100 kHz to 10 Hz with a potential amplitude of 0.05 V using an AUTOLAB-302N potentiostat/galvanostat. All experiments were performed at room temperature using γPGA as solid electrolyte. After data collection, EIS results were then processed and fitted to an electrical

equivalent circuit (EEC). The percentage error associated with each circuit element was lower than 5%.

FTIR spectroscopy

Absorption spectra of lyophilized hydrogels were recorded on a FTIR Jasco 4100 spectrophotometer. Samples were placed in an attenuated total reflection accessory (Top-plate) with a diamond crystal (Specac model MKII Golden Gate Heated Single Reflection Diamond ATR). For each sample 64 scans were performed between 4000 and 600 cm^{-1} with a resolution of 4 cm^{-1}.

Morphological characterization

Scanning electron microscopy (SEM) studies were performed by placing dried samples in a Focussed Ion Beam Zeis Neon 40 scanning electron microscope operating at 3 kV, equipped with an energy dispersive X-ray (EDX) spectroscopy system. EDX analyses were conducted to identify the presence of PEDOT and Al_2O_3 particles in PEDOT/Al_2O_3/γPGA and the success of the *in situ* PHMeDOT polymerization in [PEDOT/Al_2O_3/γPGA]PHMeDOT.

The diameter of the particles was determined from the SEM images using the software SmartTIFF (*v*1.0.1.2.), and data was fitted to a normal curve (OrginPro 8 SR0, v8.0724).

Thermal stability

The thermal stability of the prepared electrodes was studied by TGA at a heating rate of 20 ºC/ min (sample weight *ca.* 5 mg) using a Q 50 thermogravimetric analyzer of TA Instruments and under a flow of dry nitrogen. Test temperatures ranged from 30 to 600 ºC.

3.3.4. Results and Discussion

Preparation and characterization of flexible electrodes and solid electrolyte

In order to improve the electrochemical performance of flexible PEDOT/γPGA electrodes reported in previous work,[29] Al_2O_3 microparticles were loaded into the biohydrogel using the procedure described in the Methods section. Homogenization and size reduction of Al_2O_3 microparticles as obtained from synthesis [Figure 3.3-1(a)], which exhibited an averaged diameter of ~50 μm, was essential to ensure a good dispersion within the γPGA matrix. After physical treatment, Al_2O_3 particles with diameters ranging from ~1 to ~10 μm were obtained [Figure 3.3-1(b)]. PEDOT films [Figure 3.3-1(c)] were processed into particles of 3.0±1.2 μm in diameter [Figure 3.3-1(d-e)]. The successful incorporation of PEDOT and Al_2O_3 particles inside the γPGA hydrogel was corroborated by EDX, which enabled the detection of Al and S elements [Figure 3.3-1(f)].

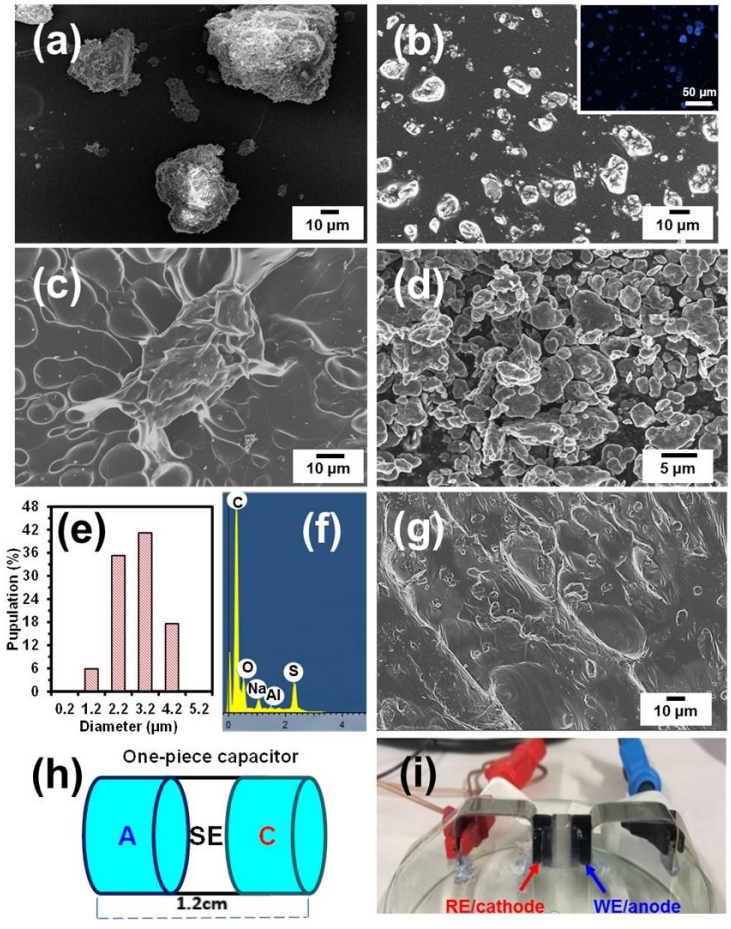

Figure 3.3-1. SEM micrographs of: alumina particles (a) before and (b) after the physical treatment; (c) PEDOT film and (d) microparticles; (e) particle size distribution with the diameter in µm (f) EDX spectrum and (g) of the [PEDOT/Al_2O_3/γ PGA]PHMeDOT electrode. (h) Scheme of assembled supercapacitor prototype and (i) photograph of the device.

The electrochemical behavior of PEDOT/Al_2O_3/γPGA was enhanced by incorporating PHMeDOT inside the hydrogel through the anodic polymerization of HMeDOT monomers in aqueous solution. In order to ensure the penetration of the monomers into the hydrogel matrix and, therefore, their access to the PEDOT particles, which act as polymerization nuclei, PEDOT/ Al_2O_3/γ-PGA was kept under stirring in the reaction medium during 24 h. It is worth noting that, although the electroactivity and *SC* of PHMeDOT and PEDOT are very similar, the solubility of HMeDOT in water is higher than that of EDOT. Accordingly, the incorporation of PHMeDOT inside the hydrogel, growing from loaded EAP microparticles, is expected to improve the electrochemical characteristics of

PEDOT/Al_2O_3/γPGA without cause detriment in the properties already induced by PEDOT.[29] The morphology of PHMeDOT in [PEDOT/Al_2O_3/γPGA]PHMeDOT resembles that of PEDOT [Figure 3.3-1(g)], as it was awaited from previous studies on such EAP.[36,37]

Figure 3.3-2(a) compares the FTIR spectra of the [PEDOT/Al_2O_3/γPGA]PHMeDOT electrode and the γPGA electrolyte. Both spectra show the typical bands of the γPGA biohydrogel, which were already compared with those of the biopolymer before the cross-linking reaction.[28] In brief, the most characteristic trend corresponds to the formation of –CONH– bonds due to the reaction between the γPGA chains and the cross-linker, which was identified by the enhancement of both the amide I (1621 cm^{-1}) and amide II (1530 cm^{-1}) bands and the disappearance of the free carboxylic acid (1718 cm^{-1}) and asymmetric COO^- bands (1595 cm^{-1}). On the other hand, the presence of PEDOT and PHMeDOT in the electrode is evidenced by the C–O–C (1090 cm^{-1}) and ethylendioxy (1180 cm^{-1}) stretching vibrations as well the shift of the broad band identified at 3298 cm^{-1} for the γPGA electrolyte (overlapping of N–H and O–H stretching bands) towards 3258 cm^{-1} in the electrode due to the increment in the amount of hydroxyl groups arising from PHMeDOT. In addition, the bands at 1092 cm^{-2} (Al–O–H bending) and at 900 and 1100cm^{-1} (Al–O–H deformations) reflect the incorporation of alumina, which converts into $Al(OH)_3$ because due to basic pH. The latter is corroborated by the band at 3092 cm^{-1}, which is used as a fingerprint of the –OH groups in boehmite structure (g-AlOOH, aluminum oxide hydroxyde).[38]

The thermal stability of γPGA, PEDOT/Al_2O_3/γPGA and [PEDOT/Al_2O_3/γPGA]PHMeDOT Figure 3.3-2(b), which displays the TGA and DGTA curves. The different shape of the TGA curves indicates that the degradation mechanism of the biohydrogel is affected by the loading. The initial loss of weight at ~100 °C, which is ascribed to the evaporation of water absorbed in the γPGA network, occurs in a different way for the electrodes than for the supporting electrolyte. Comparison of the PEDOT/Al_2O_3/γPGA and [PEDOT/Al_2O_3/γPGA]PHMeDOT curves with those previously reported for PEDOT/ γPGA and [PEDOT/γPGA]PHMeDOT indicates that alumina acts as a thermos-resistant glue, making difficult the evaporation of water. The decomposition process starts at temperatures higher than 200 °C for all samples, even though differences in the weight loss reveals that alumina has a delaying effect in the decomposition of the electrodes. However, the degradation process becomes more complex upon the incorporation of PEDOT, alumina and PHMeDOT, as is evidenced by the multiple peaks surrounding the one associated to the maximal decomposition in the DTG curves. Overall, these results prove that alumina particles enhance the thermal resistance of the proposed electrodes.

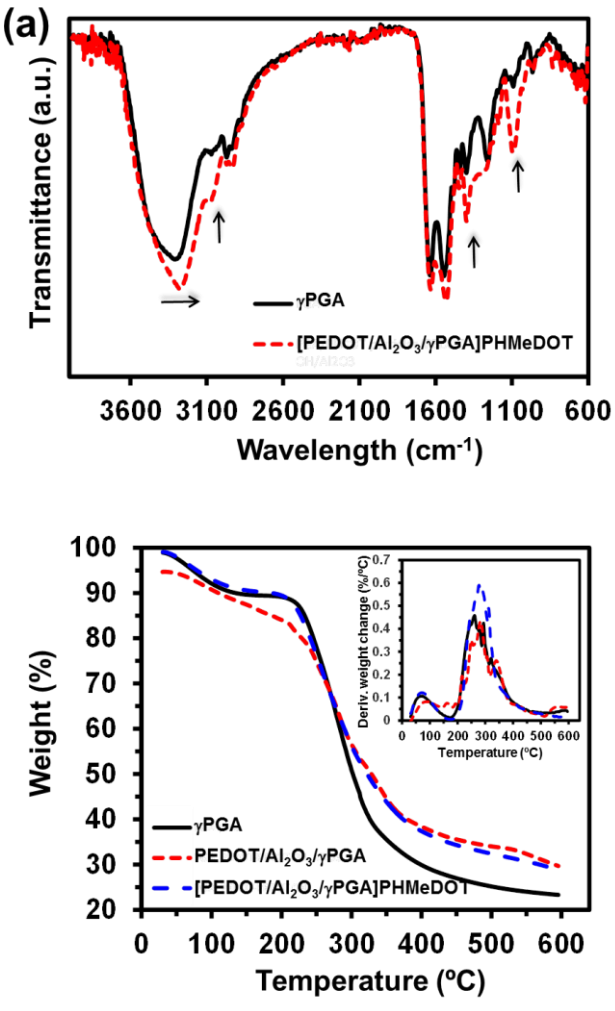

Figure 3.3-2. (a) FTIR spectra of γPGA and [PEDOT/Al_2O_3/γPGA]PHMeDOT. (b) TGA and DTGA curves of γPGA, PEDOT/Al_2O_3/γPGA and [PEDOT/Al_2O_3/γPGA]PHMeDOT.

Swelling tests proved the importance of the presence of $NaHCO_3$ during the preparation of the γPGA. Figure 3.3-3 compares the temporal evolution of the swelling ratio (Eqn) for [PEDOT/Al_2O_3/γPGA]PHMeDOT electrode when immersed into pure milli-Q water and 0.5 M $NaHCO_3$ aqueous solution. After 3 h, the swelling is 83% and 15%, respectively, reflecting that the incorporation of $NaHCO_3$ during the synthetic process contributes to the dimensional stability. Thus, the Na^+ cations of the salt neutralize the negatively charged carboxylate groups from γPGA, reducing the hydration capacity of the hydrogel and guarantying the volumetric stability of both the electrodes and the solid electrolyte.

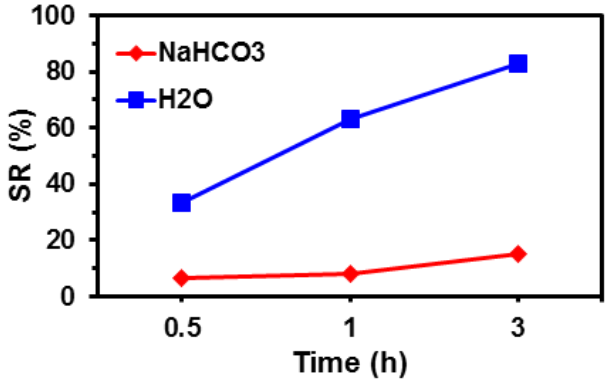

Figure 3.3-3. Swelling ratio (SR, Eqn 1) of γPGA biohydrogel immersed in milli-Q water and 0.5 M $NaHCO_3$ aqueous solution.

Assembly and optimization of the symmetric supercapacitor prototype

The compact supercapacitor was built by connecting two [PEDOT/Al_2O_3/γPGA]PHMeDOT electrodes, which acted as cathode (C) and anode (A), through a solid electrolyte (SE) made of γPGA biohydrogel, as is schematically represented in Figure 3.3-1(h). A photograph of the prototype illustrating its small dimensions, manageability, portability and robustness, is displayed in Figure 3.3-1(i).

The dimension of the supercapacitor prototype could be a relevant factor in terms of final application and specific properties requested (flexibility and elasticity). In order to find the best compromise between dimension and electrochemical performance, cyclic voltammetries were conducted on prototypes with different electrode and solid electrolyte widths. By changing the width of the electrode, the effect of the amount of electroactive material on the specific capacitance (*SC*; Eqn 2) was investigated, while the separation between the electrodes (*i.e.* solid electrolyte width) was used to examine the effect of the path length covered by the ions inside the gel on the *VC*; Eqn 3, of the entire prototype was analyzed.

Figure 3.3-4(a) represents the variation of the *SC*, as determined by CV, against the scan rate for supercapacitor prototypes in which the width of the electrode (w_c) is 2 or 4 mm, while the width of the solid electrolyte (w_s) is kept at 2 mm in both cases. As it can be seen, the increment of the *SC* with content of EAP is higher than expected, since when w_c changes from 2 to 4 mm, the *SC* increases more than double (*i.e.* from 3.8 to 10.8 mFg^{-1}). The variation of *VC* with the scan rate was

examined considering four different cases, in which variations in w_c and w_s occur simultaneously: (i) $w_c = w_s = 2$ mm; (ii) $w_c = 2$ mm and $w_s = 4$ mm; (iii) $w_c = w_s = 4$ mm; and (iv) $w_c = 4$ mm and $w_s = 8$ mm. It should be remarked that because of the symmetric supercapacitor configuration, the width is identical for the two electrodes, the cathode and the anode. Figure 3.3-4(b) indicate that *VC* decreases with increasing w_s, independently of w_c (i.e. from 0.06 to 0.03 mF cm^{-3} when w_s increases from 2 to 4 mm for w_c= 2 mm, and from 0.11 to 0.09 mF cm^{-3} when w_s increases from 4 to 8 mm for w_c= 4 mm). On the basis of these results, the optimum values chosen for the supercapacitor prototype, and used for the devices characterized in next sections, were $w_c = w_s = 4$ mm.

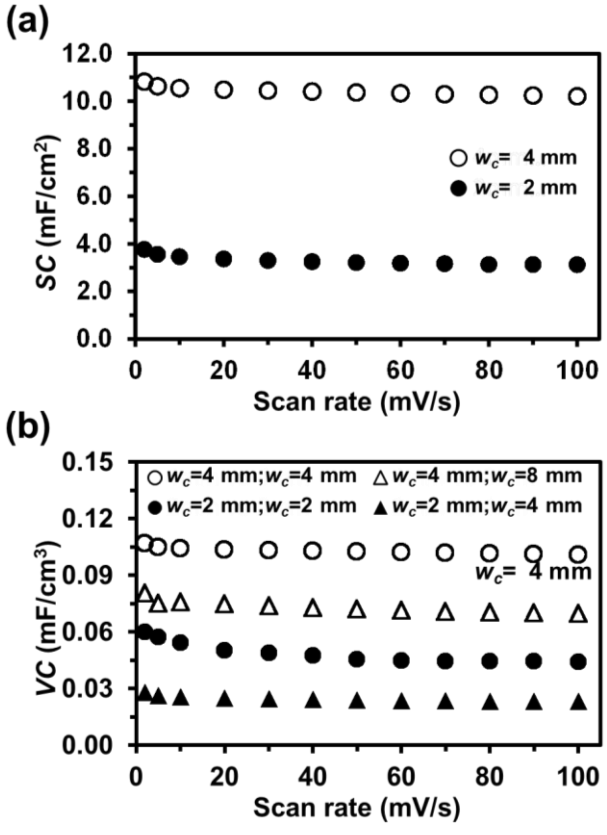

Figure 3.3-4. Optimization of the supercapacitor prototype: (a) Variation of the areal SC with the scan rate for devices prepared using electrodes of different width (w_c= 2 or 4 mm) and fixing the width of the solid electrolyte at w_s= 2 mm; (b) Variation of the VC with the scan rate for devices prepared using electrodes of different widths for the electrode and the solid electrolyte. Both the SC and the VC were determined by CV: initial and final potential= 0.00 V; reversal potential: 0.80 V.

Optimization of the electrical double layer capacitive behavior

The capacitive behavior of the prototype is relatively poor in the potential window used in the previous section to optimize the width of the electrodes and the solid electrolyte. Thus, the cyclic voltammograms recorded in the potential interval comprised between 0.00 (initial/final potential) and 0.80 V (reversal potential) do not approximate to the desired rectangular or quasi-rectangular shape (Figure 3.3-5), which has been attributed to the irreversible oxidation peak typically found in polythiophene at around 0.7 V.[39,40] In order to enhance the double layer capacitive behaviour of the device, different operation potential windows were considered. More specifically, CV assays were performed by reducing the reversal potential from 0.80 V to 0.70, 0.60 and 0.50 V, keeping the initial/final potential at 0.00 V, and decreasing the initial/final potential from 0.00 V to -0.10 and -0.30 V, maintaining the reversal potential at 0.80 V.

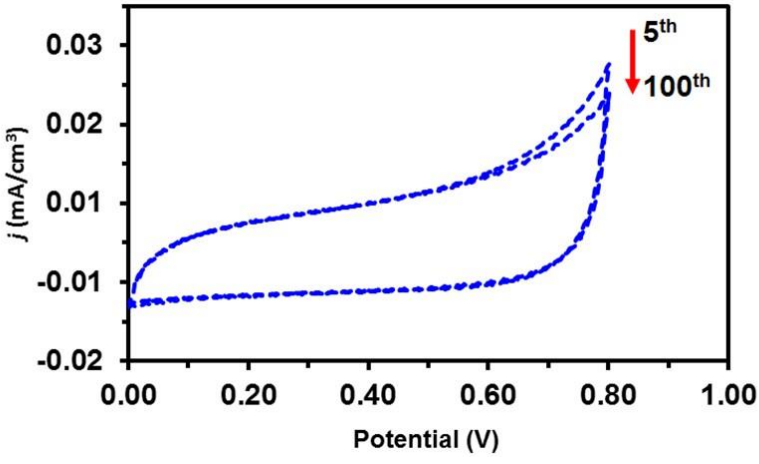

Figure 3.3-5.Cyclic voltammograms of the prototype after 5 and 100 consecutive oxidation-reduction processes. The reduction of the electrochemical activity reflects structural changes induced by overoxidation.

The influence of the irreversible oxidation peak in the distortion of the CV curves from the near-rectangular shape decreased by reducing the reversal potential (Figure 3.3-6), even though the *SC* decreased from 10.8 mF g^{-1} to 3.3 mF g^{-1}.

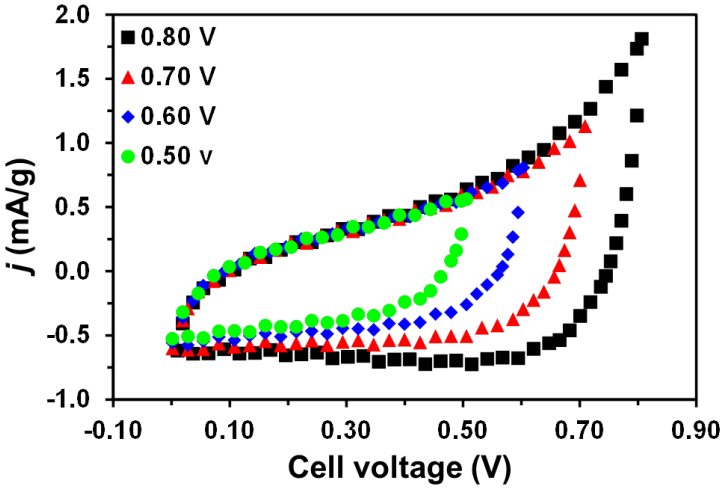

Figure 3.3-6. Cyclic voltammograms recorded at different reversal potentials (0.80, 0.70, 0.60 and 0.50 V) while the initial/final potential is kept at 0.00 V.

Similarly, a reduction from the deviation of the rectangular shape is observed when the initial/final potential is moved towards lower values (Figure 3.3-7).

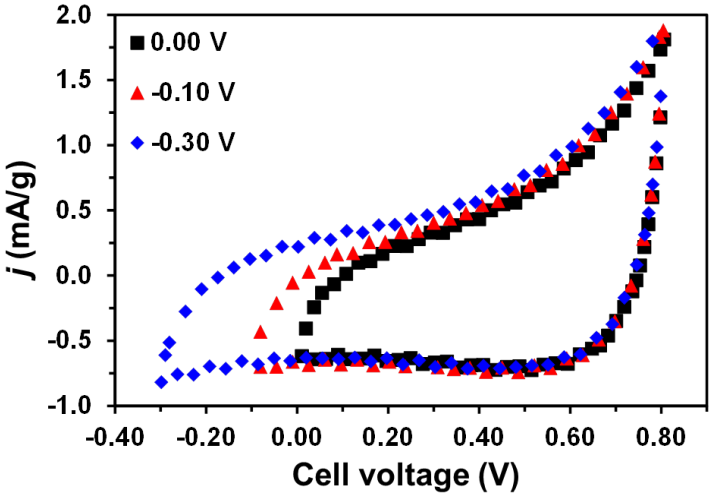

Figure 3.3-7. Cyclic voltammograms recorded at different initial and final potential (0.00, -0.10 and -0.30 V) while the reversal potential is kept at 0.80 V.

On the basis of these electrochemical assays, the operation potential window was defined by -0.50 V as initial/final potential and 0.50 V as reversal potential. Cyclic voltammograms from -0.50 to 0.50 V, which are displayed in Figure 3.3-9(a), shows an almost ideal rectangular shape for scan rates up to 500 mVs^{-1}, evidencing good capacitive performance, high rate capability, low contact resistance and the absence of Faradaic reactions. The *SC* determined using such potential window and a scan rate of 50 mV s^{-1} was 13.3 mF g^{-1}. This value decreases with increasing scan rate (*e.g.* *SC*= 8.6 m Fg^{-1} when the scan rate increases to 500 mV s^{-1}), which has been attributed to a progressively less efficient infiltration of the ions into the porous matrix. Thus, at slow scan rates, the diffusion of ions from the electrolyte can gain access to almost all available pores of the electrodes, favoring their penetration and leading to a higher *SC* values. Indeed, application of Cottrell model (Figure 3.3-8) corroborates that ion motions through the complex structures of the porous 3D electrodes and solid electrolyte depend only on the diffusion.

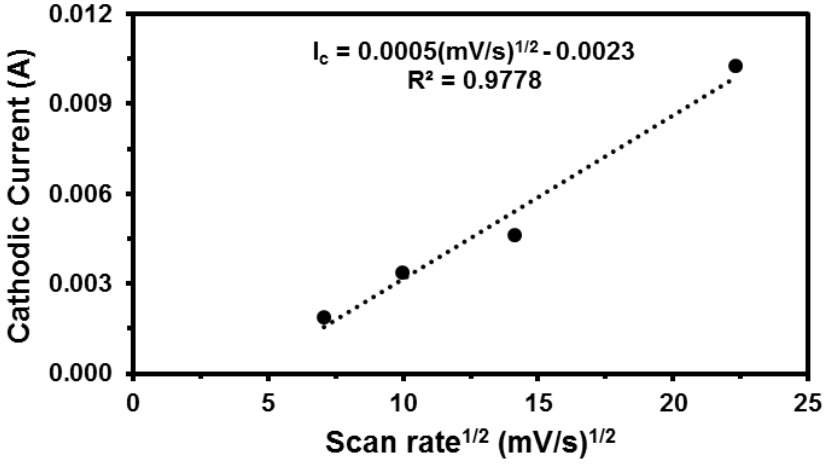

Figure 3.3-8. Cottrell graph considering high scan rates (50, 100, 200 and 500 mV s^{-1}) for the supercapacitor prototype.

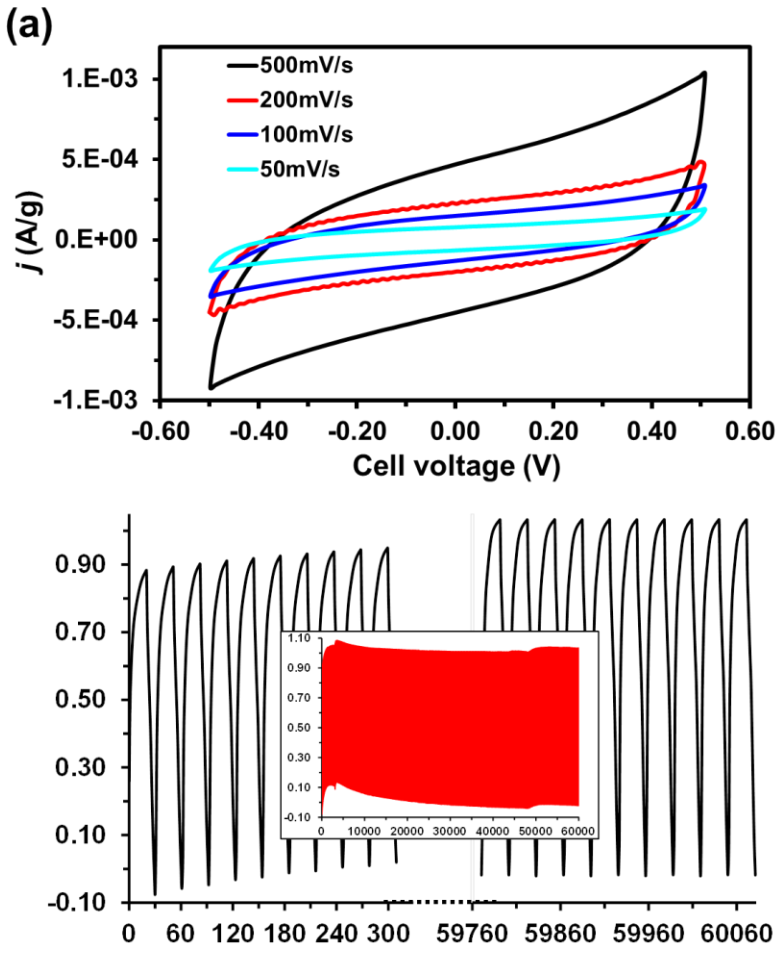

Figure 3.3-9. (a) Cyclic voltammograms of the supercapacitor prototype recorded at different scan rates. Initial and final potentials: -0.50 V; reversal potential: 0.5 V. (b) GCD cycles recorded at 0.0035 mA (charging and discharging times: 20 and 10 s, respectively). The prototype was subjected to 2000 cycles (inset). Magnification of the first and last cycles is provided.

Electrochemical performance of the prototype

In addition of previously discussed CV results, the performance of the supercapacitor device was analyzed using GCD cycles and EIS. Figure 3.3-9(b) shows the first GCD curves (charging and discharging times of 20 and 10 s, respectively) recorded at 0.0035 A, which is close to the maximum current observed in cyclic voltammograms at scan rate of 100 mVs^{-1} [Figure 3.3-9(a)]. As it can be seen, charge-discharge curves are almost linear and symmetric, while the cell potential increases slowly (*e.g.* from 0.87 to 0.93 V after 10 cycles). After ~500 cycles the cell potential reaches a value

of 1.02 V [inset in Figure 3.3-9(b)] that is preserved until the last cycle. Thus, the system reaches a steady state, as is illustrated in by the magnified plot associated to the last few cycles [Figure 3.3-9(b), right]. Along this process, the *SC* decreases from 14.8 mF g^{-1} (2nd cycle) to 13.6 mF g^{-1}, which represents 92% of retention. These results point out not only the good electrochemical performance of the device but also its high cyclability.

The 8% loss of ability to charge and discharge suggests that consecutive charge-discharge steps induce structural changes in the electrodes and solid electrolyte. Thus, swelling and shrinkage processes may alter the structure of the pores, affecting the access and/or scape of ions. Figure 3.3-10 compares SEM micrographs of the different elements of the prototype before and after 2000 GCD cycles. As it can be seen, the charge-discharge aging of the prototype clearly affects the porous structure of the two electrodes, even though in a different way. Specifically, in the cathode pores are more open, irregular and heterogeneously distributed after 2000 GCD cycles, while electrochemical aging induces the collapse and, therefore, a significant reduction in the size of the pores in the anode. Besides, inspection of the γPGA solid electrolyte reveals the dehydration of the biohydrogel during the charge-discharge cycles. Accordingly, the wide and well-defined pores observed in the fresh electrolyte converts into relatively closed channels, making more difficult the motion of the ions.

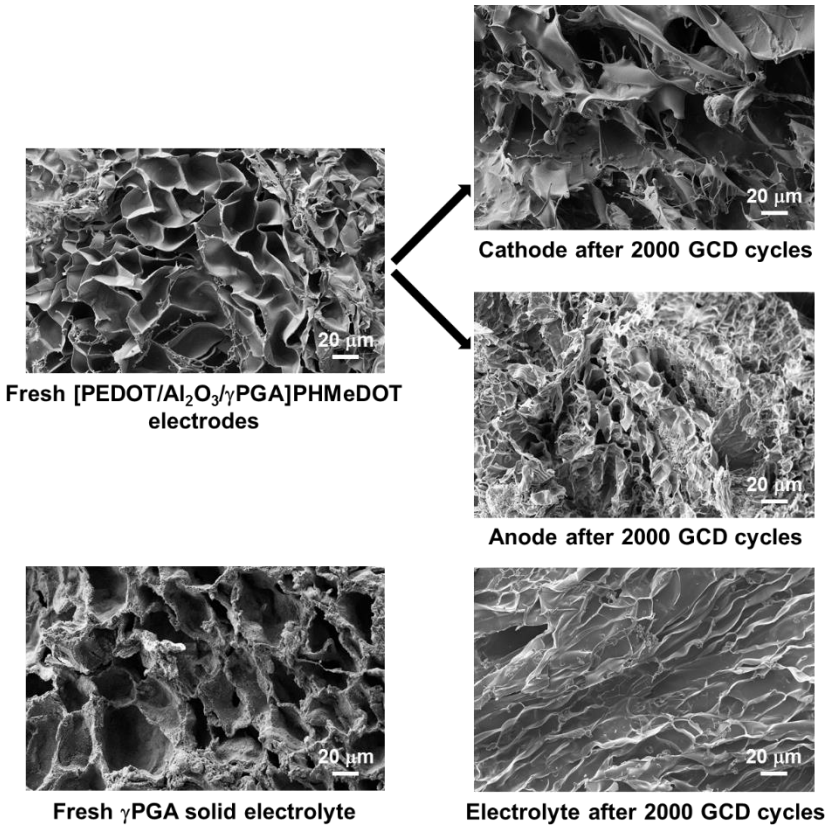

Figure 3.3-10. SEM images of fresh [PEDOT/Al_2O_3/γPGA]PHMeDOT electrodes and γPGA solid electrolyte (left) and after electrochemical aging by applying 2000 GCD cycles to the supercapacitor prototype.

The variation of *SC* as a function of the discharging current density is represented in Figure 3.3-11(a).

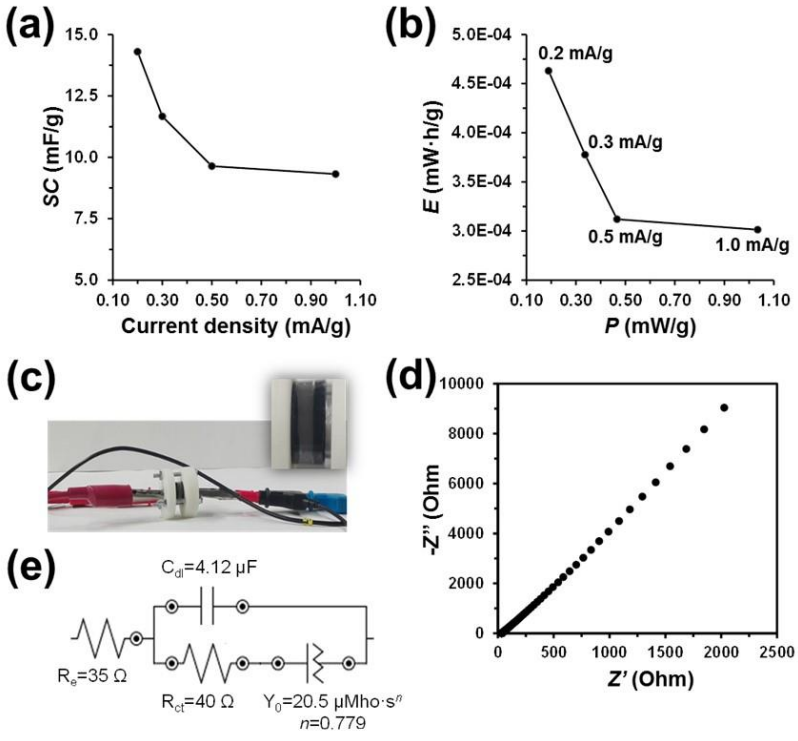

Figure 3.3-11. (a) Variation of the SC (Eqn 5) as a function of current density. (b) Variation of E (Eqn 7) against P (Eqn 8) for the indicated discharging current densities. (c) Supercapacitor prototype in the through-plane impedance cell used for EIS measurements. (d) Nyquist impedance plot showing the evolution of the impedance data of the supercapacitor prototype. (e) Equivalent circuit model used to fit the experimental data.

The *SC* decreases with increasing current density, which is consistent with literature.[41,42] At high current densities, the charge only accumulates at the outer surface of electrodes since ions do not have not enough time to enter into pores and accumulate at the inner surface, explaining the reduction of the *SC*. As it can be seen, when the current density increases from 0.5 to 1 mA g^{-1}, the rate of decrease of the *SC* is lower than that from 0.2 to 0.3 mA g^{-1}. Therefore, the prototype can be used at the highest current density while the *SC* is still as high as 8.8 mFg^{-1}. However, in order to take more advantage of the porous structure of the supercapacitor, low current densities are recommendable. These observations are supported by Figure 3.3-11(b), which represents the variation of the energy density (*E*; Eqn 7) against the power density (*P*; Eqn 8) for different discharging current densities (0.2, 0.3, 0.5 and 1.0 mA g^{-1}). As it can be seen, *E* decreases gradually with increasing *P*, evidence the superficial accumulation of charge.

EIS studies were conducted to determine the electrical conductivity of the supercapacitor. Accordingly, the impedance was measured for frequencies ranging from 10 to 10^5 Hz for the prototype using a recently developed through-plane impedance cell [Figure 3.3-11(c)].[43] The Nyquist plot and the electric equivalent circuit (EEC) are displayed in Figure 3.3-11(d, e), respectively.

The almost straight line observed in the profile suggests a Warburg-like behavior, which is characteristic of electrical double-layer porous capacitors.[44] At high frequencies, the plot shows a very soft semicircle, indicating a fast charge transfer (directed by Faradaic process) with negligible charge transfer resistance. This is consistent with the porous structure of the electrode, which favors the permeation of the electrolyte and enhances the ion transfer kinetics.[45]

The Randles-Ershler EEC model used for fitting the experimental data from EIS measurements provides not only understanding of the response of the fundamental systems with coupled processes (*e.g.* charge transfer, diffusion, electric double layer charging and uncompensated solution resistance) but also quantification of some fundamental interfacial phenomena. The solid electrolyte resistance [R_e in Figure 3.3-11(e)], which arises from the $NaHCO_3$ salt used during synthesis of the biohydrogel, is 35 Ω. This corresponds to an ionic conductivity of $4.5 \cdot 10^{-3}$ S cm^{-1}, reflecting the semiconducting behavior of the device. This is consistent with the *E* vs *P* graphic [Figure 3.3-11(b)] discussed above. On the other hand, the value of the charge-transfer resistance (R_{ct}= 40 Ω) is very similar to R_e, facilitating the exchange of ions along the double layer. The R_{ct} is in series with a constant phase element (CPE) impedance, as is typically observed in gel-based electrodes.[46] The CPE impedance has been expressed as:

$$Z_{CPE} = \frac{1}{Y_0(jw)^n} \quad (9)$$

Where Y_0 is the admittance of an ideal capacitance and *n* is an empirical constant ranging from 0 to 1. The CPE represents a capacitor and a resistor for n= 1 and n= 0, respectively, while it is associated with a diffusion process when n= 0.5 and is equivalent to the so-called Warburg element. In this work, the Z_{CPE} with *n*= 0.77 is related with the ionic diffusion through the electrode. Finally, the double layer capacitance element (C_{dl}), with a value of 4.12μF, reflects the capacitance at the electrode/electrolyte interphase.

3.3.5. Conclusions

A flexible, compact, lightweight and biocompatible symmetric supercapacitor has been developed by assembling two identical electrodes, constituted by EAPs- and alumina-containing electroactive hydrogels, through a γPGA biohydrogel doped with $NaHCO_3$, which act as a solid electrolyte. After optimization, the best configuration of the prototype exhibits the following characteristics: 4 mm as width of the electrodes, 4 mm as width of the solid electrolyte, working potential window that expands from -0.50 V to 0.50 V at a scan rate of 100 mVs^{-1}. The *SC* of the prepared supercapacitors is around 13 mFg^{-1}, a good *E* ($4.6 \cdot 10^{-4}$ mWh g^{-1}) and cyclability (92% of retention of the specific capacitance after after 2000 GCD cycles) being achieved. The excellent electrochemical properties of PEDOT and PHMeDOT, which are enhanced in presence of alumina, in combination with the mechanical strength and flexibility of the γPGA biohydrogel, suggest the supercapacitor prototype prepared in this work is a promising small-size and lightweight energy storage device.

3.3.6. References

(1) Wang, C.Y.; Ballantyne, A.M.; Hall, S.B.; Too, C.O.; Officer, D.L.; Wallace, G.G. Functionalized Polythiophene-Coated Textile: A New Anode Material for A Flexible Battery. *J. Power. Sources.* **2006**, *156* (2), 610–614.

(2) Wang, X.; Lu, X.; Liu, B.; Chen, D.; Tong, Y.; Shen, G. Flexible Energy-Storage Devices: Design Consideration and Recent Progress. *Adv. Mater*. **2014**, *26* (28), 4763–82.

(3) Zhao, Y.; Liu, B.; Pan, L,; Yu, G. 3D Nanostructured Conductive Polymer Hydrogels for High-Performance Electrochemical Devices. Environmental Science high-performance electrochemical devices. *Energy. Environ. Sci.* **2013**, *6* (10), 2856-2870.

(4) Shi, Y.; Yu, G. Designing Hierarchically Nanostructured Conductive Polymer Gels for Electrochemical Energy Storage and Conversion. *Chem. Mater.* **2016**, *28* (8), 2466–2477.

(5) Shi, Y.; Peng, L.; Ding, Y.; Zhao, Y.; Yu, G. Chem Soc Rev Nanostructured conductive polymers for Advanced Energy Storage. *Chem. Soc. Rev.* **2015**, *44* (1), 6684–6696.

(6) Kim, J.; Lee, J.; You, J.; Park, M.; Hossain, S.Al.; Ho, J. Materials Horizons Conductive Polymers for Next-Generation Energy Storage Systems: Recent Progress And New Functions. *Mater Horizons*.**2016**, *3* (6), 517–535.

(7) Kim, B.C.; Spinks, G. M.; Wallace, G. G.; John, R. Electroformation Of Conducting Polymers in A Hydrogel Support Matrix. *Polymer.* **2000**, *41* (5), 1783–1790.

(8) Brahim, S.; Narinesingh, D.; Guiseppi-Elie, A. Polypyrrole-Hydrogel Composites for the Construction of Clinically Important Biosensors. *Biosens. Bioelectron.* **2002**, *17* (1–2), 53–59.

(9) Brahim, S.; Narinesingh, D.; Guiseppi-Elie, A. Bio-Smart Hydrogels: Co-Joined Molecular Recognition and Signal Transduction in Biosensor Fabrication and Drug Delivery. *Biosens. Bioelectron.* **2002**, *17* (11–12), 973–981.

(10) Guiseppi-Elie, A. Electroconductive Hydrogels: Synthesis, Characterization and Biomedical Applications. *Biomaterials*. **2010**, *31* (10), 2701–2716.

(11) Lange, U.; Roznyatovskaya, N. V.; Mirsky, V.M. Conducting polymers in chemical sensors and arrays. *Anal. Chim. Acta*. **2008**; *614* (1), 1–26.

(12) Balint, R.; Cassidy, N. J.; Cartmell, S. H. Conductive Polymers: Towards A Smart Biomaterial For Tissue Engineering. *Acta. Biomater*. **2014,** *10* (6), 2341–2353.

(13) Hardy, J. G.; Lee, J. Y.; Schmidt, C. E. Biomimetic Conducting Polymer-Based Tissue Scaffolds. *Curr. Opin. Biotechnol.* **2013**, *24* (5), 847–854.

(14) Sasaki, M.; Karikkineth, B. C.; Nagamine, K.; Kaji, H.; Torimitsu, K.; Nishizawa, M. Highly Conductive Stretchable and Biocompatible Electrode-Hydrogel Hybrids for Advanced Tissue Engineering. *Adv. Health. Mater*. **2014**, *3* (11), 1919–1927.

(15) Lira, L.M.; Barthus, R.; Torresi, S. Conducting Polymers and Hydrogels for Electrochemically Controlled Drug Release Devices. *ECS Transactions.* **2007**, *3* (29), 105–114.

(16) Lee, H.; Hong, W.; Jeon, S.; Choi, Y.; Cho, Y. Electroactive Polypyrrole Nanowire Arrays: Synergistic Effect of Cancer Treatment by On-Demand Drug Release and Photothermal Therapy. *Langmuir*. **2015**, *31* (14), 4264–4269.

(17) Asplund, M.; Nyberg, T.; Inganäs, O. Electroactive Polymers For Neural Interfaces. *Polym. Chem.* **2010**, *1* (9), 1374–1391.

(18) Justin, G.; Guiseppi-Elie, A. Characterization of Electroconductive Blends of Poly(HEMA-Co-PEGMA-Co-HMMA-Co-SPMA) and Poly(Py-Co-Pyba). *Biomacromolecules*. **2009**, *10* (9), 2539–2549.

(19) Mawad, D.; Lauto, A.; Wallace, G. G. Conductive Polymer Hydrogels. In *Polymeric Hydrogels as Smart Biomaterials*. Kalia, S., Ed.; Springer, **2016**; pp 19–45.

(20) Snook, G.A.; Kao, P.; Best, A. S. Conducting-Polymer-Based Supercapacitor Devices and Electrodes. *J. Power Sources.* **2011**, *196* (1),1–12.

(21) Shi, Y.; Peng, L.; Yu, G. Nanostructured Conducting Polymer Hydrogels for Energy Storage Applications. *Nanoscale*. **2015**, *7* (30), 12796–12806.

(22) Pan, L.; Yu, G.; Zhai, D.; Ryoung, H.; Zhao, W.; Liu, N.; Wang, H.; Tee, B, C.-K.; Shia, Y.; Cui, Y.; et al. Hierarchical Nanostructured Conducting Polymer Hydrogel with High Electrochemical Activity. *PNAS*. **2012**, *109* (24), 1–6.

(23) Mire, C.A.; Wallace, G. G.; Calvert, P. Inkjet and Extrusion Printing of Conducting Poly (3 , 4-Ethylenedioxythiophene) Tracks On and Embedded in Biopolymer Materials. *J. Mater. Chem*. **2011**, *21* (8), 2671–2678.

(24) Glavan, A. C.; Walker, S. B.; Lewis, J. A.; Whitesides, G. M.; Link, C. Inkjet Printing of Conductive Inks with High Lateral Resolution on Omniphobic "R F Paper" for Paper-Based Electronics and MEMS. *Adv. Mat.* **2017**, *26* (27), 4677–4682.

(25) Boland, T.; Xu, T.; Damon, B.; Cui, X. Application of Inkjet Printing to Tissue Engineering. *Biotechnol J*. **2006**, *1* (9), 910–917.

(26) Brahim, S.; Slaughter, G.; Guiseppi-Elie, A. Electrical and Electrochemical Characterization of Electroconductive PPy-p (HEMA) Composite Hydrogels. *Proceedings of SPIE - The International Society for Optical Engineering.* **2003**, *5053* (1),1–12.

(27) Sekine, S.; Ido, Y.; Miyake, T.; Nagamine, K.; Nishizawa, M. Conducting Polymer Electrodes Printed on Hydrogel. *J. Am. Chem. Soc.* **2010**, *132* (38),13174–13175.

(28) Pérez-Madrigal, M. M.; Edo, M. G.; Díaz, A.; Puiggalí, J.; Alemán, C. Poly-γ-glutamic Acid Hydrogels as Electrolyte for Poly(3,4-ethylenedioxythiophene)-Based Supercapacitors. *J. Phys. Chem. C.* **2017**, *121* (6), 3182–3193.

(29) Saborío, M. C. G.; Lanzalaco, S.; Fabregat, G.; Puiggali, J.; Estrany, F.; Aleman, C. Flexible Electrodes for Supercapacitors Based on the Supramolecular Assembly of Biohydrogel and Conducting Polymer. *J. Phys. Chem. C* **2018**, *122* (2), 1078–1090.

(30) Bajaj, I.; Singhal, R. Poly (glutamic acid)--an Emerging Biopolymer of Commercial Interest. *Bioresour. Technol.* **2011**, *102*, 5551–5561.

(31) Shih, I.; Wu, P.; Shieh, C. Microbial Production of a Poly(γ-glutamic acid) Derivative by *Bacillus Subtilis*. *Process Biochem.* **2005**, *40*, 2827–2832.

(32) Thome, C. B.; Gómez, C. G.; Noyes, H. E.; Housewright, R. D. Production of Glutamyl Polypeptide by *Bacillus Subtilis*. *J. Bacteriol.* **1954**, *68*, 307–315.

(33) Armelin, E.; Perez-Madrigal, M. M.; Alemán, C.; Díaz-Díaz, D. Current Status and Challenges of Biohydrogels for Applications as Supercapacitors and Secondary Batteries. *J. Mater. Chem. A*, **2016**, *4*, 8952–8968.

(34) Saborío, M. C. G.; Estrany, F.; Alemán, C. Properties of In Situ Polymerized Poly (3, 4-ethylenedioxythiophene)/ Alumina Composites for Energy Storage Applications. *J. Polym. Sci. Part B: Polym. Phys*. **2017**, 55 (15), 1131–1141.

(35) C. Ocampo, R. Oliver, E. Armelin, C. Alemán, F. Estrany, *J. Polym. Res.* 2006, **13**, 193.

(36) Fabregat, G.; Casanovas, J.; Redondo, E.; Armelin, E.; Alemán, C. A Rational Design for the Selective Detection of Dopamine Using Conducting Polymers. *Phys. Chem. Chem. Phys.* **2014**, *16*, 7850–7861.

(37) Hocevar, M. A.; Fabregat, G.; Armelin, E.; Ferreira, C. A.; Alemán, C. Nanometric Polythiophene Films with Electrocatalytic Activity for Non-Enzymatic Detection of Glucose. *Eur. Polym. J.* **2016**, *79*, 132–139.

(38) Prado, L. A.; Sriyai, M.; Ghislandi, M.; Barros-Timmons, A.; Schulte, K. Surface Modification of Alumina Nanoparticles with Silane Coupling Agents. *J. Braz. Chem. Soc*. **2010**, *21* (12), 2238–2245.

(39) B. Teixeira-Dias, L. J. del Valle, D. Aradilla, F. Estrany and C. Alemán, Macromol. Mater. Eng. 2012, 297, 427–436.

(40) Láng, G. G.; Ujvári, M.; Vesztergom, S.; Kondratiev, V.; Gubicza, J.; Szekeres, K. J. The Electrochemical Degradation of Poly (3,4-Ethylenedioxythiophene) Films Electrodeposited from Aqueous Solutions. *Int. J. Research in PCCP*. **2016**, *230* (9), 1281–1302.

(41) Shi, Y.; Pan, L.; Liu, B.; Wang, Y.; Cui, Y.; Bao, Z.; Yu, G. Nanostructured Conductive Polypyrrole Hydrogels as High-Performance, Flexible Supercapacitor Electrodes. *J. Mater. Chem. A*. **2014**, *2* (17), 6086–6091.

(42) Chen, P.; Yang, J-J.; Li, S-S.; Wang, Z.; Xiao, T. Y.; Qian, Y-H.; Yun, S-H. Hydrothermal Synthesis of Macroscopic Nitrogen-Doped Graphene Hydrogels for Ultrafast Supercapacitor. *Nano Energy*. **2013**, *2* (2), 249–256

(43) F. Müller, C. A. Ferreira, D. S. Azambuja, C. Alemán and E. Armelin, Measuring the Proton Conductivity of Ion-Exchange Membranes Using Electrochemical Impedance Spectroscopy and Through-Plane Cell. *J. Phys. Chem. B*, 2014, 118 (4), 1102–1112.

(44) Niu, Z.; Zhou, W, Chen, J.; Feng, G.; Li, H.; Ma, W.; Li, J.; Dong, H.; Ren, Y.; Zhaoac, D.; et al. Compact-Designed Supercapacitors Using Free-Standing Single-Walled Carbon Nanotube Films. *Energy Environ. Sci*. **2011**,*4* (4), 1440–1446.

(45) Mária Ujvári, Takács, M.; Vesztergom, S.; Bazsó, F.; Ujhelyi, F.; Láng, G. G. Monitoring of the Electrochemical Degradation of PEDOT Films on Gold Using the Bending Beam Method. *J. Solid State Electrochem*. **2011**, *15* (11-12), 2341–2349.

(46) Warrena, H.; Panhuis, M. Electrical Conductivity and Impedance Behavior of Hydrogels. *Proc. of SPIE*. **2014**, *9171* (1), 3–8.

Chapter IV

4.1. Cationic ionene as n-dopant agent of PEDOT

4.1.1. Abstract

We report the reduction of PEDOT films with a cationic 1,4-diazabicyclo[2.2.2]octane-based ionene bearing N,N'-(meta-phenylene)dibenzamide linkages (mPI). Our main goal is to obtain n-doped PEDOT using a polymeric dopant agent rather than small conventional tetramethylammonium (TMA), as is usual. This has been achieved using a three-step process, which has been individually optimized: (1) preparation of p-doped (oxidized) PEDOT at a constant potential of +1.40 V in acetonitrile with $LiClO_4$ as electrolyte; (2) dedoping of oxidized PEDOT using a fixed potential of –1.30 V in water; and (3) redoping of dedoped PEDOT applying a reduction potential of –1.10 V in water with mPI. The resulting films display the globular appearance typically observed for PEDOT, mPI being structured in separated phases forming nanospheres or ultrathin sheets. This organization, which has been supported by atomistic Molecular Dynamics simulations, resembles the nanosegregated phase distribution observed for PEDOT p-doped with PSS. Furthermore, the doping level achieved using mPI as doping agent is comparable to that reached with TMA, even though the ionene provides distinctive properties to the conducting polymer. For example, films redoped with mPI exhibit much more hydrophilicity than the oxidized ones, whereas films redoped with TMA are hydrophobic. Similarly, films redoped mPI exhibit the highest thermal stability, while those redoped with TMA show a thermal stability that is intermediate between the latter and dedoped PEDOT. Overall, the incorporation of mPI polycation as n-dopant into PEDOT has important advantages for modulating the properties of this emblematic conducting polymer.

TOC graphic

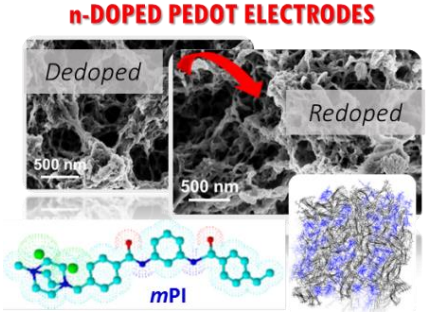

4.1.2. Introduction

Among CPs, doped PEDOT (Scheme 4.1-1), is one of the most studied because of its great environmental stability, electrical conductivity, electrochemical activity, thermoelectric behaviour and high *SC*.[1-5] Additionally, PEDOT offers two fundamental advantages as compared to unsubstituted PTh or other PTh derivatives: (1) the fused dioxane ring blocks the β-position of the thiophene ring and prevents from the formation of α-β linkages during the polymerization, which makes the resulting polymer well-defined from a regiochemical point of view; and (2) the fused dioxane ring and the electron-donating effects provided by the oxygen atoms cause the self-rigidification of polymer chains, resulting in a gain of aromaticity and in a reduction the oxidative doping potential (p-doping).[6]

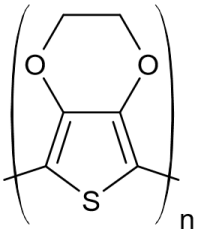

Scheme 4.1-1. Chemical structure of PEDOT

Oxidized PEDOT (p-doped) has been prepared using small anions as doping agents (*e.g.* ClO_4^-, NO_3^-, SO_4^{2-} and citrate), electrochemical activity being dominated by ionic and solvent movements.[7-9] The oxidation towards the p-doped state causes the access of solvated dopant anions inside the polymeric matrix, while they scape upon reduction towards the undoped (neutral) state. Similarly, large and even macromolecular dopant anions, as for example dodecyl sulfate and PSS, can be successfully used to produce p-doped PEDOT.[10-12] The PEDOT: PSS complex consists of a phase segregated structure in which ~30nm diameter conductive PEDOT-rich polycationic domains are encapsulated by ~1 nm thick PSS-rich polyanionic shells.[13] The domains are embedded in an electronically insulating PSS matrix loosely cross-linked by hydrogen bonding.[14] PSS-doped PEDOT polymer mixtures exhibit good film forming properties, moderate to high conductivity, high visible light transmittance and excellent stability and, therefore, are suitable for use as low-cost wearable sensors,[15] electrodes,[16,17] soft actuators,[19,20] and as hole injection/extraction material in organic optoelectronics.[21]

PEDOT is one the few CPs that are both p- and n-dopable. However, although reduced PEDOT (n-doped) was reported more than two decades ago by Inganäs and co-workers,[22] the number of studies on this material is very scarce.[22-27] More specifically, these studies were focussed on the spectroscopic, electrical and electrochemical properties of negatively charged PEDOT prepared using small tetra-alkylammonium cations as electrolyte.[22-26] However, experiments using other CPs revealed that the role of the electrolytic agent and the solvent in the n-doping is even higher than in the p-doping.[28-30] According to these observations, in a recent study, Suárez-Herrera and co-workers[27] showed that the negative charge of the n-doped PEDOT stabilizes when imidazolium-containing ionic liquids are used as dopant cations, resulting in a high n-doping concentration with respect to than obtained with tetra-alkylammonium cations.[22-26]

On the other hand, ionenes are high charged polymers (polyelectrolytes) in which the ionic groups form part of the macromolecular backbone.[31] More specifically, the term polyionene frequently invokes to polycations having quaternary ammonium in the backbone, which have been applied in diverse applications (*e.g.* antibacterial agents and functional gels).[31,32] The properties of polyionenes are determined, among others, by the charge distribution, the molecular weight, the hydrogen bonding capability and the type of counter ions.[33] Within this context, some of us recently reported a 1,4-diazabicyclo[2.2.2]octane (DABCO)-based polyionene bearing *N,N'*-(*meta*-phenylene)dibenzamide linkages, hereafter denoted *m*PI (Scheme 4.1-2).[34,35] We found that, although *m*PI chains organize forming regions dominated by ionene···ionene intermolecular interactions, these domains are much less frequent than in the isomer with *ortho* topology in the *N,N'*-(phenylene)dibenzamide linkages. This particular characteristic suggests that *m*PI polycation is suitable to interact favorably with other macromolecular compounds forming stable mixtures, whereas chains of the *ortho* isomer were found to aggregate rapidly forming gels with good properties.[34,35] Furthermore, *m*PI bears two close positive charges per repeat unit located at quaternary ammonium moieties (Scheme 4.1-2), making this polycation a very suitable candidate for the generation of negative charges at the PEDOT chains.

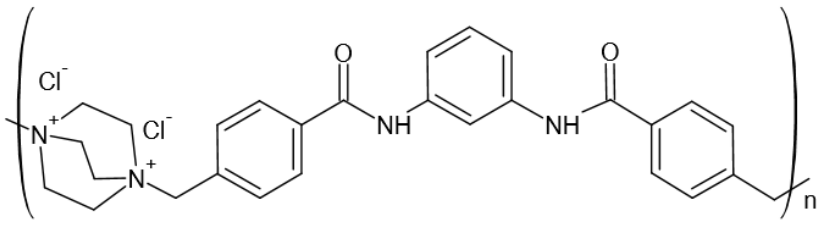

Scheme 4.1-2. Chemical structure of mPI

In this study we propose the preparation of n-doped PEDOT using *m*PI as a macromolecular dopant agent for its incorporation into pristine oxidized PEDOT films. After optimize the preparation process to achieve the highest n-doping concentration, the properties of the resulting material have been compared with those of n-doped PEDOT obtained using conventional tetramethylammonium (TMA) as dopant agent. Results have allowed us to conclude that the incorporation of *m*PI polycations into PEDOT have important advantages, as for example the improvement of the thermal stability and the preparation of superhydrophilic electroactive surfaces.

4.1.3. Experimental Section

Materials

EDOT and acetonitrile of analytical reagent grade were purchased from Aldrich. TMA; 98% was purchased from Across. Anhydrous $LiClO_4$, analytical reagent grade, from Aldrich, was stored in an oven at 80ºC before using it in the electrochemical trials. *Meta*-phenylenediamine, 4-(chloromethyl)benzoyl chloride and DABCO were purchased from TCI Europe.

Preparation of PEDOT films

Oxidized PEDOT films were prepared by CA under a constant potential of +1.40 V. Electrochemical experiments were conducted on a PGSTAT204 AUTOLAB potentiostat–galvanostat connected to a PC computer controlled through the NOVA 1.6 software using a three-electrode two-compartment cell under nitrogen atmosphere at 25 ºC. The cell was filled with 10 mL of a 10 mM monomer solution in acetonitrile with 100 mM $LiClO_4$. Steel AISI 316 sheets with an area of 1 cm^2 and 2 cm^2

were employed as working and counter electrodes, respectively. Before each trial, electrodes were cleaned with acetone and dried in a nitrogen-flow. No polishing of the sheets was necessary because of the low roughness of steel AISI 316.[37] The reference electrode was an Ag|AgCl electrode containing a KCl saturated aqueous solution (E^o = 0.222 V *vs.* standard hydrogen electrode at 25 ºC), which was connected to the working compartment through a salt bridge containing the electrolyte solution. The electrodes used for synthesis of p-doped PEDOT films were also employed for dedoping and redoping experiments.

The polymerization time was adjusted to obtain PEDOT electrodes with a polymerization charge of 0.960 C (480 mC cm^{-2}). The mass of PEDOT deposited onto the WE was determined as the weight difference between coated and uncoated steel sheets using a CPA26P Sartorius analytical microbalance with a precision of 10^{-6} g. The exact amount of electrochemically polymerized PEDOT onto the electrode was m_{pol} = 0.84 ± 0.13 mg.

Preparation of mPI

*m*PI was synthesized as previously reported[34] via a two-step reaction sequence. Briefly, the first step consisted in the amidation of *meta*-phenylenediamine with 4-(chloromethyl)benzoyl chloride in the presence of Et_3N in CH_2Cl_2 to afford the corresponding bis-benzamide monomer upon recrystallization (87% yield). Subsequent step-growth copolymerization with DABCO under equimolar conditions in DMF at 80 ºC yielded the desired polymer within 3 days as off-white slight brownish solid (69% yield) after a simple filtration, washing and drying protocol. ^{1}H-NMR (D_2O, 300 MHz) δ (ppm) = 8.00–7.18 (m, 6H), 4.44 (s, 1H), 3.91 (s, 4H), 3.34 (d, *J* = 6.6 Hz, 2H), 3.05 (d, *J* = 6.2 Hz, 2H). In order to achieve adequate solubility and mobility for GPC/SEC, counteranion exchange of chloride by bis(trifluoromethanesulfonyl)amide (TFSA) anions was carried out using LiTFSA in hot water. SEC data were obtained using a YL GPC instrument equipped with a refractive index detector (temperature of column oven = 50-60 ºC; eluent = DMF including 30 mM of LiTFSA; flow rate = 0.5 mL min^{-1}). Solution of the sample was filtered through 0.2 mm filter before injection into the 10mm column. Calibration was carried out using poly(methyl methacrylate) standards. *m*PI·TFSA: ^{1}H-NMR (DMSO-d_6, 300 MHz): δ (ppm) = 10.43 (d, *J* = 5.8 Hz, 2H), 8.42 (s, 1H), 8.25–7.98 (m, 2H), 7.67 (d, *J* = 6.3 Hz, 4H), 7.49 (t, *J* = 7.9 Hz, 2H), 7.35 (t, *J* = 8.0 Hz, 1H), 4.83 (s, 2H), 3.85 (s, 8H), 3.30 (d, *J* = 7.7 Hz, 2H), 3.03 (d, *J* = 6.9 Hz, 2H). M_w = 1.2 × 10^4 Da; M_n = 5.0 × 10^3 Da; $Đ_M$ = 2.4; *n* = 7.

Dedoping and redoping assays

Chronopotentiometric and chronoamperometric assays were performed using the equipment, cell and electrodes described above. Dedoping assays of electropolymerized p-doped PEDOT were carried out using water with 10 mM $LiClO_4$ as electrolyte solution, while redoping experiments were conducted using aqueous solutions with 10 mM *m*PI or 10 mM TMA. After redoping experiments, PEDOT films were submerged one time in acetonitrile to clean superficial *m*PI or TMA not electrostatically bounded to the polarons and bipolarons of PEDOT. In all cases, samples were softly washed with the solvent of the solution before the CV assays.

X-ray photoelectron spectroscopy (XPS)

XPS analyses were performed in a SPECS system equipped with a high-intensity twin-anode X-ray source XR50 of Mg/Al (1253 eV/1487 eV) operating at 150 W, placed perpendicular to the analyzer axis, and using a Phoibos 150 MCD-9 XP detector. The X-ray spot size was 650 µm. The pass energy was set to 25 and 0.1 eV for the survey and the narrow scans, respectively. Charge compensation was achieved with a combination of electron and argon ion flood guns. The energy and emission current of the electrons were 4 eV and 0.35 mA, respectively. For the argon gun, the energy and the emission current were 0 eV and 0.1 mA, respectively. The spectra were recorded with pass energy of 25 eV in 0.1 eV steps at a pressure below 5×10^{-9} mbar. These standard conditions of charge compensation resulted in a negative but perfectly uniform static charge. The C 1s peak was used as an internal reference with a binding energy of 284.8 eV. High-resolution XPS spectra were acquired by Gaussian–Lorentzian curve fitting after s-shape background subtraction. The surface composition was determined using the manufacturer's sensitivity factors.

Morphological and topographical characterization

SEM studies were performed to examine the surface morphology of as prepared, dedoped and redoped PEDOT films. Dried samples were placed in a Focussed Ion Beam Zeis Neon 40 scanning electron microscope operating at 3 kV, equipped with an EDX spectroscopy system.

AFM images were obtained with a Molecular Imaging PicoSPM using a NanoScope IV controller under ambient conditions. The tapping mode AFM was operated at constant deflection. The row scanning frequency was set to 1 Hz. AFM measurements were performed on various parts of the films, which provided reproducible images similar to those displayed in this work. The statistical

application of the NanoScope Analysis software was used to determine the R_q, which is the average height deviation taken from the mean data plane.

Wettability

Measurements were carried out using the sessile drop method at room temperature on an OCA 15EC with SCA20 software (Data-Physics Instruments GmbH, Filderstadt, Germany). The solvent used for these experiments was deionized water, contact angle being determined for the first drop. For measurements, the sessile drop was gently put on the surface of sample discs using a micrometric syringe with a proper metallic needle (Hamilton 500 μL). The ellipse method was used to fit a mathematical function to the measured drop contour. This procedure consists on approximate the drop contour to the line of an ellipse, deviations from the true drop shape being in the range of a few percent. The ellipse method provides accurate measure of the contact angle and holds the advantage that it is extremely fast. For each sample, no less than fifteen drops were examined.

Thermal stability

The thermal stability was studied by TGA at a heating rate of 20 ºC min^{-1} (sample weight *ca.* 5 mg) with a Q50 thermogravimetric analyzer of TA Instruments (New Castle, DE, USA) and under a flow of dry nitrogen. Test temperatures ranged from 30 to 600 ºC.

Molecular dynamics (MD) simulations

All MD trajectories were generated using the scalable computer program NAMD.[38] The energy was calculated using the AMBER all-atom force-field.[39] All parameters, with the exception of the equilibrium parameters and the partial charges of the EDOT repeating unit, were taken from previous studies in which parameters compatible with the AMBER force-field were developed.[37,40] Atomic electrostatic parameters for redoped EDOT units (*i.e.* $EDOT^{-0.2}$) were derived using the Restrained Electrostatic Potential (RESP) method[41] using $(EDOT)_5^{-1}$ (*i.e.* considering a doublet electronic state). The resulting charges are displayed in Figure 4.1.-1. Equilibrium parameters for $EDOT^{-0.2}$ units were taken from quantum mechanical calculations at the UB3LYP/6-31G(d,p) level.

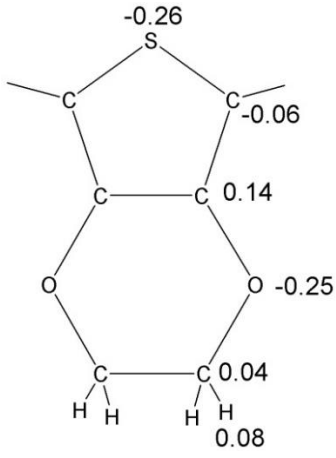

Figure 4.1-1. RESP charges calculated for n-doped EDOT unit.

All MD simulations were performed using the NAMD 2.9 program.[42] Each of the two simulated systems (**m1** and **m2**, which are described in the main text) was subjected to 20000 steps of energy minimization (Newton Raphson method) before any MD trajectory was run in order to relax conformational and structural tension. The temperature and pressure of **m1** were equilibrated by applying two MD runs. The first consisted on an NVT-MD simulation at 298 K for 0.5 ns. The resulting atom velocities and coordinates were used as starting point for the second run: a 1.0 ns NPT-MD trajectory at 298 K and 1 bar. For **m2** this process was repeated ten times consecutively, the equilibration taken 5 and 10 ns of NVT-MD and NVT-MD, respectively, distributed in 10 different runs each one. The last step of the equilibration run was the starting point of the productive trajectories presented in this work (298 K and 1 bar pressure).

Bond lengths involving hydrogen atoms were kept at their equilibrium distances using the RATTLE algorithm.[43] Atom pair distance cutoffs were applied at 14.0 Å to compute the van der Waals interactions. To avoid discontinuities in this energy component, the van der Waals energy term was forced to slowly converge to zero by applying a smoothing factor from a distance of 12.0 Å. Electrostatic interactions were extensively computed by means of Ewald summations. The real space term was defined by the van der Waals cutoff (14.0 Å), while the reciprocal space was computed by interpolation of the effective charge into a charge mesh with a grid thickness of 5 points per volume unit (particle mesh Ewald).[44]

For the equilibration and production runs, both temperature and pressure were controlled by the Nose-Hoover pistons[45] combined with the piston fluctuation control of temperature implemented for Langevin dynamics.[46] Pressure was kept at 1.01325 bars, the oscillation period was set to 1 ps while the piston decay time was set to 0.001 ps. The piston temperature was set to the same value as the thermostat control, 298 K, which used a damping coefficient of 2 ps. The integration step was 2 fs in all simulations.

4.1.4. Results and discussion

Preparation of p-doped PEDOT and mPI.

Oxidized PEDOT films were prepared by potentiostatic electropolymerization at +1.40 V in an acetonitrile solution containing 10 mM of monomer and 100 mM $LiClO_4$.[36] The polymerization charge was adjusted to 0.96 C (480 mC cm^{-2}). The polymer doped with ClO_4^- presents a film thickness of 6.8±0.6 μm. The monomeric units support average positive charges of +0.16, balanced with ClO_4^- counterions (*i.e.* 6.25 monomeric units per ClO_4^- anion).

A complete description of the procedure for the preparation of *m*PI was detailed in a previous work.[34] The molecular weights of the resulting *m*PI, which were calibrated using poly(methyl methacrylate) standards are: $M_n = 5.0 \cdot 10^3$ Da, $M_w = 1.2 \cdot 10^3$ Da and the average number of chemical repeating units per chain (*n* in Scheme 4.1-2) = 7.

Dedoping of p-doped PEDOT films.

The aim of the dedoping is to deprive the CP of the anionic dopant. For this purpose, choronopotentiograms of the p-doped PEDOT were recorded in water with 10 mM $LiClO_4$ at –1.0 mA to characterize the dedoping process. The change in the slope of the resulting potential–time profiles indicated that the dedoping of p-doped PEDOT occurs after ~135 s at a potential close to –0.8 V Figure 4.1-2(a). Accordingly, the dedoping occurs at a slow rate allowing the polymer chains to rearrange and minimize the film stress. Besides, Figure 3.1-1 (a) indicates that the reduction potential in water with 10 mM $LiClO_4$ stabilizes at around –1.40 V after ~150 s. The charge consumed during the dedoping, Q_{ddop}, in water with 10 mM $LiClO_4$ applying –1.0 mA during 150 s, once the reduction potential reached the value of –1.40 V, was –0.132 C Figure 4.1-2(b). Application of a second chronopotentiometric dedoping using the same experimental conditions, intensity and time, led to a reduction potential of –0.68 V only Figure 4.1-2 (b), indicating that such additional process does not represent a significant improvement.

Chronopotentiometric Figure 4.1-2(a,b), were used to propose the experimental conditions used for new chronoamperometric dedoping assays. Specifically, these measures were performed fixing the reduction potential at –1.10, –1.20, –1.30, –1.40, –1.50 or –1.60 V during 100 s in a 10 mM $LiClO_4$ water solution. Figure 4.1-2(c) represents the value of Q_{ddop} obtained at each of such potentials. As it can be seen, the chronoamperometric dedoping is considerably more pronounced than the chronopotentiometric one, independently of the reduction potential (*i.e.* $Q_{ddop} < –0.132$ C for all reduction potentials). In spite of this, the reduction potential has a very remarkable effect in chronoamperomperic Q_{ddop} values, which range from –0.192 C for –1.60 V to –0.264 C for –1.30 V.

According to results displayed in Figure 4.1-2, the application of a fixed potential of –1.30 V during 100 s in a 10 mM $LiClO_4$ water solution was selected as the most efficient procedure for the dedoping of p-doped PEDOT. Hereafter, this dedoping procedure is the only applied for subsequent studies.

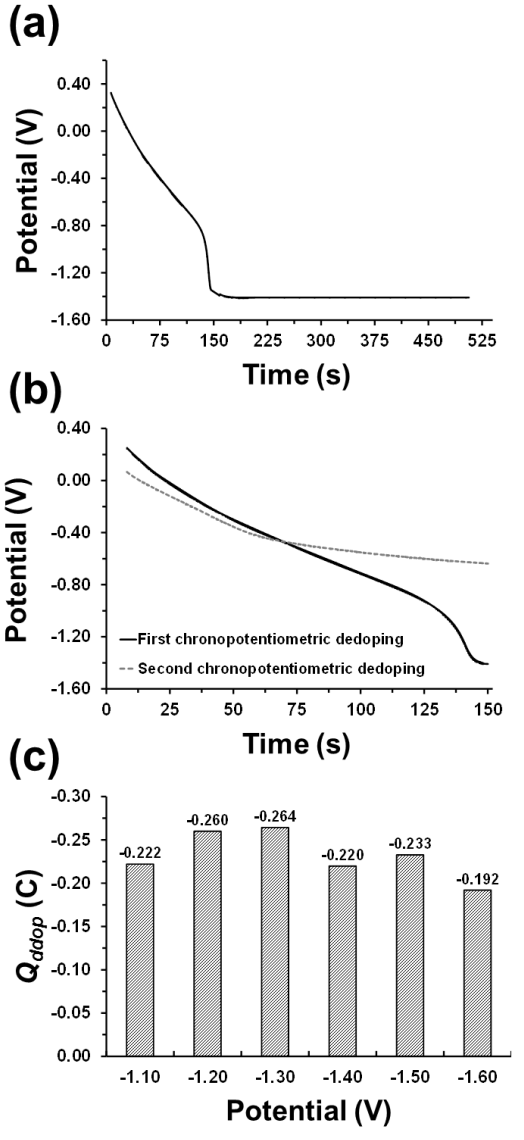

Figure 4.1-2 (a) Chronopotentiometric time-potential profile obtained for p-doped PEDOT at –1.0 mA in water with 10 mM $LiClO_4$. (b) Chronopotentiometric dedoping for p-doped PEDOT in water with 10 mM $LiClO_4$ applying –1.0 mA during 150 s two consecutive times (first and second processes). (c) Charge consumed during the chronoamperometric dedoping (Q_{ddop}, in C) at a fixed potential (from –1.10 to –1.60 V) during 100 s in a 10 mM $LiClO_4$ water solution.

The surface morphology of p-doped (as prepared) and dedoped PEDOT samples is displayed in Figure 4.1-3(a,b), respectively. Low and high resolution SEM images reflect not only the

homogeneous globular morphology typically observed for p-doped PEDOT, but also the existence of multiple and tortuous pores. The diameter of these pores, which are defined by thin sticks that connect dense clusters of polymer chains [Figure 4.1-3(a)], is variable and ranges from ~0.4 to ~2.0 μm. Application of a potential of –1.30 V results in a drastic reduction of the porosity, even though the surface retains the globular appearance [Figure 4.1-3(b)]. More specifically, the applied reduction potential induces the partial collapse of the clusters, which is probably caused by the breakage of some of the above mentioned sticks (*i.e.* the thinner ones). Consequently, the shape of pores becomes less defined and their diameter rarely exceeds ~1.1 μm. Height AFM images displayed in Figure 4.1-3(c,d) are fully consistent with SEM micrographs, evidencing that PEDOT clusters approach after the dedoping process. The roughness of the sample increases from R_q= 600-700 nm for p-doped PEDOT to R_q= 720-850 nm for the dedoped CP.

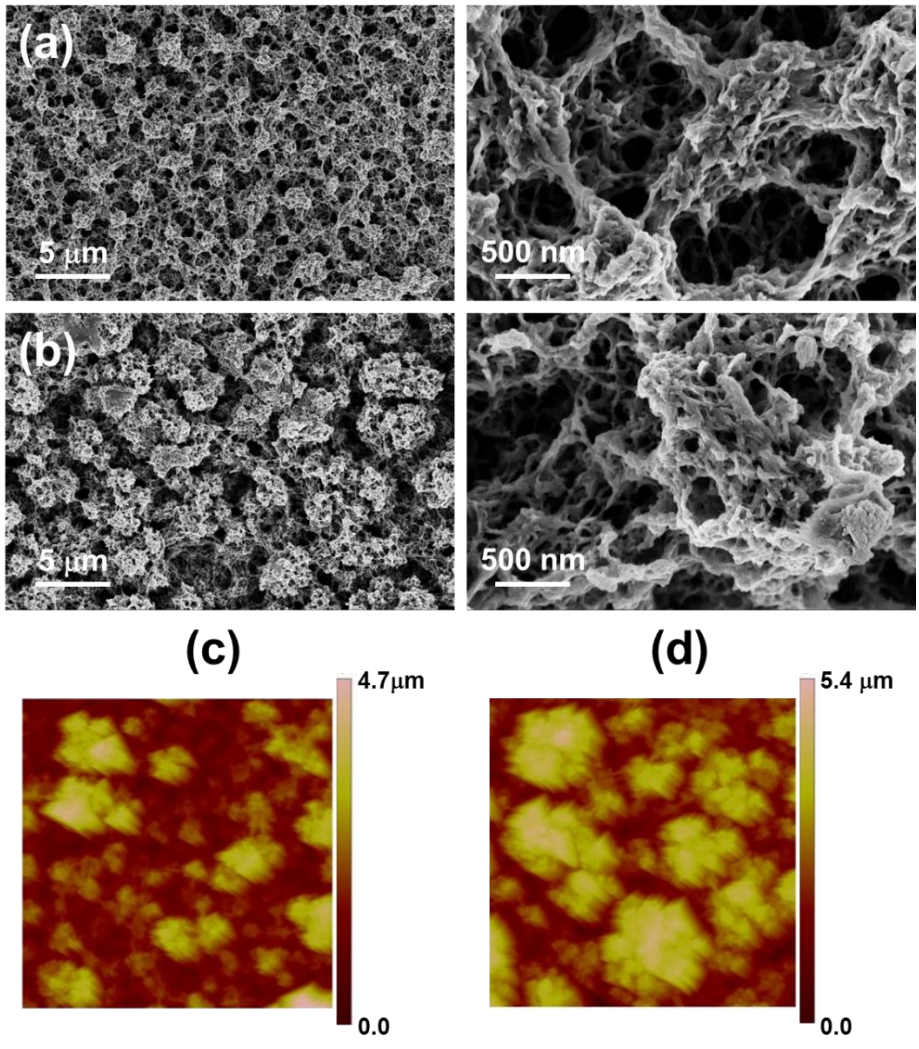

Figure 4.1-3. Low and high resolution SEM images (left and right, respectively) of: (a) p-doped PEDOT prepared in acetonitrile with 100 mM $LiClO_4$ at a constant potential of +1.40 V; and (b) Dedoped PEDOT in water with 10 mM $LiClO_4$ at a constant potential of –1.30 V. Height AFM images (5× 5 μm^2) of (c) p-doped and (d) dedoped PEDOT are also displayed.

Redoping of PEDOT films with mPI for n-doping

The aim of the redoping is to incorporate the polycation into the PEDOT matrix. This electrochemical reduction (n-doping) was performed by chronoamperometry applying a constant reduction potential. Although initially experiments were conducted using a reduction potential of –0.50 V, electrochemical assays using more negative reduction potentials proved that the doping level

depend significantly on this parameter. In order to reflect and rationalize such dependence, systematic studies were performed applying reduction potentials of –0.50, –0.70, –0.90 and –1.10 V applied during 150 s to dedoped PEDOT films in 10 mM *m*PI aqueous solutions. Additionally, control assays (blank) were performed using identical conditions but in absence of PEDOT (*i.e.* using bare steel as working electrode).

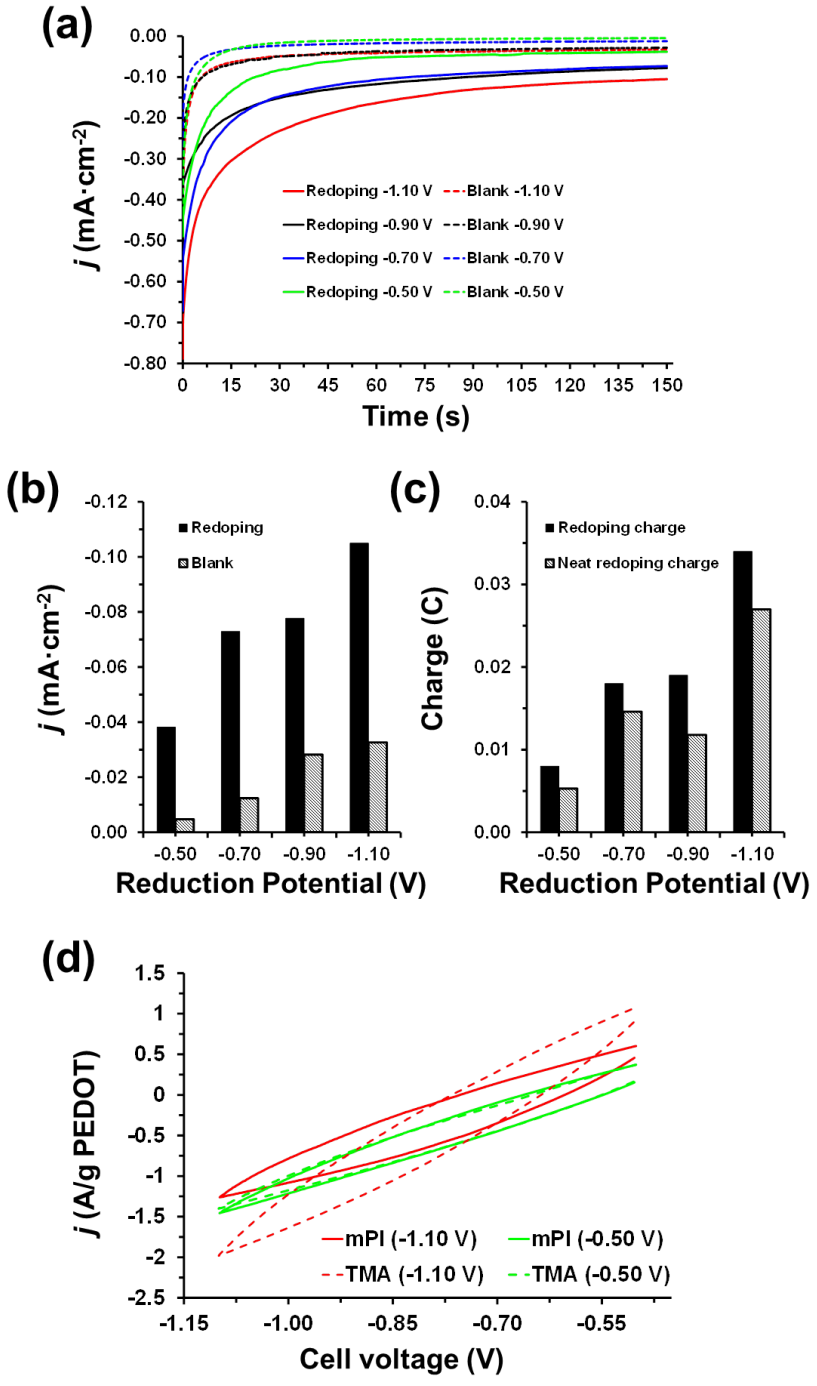

Figure 4.1-4. Chronopotentiometric time-current density (j) profiles obtained for the redoping of PEDOT films and blank assays (see text) in water with 10 mM mPI using different reduction potentials. (b) Variation of the current density reached after 150 s against the reduction potential for the redoping and blank assays. (c) Variation of the redoping charge and the neat redoping charge (Eq 1) against the reduction potential. (d) Cyclic voltammograms of PEDOT films redoped with mPI or TMA using –1.10 V and–0.50 V as reduction potential.

Chronoamperograms recorded for the different reduction potentials, which are displayed in Figure 4.1-4(a), show that the current density of n-doped PEDOT films stabilizes at a lower value when more negative is potential, evidencing that the success of the redoping process increases from –0.50 to –1.10 V. The potential also affects the blank assays, even though the current density stabilizes at values significantly higher than those reached in redoping experiments. This feature is clearly reflected in Figure 4.1-4(b), which compares the current density for the redoping and blank assays reached after 150 s.

Another important difference between the chronoamperograms recorded for redoping and blank assays is the time required by current density to reach the steady state. Independently of the reduction potential, this time is very short for blank assays since the diffusion rate of the *m*PI molecules through the electrochemical solution is very fast. In contrast, the stabilization time in redoping experiments, which is considerably higher than for the blank assays, increases with decreasing reduction potential. This behaviour evidences that the number of *m*PI molecules entering into the PEDOT film grows with decreasing reduction potential and, also, that the movement of the dopant molecules is slower into the CP matrix than in the electrochemical solution.

For each reduction potential, the neat redoping charge (Q_{rdop}^{neat}) was estimated as the difference between the chronoamperometric charge obtained for the redoped PEDOT film (Q_{rdop}) and the chronoamperometric charge derived for the corresponding blank (Q_{blank}):

$$Q_{rdop}^{neat} = Q_{rdop} - Q_{blank} \quad (1)$$

Figure 4.1-4(c) compares the values of Q_{rdop} and Q_{rdop}^{neat} for the four used reduction potentials. The value of Q_{rdop}^{neat}, which indicates the charge for PEDOT averaged by repeat unit after the incorporation of *m*PI polycations, becomes one of magnitude more negative when the reduction potential decreases to –1.10 V. The values of Q_{rdop}^{neat} were used to estimate moles of ionene repeating units (N_{mPI}) incorporated during the redoping process for each reduction potential (Table 4.1-1):

Table 4.1-1. Neat redoping charge (Q_{rdop}^{neat}; Eq 1), moles of ionene repeating units incorporated during the redoping process (N_{mPI}), Q_{ddop} is the charge consumed during the de-doping process (Q_{ddop}; Eq 3), moles of escaping from the film during the dedoping process (N_{ClO4-}), and doping level expressed as the fraction of dicationic mPI unit per EDOT unit (dl_{mPI}; Eq 5).

Reduction potential (V)	Q_{rdop}^{neat}	N_{mPI}	Q_{ddop}	N_{ClO4-}	dl_{mPI}
–0.50	-0.0110	$5.68\cdot10^{-8}$	-0.1267	$1.31\cdot10^{-6}$	0.015
–0.70	-0.0151	$7.80\cdot10^{-8}$	-0.1382	$1.43\cdot10^{-6}$	0.022
–0.90	-0.0166	$8.59\cdot10^{-8}$	-0.1345	$1.39\cdot10^{-6}$	0.021
–1.10	-0.0398	$2.06\cdot10^{-7}$	-0.1605	$1.66\cdot10^{-6}$	0.063
	Q_{rdop}^{neat}	N_{TMA}	Q_{ddop}	N_{ClO4-}	dl_{TMA}
–0.50	-0.0127	$1.32\cdot10^{-7}$	-0.0820	$8.50\cdot10^{-7}$	0.032
–1.10	-0.0272	$2.82\cdot10^{-7}$	-0.1749	$1.81\cdot10^{-6}$	0.089

$$N_{mPI} = \frac{Q_{rdop}^{neat}}{2F} \tag{2}$$

where F is the Faraday's constant and include two positive charges of every *m*PI repeat unit. The moles of EDOT repeat units incorporated to the film during the polymerization process (N_{EDOT}) and the moles of (N_{ClO4-}) escaping from the film during the dedoping process were determined using similar expressions:

$$N_{EDOT} = \frac{\left(Q_{pol} - Q_{ddop}\right)}{2F} \tag{3}$$

$$N_{ClO_4} = \frac{Q_{ddop}}{1F} \quad (4)$$

where Q_{pol} is the charge consumed during the polymerization process of p-doped PEDOT films and Q_{ddop} is the charge consumed during the dedoping process. As Q_{pol} was fixed at 0.960 C, the value derived from was equation in average for all potentials is $N_{EDOT} = 4.26 \cdot 10^{-6}$ moles of EDOT (Eq 3). The values of Q_{ddop} and N_{ClO4-} depended not only on the reduction potential (–1.30 V) but also on the structure of the sample. Average values of Q_{ddop} and N_{ClO4-} (Eq 4) for the set samples used for each redoping potential, which are relatively similar for all sets, are included in Table 4.1-1. Finally, the doping level, which expresses the fraction of *m*PI unit per EDOT unit, was derived from:

$$dl_{mPI} = \frac{N_{mPI}}{N_{EDOT}} \quad (5)$$

The values of dl_{mPI} for each reduction potential (Table 4.1-1) indicates one dicationic *m*PI unit for every ~16, ~48, ~45 and ~67 EDOT units when the reduction potential is –1.10, –0.90, –0.70 and –0.50 V, respectively. Unfortunately, the redoping process is limited by the electrolysis of water into oxygen and hydrogen gas, which occurs at –1.23 V, precluding the use of lower reduction potentials. Comparison of the cyclic voltammograms recorded for films redoped using –1.10 and –0.50 V indicates that the electrochemical activity is higher for the former than for the latter [Figure 4.1-4(d)]. The successful incorporation of *m*PI has been proved by X-ray photoelectron spectroscopy (XPS).

Table 4.1-2. Atomic percent composition (C 1s , N 1s, O 1s and S 2p) obtained by XPS for PEDOT: p-doped, dedoped, and redoped (n-doped) with mPI or TMA.

Sample	*C 1s*	*N 1s*	*O 1s*	*S 2p*
p-doped	59.2	0.0	30.2	10.6
Dedoped	63.3	0.0	25.5	11.2
n-doped TMA	64.6	0.5	23.8	11.1
n-doped *m*PI	72.8	4.9	16.3	6.0

Table 4.1-2 compares the atomic percent compositions of p-doped PEDOT, dedoped PEDOT, and PEDOT redoped with *m*PI using a potential of –1.10 V. As it can be seen, the C / S ratio (5.6) is close to the expected value (6.0) for both p-doped and dedoped PEDOT. In contrast, the O / S decreases from 2.8 (p-doped) to 2.3 (dedoped), reflecting the success of the dedoping process. The C / S and O / S ratios for PEDOT redoped with *m*PI are 12.1 and 2.7, which are far from the values expected to PEDOT, corroborating the incorporation of the dopant agent. However, the most noticeable result is the apparition of nitrogen that is due solely to the *m*PI incorporation.

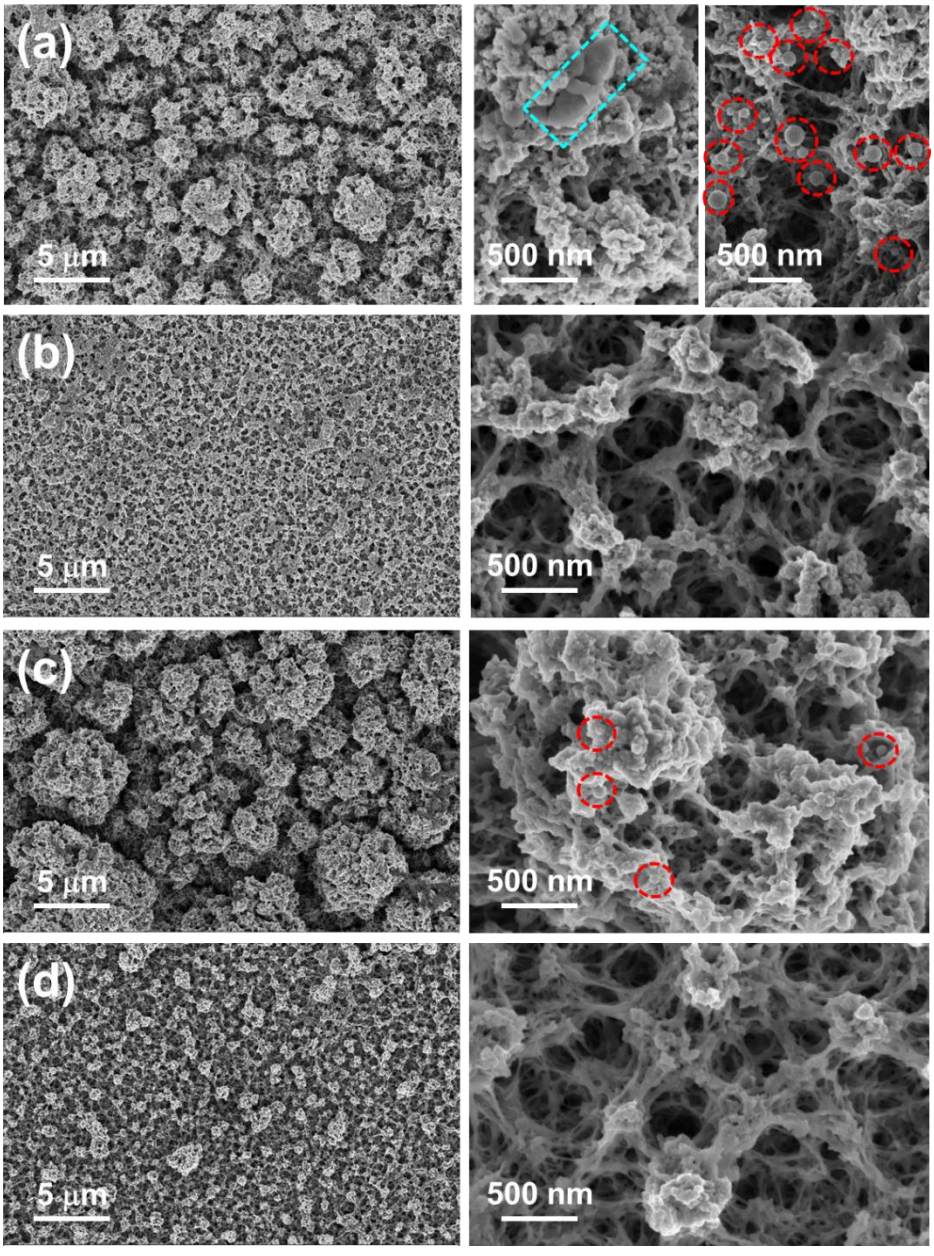

Figure 4.1-5. Low and high resolution (left and right, respectively) SEM micrographs of PEDOT films redoped with (a, b) mPI and (c, d) TMA using a reduction potential of (a, c) –1.10 V or (b, d) –0.50 V. The blue square and the red circles in (a) highlight the presence of mPI organized in ultrathin sheets (eventually observed) and nanospheres (frequently observed), respectively. Nanospheres are also detected in (c).

Figure 4.1-5 compares de surface morphology of samples redoped using –1.10 and –0.50 V reduction potentials. As it can be seen, the 1.10 V potential does not induce changes in the CP morphology [Figure 4.1-5(a)], which preserves the globular appearance and porosity of the dedoped sample [Figure 4.1-5(b)]. However, nanostructured *m*PI is clearly observed at the surface of the samples. Thus, this polycation frequently organizes in nanospheres with diameters ranging from 25 to 75 nm [Figure 4.1-5(a), right], even though ultrathin sheets are also eventually detected [Figure 4.1-5(a), middle]. These results are consistent with the relatively high doping level obtained at such potential (*i.e.* one dicationic *m*PI unit every 16 EDOT units). In opposition, the highest reduction potential (–0.50 V) severely affects the surface morphology of PEDOT films [Figure 4.1-5(b)]. Thus, CP aggregates undergo a drastic shrink, reducing their diameter more than a half. Although the porosity is retained after such shrinking process [Figure 4.1-5(b)], right), the diffusion of *m*PI chains at –0.50 V is very slow, limiting their entrance into the CP matrix (*i.e.* one dicationic mPI unit every ~67 EDOT units). In contrast, this potential is enough to expel solvent molecules and residual perchlorate anions embedded into the CP clusters, causing the observed shrinking phenomenon.

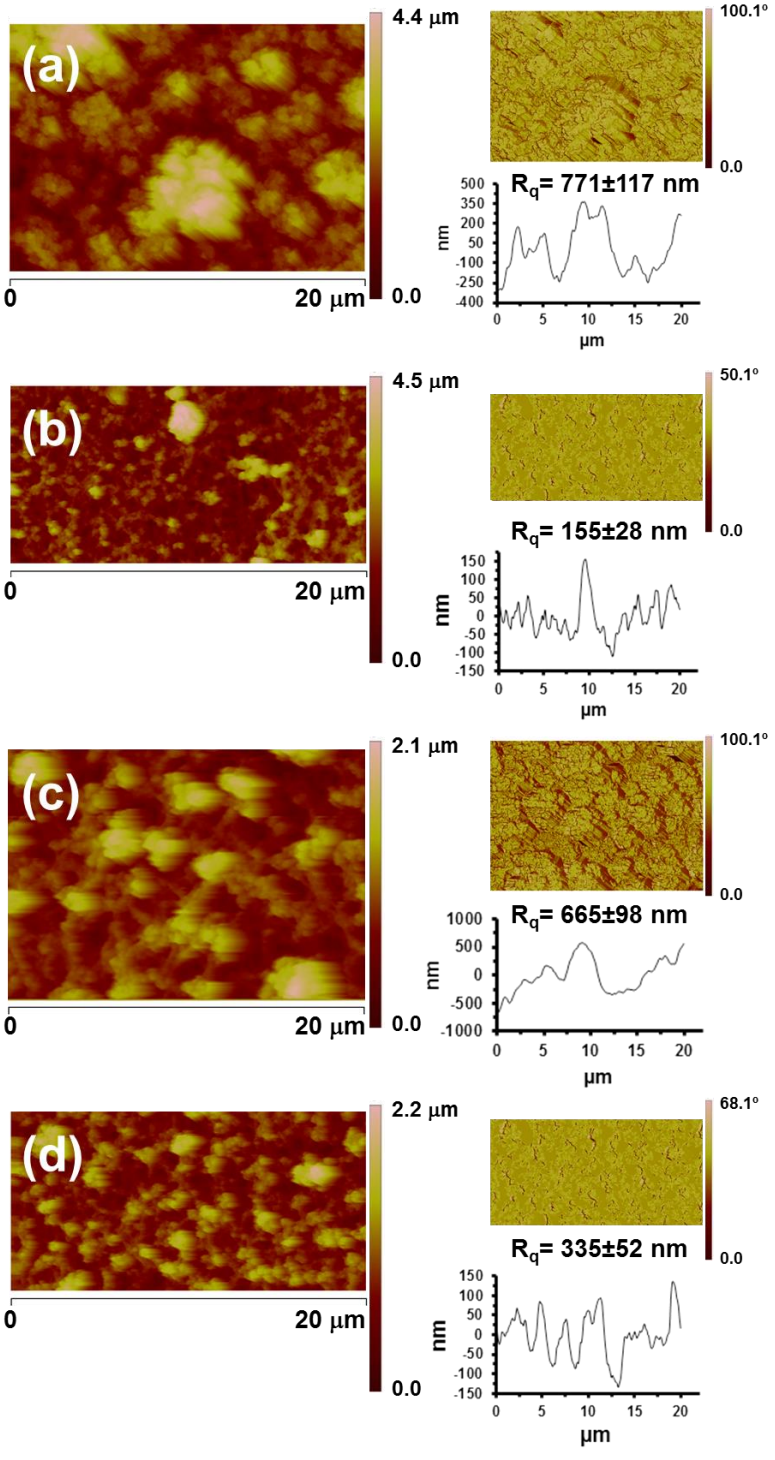

Figure 4.1-6. Height and phase (left and right, respectively) AFM images of PEDOT films redoped with (a, b) mPI and (c, d) TMA using a reduction potential of (a, c) –1.10 V or (b, d) –0.50 V. Representative cross-sectional profiles showing the topography and the Rq values are also displayed.

Height and phase AFM images [Figure 4.1-6(a,b)] corroborate SEM observations. In particular, phase imaging based on material differences, which is sensitive to surface stiffness/softness, has been used for the surface chemical mapping. Phase shifts, registered as bright and dark regions in phase images, are more abundant and contrasted for samples redoped at –1.10 V than at –0.50 V. This observation is consistent with the nanorganization of the *m*PI molecules discussed above. Indeed, the structure of n-doped samples obtained at –1.10 V is pretty similar to the nanosegregated phase distribution observed for PEDOT with PSS,[13] evidencing that polymeric dopant agents provide significant differences with respect to small dopants. Moreover, the R_q of samples obtained using –1.10 V as redoping potential is significantly higher than that of samples redoped using–0.50 V [Figure 4.1-6(a,b)].

Comparison between PEDOT n-doped with mPI and TMA

PEDOT films redoped with TMA were obtained as described in the previous subsection for *m*PI. More specifically, dedoped PEDOT films were electrochemically reduced by chronoamperometry applying a constant reduction potential of –0.50 or –1.10 V during 150 s in 10 mM TMA aqueous solutions. The successful incorporation of TMA is proved by XPS, the elemental composition of the films redoped using a potential of –1.10 V being included in Table 4.1-2. Thus, nitrogen is successfully detected in PEDOT samples redoped with TMA. The doping level, expressed as the fraction of TMA molecules per EDOT unit, was calculated using Eq 5 but replacing N_{mPI} by N_{TMA}, which corresponds to the moles of TMA incorporated during the redoping process:

$$N_{TMA} = \frac{Q_{rdop}^{neat}}{1F} \tag{6}$$

The doping level (dl_{TMA}), expressed as the fraction of TMA molecules per EDOT unit, Q_{rdop}^{neat} and N_{TMA} average values are included in Table 4.1-1. Considering that a TMA molecule and an *m*PI repeat unit involve one and two positive charges, respectively, comparison of the dl_{TMA} and dl_{mPI} indicates that the two n-dopant anions behave similarly. However, the mobility of small TMA molecules is higher than that of *m*PI chains and, therefore, the influence of the reduction potential

in dl_{TMA} is more important than in dl_{mPI}. Thus, the amount of negative charge incorporated by EDOT repeat unit is higher by more twice for TMA. More specifically, one cationic TMA molecule has been incorporated every ~31 and ~11 EDOT units when the redoping potential is –1.10 and –0.50 V, respectively.

SEM micrographs and AFM images recorded form PEDOT samples redoped with TMA [Figure 4.1-5(c,d) and Figure 4.1-6(c,d), respectively] display features similar to those discussed above for samples redoped with *m*PI [Figure 4.1-5(a,b) and Figure 4.1-6(a,b)], even though the apparition of organized nanostructures when the reduction potential is –1.10 V is much less pronounced for TMA than for *m*PI. Indeed, TMA nanospheres are not only less abundant but also smaller than *m*PI nanospheres [Figure 4.1-5(d) and Figure 4.1-5(a), respectively].

Computer simulations

Atomistic molecular dynamics (MD) simulations were performed considering 48 PEDOT and 32 *m*PI chains, each one consisting of 40 and 6 repeat units, respectively (*i.e.* 48 × 40 = 1920 EDOT repeat units and 32 × 6= 192 ionene repeat units). Although recent computational advances allow the study of relatively large polymeric systems, as the one studied in this work, their size is still limited in comparison with the experimental one. In order to overcome this limitation, the doping level of the simulated PEDOT chains has been increased with respect to that electrochemically measured (Table 4.1-1). More specifically, a charge of -1 was accounted for every five EDOT units, while a total charge of +2 was considered for each ionene repeat unit (*i.e.* the model contains one dicationic *m*PI unit for every 10 EDOT units rather than for every 16, as observed).

Computer simulations were performed considering two different models, hereafter **m1** and **m2**, which differ in the initial disposition of PEDOT and *m*PI chains. In **m1** both *m*PI and PEDOT chains were regularly arranged (*i.e.* each *m*PI chain was surrounded by three PEDOT chains), while in **m2** the polymeric chains of the two species were distributed in two groups that in turn were arranged in separated blocks.

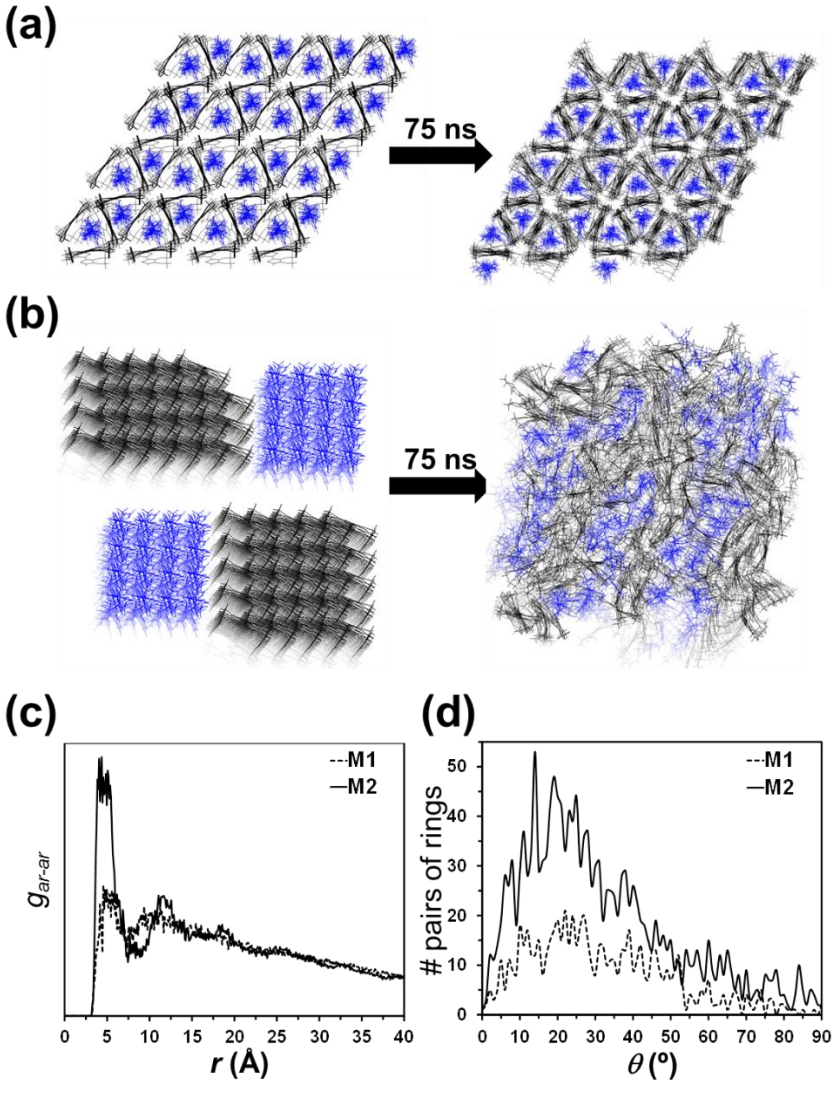

Figure 4.1-7. Initial geometry (left) and last snapshot from the productive NPT-MD trajectory (right) for (a) M1 and (b) M2 models. (c) Partial radial distribution functions for the pairs of centres of masses of aromatic rings belonging to different polymer chains for both M1 and M2. (d) Distribution of the number of pairs of interacting aromatic rings as a function of the angle θ formed by such planar rings for both M1 and M2. Only ring belonging to different polymer chains and with the centers of masses separated by ≤5.5 Å have been considered.

Figure 4.1-7(a,b) depict the starting points used for MD simulations. The density was ρ= 1.0 g cm^{-3} for both initial models, which is much lower than the experimentally determined value (see below).

After equilibration of the starting geometries, as is described in the Supplementary Information, productive trajectories of 75 ns NPT-MD were run at room temperature for both **m1** and **m2** models.

PEDOT and *m*PI chains underwent significant rearrangements during the first period of the two simulations (~15 ns), especially in **m2**, while only local conformations changes were observed during the last 25 ns. The reproduction of the experimental density is frequently used to know the level of goodness of a computer model or, if the case, to discern among different computer models. Unfortunately, both **m1** and **m2** stabilize at same density, ρ=1.44 g cm^{-3} and, therefore, no differentiation between both models is possible. However, comparison of the latter value with that of the initial models (ρ= 1.0 g cm^{-3}) indicates that polymer chains approached during the simulations (*i.e.* compression behavior). The experimental density of PEDOT samples redoped with *m*PI using a reduction potential of –1.10 V was estimated using the flotation method (see Supplementary Information). The resulting value, ρ=1.55 g cm^{-3}, differs from the theoretical predictions by 7.6% only, evidencing that, despite the artificial increase of doping level introduced in the polymeric models, MD simulations successfully capture polymer⋯polymer interactions.

The structures obtained for the two models at the end of the production trajectories are included in Figure 4.1-7(a,b). Although **m1** is enthalpically favored (*i.e.* negatively charged PEDOT chains and cationic *m*PI are individually confronted and, therefore, repulsive interactions between chains with the same charge are avoided), the preferred model is **m2**. Thus, the entropic contribution is significantly more favorable for disordered **m2** than for the highly ordered **m1**, compensating the enthalpic contribution.

m1 is dominated by electrostatic PEDOT⋯*m*PI interactions, even though π-π stacking interactions are expected to play a crucial role in **m2** where PEDOT⋯PEDOT and *m*PI⋯*m*PI interactions are more abundant. Figure 4.1-7(c) represents the partial radial distribution function for pairs of centers of masses of aromatic rings belonging to different chains, $g_{ar\text{-}ar}$. The intense and relatively broad peak centered at $r\approx$ 4.5 Å for **m2** demonstrates the importance of the π-π stacking in the stability of this model. Besides, **m2** shows two less intense peaks centered at r= 11.5 and 18.4 Å, , reflecting the local order induced by the all-*anti* conformation of the PEDOT chains. On the other hand, the peak at $r\approx$ 4.5 Å is much less intense for **m1** indicating that π-π stacking interactions between aromatic rings located at neighboring PEDOT and *m*PI chains are less abundant than in **m2** (*i.e.* the total number of π-π interactions is around 2.5 higher for **m2** than for **m1** when a cutoff distance of 5.0 Å is used). Consequently, the peaks at r > 10 Å, attributed to the polymer chains periodicity, are imperceptible or inexistent in **m1**.

The broadness of the peak identified at $r\approx$ 4.5 Å for **m2**, which extends from 3.8 to 5.3 Å [Figure 4.1-7(c)], is compatible with the co-existence of π-π stacking interactions in which the two aromatic

rings are coplanar (sandwich configuration) or perpendicular (T-shaped configuration). Previous theoretical studies based on sophisticated quantum mechanical methods evidenced that the center of masses of two interacting thiophene or benzene aromatic rings are ideally separated by ~3.7 Å and ~5.0 Å for the sandwich and T-shaped configuration, respectively.[47-49] In order to examine more exhaustively this hypothesis, the angle (θ) formed by aromatic rings involved in the π-π stacking interactions of **m1** and **m2** was evaluated. Specifically, θ was calculated for all pairs of ring belonging to different polymer chains and with the centers of masses separated by ≤ 5.5 Å. This angle is $\theta \leq 45^{o}$ for the sandwich configuration (ideally, $\theta = 0^{o}$), whereas the T-shaped configuration corresponds to angles comprised between 45º and 90º (ideally, $\theta = 90^{o}$).

The distribution of π-π stacking interactions is displayed in Figure 4.1-7(d) for both **m1** and **m2**. The two models show a clear preference towards the sandwich configuration (78%), even though θ deviates considerably from the ideal value. Thus, the two interacting rings exhibit some tilting, as is evidenced by both the broad distribution profile and the peaks appearing in the interval comprised between 15º and 30º. Similarly, the small fraction of aromatic ring interacting through the T-shaped configuration displays important distortions with respect to the ideal value of $\theta = 90^{o}$, the latter exhibiting a very low population.

Effect of the dopant in the surface wettability and the thermal stability

The very different chemical nature of *m*PI and TMA dopant anions is expected to affect the properties of the CP. In this work we have compared the influence of *t*he dopants in the wettability and the thermal stability of redoped PEDOT by measuring the contact angle (θ) in water and by TGA, respectively.

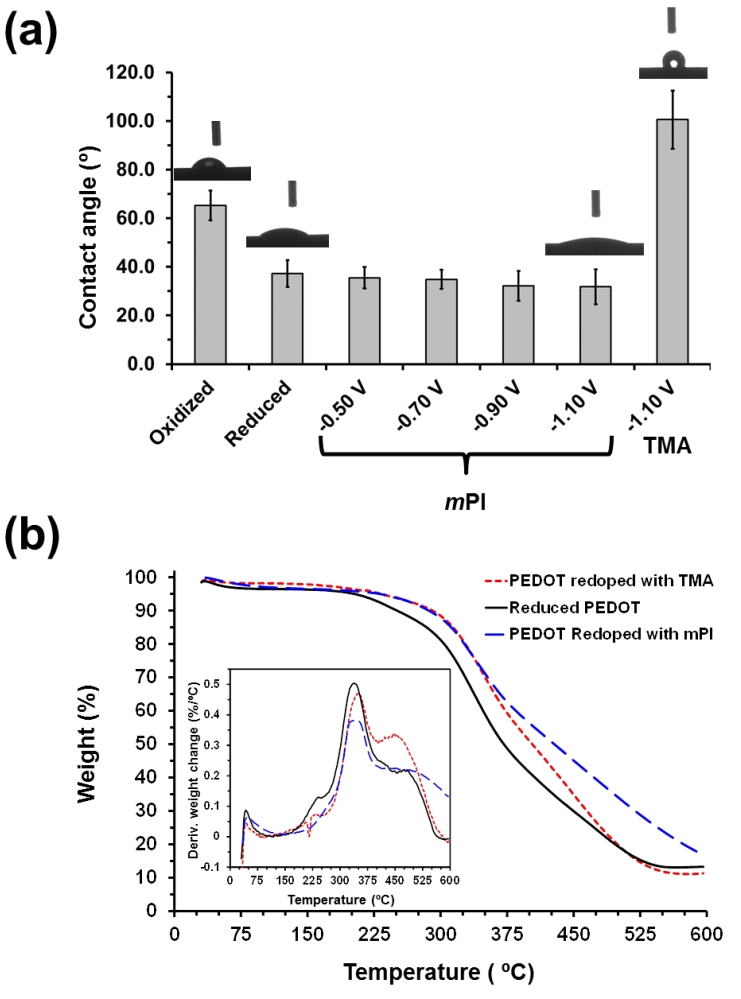

Figure 4.1-8. (a) Contact angle of water measured for oxidized (p-doped) PEDOT, PEDOT reduced by chronoamperometry at constant potential of –1.30 V, PEDOT redoped with mPI using a reduction potential of –0.50, –0.70, –0.90 and –1.10 V, and PEDOT redoped with TMA using a reduction potential of –1.10 V. (b) TGA and DTGA (inset) curves of PEDOT reduced at constant potential of –1.30 V, and PEDOT redoped with TMA or mPI using a reduction potential of –1.10 V.

Wettability is related with both surface topography, the chemical nature of the surface and the doping level. Oxidized PEDOT is a hydrophilic material with $\theta = 65^{o} \pm 6^{o}$ [Figure 4.1-8(a)], which should be attributed to the oxygen atoms of the fused dioxane ring and the positive charge delocalized through the polymer chains. Amazingly, the reduction process increases considerably the hydrophilicity of PEDOT ($\theta = 37^{o} \pm 5^{o}$). Thus, although reduced polymer chains are expected to exhibit less affinity by water than oxidized polymer chains, the drastic reduction of the surface roughness from submicrometric to nanometric scale (Figure 4.1-6) causes the opposite effect.

Re-doping with TMA results in a hydrophobic surface, $\theta = 101^{o}\pm12^{o}$, which has been attributed to the TMA nanostructures observed at the surface of the films (Figure 4c). Both the accumulated exposition of hydrophobic methyl groups arising from those superficial nanostructures and the shielding of the positively charged nitrogen atom due to the tetrahedron geometry of TMA molecules drastically reduce the affinity towards water. Besides, the surface roughness of PEDOT redoped with TMA is intermediate between those of the oxidized and reduced CP. In opposition, PEDOT films redoped with *m*PI results in hydrophilic surfaces that, independently of the redoping potential, exhibit higher affinity by water than p-doped PEDOT. Indeed, the wettability of redoped PEDOT is comparable to that of the reduced polymer. This cannot be associated to the low doping level of PEDOT redoped with *m*PI, which is comparable to that obtained with TMA (Table 4.1-1), nor to the surface roughness, which is similar to that of p-doped PEDOT (Figure 4.1-6). Indeed, the hydrophilic character of PEDOT redoped with *m*PI has been attributed to the accessibility of the polar amide groups of the polycation, which facilitate the formation of hydrogen bonding interactions with water molecules at the film/drop interface.

Thermogravimetric analyses [Figure 4.1-8(b)] reflect the significant influence of the dopant agent in the thermal stability of n-doped PEDOT. First, differential thermogravimetric analysis (DGTA) curves of dedoped and redoped PEDOT show that solvent evaporation starts at ~45º. After this, a pronounced degradation step is observed for all systems. The maximum temperature (T_{max}) for this degradation is around 15 ºC lower for dedoped PEDOT (T_{max}= 338 ºC) than for redoped PEDOT (T_{max}= 352 ºC), independently of the dopant. However, the temperature at a 50% weight loss ($T_{50\%}$) increases as follows: dedoped PEDOT ($T_{50\%}$= 371 ºC) < PEDOT redoped with TMA ($T_{50\%}$= 403 ºC) < PEDOT redoped with *m*PI ($T_{50\%}$= 427 ºC). Moreover, these differences are preserved at a 70% weight loss ($T_{70\%}$) with values of 449, 465 and 518 ºC, respectively. Overall, the profiles displayed in Figure 4.1-8(b) show that the ionene enhances the thermal stability of the n-doped CP with respect to conventional small organic molecules, like TMA. This has been attributed to the fact that PEDOT⋯*m*PI interactions are stronger than PEDOT⋯TMA due to both the polymeric nature and the presence of polar amide groups in *m*PI chains.

4.1.5. Conclusions

Our studies on the properties of redoped PEDOT have demonstrated for the first time that ionenes can be successfully used as n-dopant agents, offering an important alternative to conventional TMA and its, also small, derivatives. The highest doping level has been achieved applying a redoping

potential of –1.10 V to a PEDOT film, which was previously dedoped at a fixed potential of –1.30 V, in an aqueous solution of mPI. SEM and AFM analyses reveal some segregation between the PEDOT matrix, which retain the typical globular and porous morphology, and the ionene that organization into nanospheres and ultrathin sheets. This particular organization is consistent with results derived from atomistic MD simulations, which show that PEDOT⋯PEDOT and mPI⋯mPI interactions predominate over PEDOT⋯mPI interactions. On the other hand, the doping level achieved for PEDOT films n-doped with mPI is similar to that obtained using TMA, even though properties of the material are significantly different. More specifically, the incorporation of mPI results in a significant increment of the hydrophilicity and the thermal stability in comparison to p-doped and dedoped PEDOT, respectively. In contrast, TMA converts the film into hydrophobic and the thermal stability is intermediate between those of films dedoped and redoped with mPI. Overall, these results indicate that redoping with ionenes can be a successful strategy to produce n-doped PEDOT electrodes with properties very different from those achieved using small organic cations.

4.1.6. References

(1) Lei, C.; Wilson, P; Lekakou, C. Effect of Poly(3,4-Ethylenedioxythiophene) (PEDOT) in Carbon-Based Composite Electrodes for Electrochemical Supercapacitors. *J. Power Sources*. **2011**, *196* (18), 7823–7827.

(2) Ryu, K. S.; Lee, Y. G.; Hong, Y. S.; Park, Y.J.; Wu, X. L.; Kim, K. M.; Kang, M. G.; Park, N. G.; Chang, S. H. Poly(Ethylenedioxythiophene) (PEDOT) as Polymer Electrode in Redox Supercapacitor. *Electrochim. Acta.* **2004**, *50* (2-3), 843–847.

(3) Groenendaal, L. B.; Jonas, F.; Freitag, D.; Pielartzik, H.; Reynolds, J. R. Poly(3,4-ethylenedioxythiophene) and its Derivatives: Past, Present, and Future. *Adv. Mater.* **2000**, *12* (7), 481–494.

(4) Aradilla, D.; Estrany, F.; Alemán, C. Symmetric Supercapacitors Based on Multilayers of Conducting Polymers. *J. Phys. Chem. C*. **2011**, *115* (16), 8430–8438.

(5) Wei, Q.; Mukaida, M.; Kirihara, K.; Naitoh, Y.; Ishida, T. Recent Progress on PEDOT-Based Thermoelectric Materials. *Materials*, **2015**, *8* (2), 732−750.

(6) Poater, J.; Casanovas, J.; Solà, M.; Alemán, C. Examining the Planarity of Poly(3,4-ethylenedioxythiophene): Consideration of Self-Rigidification, Electronic, and Geometric Effects. *J. Phys. Chem. A*. **2010**, *114* (2), 1023–1028.

(7) Plieth, W.; Bund, A.; Rammelt, U.; Neudeck, S. and Duc, L. M. The Role of Ion and Solvent Transport during the Redox Process of Conducting Polymers. *Electrochim. Acta*. **2006**, *51* (11), 2366−2372.

(8) Ocampo, C.; Oliver, R.; Armelin, E.; Alemán, C.; Estrany, F. Electrochemical Synthesis of Poly(3,4-ethylenedioxythiophene) on Steel Electrodes: Properties and Characterization. *J. Polym. Res.* **2006**, *13* (3), 193–200.

(9) Bund, A.; Neudeck, S. Effect of the Solvent and the Anion on the Doping/Dedoping Behavior of Poly(3,4-ethylenedioxythiophene) Films Studied with the Electrochemical Quartz Microbalance. *J. Phys. Chem. B*. **2004**, *108* (46), 17845−17850.

(10) Li, C.; Imae, T. Electrochemical and Optical Properties of the Poly(3,4-ethylenedioxythiophene) Film Electropolymerized in an Aqueous Sodium Dodecyl Sulfate and Lithium Tetrafluoroborate Medium. *Macromolecules*. **2004**, *37* (7), 2411−2416.

(11) Huang, J.; Miller, P. F.; Wilson, J. S.; de Mello, A. J.; de Mello, J. C.; Bradley, D. D. Investigation of the Effects of Doping and Post-Deposition Treatments on the Conductivity, Morphology, and Work Function of Poly(3,4-ethylenedioxythiophene)/Poly(styrene sulfonate) Films. *Adv. Funct. Mater.* **2005**, 15 (2), 290−296.

(12) Nardes, A. M.; Kemerink, M.; De Kok, M.; Vinken, E.; Maturova, K.; Janssen, R.. Conductivity, Work Function, and Environmental Stability of PEDOT: PSS Thin Films Treated with Sorbitol. *Org. Electron.* **2008**, *9* (5), 727−734.

(13) Lang, U.; Naujoks, N.; Dual, J. Mechanical Characterization of PEDOT: PSS Thin Films. *Synth. Met.* **2009**, *159* (5-6), 473−479.

(14) Stöcker, T.; Köhler, A.; Moos. R. Why Does the Electrical Conductivity in PEDOT: PSS Decrease with PSS Content? A Study Combining Thermoelectric Measurements with Impedance Spectroscopy. *J. Polym. Sci. Part B: Polym. Phys.* **2012**, *50* (14), 976−983.

(15) Kuş, M.; Okur, S. Electrical Characterization of PEDOT: PSS Beyond Humidity Saturation. *Sens. Actuators B*. **2009**, *143* (1), 177−181.

(16) Jiang, Y.; Luo, B.; Jiang, F.; Jiang, F.; Fuentes-Hernandez, C.; Liu, T.; Mao, L.; Xiong, S.; Li, Z.; Wang, T. Efficient Colorful Perovskite Solar Cells Using a Top Polymer Electrode Simultaneously as Spectrally Selective Antireflection Coating. *Nano Lett.* **2016**, *16* (12), 7829−7835.

(17) Tong, J.; Xiong, S.; Zhou, Y.; Mao, L.; Min, X.; Li, Z.; Jiang, F.; Meng, W.; Qin, F.; Liu, T. Flexible All-Solution-Processed All-Plastic Multijunction Solar Cells for Powering Electronic Devices. *Mater. Horiz.* **2016**, *3* (5), 452−459.

(18) Okuzaki, H.; Kuwabara, T.; Funasaka, K.; Saido, T. Humidity-Sensitive Polypyrrole Films for Electro-Active Polymer Actuators. *Adv. Funct. Mater.* **2013**, *23* (36), 4400−4407.

(19) Taccola, S.; Greco, F.; Sinibaldi, E.; Mondini, A.; Mazzolai, B.; Mattoli, V. Toward a New Generation of Electrically Controllable Hygromorphic Soft Actuators. *Adv. Mater.* **2015**, *27* (10), 1668−1675.

(20) Li, Y.; Liu, M.; Li, Y.; Yuan, K.; Xu, L.; Yu, W.; Chen, R.; Qiu, X.; Yip, H.-L. Poly(3,4-Ethylenedioxythiophene): Methylnaphthalene Sulfonate Formaldehyde Condensate: The Effect of Work Function and Structural Homogeneity on Hole Injection/Extraction Properties. *Adv. Energy Mater*. **2017**, *7* (6), 1601499.

(21) Pei, Q.B.; Zuccarello, G.; Ahlskog, M.; Inganäs, O. Electrochromic and Highly Stable Poly(3,4-Ethylenedioxythiophene) Switches Between Opaque Blue-Black and Transparent Sky Blue. *Polymer*. **1994**, *35* (7), 1347−1351.

(22) Kvarnström, C.; Neugebauer, H.; Ivaska, A.; Sariciftci, N. S. Vibrational Signatures of Electrochemical P- and N-Doping of Poly(3,4-Ethylenedioxythiophene) Films: an In Situ Attenuated Total Reflection Fourier Transform Infrared (ATR-FTIR) Study. *J. Mol. Struct.* **2000**, *521* (1-3), 271−277.

(23) Ahonen, H. J.; Lukkari, J.; Kankare, J. n- and p-Doped Poly(3,4-ethylenedioxythiophene): Two Electronically Conducting States of the Polymer. *Macromolecules*. **2000**, *33* (18), 6787−6793.

(24) Skompska, M.; Mieczkowski, J.; Holze, R.; Heinze, J. In Situ Conductance Studies of p- and n-Doping of Poly(3,4-dialkoxythiophenes). *Electroanal. Chem.*, **2005**, *577* (1), 9−17.

(25) Hillman, A. R.; Daisley, S. J.;Bruckenstein, S. Ion and Solvent Transfers and Trapping Phenomena during n-Doping of PEDOT films. *Electrochim. Acta.* **2008**, *53* (11), 3763–3771.

(26) Gustafsson, H.; Kwarnström, C.; Ivaska, A. Comparative Study of n-Doping and p-Doping of Poly(3,4-Ethylenedioxythiophene) Electrosynthesised on Aluminium. *Thin Solid Films*. **2008**, *517* (2), 474–478.

(27) Sandoval, A. P.; Feliu, J. M.; Torresi, R.; Suárez, M. F. Electrochemical Properties of Poly(3,4-ethylenedioxythiophene) Grown on Pt (111) in Imidazolium Ionic Liquids. *RSC Adv.* **2014**, *4* (7), 3383–3391.

(28) Pokhodenko, V. D.; Krylov, V. A.; Konoshchuk, N. V. Effect of the Electrolyte Nature on the Electrochemical Doping of Poly-3-Phenylthiophene. *Synth. Met.* **1999**, 99 (2), 91−95.

(29) Pokhodenko, V. D.; Krylov, V. A. Effect of Electrolyte Nature on the Electrochemical Synthesis and Doping of Polyaniline and Poly-3-Phenylthiopene. *Synth. Met.* **1991**, *41* (1-2), 533−536.

(30) Mastragostino, M.; Soddu, L. Electrochemical Characterization of "N" Doped Polyheterocyclic Conducting Polymers—I. Polybithiophene. *Electrochim. Acta.* **1990**, *35* (2), 463−466.

(31) Jaeger, W.; Bohrisch, J.; Laschewsky, A. Synthetic Polymers with Quaternary Nitrogen Atoms—Synthesis and Structure of the Most Used Type of Cationic Polyelectrolytes. *Prog. Polym. Sci.* **2010**, *35* (5), 511−577.

(32) Oha, J. K.; Drumright, R.; Siegwart, D. J.; Matyjaszewski, K. The Development of Microgels/Nanogels for Drug Delivery Applications. *Prog. Polym. Sci.* **2008**, *33* (4), 448−477.

(33) Tant, M. R.; Mauritz, K. A.; Wilkes, G. L. Ionomers: Synthesis, Structure, Properties, and Applications, Blackie Academic and Professional, London, **1997**.

(34) Bachl, J.; Zanuy, D.; López-Pérez, D. E.; Revilla-López, G.; Cativiela, C.; Alemán, C.; Díaz-Díaz, D. Synergistic Computational-Experimental Approach to Improve Ionene Polymer-Based Functional Hydrogels. *Adv. Funct. Mater.* **2014**, *24* (31), 4893−4904.

(35) Bachl, J.; Bertran, O.; Mayr, J. ; Alemán, C.; Díaz-Díaz, D. Aromatic Ionene Topology and Counterion-Tuned Gelation of Acidic Aqueous Solutions. *Soft Matter*. **2017**, *13* (16), 3031−3041.

(36) Ocampo, C.; Oliver, R.; Armelin, E.; Alemán C.; Estrany, F. Electrochemical Synthesis of Poly(3,4-ethylenedioxythiophene) on Steel Electrodes: Properties and Characterization. *J. Polym. Res.*, **2006**, *13* (3), 193−200.

(37) Aradilla, D.; Estrany, F.; Armelin, E.; Alemán, C. Morphology and Growing of Nanometric Multilayered Films Formed by Alternated Layers of Poly(3,4-Ethylenedioxythiophene) and Poly(N-Methylpyrrole). *Thin Solid Films*. **2010**, *518* (15), 4203−4210.

(38) Kale, L.; Skeel, R.; Bhandarkar, M.; Brunner, R.; Gursoy, A.; Krawtz, N.; Phillips, J.; Shinozaki, A.; Varadarajan, K.; Schulten, K. J. NAMD2: Greater Scalability for Parallel Molecular Dynamics. *Comput. Phys.* **1999**, *151* (1), 283−312.

(39) Cornell, W. D.; Cieplak, P.; Bayly, C. I.; Gould, I. R.; Merz, K. M.: Ferguson, D. M.; Spellmeyer, D. C.; Fox, T.; Cadwell, J. W.; Kollman, P. A. A Second Generation Force Field for the Simulation of Proteins, Nucleic Acids, and Organic Molecules. *J. Am. Chem. Soc.* **1995**, *117* (19), 5179−5197.

(40) Zanuy, D.; Alemán, C. Resolving the Subnanometric Structure of Ultrathin Films of Poly(3,4-ethylenedioxythiophene) on Steel Surfaces: A Molecular Modeling Approach. *Soft Matter*. **2013**, *9* (48), 11634−11644.

(41) Baily, C. I.; Cieplak, P.; Cornell, W.; Kollman, P. A. A Well-Behaved Electrostatic Potential Based Method Using Charge Restraints for Deriving Atomic Charges: The RESP Model. *J. Phys. Chem.* **1993**, *97* (40), 10269-10280.

(42) Phillips, J. C.; Braun, R.; Wang, W.; Gumbart, J.; Tajkhorshid, E.; Villa, E.; Chipot, C.; Skeel, R. D.; Kale, L.; Schulten, K. Scalable Molecular Dynamics with NAMD. *J. Comput. Chem.* **2005**, *26* (16), 1781−1802.

(43) Andersen, H. C. Rattle: A "Velocity" Version of the Shake Algorithm for Molecular Dynamics Calculations. *J. Comput. Phys.* **1983**, *52* (1), 24−34.

(44) Darden, T.; York, D.; Pedersen, L. Particle Mesh Ewald: an N·Log(N) Method for Ewald Sums in Large Systems. *J. Chem. Phys.***1993**, *98* (12), 10089−10092.

(45) Duan, Y.; Wu, C.; Chowdhury, S.; Lee, M. C.; Xiong, G.; Zhang, W.; Yang, R.; Cieplak, P.; Luo, R.; Lee, T. et al. A Point-Charge Force Field for Molecular Mechanics Simulations of Proteins Based on Condensed-Phase Quantum Mechanical Calculations. *J. Comput. Chem.* **2003**, *24* (16), 1999−2012.

(46) Martyna, G. J.; Tobia, D. L.; Klein, M. L. Constant Pressure Molecular Dynamics Algorithms. *J. Chem. Phys.* **1994**, *101* (5), 4177−4189.

(47) Tsuzuki, S.; Honda, K.; Uchimaru, T.; Mikami, M.; Tanabe, K. Origin of Attraction and Directionality of the π/π Interaction: Model Chemistry Calculations of Benzene Dimer Interaction. *J. Am. Chem. Soc.* **2002**, *124* (1), 104−112.

(48) F. Rodriguez-Ropero, J. Casanovas; C. Alemán. Ab Initio Calculations on π-Stacked Thiophene Dimer, Trimer, and Tetramer: Structure, Interaction Energy, Cooperative Effects, and Intermolecular Electronic Parameters. *J. Comput. Chem.* **2008**, *29* (1), 69−78.

(49) Tsuzuki, S.; Honda, K.; Azumi, R. Model Chemistry Calculations of Thiophene Dimer Interactions: Origin of π-Stacking. *J. Am. Chem. Soc.* **2002**, *124* (41), 12200−12209.

4.2. Isomeric Cationic Ionene as n-Dopant Agents of Poly(3,4-ethylenedioxythiophene) for *In Situ* Gelation.

4.2.1. Abstract

Three isomeric ionene polymers containing DABCO and *N*,*N*'-(*x*-phenylene)dibezamide (*x*= *ortho*- / *meta*- / *para*-) linkages have been used as dopant agents to produce n-doped PEDOT electrodes by reducing already dedoped conducting polymer (CP) films. This work focuses on the influence of the ionene topology in both the properties of n-doped PEDOT:ionene electrodes and the success of the *in situ* thermal gelation of the ionene inside the CP matrix. The highest doping level is reached for the *para*-isomeric ionene-containing electrode, even though the content of *ortho*- and *meta*-topomers into the corresponding n-doped PEDO:ionene electrodes is greater. Thus, many of the incorporated ionene units are not directly interacting with CP chains and, therefore, do not play an active role as n-dopant agent but they are crucial for the *in situ* formation of ionene hydrogels. The effect of the ionene topology is practically inexistent in properties like the *SC* and wettability of PEDOT:ionene films, it is small but non-negligible in the electrochemical and thermal stability. In contrast, the surface morphology, topography, and distribution of dopant molecules significantly depend on the ionene topology. *In situ* thermal gelation was successful in PEDOT films n-doped with the *ortho*- and *para*-topomers PEDOT, even though this assembly process was much faster for the former than for the latter. The gelation considerably improved the mechanical response of electropolymerized PEDOT film, which was practically non-existent before it. Molecular dynamics simulations prove that the strength and abundance of PEDOT⋯ionene specific interactions (*i.e.* π-π stacking, N–H⋯S hydrogen bonds and both N^+⋯O and N^+⋯S interactions) are higher for the *meta*-isomeric ionene, for which the *in situ* gelation was not achieved, than for the *ortho*- and *para*-ones

4.2.2. Introduction

Cationic polyelectrolytes bearing quaternary ammonium in the backbone constitute an important group of highly charged polymers, named ionenes, with potential uses in the biomedical[1-3] and catalytic applications.[4-7] The synthesis of new ionene polymers (Scheme 4.2-1) containing DABCO and N,N'-(*x*-phenylene)dibezamide (*x*= *ortho*- / *meta*- / *para*-) was described and their gelation capacity in aqueous media was reported by some of us.[8,9] It was found that the topology of this

polymers plays a fundamental role in their self-assembly properties in pure water[8] and in aqueous solutions with different acidic pH and ionic strength.[9] Specifically, the properties of hydrogels formed by the *ortho*-ionene (**1**) were superior to those of the *meta*- and *para*-isomeric analogues (**2** and **3**, respectively) in all cases.

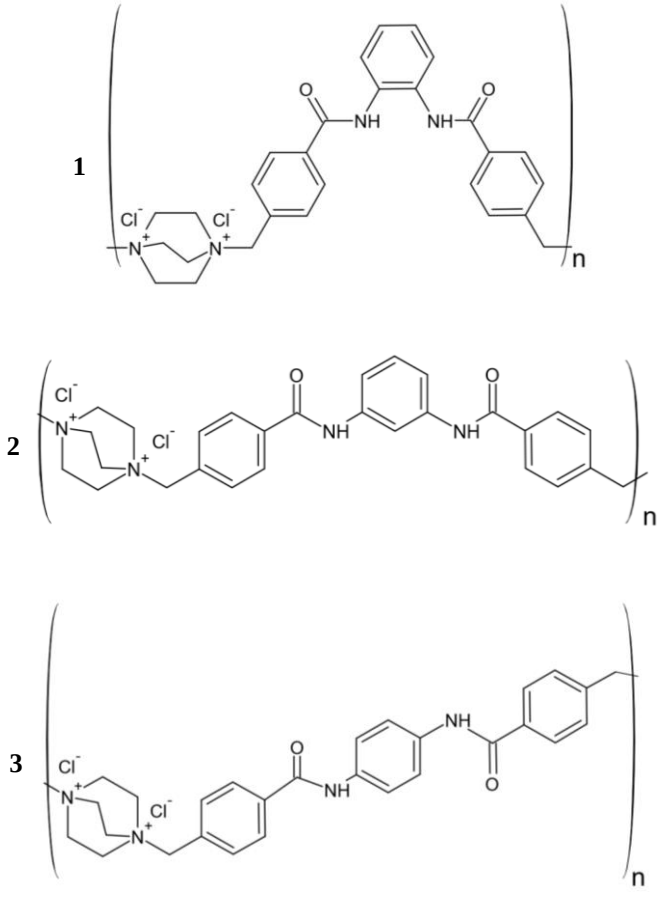

Scheme 4.2-1. Structures of topologically different DABCO-containing ionene polymers 1. ortho, 2. meta and 3. para-ionene.

In this work we focus our interest on the use of ionenes for applications related with energy storage. More specifically, we put our focus on the preparation of capacitive n-doped electrodes using ionenes as polycationic dopants of PEDOT, an important CPs frequently employed for the fabrication of supercapacitors,[10-15] Although the literature about p-doped PEDOT electrodes prepared using polyanionic dopants, as for example PSS, is very abundant,[16-22] the number of studies on n-doped PEDOT is very scarce.[23-26] Moreover, these studies were focussed on the spectroscopic,

electrical and electrochemical properties of negatively charged PEDOT prepared using very small tetra-alkylammonium cations as electrolyte, as for example TMA.[23-25]

In a very recent study we considered a cationic polyelectrolyte as n-dopant agent of PEDOT.[26] Specifically, the electrochemical conditions required for the n-redoping of PEDOT films, previously dedoped, using **2** as reducing agent, were examined. The advantages and disadvantages of **2** as n-dopant agent with respect to conventional TMA were deeply analysed and discussed. However, the use of ionenes with hydrogel-forming capability, as **1** and **3**, as n-dopant agents has not been attempted until now. In this work, we investigate the abilities of the three different DABCO-containing ionenes as reducing agents by comparing the properties of the resulting n-doped PEDOT films, hereafter denoted PEDOT:**1**, PEDOT:**2** and PEDOT:**3**, respectively. Discussion of the results has been focused on the influence of the ionene topology in the preparation and properties of n-doped PEDOT. Furthermore, the challenging hydrogelation of the ionenes once incorporated into the PEDOT matrix has been attempted considering thermally-induced aggregation phenomena in acidic conditions. The effects of such *in situ* hydrogelation on the properties of the films have been experimentally evaluated, while the impact of the gelator-topology in PEDOT⋯ionene interactions have been understood through computational MD simulations.

4.2.3. Experimental Section

Materials

EDOT and acetonitrile of analytical reagent grade were purchased from Aldrich. TMA; 98% was purchased from Across. Anhydrous $LiClO_4$, analytical reagent grade, from Aldrich, was stored in an oven at 80 ºC before using it in the electrochemical trials. *Orto*-, *meta*-and *para*-phenylenediamine, 4-(chloromethyl)benzoyl chloride and DABCO were purchased from TCI Europe.

Preparation of PEDOT films

Oxidized PEDOT films were prepared by CA under a constant potential of +1.40 V. Electrochemical experiments were conducted on a PGSTAT204 AUTOLAB potentiostat–galvanostat connected to a PC computer controlled through the NOVA 1.6 software using a three-electrode two-compartment

cell under nitrogen atmosphere at 25 ºC. The cell was filled with 10 mL of a 10 mM monomer solution in acetonitrile with 100 mM $LiClO_4$. Steel AISI 316 sheets with an area of 1 cm^2 and 2 cm^2 were employed as working and counter electrodes, respectively. Before each trial, electrodes were cleaned with acetone and dried in a nitrogen-flow. The reference electrode was an Ag|AgCl electrode containing a KCl saturated aqueous solution (E^o = 0.222 V *vs.* standard hydrogen electrode at 25 ºC), which was connected to the working compartment through a salt bridge containing the electrolyte solution.

The polymerization time was adjusted to obtain PEDOT electrodes with a polymerization charge of 0.960 C (480 mC cm^{-2}). The mass of PEDOT deposited onto the working electrode was determined as the weight difference between coated and uncoated steel sheets using a CPA26P Sartorius analytical microbalance with a precision of 10^{-6} g. The exact amount of electrochemically polymerized PEDOT onto the electrode was m_{pol} = 0.84 ± 0.13 mg.

Preparation of ionenes 1-3

1-3 were synthesized as previously reported[26] via a two-step reaction sequence. Briefly, the first step consisted in the amidation of *x*-phenylenediamine (*x*= *ortho-* / *meta-* / *para-*) with 4-(chloromethyl)benzoyl chloride in the presence of Et_3N in CH_2Cl_2 to afford the corresponding bis-benzamide monomer upon recrystallization (87-96% yields). Subsequent step-growth copolymerization with DABCO under equimolar conditions in DMF at 80 ºC yielded the desired polymers within 3 days (69-98% yields) after a simple filtration, washing and drying protocol. ^{1}H-NMR (D_2O, 300 MHz) δ (ppm) = 8.00–7.18 (m, 6H), 4.44 (s, 1H), 3.91 (s, 4H), 3.34 (d, *J* = 6.6 Hz, 2H), 3.05 (d, *J* = 6.2 Hz, 2H). In order to achieve adequate solubility and mobility for GPC/SEC, counteranion exchange of chloride by bis(trifluoromethanesulfonyl)amide (TFSA) anions was carried out using LiTFSA in hot water. SEC data were obtained using a YL GPC instrument equipped with a refractive index detector (temperature of column oven = 50-60 ºC; eluent = DMF including 30 mM of LiTFSA; flow rate = 0.5 mL min^{-1}). Solution of the sample was filtered through 0.2 mm filter before injection into the 10 mm column. Calibration was carried out using poly(methyl methacrylate) standards.

Dedoping and redoping assays

Dedoping and redoping assays were performed using the equipment, cell and electrodes described above. Dedoping of electropolymerized p-doped PEDOT was carried out applying a fixed potential of –1.30 V during 145 s in a 10 mM $LiClO_4$ water solution, while redoping experiments were conducted using aqueous solutions with 10 mM ionene (**1**, **2** and **3**) or 10 mM TMA and applying a reduction potential of –0.50, –0.70, –0.90 or –1.10 V during 150 s. After redoping experiments, PEDOT films were submerged one time in acetonitrile to clean n-dopant molecules from the surface (*i.e.* removal of ionene molecules non-electrostatically bounded to the polarons and bipolarons of PEDOT). In all cases, samples were softly washed with the solvent of the solution before the CV assays.

X-ray photoelectron spectroscopy (XPS)

XPS analyses were performed in a SPECS system equipped with a high-intensity twin-anode X-ray source XR50 of Mg/Al (1253 eV/1487 eV) operating at 150 W, placed perpendicular to the analyzer axis, and using a Phoibos 150 MCD-9 XP detector. The X-ray spot size was 650 µm. The pass energy was set to 25 and 0.1 eV for the survey and the narrow scans, respectively. Charge compensation was achieved with a combination of electron and argon ion flood guns. The energy and emission current of the electrons were 4 eV and 0.35 mA, respectively. For the argon gun, the energy and the emission current were 0 eV and 0.1 mA, respectively. The spectra were recorded with pass energy of 25 eV in 0.1 eV steps at a pressure below 5×10^{-9} mbar. These standard conditions of charge compensation resulted in a negative but perfectly uniform static charge. The C 1s peak was used as an internal reference with a binding energy of 284.8 eV. High-resolution XPS spectra were acquired by Gaussian–Lorentzian curve fitting after s-shape background subtraction. The surface composition was determined using the manufacturer's sensitivity factors.

Raman spectroscopy

Samples were characterized by micro-Raman spectroscopy using a commercial Renishaw inVia Qontor confocal Raman microscope. The Raman setup consists of a laser (at 785 nm with a nominal 100 mW output power) directed through a microscope (specially adapted Leica DM2700 M microscope) to the sample after which the scattered light is collected and directed to a spectrometer

with a 1200 lines mm^{-1} grating. The exposure time was 10 s, the laser power was adjusted to 1% of its nominal output power and each spectrum was collected with 3 accumulations.

Specific capacitance

The *SC* (in Fg^{-1} referred to the mass of PEDOT) of the active materials in the electrode was calculated as:

$$SC = \frac{Q}{\Delta V m} \quad (1)$$

where *Q* is voltammetric charge, which is determined by integrating either the oxidative or the reductive parts of the cyclic voltammogram curve, ΔV is the potential window and *m* is the mass of PEDOT on the surface of the working electrode. The latter is derived from the productivity current and polymerization charge.[27]

Thermal stability

The thermal stability was studied by TGA at a heating rate of 20 ºC min^{-1} (sample weight *ca.* 5 mg) with a Q50 thermogravimetric analyzer of TA Instruments (New Castle, DE, USA) and under a flow of dry nitrogen. Test temperatures ranged from 30 to 600 ºC.

Wettability

Measurements were carried out using the sessile drop method at room temperature on an OCA 15EC with SCA20 software (Data-Physics Instruments GmbH, Filderstadt, Germany). The solvent used for these experiments was deionized water, contact angle being determined for the first drop. For measurements, the sessile drop was gently put on the surface of sample discs using a micrometric syringe with a proper metallic needle (Hamilton 500 µL). The ellipse method was used to fit a mathematical function to the measured drop contour. This procedure consists on approximate the drop contour to the line of an ellipse, deviations from the true drop shape being in the range of a few

percent. The ellipse method provides accurate measure of the contact angle and holds the advantage that it is extremely fast. For each sample, no less than fifteen drops were examined.

Atomic Force Microscopy

AFM images were obtained with a Molecular Imaging PicoSPM using a NanoScope IV controller under ambient conditions. The tapping mode AFM was operated at constant deflection. The row scanning frequency was set to 1 Hz. AFM measurements were performed on various parts of the films, which provided reproducible images similar to those displayed in this work. The statistical application of the NanoScope Analysis software was used to determine the R_q, which is the average height deviation taken from the mean data plane.

Scanning Electron Microscopy

SEM studies were performed to examine the surface morphology of PEDOT:ionene films. Dried samples were placed in a Focussed Ion Beam Zeis Neon 40 scanning electron microscope operating at 3 kV, equipped with an EDX spectroscopy system.

Computer simulations

MD trajectories were conducted using the scalable computer program NAMD 2.9.[28] The energy was calculated using the AMBER all-atom force-field.[29] All parameters, including the equilibrium parameters and the partial charges of the $EDOT^{-0.2}$ repeating unit, were taken from previous studies in which parameters compatible with the AMBER force-field were developed.[26,30]

Each of the three simulated systems (**m1**, **m2** and **m3**, which are described in the main text) was subjected to 20000 steps of energy minimization (Newton Raphson method) before any MD trajectory was run in order to relax conformational and structural tension. The temperature and pressure of each model were equilibrated by applying a two-step process, which was repeated ten times consecutively. The first step consisted on an NVT-MD simulation at 298 K for 0.5 ns. The resulting atom velocities and coordinates were used as starting point for the run of the second-step: a 1.0 ns NPT-MD trajectory at 298 K and 1 bar. As a consequence of the ten-times repetition, the

equilibration of each model took 5 and 10 ns of NVT-MD and NPT-MD, respectively, distributed in 10 different runs each one. The last step of the equilibration run was the starting point of the productive trajectories presented in this work (298 K and 1 bar pressure).

Bond lengths involving hydrogen atoms were kept at their equilibrium distances using the RATTLE algorithm.[31] Atom pair distance cutoffs were applied at 14.0 Å to compute the van der Waals interactions. To avoid discontinuities in this energy component, the van der Waals energy term was forced to slowly converge to zero by applying a smoothing factor from a distance of 12.0 Å. Electrostatic interactions were extensively computed by means of Ewald summations. The real space term was defined by the van der Waals cutoff (14.0 Å), while the reciprocal space was computed by interpolation of the effective charge into a charge mesh with a grid thickness of 5 points per volume unit (particle mesh Ewald).[32]

For the equilibration and production runs, both temperature and pressure were controlled by the Nose-Hoover pistons[33] combined with the piston fluctuation control of temperature implemented for Langevin dynamics.[34] Pressure was kept at 1.01325 bars, the oscillation period was set to 1 ps while the piston decay time was set to 0.001 ps. The piston temperature was set to the same value as the thermostat control, 298 K, which used a damping coefficient of 2 ps. The integration step was 2 fs in all simulations.

4.2.4. Results and discussion

Preparation of n-doped PEDOT:ionene films

p-Doped PEDOT films were deposited onto steel electrodes by anodic polymerization in acetonitrile, using a constant potential of +1.40 V and adjusting the polymerization charge to 480 mC cm^{-2}. These films were subsequently dedoped applying a potential of –1.30 V during 145 s in a 10 mM $LiClO_4$ water solution. After this, the electrochemical n-redoping of the dedoped films was performed by CA using a constant reduction potential (–0.50, –0.70, –0.90 or –1.10 V), which was applied during 150 s, and a 10 mM ionene (**1**, **2** or **3**) aqueous solutions. Details about the experimental conditions used for the preparation of p-doped, dedoped and redoped PEDOT films are provided in Experimental Section..

Control assays (blank) were conducted applying identical experimental conditions using bare steel electrodes (*i.e.* in absence of dedoped PEDOT). For a given reduction potential, the neat redoping

charge (Q_{rdop}^{neat}) was estimated as the difference between the chronoamperometric charges determined for the redoped PEDOT:ionene films (Q_{rdop}) and the corresponding blanks (Q_{blank}):

$$Q_{rdop}^{neat} = Q_{rdop} - Q_{blank} \quad (1)$$

Figure 4.2-1(a) displays the absolute values of Q_{rdop}^{neat} obtained for **1-3** with the four tested reduction potentials. The value of Q_{rdop}^{neat}, which reflects the charge of PEDOT normalized by repeat unit after the redoping process, becomes more negative with the reduction potential. However, the response of the ionenes to the reduction potential clearly depends on their molecular topology. Thus, **1** and **3** are very sensitive to the redoping potential, while **2** exhibits similar and relatively low Q_{rdop}^{neat} values for all reduction potentials with exception of –1.10 V. For the latter potential, the absolute value of Q_{rdop}^{neat} grows as follows: **3** > **2** > **1**. This suggests that under such conditions the PEDOT⋯ionene interactions are more effective for the para-isomeric topomer. The moles of ionene repeating units ($N_{\#}$ with # = **1**, **2** or **3**) incorporated during the redoping process were estimated using the values of Q_{rdop}^{neat} for each reduction potential (Eqn 2):

$$N_{\#} = \frac{Q_{rdop}^{neat}}{2F} \quad (2)$$

where F is the Faraday's constant and includes two positive charges of every ionene repeat unit. The resulting values were combined with the moles of EDOT repeat units in the CP chains (N_{EDOT}; Eqn 4) to calculate the doping level of each ionene ($dl_{\#}$ with # = **1**, **2** or **3**) at a given reduction potential, which expresses the percentage (in %) of dicationic ionene unit per EDOT unit:

$$dl_{\#} = \frac{N_{mPI}}{N_{EDOT}} \times 100 \quad (3)$$

$$N_{EDOT} = \frac{(Q_{pol} \quad Q_{ddop})}{2F} \quad (4)$$

where Q_{pol} is the charge consumed during the polymerization process of p-doped PEDOT films and Q_{ddop} is the charge consumed during the dedoping process corresponding to ClO_4^- counterions.

Figure 4.2-1(b), which represents the $dl_{\#}$ values obtained for each reduction potential, proves the successful incorporation of ionene molecules during the redoping process. As it was expected, $dl_{\#}$ increases with the absolute reduction potential, even though the dependence on the ionene topology is not clear. When the reduction potential decreases from –0.50 V to –1.10 V, $dl_{\#}$ increases by 1.9%, 3.5% and 2.8% for **1**, **2** and **3**, respectively. However, the values of $dl_{\#}$ obtained using –1.10 V are practically identical for **2** and **3**, which in turn are higher than that achieved for **1**.

The maximum doping level achieved for PEDOT:**1**, PEDOT:**2** and PEDOT:**3** corresponds to one dicationic ionene unit for every ~28, ~20 and ~20 EDOT units, respectively. The doping level achieved for monocationic TMA using identical experimental conditions was reported to be dl_{TMA}= 8.9% (*i.e.* one cationic TMA molecule has been incorporated every ~31 EDOT units).[35] Accordingly, the n-doping capacity of the TMA and DABCO-containing ionenes are similar, even though the mobility of former is greater than that of the cationic polyelectrolytes.

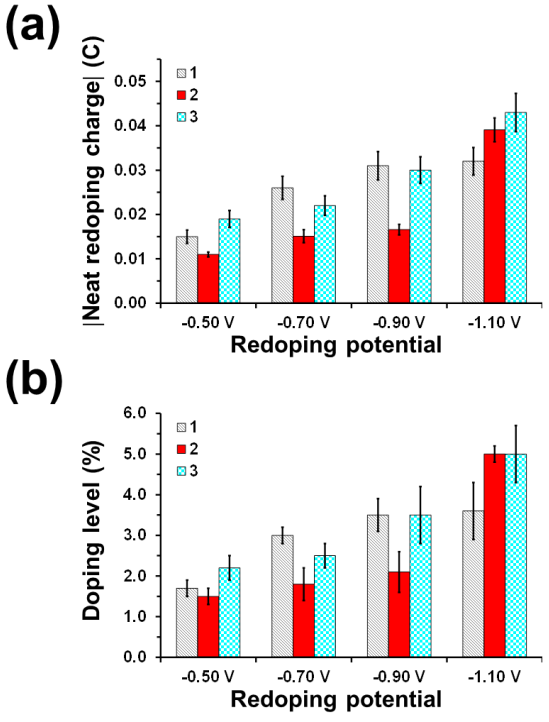

Figure 4.2-1.Variation of (a) the absolute value of the neat redoping charge (Q_{rdop}^{neat}, Eqn 1) and (b) the doping level (dl#, Eqn 3) against the reduction potential for n-doped PEDOT:1, PEDOT:2 and PEDOT:3.

Chemical characterization of PEDOT:ionene films

The success of the redoping process and the structural changes of PEDOT chains as a function of the ionene were investigated using XPS and Raman spectroscopy, respectively. Results derived from XPS analyses, which were performed considering PEDOT: ionene films prepared by applying a reduction potential of –1.10 V, are displayed in Table 4.2-1.

Table 4.2-1. Atomic percent composition (C 1s , N 1s, O 1s and S 2p) obtained by XPS for PEDOT: p-doped, dedoped, and redoped (n-doped) with 1, 2 or 3.

Sample	**C 1s**	**N 1s**	**O 1s**	**S 2p**
p-doped PEDOT	59.2	0.0	30.2	10.6
dedoped PEDOT	63.3	0.0	25.5	11.2
n-doped PEDOT:**1**	69.6	3.7	18.7	8.0
n-doped PEDOT:**2**	72.8	4.9	16.3	6.0
n-doped PEDOT:**3**	67.2	2.8	20.8	9.1

The apparition of N 1s demonstrates the incorporation of the ionene into the PEDOT matrix. However, the variation of the atomic content of N 1s, **2** > **1** > **3**, is not consistent with the variation of $dl_{\#}$ [Figure 4.2-1(b)], **2** ≈ **3** > **1**. Thus, the S / N ratios derived from the XPS atomic percent compositions for samples redoped with **1**, **2** and **3** suggest the presence of one dicationic ionene unit for approximately every 9, 5 and 13 EDOT units (*i.e.* each ionene unit contains four nitrogen atoms, while there is one sulfur per EDOT unit). The difference between the electrochemical and XPS doping levels has been attributed to the fact that many of the incorporated ionene units are not directly interacting with PEDOT chains and, therefore, do not play a role as active n-dopant agents. This may represent an advantage for the *in situ* hydrogelation of PEDOT:ionene films since polycationic chains could form stable gels without affect the electrochemical performance of n-doped PEDOT.

Figure 4.2-2(a) displays the Raman spectra obtained for p-doped PEDOT (as prepared), PEDOT:**1**, PEDOT:**2** and PEDOT:**3**. Worth mentioning that the Raman spectra were obtained using PEDOT samples electropolymerized at +1.40 V but adjusting the polymerization charge to 30 mC cm^{-2} rather than the 480 mC cm^{-2} used for all assays.

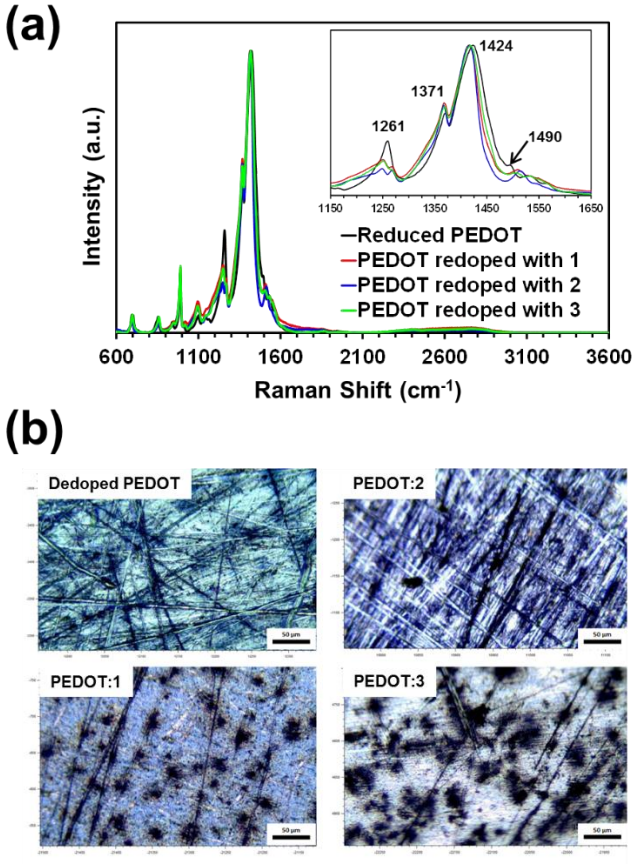

Figure 4.2-2. (a) Raman spectra of dedoped PEDOT and n-doped PEDOT:ionene films upon excitation with a laser at 785 nm. Samples were obtained using a polymerization charge of 30 mC cm^{-2}. Inset: Magnified Raman spectra between 1150 and 1650 cm^{-1}. (b) Optical micrographs recorded with the confocal Raman microscope of dedoped PEDOT, PEDOT:1, PEDOT:2 and PEDOT:3.

This was because, although the latter polymerization charge produced films of higher thickness, their roughness did not allow us to obtain a good peak resolution. This feature is illustrated in Figure 4.2-3, which compares the spectra recorded for PEDOT:**1** films that were redoped using p-doped PEDOT obtained using polymerization charges of 30 and 480 mC cm^{-2}.

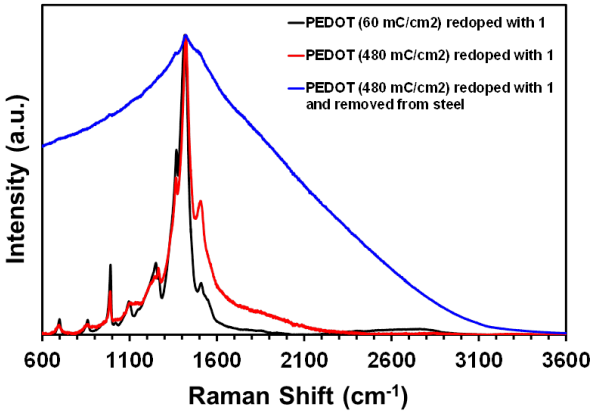

Figure 4.2-3.Comparison of the Raman spectra recorded for PEDOT:1 films obtained by redoping p-doped PEDOT electropolymerized using charges of 30 and 480 mC cm^{-2}. Both the latter polymerization charge and the removal of PEDOT:1 from the steel support damaged the peak resolution.

The Raman fingerprints of PEDOT were reported in previous studies.[36-38] The main vibrational modes of this CP are located at 1490 cm^{-1}, 1424 cm^{-1}, 1371 cm^{-1} and 1261 cm^{-1}, which correspond to asymmetric C_α=C_β stretching, symmetric C_α=C_β stretching, C_β=C_β stretching and C_α–C_α, inter-ring stretching vibrations, respectively. Other important bands are located at 438, 700, and 991cm^{-1}, assigned to the deformation of C–O–C, symmetric C–S–C and oxyethylene ring, respectively.

Comparison between dedoped PEDOT and PEDOT:ionene samples [Figure 4.2-2(a)] shows the appearance and disappearance of several bands. Some interesting remarks are:

- Both types of samples present different Raman shift and width of the peak centered at 1424 cm^{-1}.
- The band located at 1261 cm^{-1} splits into two peaks in the presence of the ionenes.
- The peak at 1490 cm^{-1} disappears.

Changes in the characteristic band at 1424 cm^{-1} are related with a variation in the electronic structure of PEDOT chains that affects to the C_α=C_β stretching.[39,40] This peak, which is pointed at 1424 cm^{-1} for dedoped PEDOT, shifts to 1416 cm^{-1} for n-doped samples, indicating that this vibration mode is sensitive to the reduction caused by the n-dopant agent. More specifically, this red shift has been associated with ionene-induced benzenoid-to-quinoid conversion of PEDOT chains, which is consistent with earlier theoretical studies.[41]

Cho *et al.*[42] reported that the width of the characteristic band of C_α=C_β can be correlated with the resonant structure of PEDOT: narrower peaks correspond to a higher content of quinoid structure. The inset in Figure 4.2-2(a) reflects that this peak becomes narrower for all PEDOT:ionene films, even though this is slightly more evident for PEDOT n-doped with **2** than with **1** and **3**. The width of the C_α=C_β stretching peak can be also related with the crystallinity: narrower peaks associated with more crystalline samples.[43] Accordingly, Figure 4.2-2(a) suggests that the crystallinity is higher for PEDOT:**2** than for PEDOT:**1** and PEDOT:**3**. This feature, together with the fact that the quinoid structure is more expanded and rigid than the benzoid one, suggest that PEDOT:**2** presents stronger PEDOT⋯ionene interactions than PEDOT:**1** and PEDOT:**3**. The crystallinity has been reported to exert an important effect on the gelation capacity,[44] being lower or even completely absent when the crystallinity of the sample is too high. In this case, the width of the C_α=C_β stretching peak [Figure 4.2-2(a)] is consistent with the *in situ* gelation capacity of the ionenes in the examined PEDOT:ionene samples that, as it is described below, was higher for **1** and **3** than for **2**.

The C_α–$C_{\alpha'}$ inter-ring stretching at 1261 cm^{-1} [Figure 4.2-2(a)] is also connected with the percentage of benzoid and quinoid structures.[45] After redoping with the ionene, this peak becomes broader and splits into two bands located at 1249 and 1268 cm^{-1}. The observed Raman shifts and reduction in the intensity are ascribable to the variation of C_α–$C_{\alpha'}$ and C_β=$C_{\beta'}$ to C_α=$C_{\alpha'}$ and C_β–$C_{\beta'}$, respectively, suggesting the conversion from the benzoid to the quinoid electronic structure, in agreement with the interpretation of the changes in the peak at 1424 cm^{-1}. On the other hand, the peak at 1371 cm^{-1}, which is related with C_β=$C_{\beta'}$, decreases in intensity in the presence of ionenes, confirming its conversion to C_β–$C_{\beta'}$. Furthermore, the disappearance of the peak centered at 1490 cm^{-1}, which corresponds to the asymmetric C_α=C_β stretching, could be also related with the reduction of the double bond character due to the benzoid-to-quinoid conversion.

Figure 4.2-2(b) displays optical images taken with the Raman confocal microscope of dedoped PEDOT and PEDOT:ionene prepared using a polymerization charge of 30 mC cm^{-2}. Interestingly, PEDOT:**1** and, especially, PEDOT:**3** shows dark and large agglomerates homogeneously distributed onto the surface. These agglomerates have been attributed to regions in which the n-dopant agents, **1** and **3**, are segregated from the CP forming a micrometric ionene phase. The presence of the latter suggests that the balance between PEDOT⋯ionene and ionene⋯ionene interactions is regulated by the ionene topology, which is expected to play a very important role in the properties of such n-doped films.

Physical characterization of PEDOT: ionene films

Figure 4.2-4(a) displays the variation of the *SC*, as determined by CV, for PEDOT:ionene against the reduction potential. As it is expected, the resulting *SC*s values, which express the ability to store charge of n-doped films referred to the PEDOT mass, are very low (*i.e. SC* ranged from 3.0 to 6.1 F g^{-1}) with respect to p-doped PEDOT (*SC*=56 F g^{-1} doped with ClO_4^-)[46] and PEDOT-nanocomposites involving MoO_3, RuO_2, carbon nanotubes, MnO_2, and clays (*SC* varying between 96 and 375 F g^{-1}).[46-52] These differences are associated to the low doping level n-doped PEDOT, which in general is significantly smaller than that of p-doped, and to the fact that negative polarons are the only charge carriers in n-doped PEDOT, as proved by Ahonen and co-workers.[53] These observations are consisted with the *SC*s obtained for PEDOT films redoped with TMA, which ranged from 3.9 to 4.7 F g^{-1} depending on the reduction potential,[35] and with the fact that the *SC*s of PEDOT:ionene films are relatively independent of the polycation topology. Thus, the *SC*s obtained for the three systems are very similar with exception of the films redoped at –0.50 V with **3**, which exhibits slightly higher values.

The cyclic stability of PEDOT:ionene electrodes was evaluated by CV. After 100 consecutive oxidation-reduction cycles, which were applied using –0.50 V as initial and final potentials and –1.10 V as reversal potential (scan rate: 50 mVs^{-1}), the *SC* of films redoped with **1** and **3** decreases around ~50%, independently of the reduction potential [Figure 4.2-4(b)]. However, PEDOT:**2** shows a higher dependence on the redoping potential, the reduction of the *SC* ranging between 40% (–0.90 V) and 70% (–0.50 V). Although the electrochemical stability of films doped with ionenes is apparently low, it should be remarked that this behavior is similar to that observed using TMA as n-dopant agent.[35] Thus, the *SC* of PEDOT redoped with TMA decreases 62% and 52% when the reduction potential is –1.10 and –0.50 V, respectively.

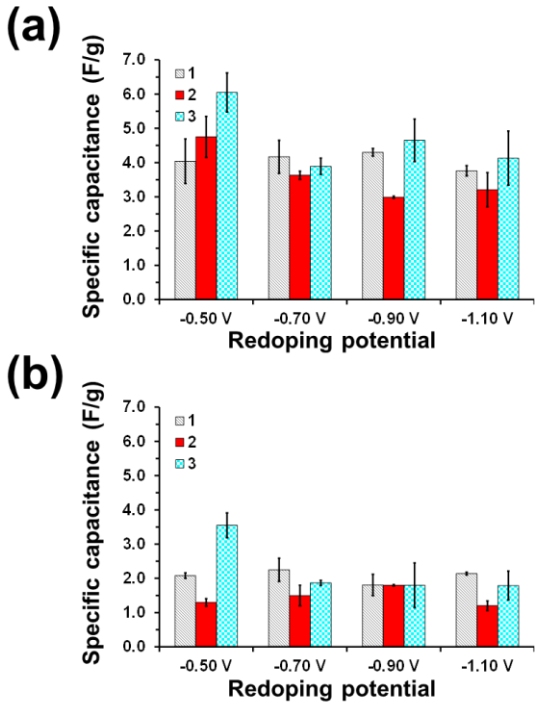

Figure 4.2-4. SC of PEDOT:ionene (a) as prepared and (b) after 100 consecutive redox cycles, as a function of the reduction potential. Redox cycles were applied by CV: initial and final potentials, –0.50 V; reversal potential, –1.10 V; scan rate, 50 mVs^{-1}.

Thermogravimetric analyses [Figure 4.2-5(a)] showed that the topology of the ionene has a small but non-negligible effect in the thermal stability of n-doped PEDOT. Inspection of DGTA curves of redoped PEDOT:ionene indicates that solvent evaporation starts at around 45-50 ºC. After this, all systems exhibit a pronounced degradation step, the maximum temperature (T_{max}) being at 345 ºC, 350 ºC and 360 ºC for PEDOT:**1**, PEDOT:**2** and PEDOT:**3**, respectively. These values are higher than those observed for dedoped PEDOT (T_{max}= 340 ºC) but similar to those observed for PEDOT redoped with TMA[35] (T_{max}= 350 ºC). The temperature at a 50% weight loss ($T_{50\%}$) increases as follows: dedoped PEDOT ($T_{50\%}$= 371 ºC) < PEDOT:**3** ($T_{50\%}$= 403 ºC) < PEDOT:**1** ($T_{50\%}$= 410 ºC) < PEDOT:**2** ($T_{50\%}$= 427 ºC). Although the order is preserved, differences among $T_{50\%}$ values increase at a 70% weight loss ($T_{70\%}$): 449 (dedoped), 469 (PEDOT:**3**) 480 (PEDOT:**1**) and 518 ºC (PEDOT:**2**), respectively. According to these results and by comparison with TMA ($T_{50\%}$= 403 ºC, $T_{70\%}$= 465 ºC), ionenes improve the thermal stability of PEDOT, the maximum protection being

provide by the *meta*-topomer. This feature suggests that the strength and amount PEDOT⋯ionene interactions is higher for the *meta*-isomeric ionene than for the *ortho*- and *para*-ones.

Contact angle (θ) measurements were performed to examine the influence of the ionene in the film wettability. As it was previously reported,[35] the hydrophilicity of oxidized PEDOT increases significantly upon dedoping (*i.e.* θ decreases from 65º±6º to 37º±5º) due to a drastic reduction in the R_q, which decreases from 771±117 to 155±28 nm. The high hydrophilicity of dedoped PEDOT is maintained by the three ionene-containing films (*i.e.* θ= 34º±8º, 31º±6º and 37º±5º for PEDOT:**1**, PEDOT:**2** and PEDOT:**3**, respectively), as is reflected

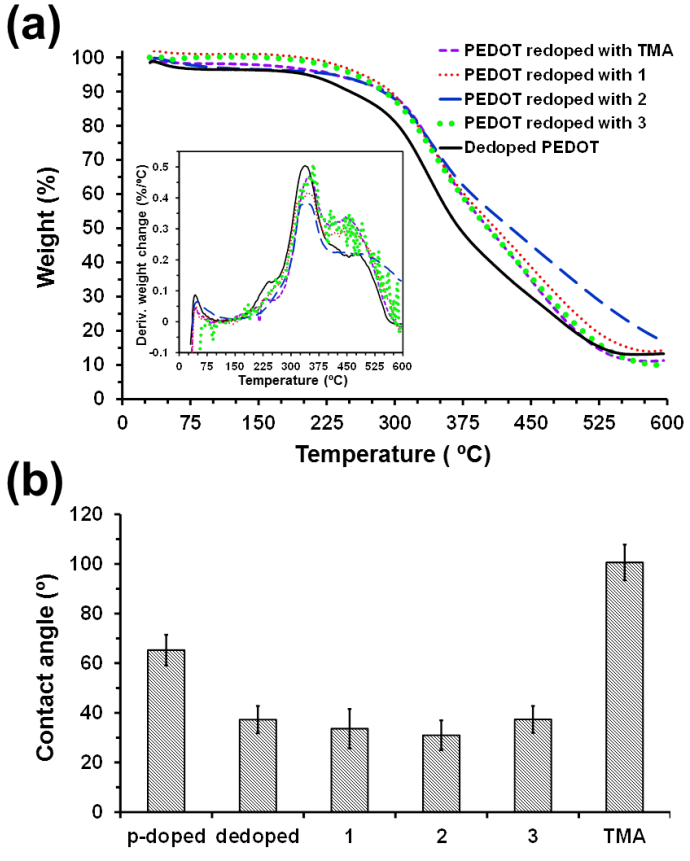

Figure 4.2-5. (a) TGA and DTGA (inset) curves and (b) contact angle of water for PEDOT as prepared (p-doped), reduced at constant potential of –1.30 V, and PEDOT redoped with 1, 2, 3 or TMA using a reduction potential of –1.10 V.

The wettability of redoped PEDOT is not only practically independent of the ionene topology but also of the redoping potential (Figure 4.2-6).

These results together with the fact that the R_q of the three ionenes is submicrometric and relatively close to that of p-doped PEDOT (see below), suggest that the affinity of PEDOT:ionene films towards water is due to the charged and polar groups contained in the ionene. In opposition, redoping with TMA resulted in a hydrophobic material (θ= 101º±12º), which was explained by the formation of a highly hydrophobic TMA layer at the surface of the films.[35] Thus, this small organic molecule was found to act not only as n-dopant agent but also as organic coating.

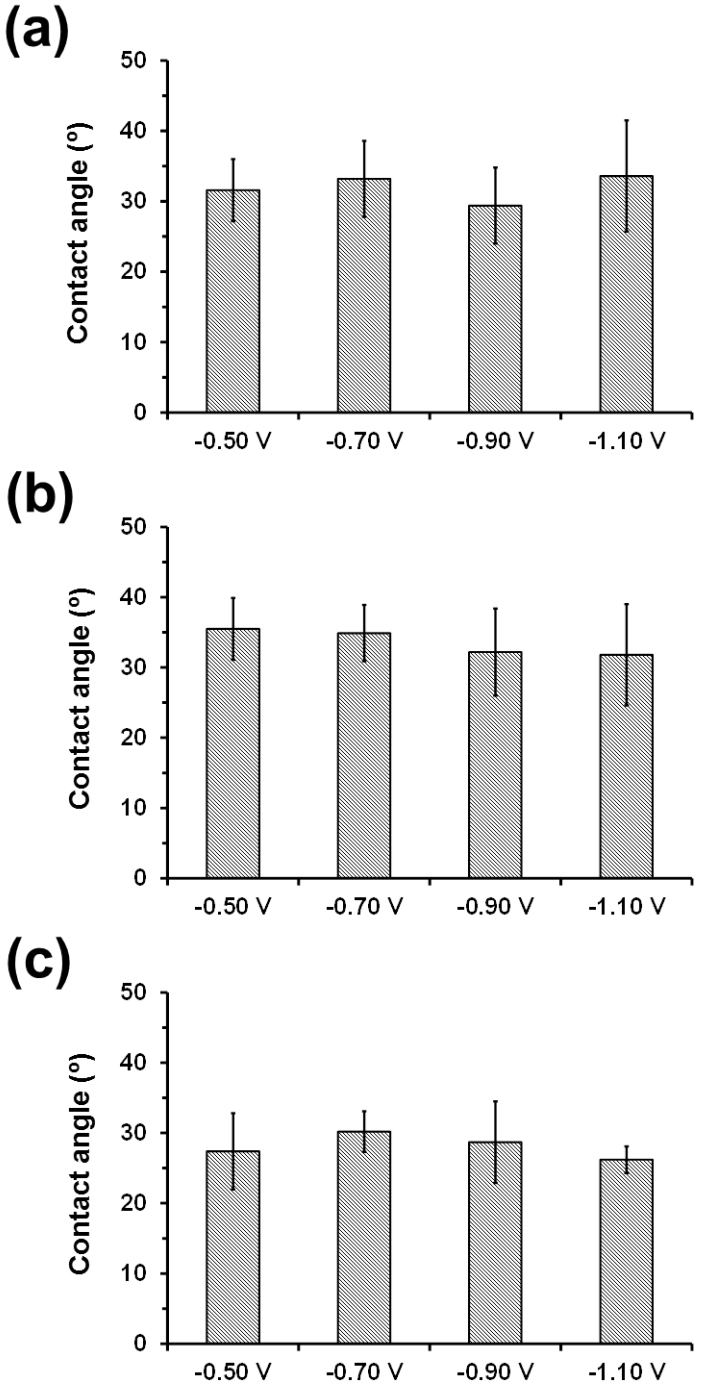

Figure 4.2-6. Contact angle of water measured for PEDOT redoped with (a) 1, (b) 2 and (c) 3 as a function of the reduction potential (i.e. –0.50, –0.70, –0.90 and –1.10 V).

Height and phase AFM images of PEDOT:ionene films obtained using a reduction potential of –1.10 V are shown in Figure 4.2-7. As it can be seen, both the surface topography and the distribution of dopant polycations drastically depend on the ionene topology. The R_q of PEDOT:ionene films grows progressively when the ionene topology varies as follows: *ortho* (**1**) > *meta* (**2**) > *para* (**3**) (Figure 4.2-7). Thus, the surface topography of the CP redoped with the *ortho*-isomeric ionene consists in a homogeneous distribution of abundant and relatively small PEDOT clusters. This distribution becomes more heterogeneous for films redoped with the *meta*-DABCO containing ionene. In this case, small clusters are accompanied by large aggregates, even though the former ones abound more than the latter ones. Finally, the topography of films containing the *para*-topomer can be described as a heterogeneous distribution of large PEDOT clusters, albeit some small aggregates are still present. Regarding to the distribution of the ionene molecules, phase images that are sensitive to the surface stiffness / softness reveal significant differences. Specifically, phase shifts, which are registered as bright and dark regions in phase images, are more abundant and contrasted in samples redoped with **1** and **3** than with **2**. The *ortho*- and *para*-topomers, which are clearly detected in the contrasted images, form submicro- and nanometric organizations, respectively, that remain relatively close among them. These microstructures are expected to favor the *in situ* gelation process of **1** and **3**, as will be demonstrated in the next sub-section. In contrast, the presence of the *meta*-isomeric ionene is much less appreciated in films redoped using a reduction potential of –1.10 V (Figure 4.2-7(b), right).

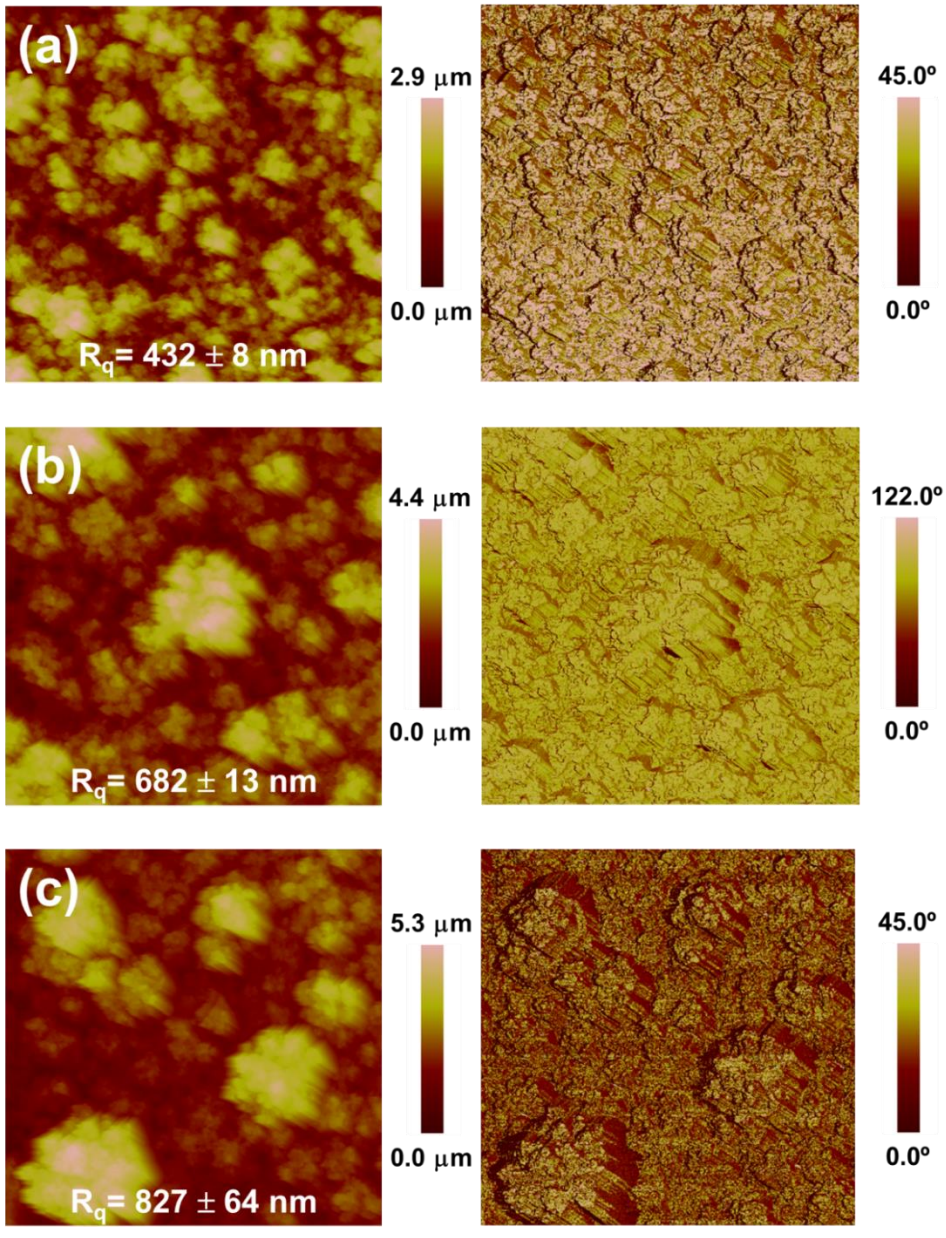

Figure 4.2-7. Height (left) and phase (right) AFM images (20 ×20 μm2) of (a) PEDOT:1, (b) PEDOT:2 and (c) PEDOT:3 prepared using a reduction potential of –1.10 V. Rq and the corresponding standard deviation is displayed for each PEDOT:ionene system.

The roughness, surface topography and phase distributions are also affected by the redoping potential, even though distinctive characteristics that can be only attributed to the ionene topology are still observed. For example, when the reduction potential is –0.50 V, the R_q values determined for PEDOT:**1** and PEDOT:**3** films are very similar and significantly higher than those of PEDOT:2 (Figure 4.2-8). In addition, height images reflect that the size of the CP clusters is significantly lower for films redoped at –0.50 V than at –1.10 V (Figure 4.2-8). This is particularly noticeable for PEDOT:**2** films, which exhibits a leveled topography formed by a homogeneous distribution of very small PEDOT clusters.

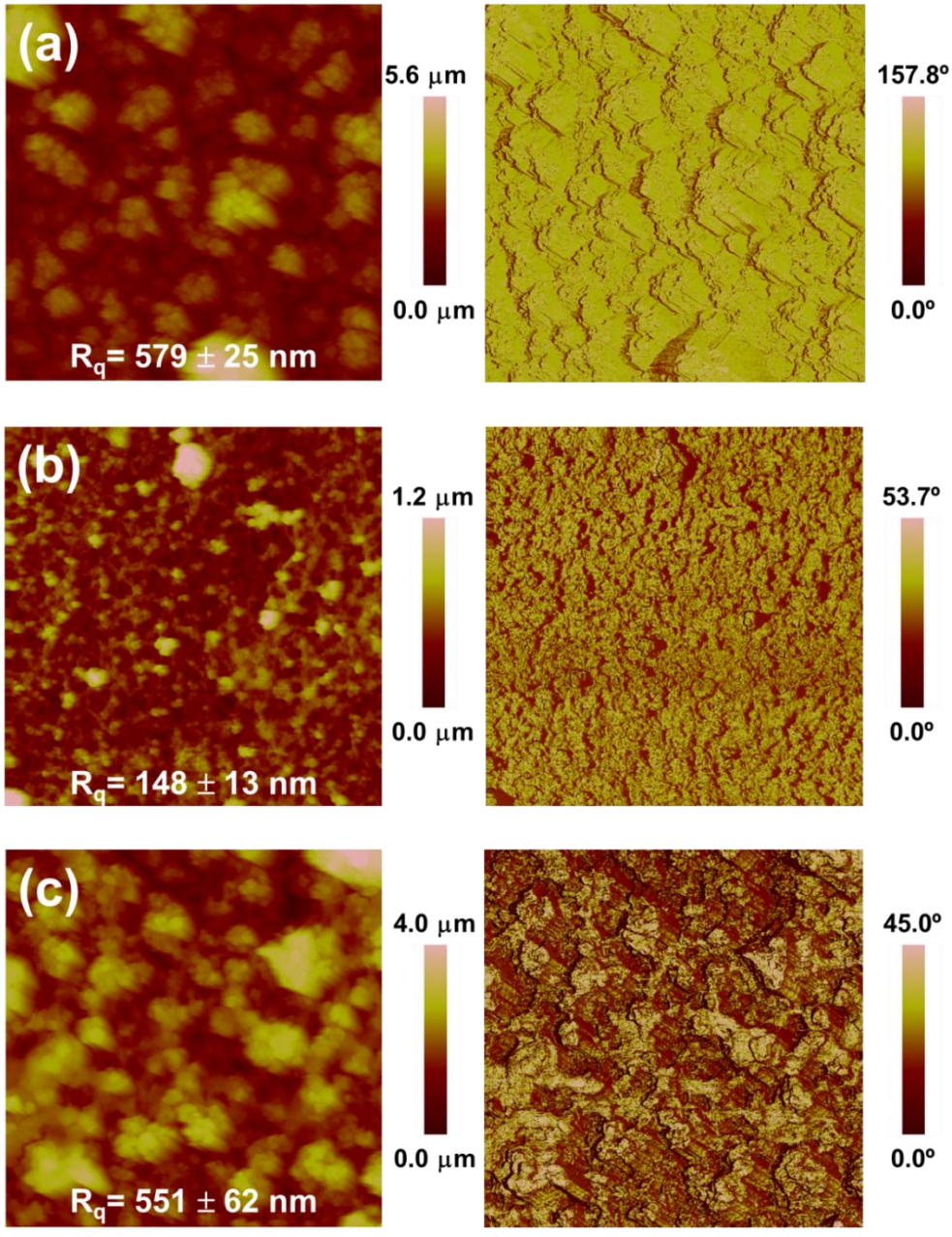

Figure 4.2-8. Height (left) and phase (right) AFM images (20 ×20 μm2) of (a) PEDOT:1, (c) PEDOT:2 and (e) PEDOT:3 prepared using a reduction potential of –0.50 V. The Rq and the corresponding standard deviation is also displayed for each PEDOT:ionene system.

AFM topographic images are fully consistent with representative SEM micrographs. (Figure 4.2-9, Figure 4.2-10 and Figure 4.2-11) for 50 KX, 10 KX and 100 KX magnification, respectively), which reflect the influence of the ionene architecture in the morphology and, especially, the size of globular PEDOT clusters. The globular appearance of n-doped PEDOT:ionene films is similar to that reported for p-doped and dedoped PEDOT.[35,36]

Moreover, the incorporated ionenes preserve the porosity of the films, which is more affected by the reduction potential than by the topology of the n-dopant agent. Thus, the diameter and tortuosity of the pores is higher for the films obtained using –0.50 V than for those redoped at –1.10 V, independently of the ionene topology (Figure 4.2-11).

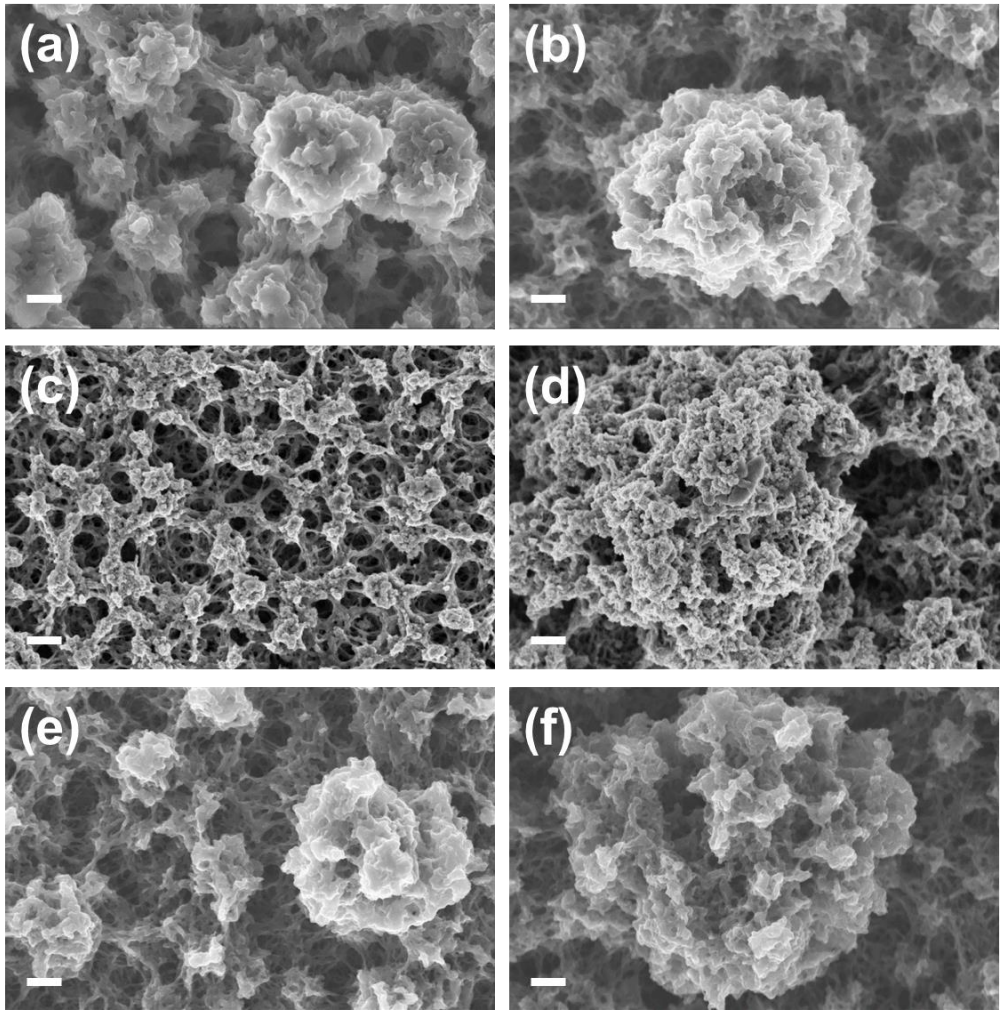

Figure 4.2-9. SEM micrographs (magnification: 50 KX) of (a,b) PEDOT:1, (c,d) PEDOT:2 and (e,f) PEDOT:3 prepared using a reduction potential of (a,c,e) –0.50 V and (b,d,f) –1.10 V. Scale bar: 400 nm.

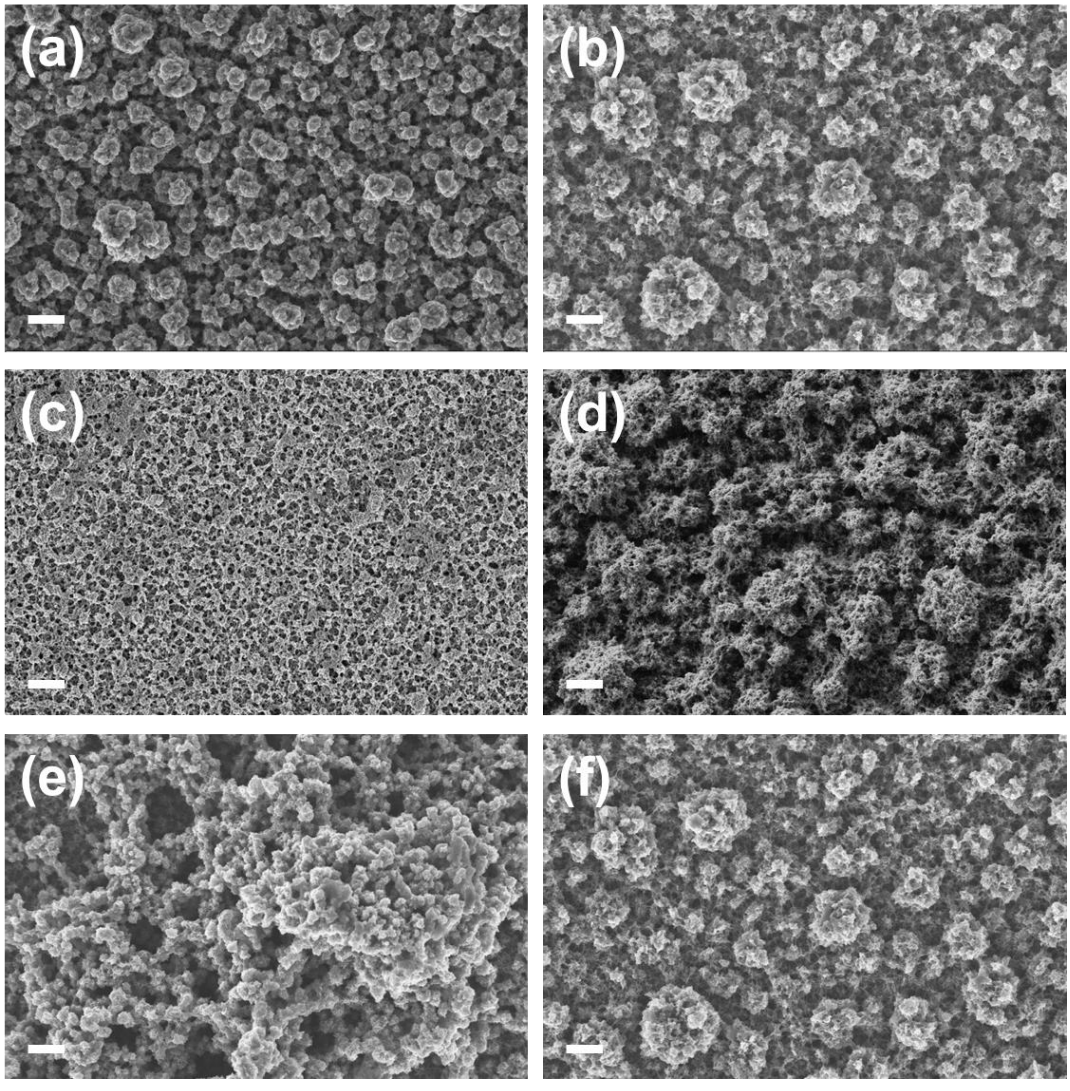

Figure 4.2-10. SEM micrographs (magnification: 10 KX) of (a,b) PEDOT:1, (c,d) PEDOT:2 and (e,f) PEDOT:3 prepared using a reduction potential of (a,c,e) –0.50 V and (b,d,f) –1.10 V. Scale bar: 2 μm.

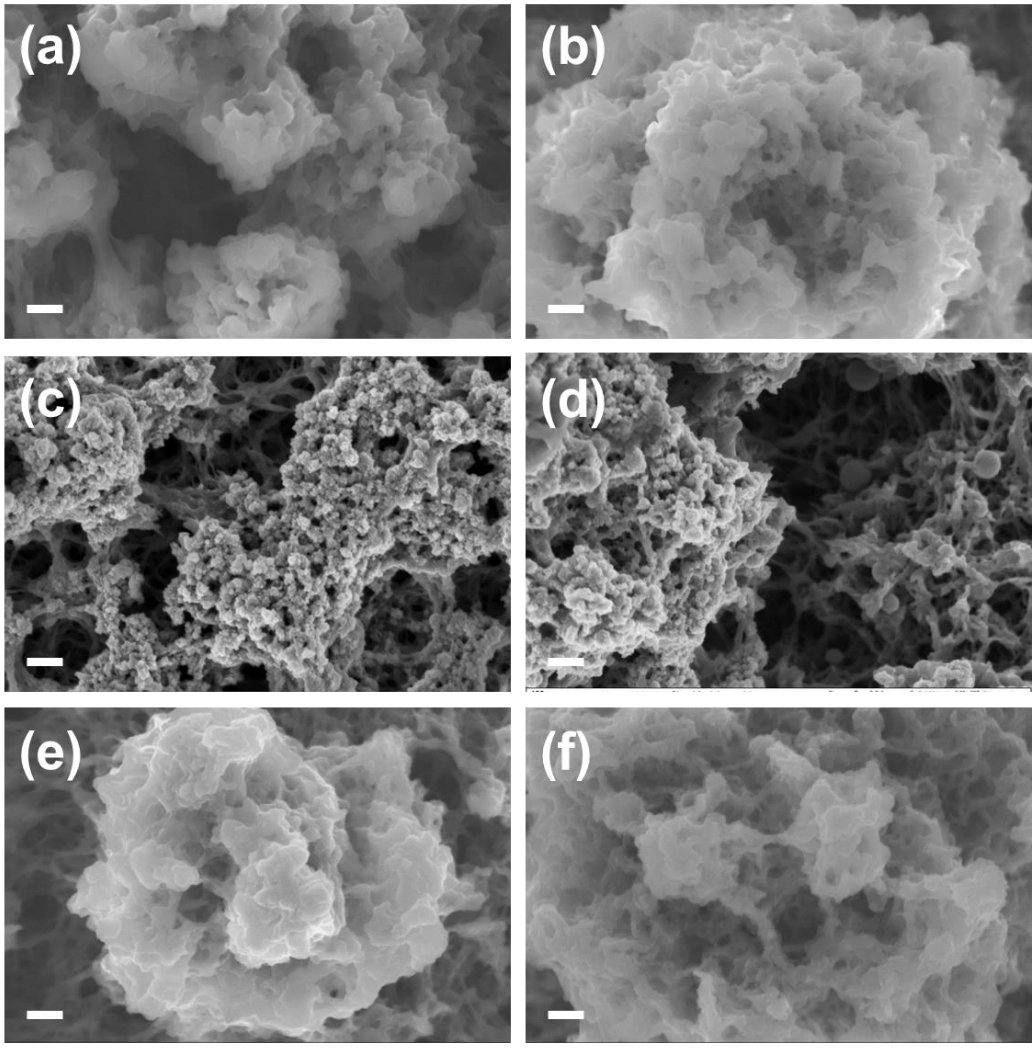

Figure 4.2-11. SEM micrographs (magnification: 100 KX) of (a,b) PEDOT:1, (c,d) PEDOT:2 and (e,f) PEDOT:3 prepared using a reduction potential of (a,c,e) –0.50 V and (b,d,f) –1.10 V. Scale bar: 200 nm.

In situ thermal hydrogelation of ionenes in n-redoped films

PEDOT:ionene films (surface area: 1 cm^2) prepared using a reduction potential of –1.10 V, were subjected to thermal hydrogelation tests. After wetting by depositing 80 μL of 0.1 M HCl at each side, supported films were heated in an oven at a temperature comprised between 55 ºC and 65 ºC during a time comprised between 5 and 60 min. The changes in the aspect and texture of PEDOT:**1** and PEDOT:**3** films [Figure 4.2-12(a)] suggested the successful gelation of **1** and **3**. In contrast, the thermally-induced gelation was unsuccessful for PEDOT:**2** films, which did not exhibit any change in their appearance. This was an expected result because of the poor gelation capacity reported for the *meta*-isomeric ionene.[17,18]

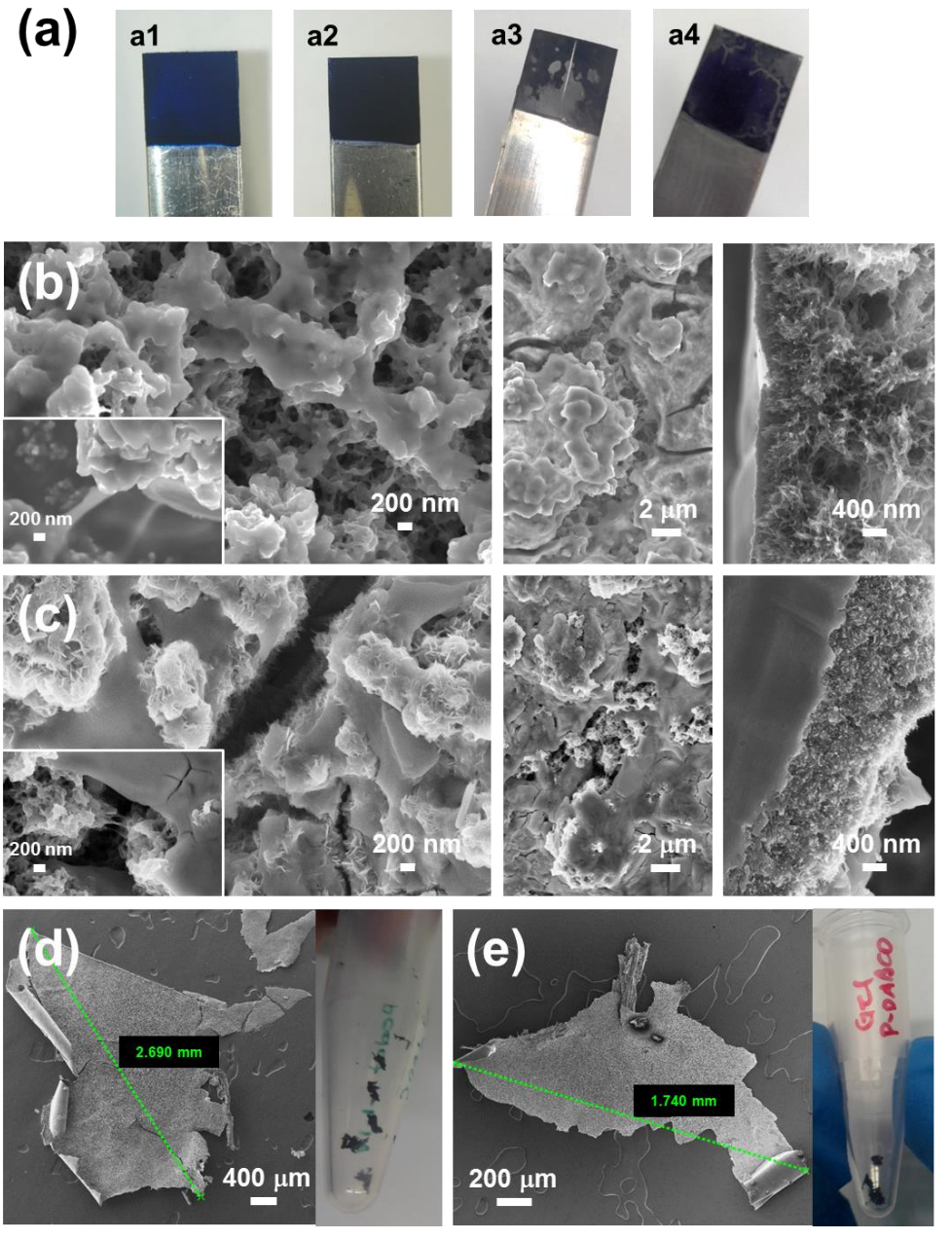

Figure 4.2-12. (a) From left to right: a1) Dedoped PEDOT; a2) redoped PEDOT:1 using a reduction potential of –1.10 V (PEDOT:3 is not shown because its aspect is identical to that of PEDOT:1); a3) PEDOT:1 after 10 min in an oven at 60 ºC under acid wetting conditions; and a4) PEDOT:3 after 50 min in an oven at 60 ºC under acid wetting conditions. Surface (left and center) and cross-sectional (right) SEM micrographs of (b) PEDOT:1 and (c) PEDOT:3 after the in situ gelation. SEM micrograph and photograph (left and right respectively) of (d) PEDOT:1 and (e) PEDOT:3 slices obtained after ionene gelation by scratching the substrate.

The effective changes in n-doped PEDOT films promoted by both **1** and **3** were attributed to the acid wetting and heating conditions,[18]which changed the aggregation behavior of neighboring ionene molecules and caused the formation of micro/nano-hydrogels. However, the topology clearly affected the kinetics of the gelation, which was much faster for **1** than for **3** at all the tested temperatures. For example, the time required to change the aspect and texture of PEDOT:**1** films at 60 ºC (10 min) was 6-times shorter than that needed for PEDOT:**3** 56°C (60 min). This observation is fully consistent with that reported for the thermal hydrogelation of **1** and **3** from the corresponding water solutions,[8] even though it should be remarked that the gelation time in PEDOT:ionene films is also influenced by the amount (**1** > **3**, in Table 4.2-1) and distribution of the ionene molecules inside the CP matrix (*i.e.* microstructure).

SEM micrographs of gel-containing PEDOT:**1** and PEDOT:**3** films [Figure 4.2-12 (b,c) respectively] reveal significant changes with respect to films before conducting the thermal hydrogelation assays (Figure 4.2-9). As it can be seen, mild heating combined with acidic wetting conditions gave place to the gradual aggregation of neighboring ionene molecules, inducing the formation of crosslinked ionene networks and forming gel domains with a smooth texture. Although these newly formed domains are mainly located at the surface of films, cross section SEM micrographs reflect the presence of gel also inside the CP matrix. This characteristic is particularly evident for PEDOT:**1**, as is reflected by the progressively magnified cross section SEM micrographs

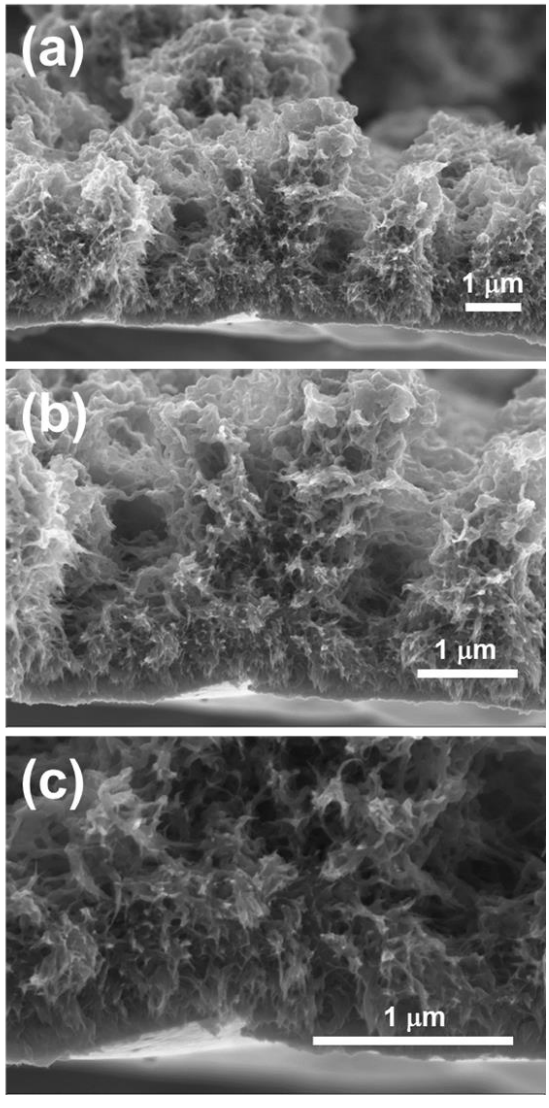

Figure 4.2-13. Cross section SEM micrographs of PEDOT:1 after 10 min in an oven at 60 ºC under acid wetting conditions. Magnification: (a) 30 KX; (b) 50 KX; and (c) 100 KX. Films were redoped using a reduction potential of–1.10 V.

Although the gelation kinetics is faster for **1** than for **3**, ionene-forming hydrogel surface domains are more abundant in PEDOT:**3** than in PEDOT:**1** (Figure 4.2-14). The latter observation is consistent with the phase AFM images displayed in Figure 4.2-7, which show that the *para*-topomer abound more at the surface of films redoped at –1.10 V than the *ortho*-one. These features suggest that the kinetics of self-assembly via facilitated diffusion of the *ortho*-ionene molecules is compensated by the *para*-ionene through the formation of abundant and very stable interactions.

MD simulations on representative model systems to provide additional microscopic information about the *in situ* formed hydrogels are discussed in the next sub-section.

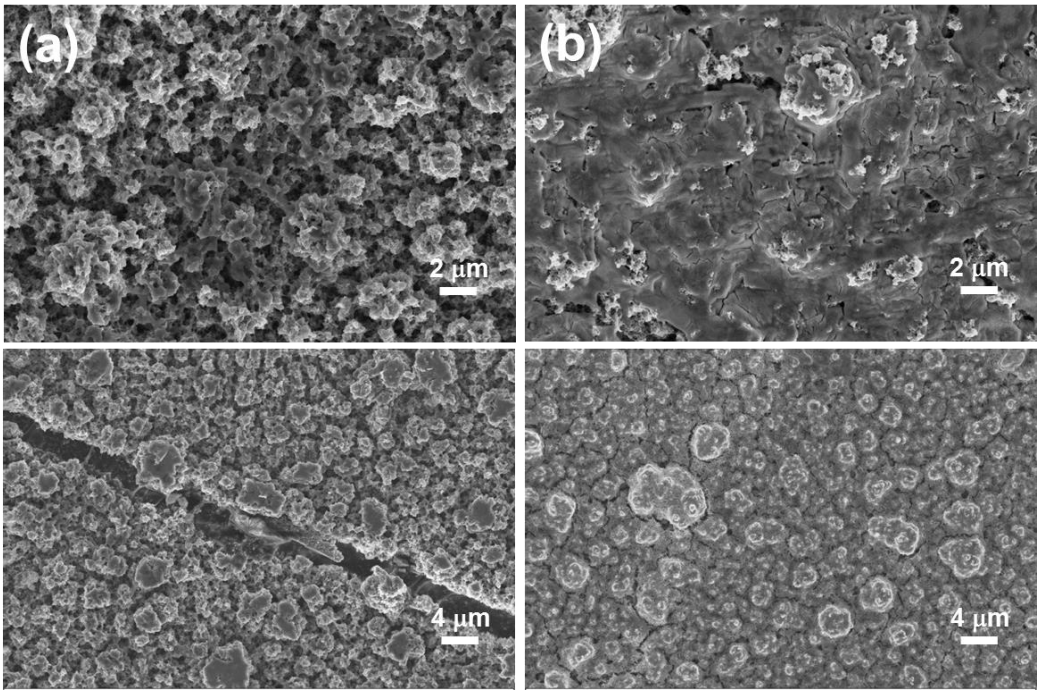

Figure 4.2-14.. SEM micrographs of (a) PEDOT:1 and (b) PEDOT:3 after 10 min in an oven at 60 ºC under acid wetting conditions. Films were redoped using a reduction potential of–1.10 V.

The *SC* of PEDOT:**1** and PEDOT:**3** films after gelation of the corresponding ionene, *SC*= 12.9 and 7.0 F g^{-1}, respectively, were noticeably high in comparison with those discussed above for as prepared redoped films (*SC*= 3.8 and 4.1 F g^{-1}, respectively, in Figure 4.2-4(a). Thus, the gain in the ability for charge storing clearly indicates the ionene hydrogel facilitates the charge mobility. Furthermore, the thermally-induced ionene hydrogel phases formed inside PEDOT film supports that the amount of ionene molecules in PEDOT:ionene is closer to that determined by XPS (Table 4.2-1) than to the one reflected by the electrochemical doping level [Figure 4.2-1(b)].

The *in situ* gelation of the ionenes provides important advantages from a mechanical point of view. More specifically, the mechanical response of p-doped PEDOT films prepared by anodic polymerization, as well as of the films dedoped and n-redoped with ionene (before gelation) or TMA, is null. Thus, PEDOT films adhered to the surface of the substrate used as working electrode during the electropolymerization, disintegrate as a powder when they are tried to separate by scratching. Moreover, the mechanical characteristics of films adhered to the substrate is also very poor, tending to undergo cracking when exerted the slightest touch or pressure. In contrast, mechanical failures are much less evident in PEDOT:**1** and PEDOT:**3** after the ionene gelation. Accordingly, ionene nano- and micro-hydrogels act as cement that prevents from the cracking to the adhered films and, in addition, allows to obtain small slices of films (*i.e.* of millimetric dimensions) by scratching the substrate [Figure 4.2-12(d-e)]. Obviously, in order to extend the applicability of n-doped PEDOT:ionene films, such mechanical response must be further improved. This could be possible by looking for new *in situ* or *ex situ* strategies that would allow a greater incorporation of ionene into the CP matrix.

Computational studies on the self-assembly process

Molecular dynamics (MD) simulations were conducted on atomistic models formed by 48 PEDOT chains, each having 40 chemical repeat units, and 32 ionene (**1**, **2** or **3**) chains, each containing 6 repeat units. Hereafter, models for PEDOT:ionene systems involving the *ortho*-, *meta*- and *para*-topomer are denoted **m1**, **m2** and **m3**, respectively. A charge of –0.2 was accounted for each EDOT unit and, therefore, 10 EDOT units were needed to neutralize each dicationic ionene repeat unit. Thus, the ratio between PEDOT and ionene repeat units was close to that determined by XPS (Table 4.2-1), which ranged from 5 (PEDOT:**2**) to 13 (PEDOT:**3**), even though the doping level of PEDOT chains was higher than that observed experimentally [Figure 4.2-1(b)]. However, the use of these proportions between PEDOT and ionene chains allowed us to perform simulations using models with a manageable number of explicit particles manageable (*i.e.* 37504 explicit atoms), which would not have been possible considering the proportions derived from the doping level.

PEDOT and ionene chains were initially distributed in two groups that, in turn, were arranged in separated blocks (Figure 4.2-15). Thus, the density for the initial geometry of the **m1**-**m3** models was ρ= 1.0 g cm^{-3}, which is much lower than the experimentally determined value (see below). After thermalize and equilibrate the starting geometries using the protocol provided in the experimental section (100 ns NPT-MD , run at 298 K). During the first half of such trajectories, PEDOT and

ionene chains experienced significant re-distributions with respect to the initial geometry. This is reflected in Figure 4.2-16(a), which represents the last snapshot of the 100 ns trajectory for **m1**, **m2** and **m3**.

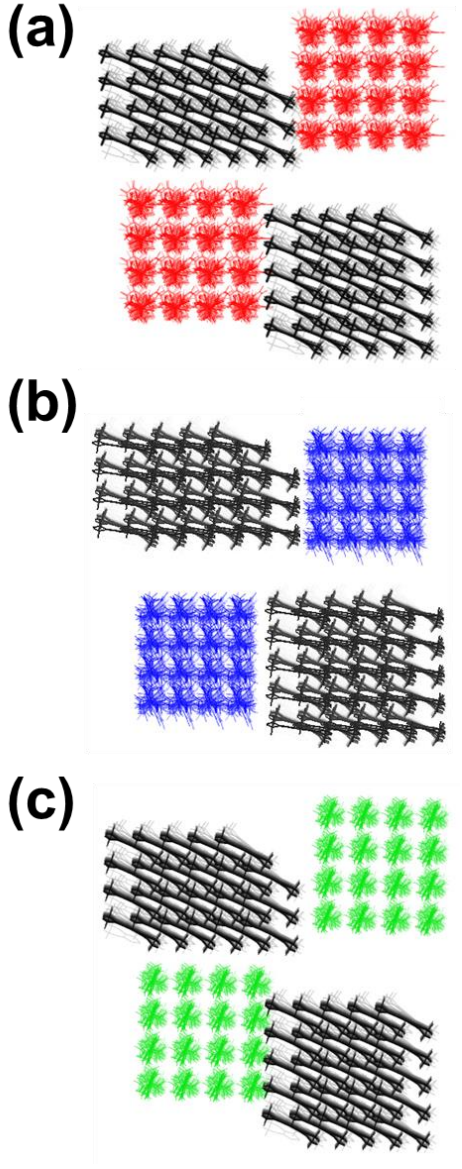

Figure 4.2-15. Geometry of the (a) m1, (b) m2 and (c) m3 models used as starting point for productive MD simulations. Ionene molecules 1, 2 and 3 are displayed in (a) red, (b) blue and (c) green, respectively, while PEDOT molecules are represented in black.

Models **m1**, **m2** and **m3** stabilized at a density of ρ= 1.34, 1.44 and 1.44 g cm-3, reflecting the compression of the simulation box (*i.e.* the distance between PEDOT and/or ionene chains became smaller). The experimental density of PEDOT samples redoped with **1**, **2** or **3** at –1.10 V, which was estimated using the flotation method, was ρ=1.46, 1.55 and 1.54 g cm^{-3}, respectively. Thus, theoretical prediction for **m1**, **m2** and **m3** differ from experimental values in 8.2%, 7.7% and 6.5% only, evidencing that MD simulations satisfactorily represent PEDOT···ionene, ionene···ionene and PEDO···PEDOT interactions.

Although the three examined systems are dominated by the electrostatic interactions between the negatively charged CP and the polycation, specific π-π stacking and hydrogen bonds are expected to play also an important role. Figure 4.2-16(b) represents the partial radial distribution functions (RDF) for pairs of centers of masses of aromatic rings belonging to different PEDOT and/or ionene chains. Thus, RDFs have allowed to distinguish between PEDOT···PEDOT ($RDF_{PEDOT\text{-}PEDOT}$), PEDOT···ionene ($RDF_{PEDOT\text{-}ionene}$) and ionene···ionene ($RDF_{ionene\text{-}ionene}$) π-π stacking interactions. Previous studies based on quantum mechanical methods indicated that the center of masses of two interacting aromatic rings are separated by ~3.7 Å and ~5.0 Å when they adopt sandwich and T-shaped arrangements, respectively.[55-57] In this work the relative disposition of two interacting aromatic rings has been examined by calculating the tilting angle, θ, formed by their respective planes (*i.e.* ideally, θ is 0º and 90º for sandwich and T-shaped arrangements, respectively). Figure 4.2-16(c) displays the tilting angle calculated for PEDOT···PEDOT, PEDOT···ionene and ionene···ionene π-π stacking interactions using cut-off distances extracted from the corresponding RDFs (see below).

The calculated $RDF_{PEDOT\text{-}PEDOT}$ (Figure 4.2-16(b), left) is practically independent of the ionene topology. Thus, the three models present a very intense and sharp peak centered at *r*= 3.9 Å and a less intense peak at *r*= 7.7 Å. The latter reflects the local order induced by the rigid conformation of PEDOT chains. The distribution profiles of the angle θ, which were calculated considering a cutoff distance of 5.0 Å between the centers of masses of the interacting EDOT units, show a well-defined maximum centered at ~15 º (Figure 4.2-16(b), left). Thus, PEDOT···PEDOT π-π stacking interactions prefer a slightly distorted coplanar disposition of the aromatic rings.

PEDOT···ionene π-π stacking interactions are slightly more abundant (~5%) in **m2** than in **m1** and **m3** models, as suggested previously discussed experimental results. The $RDF_{PEDOT\text{-}ionene}$ calculated for **m2** exhibits peaks centered at *r*= 4.1, 5.1 and 5.7 Å (Figure 4.2-16(b), center). Although the peaks at *r*= 5.1 and 5.7 Å are maintained in **m1** and **m3**, the peak at *r*= 4.1 Å is less intense (**m3**) or

practically inexistent (**m1**) in such models. The increment of the distance between the interacting aromatic rings indicates that PEDOT⋯ionene π-π stacking interactions are stronger for the *meta*-isomeric ionene than for the *ortho*- and *para*-ones. The θ distribution profiles (Figure 4.2-16(c), center), calculated considering a cutoff distance of 7.0 Å, evidence the preference towards a distorted T-shape configuration for the three models. Thus, the population of pairs of aromatic interacting rings with $\theta > 45^{o}$ is 67%, 55% and 66% for **m1**, **m2** and **m3**, respectively. However, the degree of distortion is very variable since the interval of θ values with significant population extended from 46^{o} to 90^{o} in all cases.

Finally, ionene⋯ionene π-π stacking interactions are considerably less abundant for **m1** (31%) and **m3** (16%) than for **m2**. Moreover, the number of detected ionene⋯ionene π-π stacked pairs is about twice the number of PEDOT⋯ionene π-π stacked pairs using a cut-off of 7 Å in both cases. The calculated $RDF_{ionene\text{-}ionene}$ profiles (Figure 4.2-16(b), right) display small and relatively broad peaks at *r* values comprised between 4 and 6 Å, which have been attributed to the periodicity of the ionene chains (*i.e.* ionenes contain 3 aromatic rings per repeat unit), and a sharp peak at $r \approx 6.5$ Å that actually corresponds to the inter-chain π-π stacking. The preferred arrangement of the interacting rings is the T-shape, even though a dependence on the ionene topology is clearly observed. Thus, the population of interacting aromatic rings (Figure 4.2-16(c), right) with $\theta > 45^{o}$ grows as follows: 57% (**m3**) < 67% (**m2**) < 71% (**m1**).

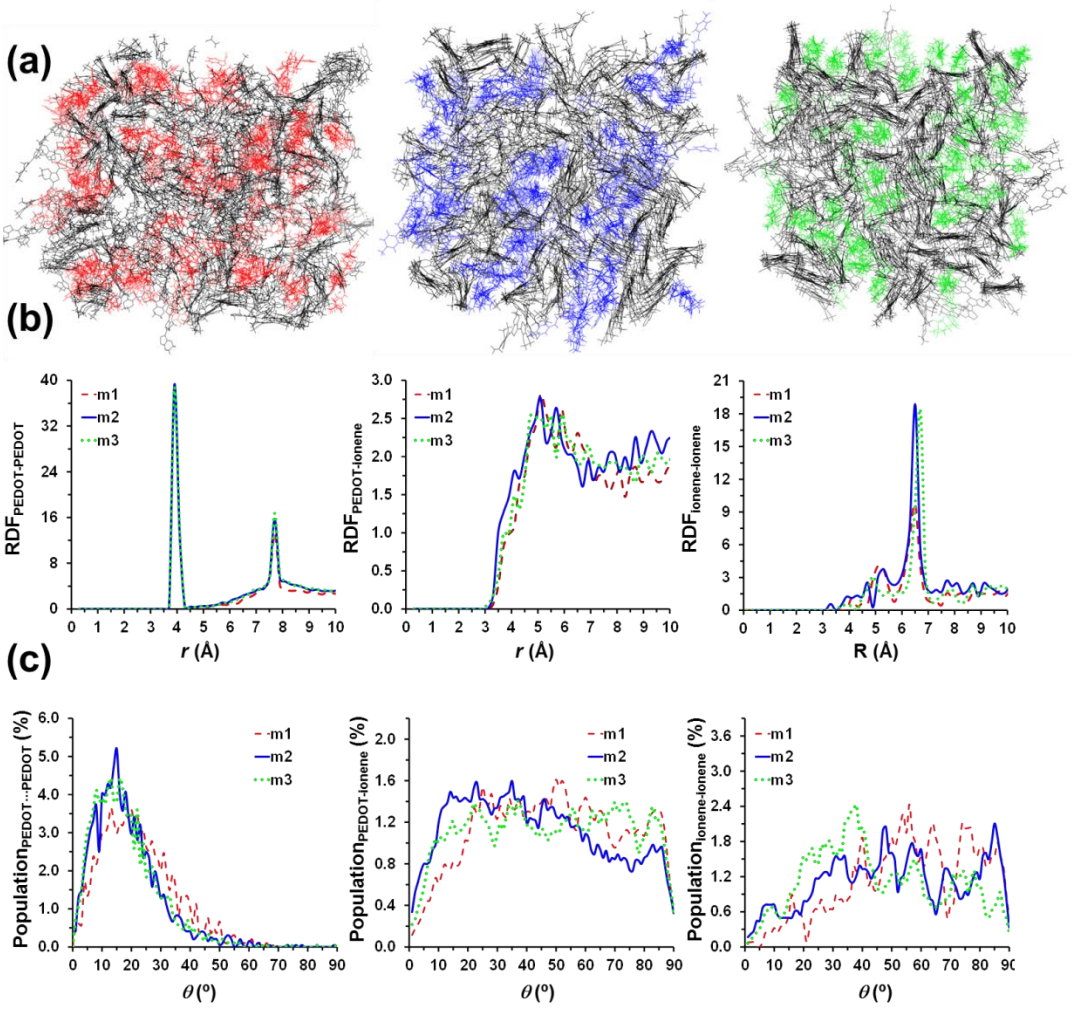

Figure 4.2-16. (a) Representation of the last snapshot from the productive 100 ns NPT-MD trajectory for m1 (left), m2 (centre) and m3 (right) models. (b) Radial distribution functions (RDFs) for the pairs of centres of masses of aromatic rings belonging to two different PEDOT chains ($RDF_{PEDOT\text{-}PEDOT}$; left), to one PEDOT chain and one ionene chain ($RDF_{PEDOT\text{-}ionene}$; center), and to two different ionene chains ($RDF_{ionene\text{-}ionene}$; right) for m1-m3 models. (c) Distribution of the number of pairs of interacting aromatic rings as a function of the tilting angle θ for PEDOT···PEDOT (left), PEDOT···ionene (center) and ionene···inene (right) interactions in m1-m3 models. Only rings belonging to different polymer chains and with the centers of masses separated by ≤5.0 Å have been considered for PEDOT···PEDOT interactions, while a cut-off distance of 7.0 Å has been used for PEDOT···ionene and ionene···ionene interactions.

As ionene···ionene hydrogen bonds were examined in previous work,[17,18] in this study we report the analysis of PEDOT···ionene hydrogen bonds. More specifically, such kind of specific interactions has been analyzed through the RDFs for (N–)H···O and (N–)H···S pairs ($RDF_{N\text{-}H\cdots O}$ and $RDF_{N\text{-}}$

$_{H\cdots S}$), where N–H, O and S refer to the amide group of ionene chains, the oxygen atom of the dioxane ring and the sulfur atom of the thiophene ring, respectively. Analysis of the calculated $RDF_{N\text{-}H\cdots O}$ [Figure 4.2-17(a)] indicates that the presence of N–H···O hydrogen bonds is practically null. Thus, the first peak (**m2** and **m3**) or shoulder (**m1**) is centered at a distance ($r \approx$ 4.5 Å) much larger than those typically found for H···O hydrogen bonds,[58] even when this interaction involves the dioxane of EDOT units.[59] Accordingly, such peaks have been related to the periodicity of the PEDOT chains rather than to N–H···O hydrogen bonds.

Regarding N–H···S hydrogen bonds, inspection of the calculated $RDF_{N\text{-}H\cdots S}$ [Figure 4.2-17(b)] reflects a peak centered at r= 2.75 Å for **m1**, which is fully consistent with the H···S distance typically found in hydrogen bonds involving the sulfur atom of the thiophene rings (*i.e.* ~2.8 Å).[59,60] This peak is more intense and much broader for **m2** (*i.e.* it extends from 2.6 to ~4.3 Å), which reflects the very remarkable tendency of *meta*-topomer to form weak PEDOT···ionene interactions through specific N–H···S hydrogen bonds. Finally, the *para*-topomer exhibits the lowest affinity towards the sulfur atom of the thiophene ring, the $RDF_{N\text{-}H\cdots S}$ calculated for **m3** model exhibiting a shoulder and a peak at r= 3.2 and 4.1 Å, respectively.

Finally, the role of intermolecular $N^+\cdots O$ and $N^+\cdots S$ interactions, which involve the positively charged nitrogen atoms of the ionene chains and the oxygen and sulfur atoms of PEDOT, is evaluated through the corresponding RDFs, $RDF_{N^+\cdots O}$ and $RDF_{N^+\cdots S}$ [Figure 4.2-17(c,d), respectively]. The former profile exhibits a relatively broad peak that extends from 4.6 to 5.4 Å, suggesting that the strength of $N^+\cdots O$ is very variable. Considering cut-off distances of 4 and 7 Å for N–H···S and $N^+\cdots O$ interactions, respectively, the population of the former hydrogen bond is half that of the latter one. Moreover, $N^+\cdots O$ interactions are significantly more abundant (~12%) in **m2** than in **m1** and **m3**. Besides, $RDF_{N^+\cdots S}$ profiles also exhibit a sharp peak centered at r= 4.5 Å that is more intense for **m2** than for **m1** and **m3**. Thus, considering a cut-off distance of 7 Å, $N^+\cdots S$ are 16 % more abundant for **m2** than for both **m1** and **m3**, which differ by less than 1%.

Overall, results displayed in Figure 4.2-17 indicate that attractive N–H···S, $N^+\cdots O$ and $N^+\cdots S$ PEDOT···ionene interactions are more abundant and stronger for **2** than for **1** and **3**. These specific interactions combined with the fact that ionene···ionene interactions are stronger for **1** and **3** than for **2**, as was demonstrated in previous work,[17,18] explains that the *in situ* hydrogelation was only successful for PEDOT:**1** and PEDOT:**3**.

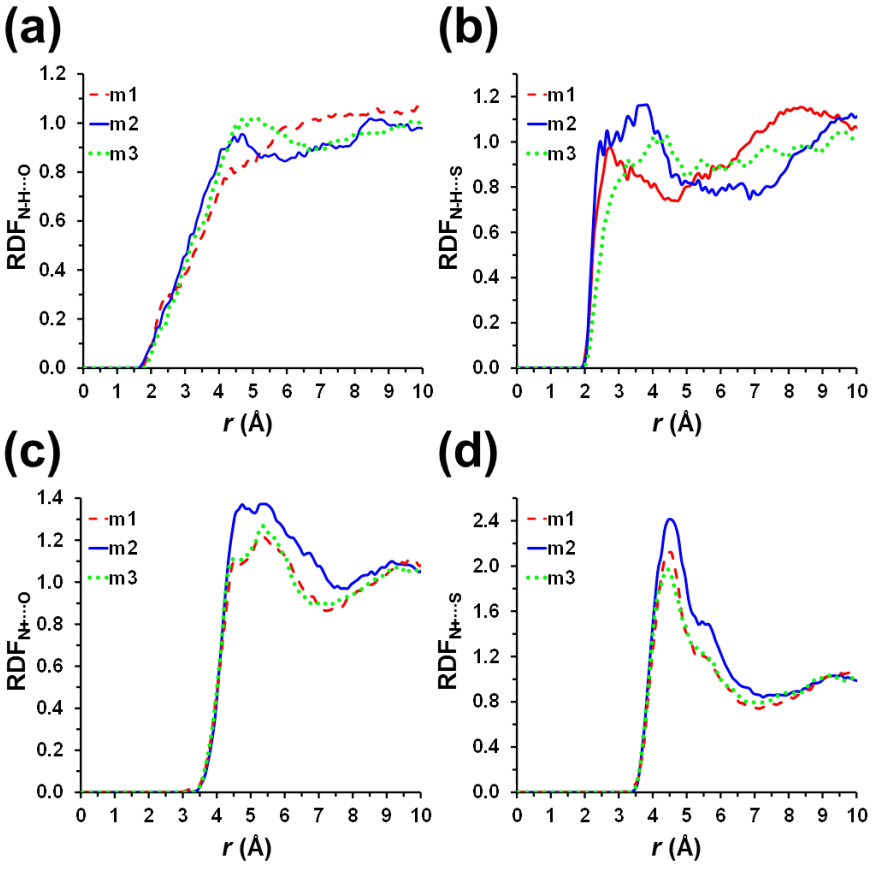

Figure 4.2-17. Radial distribution functions used to evaluate the population and strength of specific PEDOT···ionene interactions: (a) (N–)H···O ($RDF_{N\text{-}H\cdots O}$), (b) (N–)H···S ($RDF_{N\text{-}H\cdots S}$), (c) $N^+\cdots O$ ($RDF_{N+\cdots O}$) and (d) $N^+\cdots S$ ($RDF_{N+\cdots S}$) pairs in m1-m3 models, where the N–H and N^+ moieties belong to the ionene chains and the oxygen and sulphur atoms are located in the dioxane and thiophene rings of PEDOT chains.

4.2.5. Conclusions

We have prepared novel n-doped PEDOT:ionene modified electrodes by electro-oxidative polymerization of EDOT in acetonitrile with $LiClO_4$. The obtained p-doped films are dedoped in aqueous medium and subsequently redoped in presence of ionene aqueous solutions by applying a reduction potential. Three DABCO-containing ionene polymers, which differ in the isomeric form of the *N*,*N*'-(phenylene)dibenzamide linkage (*i.e. ortho*, *meta* and *para*) have been compared to investigate the influence of the topology in the properties of the resulting films.

The *SC*s and electrochemical stability of PEDOT:ionene, which as usual for n-type CPs are low, and the high wettability are relatively independent of the polycation topology. In contrast, the thermal stability provided by the ionene dopants to the CP increases with the strength of PEDOT···ionene interactions, which are stronger for the *meta*-topomer than for the *ortho*- and *para*-ones. Also, the ionene topology has a pronounced effect on the surface topography and microstructure of the films, even though such two properties are also affected by the reduction potential. Interestingly, PEDOT:**1** and PEDOT:**3** films experience *in situ* thermally-induced hydrogelation, forming ionene micro/nano-hydrogels at the surface and inside the CP matrix. After gelation, PEDOT:**1** and PEDOT:**3** exhibit a noticeable improvement of the mechanical response and a significant enhancement of the *SC* increases, evidencing that ionene hydrogels act as a cement and facilitate the charge movement.

Classical MD simulations have been conducted to unravel which specific interactions accompany and reinforce the predominant electrostatic interactions between the negatively charged CP and the posivitely charged ionene. As suggested experimental observations, PEDOT···ionene π-π stacking interactions are more abundant and stronger in PEDOT:**2** than in PEDOT:**1** and PEDOT:**3**. Similarly, ionene···ionene π-π stacking interactions are less abundant in PEDOT:**1** and PEDOT:**3** than in PEDOT:**2**. On the other hand, N–H···S hydrogen bonds and both N^+···O and N^+···S interactions seem to play a decisive role in the stabilization of the PEDOT···**2** interactions. More specifically, such three kind of interactions are more abundant and stronger in PEDOT:**2** than in PEDOT:**1** and PEDOT:**3**, explaining that the successful *in situ* hydrogelation of the latter two.

Results presented in this work open a new door for the future preparation of self-supported n-doped PEDOT electrodes using the *in situ* hydrogelation approach. Detailed investigations on new strategies to increment the amount of ionene loaded during the redoping process are currently underway in our laboratories.

4.2.6. References

(1) Strassburg, A.; Petranowitsch, J.; Paetzold, F.; Krumm, C.; Peter, E.; Meuris, M.; Koller, M.; Tiller, J. C. Cross-Linking of a Hydrophilic, Antimicrobial Polycation toward a Fast-Swelling, Antimicrobial Superabsorber and Interpenetrating Hydrogel Networks with Long Lasting Antimicrobial Properties. *ACS Appl. Mater. Interfaces.* **2017**, *9* (42), 36573–36582.

(2) Williams, S. R.; Borgerding, E. M.; Layman, J. M.; Wang, W.; Winey, K. I.; Long, T. E. Synthesis and Characterization of Well-Defined 12,12-Ammonium Ionenes: Evaluating Mechanical Properties as a Function of Molecular Weight. *Macromolecules.* **2008**, *41* (14), 5216–5222.

(3) Yoshida, M.; Koumura, N.; Misawa, Y.; Tamaoki, N.; Matsumoto, H.; Kawanami, H.; Kazaouni, S.; Minami, N. Oligomeric Electrolyte as a Multifunctional Gelator. *J. Am. Chem. Soc.* **2007**, *129* (36), 11039–11041.

(4) Yamada, Y. M. A.; Uozumi, Y. A. Solid-Phase Self-Organized Catalyst of Nanopalladium with Main-Chain Viologen Polymers: α-Alkylation of Ketones with Primary Alcohols. *Org. Lett.* **2006**, *8* (7), 1375–1378.

(5) Ahamed, P.; Haque, Md. A.; Ishimoto, M.; Parvez, Md. M.; Haraguchi, N.; Itsuno, S. Synthesis of Chiral Quaternary Ammonium Polymers for Asymmetric Organocatalysis Application. *Tetrahedron.* **2013**, *69* (19), 3978–3983.

(6) Berlamino, A. T. N.; Orth, E. S.; Mello, R. S.; Medeiros, M.; Nome, F. Catalytic Nanoreactors for Ester Hydrolysis. *J. Mol. Catalysis A.* **2010**, *332* (1–2), 7–12.

(7) Tiffner, M.; Zielke, K.; Mayr, J.; Häring, M.; Díaz-Díaz, D.; Waser, M. *Phase-Transfer Catalysis with Ionene Polymers. Chem. Select.* **2016**, *1* (13), 4030–4033

(8) Bachl, J.; Zanuy, D.; Lopez-Perez, D. E.; Revilla-Lopez, G.; Cativiela, C.; Aleman, C.; Diaz, D. D. Synergistic Computational-Experimental Approach to Improve Ionene Polymer-Based Functional Hydrogels. *Adv. Funct. Mater.* **2014**, *24* (31), 4893–4904.

(9) Bachl, J.; Bertran, O.; Mayr, J.; Alemán, C.; Díaz Díaz, D. Aromatic Ionene Topology and Counterion-Tuned Gelation of Acidic Aqueous Solutions. *Soft Matter.* **2017**, *13* (16), 3031–3041.

(10) Zhao, D. W.; Zhang, Q.; Chen, W. S.; Yi, X.; Liu, S. X.; Wang, Q. W.; Liu, Y. X.; Li, J.; Li, X. F.; Yu, H. P. Highly Flexible and Conductive Cellulose-Mediated PEDOT:PSS/MWCNT Composite Films for Supercapacitor Electrodes. *ACS Appl. Mater. Interfaces.* **2017**, *9* (15), 13213–13222.

(11) Sun, J. F.; Huang, Y.; Fy, C. X.; Huang, Y.; Zhu, M. S.; Tao, X. M.; Zhi, C. Y.; Hu, H. A High Performance Fiber-Shaped PEDOT@MnO_2//C@Fe_3O_4 Asymmetric Supercapacitor for Wearable Electronics. *J. Mater. Chem. A.* **2016**, *4* (38), 14877–14883.

(12) Liu, Y. Q.; Weng, B.; Razal, J. M.; Xu, Q.; Zhao, C.; Hou, Y. Y.; Sevedin, S.; Jalili, R.; Wallace, G. G.; Chen, J. High-Performance Flexible All-Solid-State Supercapacitor from Large Free-Standing Graphene-PEDOT/PSS Films. *Sci. Rep.* **2015**, *5* (17045), 1–11.

(13) Higgins, T. M.; Coleman, J. N. Avoiding Resistance Limitations in High-Performance Transparent Supercapacitor Electrodes Based on Large-Area, High-Conductivity PEDOT:PSS Films. *ACS Appl. Mater. Interfaces.* **2015**, *7* (30), 16495–16506.

(14) Anothumakkool, B.; Soni, R.; Bhange, S. N.; Kurungot, S. Novel Scalable Synthesis of Highly Conducting and Robust PEDOT Paper for a High Performance Flexible Solid Supercapacitor. *Eng. Environ. Sci.* **2015**, *8* (4), 1339–1347.

(15) Pérez-Madrigal, M. M.; Estrany, F.; Armelin, E.; Díaz-Díaz, D.; Alemán C. Towards Sustainable Solid-State Supercapacitors: Electroactive Conducting Polymers Combined with Biohydrogels**.** *J. Mater. Chem. A***. 2016**, ***4*** (5), 1792–1805.

(16) Lim, J. E.; Lee, S. M.; Kim, S. S.; Kim, T. W.; Koo, H. W.; Kim, H. K. Brush-Paintable and Highly Stretchable Ag Nanowire and PEDOT:PSS Hybrid Electrodes. *Sci. Rep.* **2017**, *7*, 14685, 1–12.

(17) Teo, M. Y.; Kim, N.; Kee, S.; Kim, B. S.; Kim, G.; Hong, S.; Jung, S.; Lee, K. Highly Stretchable and Highly Conductive PEDOT:PSS/Ionic Liquid Composite Transparent Electrodes for Solution-Processed Stretchable Electronics. *ACS Appl. Mater. Inferfaces.* **2017**, *9* (1), 819–826.

(18) Cai, G. F.; Darmawan, P.; Cui, M. Q.; Wang, J. X.; Chen, J. W.; Magdassi, S.; Lee, P. S. Supercapacitors: Highly Stable Transparent Conductive Silver Grid/PEDOT:PSS Electrodes for Integrated Bifunctional Flexible Electrochromic Supercapacitors. *Adv. Energy Mater.* **2016**, *6* (4), 1501882.

(19) Vosgueritchian, M.; Lipomi, D. J.; Bo, Z. A. Highly Conductive and Transparent PEDOT:PSS Films with a Fluorosurfactant for Stretchable and Flexible Transparent Electrodes. *Adv. Funct. Mater.* **2012**, *22* (2), 421–428.

(20) Huang, J.; Miller, P. F.; Wilson, J. S.; de Mello, A. J.; de Mello, J. C.; Bradley, D. D. Investigation of the Effects of Doping and Post-Deposition Treatments on The Conductivity, Morphology, and Work Function of Poly(3,4-ethylenedioxythiophene)/Poly (styrene sulfonate) Films. *Adv. Funct. Mater.* **2005**, *15* (2), 290–296.

(21) Nardes, A. M.; Kemerink, M.; De Kok, M.; Vinken, E.; Maturova, K.; Janssen, R. Conductivity, Work Function, and Environmental Stability of PEDOT:PSS Thin Films Treated with Sorbitol. *Org. Electron.* **2008**, *9* (5), 727−734.

(22) Crispin, X.; Jakobsson, F. L. E.; Crispin, A.; Grim, P. C. M.; Andresson, P.; Volodin, A.; van Haesendonck, C.; Van der Auweraer, M.; Salaneck, W. R.; Berggren, M. The Origin of the High Conductivity of Poly(3,4-ethylenedioxythiophene)− Poly(styrenesulfonate) (PEDOT−PSS) Plastic Electrodes. *Chem. Mater.* **2006**, *18* (18), 4354−4360.

(23) Hillman, A. R.; Daisley, S. J.; Bruckenstein, S. Ion and Solvent Transfers and Trapping Phenomena During n-Doping of PEDOT Films. *Electrochim. Acta.* **2008**, *53* (11), 3763–3771.

(24) Gustafsson, H.; Kwarnström, C.; Ivaska, A. Comparative Study of n-Doping and p-Doping of Poly(3,4-ethylenedioxythiophene) Electrosynthesised on Aluminium. *Thin Solid Films.* **2008**, *517* (2), 474–478.

(25) Sandoval, A. P.; Feliu, J. M.; Torresi, R.; Suárez, M. F. Electrochemical Properties of Poly(3,4-ethylenedioxythiophene) Grown on Pt(111) in Imidazolium Ionic Liquids. *RSC Adv.* **2014**, *4* (7), 3383–3391.

(26) Bachl, J.: Zanuy, D., López-Pérez, D. E.; Revilla-López, G.; Cativiela, C.; Alemán C.; Díaz Díaz, D. Synergistic Computational-Experimental Approach to Improve Ionene Polymer-Based Functional Hydrogels. *Adv. Funct. Mater.* **2014**, *24* (31), 4893-4904.

(27) Ocampo, C.; Oliver, R.; Armelin, R.; Alemán C.; Estrany, F. Electrochemical Synthesis of Poly(3,4-ethylenedioxythiophene) on Steel Electrodes: Properties and Characterization *J. Polym. Res.* **2006**, *13* (3), 193-200.

(28) Phillips, J. C.; Braun, R.; Wang, W.; Gumbart, J.; Tajkhorshid, E.; Villa, E.; Chipot, C.; Skeel, R. D.; Kale L.; Schulten, K. Scalable molecular dynamics with NAMD. *J. Comput. Chem.* **2005**, *26 (16)*, 1781-802.

(29) Cornell, W. D.; Cieplak, P.; Bayly, C. I.; Gould, I. R.; Merz, K. M.; Ferguson, D. M.; Spellmeyer, D. C.; Fox, T.; Cadwell J. W.; Kollman, P. A. A Second Generation Force Field for the Simulation of Proteins, Nucleic Acids, and Organic Molecules. *J. Am. Chem. Soc.***1995**, *117* (19), 5179-5197.

(30) Zanuy, D.; Alemán, C. Resolving the subnanometric structure of ultrathin films of poly(3,4-ethylenedioxythiophene) on steel surfaces: a molecular modeling approach *Soft Matter*. **2013**, *9* (48), 11634-11644.

(31) Andersen, H. C. Rattle: A "velocity" version of the shake algorithm for molecular dynamics calculations *J. Comput. Phys.* **1983**, *52* (1), 24-34.

(32) Darden, T.; York D.; Pedersen, L. Particle mesh Ewald: An N·log(N) method for Ewald sums in large systems. *J. Chem. Phys.* **1993**, *98* (12), 10089.

(33) Duan, Y.; Wu, C.; Chowdhury, S.; Lee, M. C.; Xiong, G. M.; Zhang, W.; Yang, R.; Cieplak, P.; Luo, R.; Lee, T.; Caldwell, J.; Wang J. M.; Kollman, P. A point-charge force field for molecular mechanics simulations of proteins based on condensed-phase quantum mechanical calculations. *J. Comput. Chem.* **2003**, *24* (16), 1999.

(34) Martyna, G. J.; Tobia D. L.; Klein, M. L. Constant pressure molecular dynamics algorithms. *J. Chem. Phys.* **1994**, *101* (5), 4177.

(35) Saborío, M. G.; Bertran, O.; Lanzalaco, S.; Häring, M.; Díaz-Díaz, D.; Estrany, F.; Alemán, C. Cationic Ionene as n-Dopant Agent of Poly(3,4-ethylenedioxythiophene). *Physc. Chem. Chem. Phys.* **2018**, in press.

(36) Garreau, S.; Duvail, J. L.; Louarn, G. Spectroelectrochemical Studies of Poly(3,4-ethylenedioxythiophene) in Aqueous Medium. *Synth. Met.* **2002**, *125* (3), 325–329.

(37) Han, Y.-K.; Chang, M.-Y.; Huang, W.-Y.; Pan, H.-Y.; Ho, K.-S.; Hsieh, T.-H.; Pan, S.-Y. Improved Performance of Polymer Solar Cells Featuring One-Dimensional PEDOT Nanorods in a Modified Buffer Layer. *J. Electrochem. Soc.* **2011**, *158* (3), K88–K93.

(38) Farah, A. A.; Rutledge, S. A.; Schaarschmidt, A.; Lai, R.; Freedman, J. P.; Helmy, A.S. Conductivity Enhancement of Poly(3,4-ethylenedioxythiophene)-Poly(styrenesulfonate) Film Postspincasting. *J. Appl. Phys.* **2012**, *112* (113709), 1–8.

(39) Wu, D.; Zhang, J.; Dong, W.; Chen, H.; Huang, X.; Sun, B.; Chen, L. Temperature Dependent Conductivity of Vapor-Phase Polymerized PEDOT Films. *Synth. Met.* **2013**, *176* (13), 86–91.

(40) Ely, F.; Matsumoto, A.; Zoetebier, B.; Peressinotto, V. S.; Hirata, M. K.; Sousa, D. A.; Maciel, R. Handheld and Automated Ultrasonic Spray Deposition of Conductive PEDOT:PSS Films and Their Application in AC EL Devices. *Org. Electron.* **2014**, *15* (5), 1062–1070.

(41) Aleman, C.; Curcó, D.; Casanovas, J. A Density Functional Theory Study of n-Doped 3,4-Ethylenedioxythiophene Oligomers. *Chem. Phys. Lett.* **2004**, *386* (4–6), 408–413.

(42) Cho, M. S.; Yun, Y. Y.; Nam, J. D.; Son, Y.; Lee, Y. Effect of Magnetic Field on Electrochemical Polymerization of EDOT. *Synth. Met*. **2008**, *158* (21–24),1043–1046.

(43) Strobl, G. R.; Hagedorn, W. Raman Spectroscopic Method for Determining the Crystallinity of Polyethylene. *J. Polym. Sci.: Polym. Phys. Ed.* **1978**, *16* (7), 1181–1193.

(44) Tan, H. M.; Chang, B. H.; Baer, E.; Hiltne, A. Relationship between Crystallinity and Thermoreversible Gelation. *Eur. Polym. J.* **1983**, *19* (10–11), 1021–1025.

(45) Chang, S. H.; Chiang, C.-H.; Kao, F.-S.; Tien, C.-L.; Wu, C.-G. Unraveling the Enhanced Electrical Conductivity of PEDOT:PSS Thin Films for ITO-Free Organic Photovoltaics. *IEEE Photonic Journal.* **2014**, *6* (4), 1–7.

(46) Aradilla, D.; Azambuja, D. S.; Estrany, F.; Casas, M. T.; Ferreira, C. A.; Alemán, C. Hybrid Polythiophene–Clay Exfoliated Nanocomposites for Ultracapacitor Devices. *J. Mater. Chem.* **2012**, *22* (26), 13110–13122.

(47) Chen, L.; Yuan, C.; Dou, H.; Gao, B.; Chen, S.; Zhang, X. Synthesis and Electrochemical Capacitance of Core–Shell Poly (3,4-ethylenedioxythiophene)/Poly (sodium 4-styrenesulfonate)-Modified Multiwalled Carbon Nanotube Nanocomposites. *Electrochim. Acta.* **2009**, *54* (8), 2335–2341.

(48) Murugan, A. V.; Viswanath, A. K.; Gampet, G.; Gopinath, C. S.; Vijayamohanan, K. Enhancement of Double-Layer Capacitance Behavior and Its Electrical Conductivity in Layered Poly (3, 4-ethylenedioxythiophene)-based Nanocomposites. *Appl. Phys. Lett.* **2005**, *87* (24), 243511.

(49) Sharma, R.; Zhai, L. Multiwall Carbon Nanotube Supported Poly(3,4-ethylenedioxythiophene)/Manganese Oxide Nano-Composite Electrode for Super-Capacitors. *Electrochim. Acta*. **2009**, *54* (27), 7148–7155.

(50) Sen, P. M.; De, M. Electrochemical Performances of Poly(3,4-ethylenedioxythiophene)–$NiFe_2O_4$ Nanocomposite as Electrode for Supercapacitor. *Electrochim. Acta*. **2010**, *55* (16), 4677–4684.

(51) Babakhani, B.; Ivey, D. G. Improved Capacitive Behavior of Electrochemically Synthesized Mn Oxide / PEDOT electrodes Utilized as Electrochemical Capacitors. *Electrochim. Acta.* **2010**, *55* (12), 4014–4024.

(52) Murugan, A. V.; Viswanath, A. K.; Gopinath, C. S.; Vijayamohanan, K. Highly Efficient Organic-Inorganic Poly(3,4-ethylenedioxythiophene)-Molybdenum Trioxide Nanocomposite Electrodes for Electrochemical Supercapacitor. *J. Appl. Phys.* **2006**, *100* (7), 074319.

(53) Ahonen, H. J.; Lukkari, J.; Kankare, J. N- and p-Doped Poly(3,4-ethylenedioxythiophene): Two Electronically Conducting States of the Polymer. *Macromolecules* **2000**, *33* (18), 6787–6793.

(54) Tsuzuki, S.; Honda, K.; Uchimaru, T.; Mikami, M.; Tanabe, K. Origin of Attraction and Directionality of the π/π Interaction: Model Chemistry Calculations of Benzene Dimer Interaction. *J. Am. Chem. Soc.* **2002**, *124* (1), 104−112.

(55) Rodriguez-Ropero, F.; Casanovas, J.; Alemán, C. Ab Initio Calculations on π-Stacked Thiophene Dimer, Trimer, and Tetramer: Structure, Interaction Energy, Cooperative Effects, and Intermolecular Electronic Parameters. *J. Comput. Chem.* **2008**, *29* (1), 69−78.

(56) Tsuzuki, S.; Honda, K.; Azumi, R. Model Chemistry Calculations of Thiophene Dimer Interactions: Origin of π-Stacking. *J. Am. Chem. Soc.* **2002**, *124* (41), 12200−12209.

(57) Huber, R. G.; Margreiter, M. A.; Fuchs, J. E.; von Grafenstein, S.; Tautermann, C. S.; Liedl, K. R.; Fox, T. Heteroaromatic π-Stacking Energy Landscapes. *J. Chem. Inf. Model.* **2014**, 54 (5), 1371–1379.

(58) Alemán, C. On the Ability of Modified Peptide Links to Form Hydrogen Bonds. *J. Phys. Chem. A.* **2001,** *105* (27), 6717–6723

(59) Alemán, C.; Teixeira-Dias, B.; Zanuy, D.; Estrany, F.; Armelin, E.; del Valle, L. J. A Comprehensive Study of the Interactions between DNA and Poly(3,4-ethylenedioxythiophene). *Polymer*. **2009**, *50* (8), 1965–1974.

(60) Zanuy, D.; Aleman, C. DNA-Conducting Polymer Complexes: A Computational Study of the Hydrogen Bond between Building Blocks. *J. Phys. Chem. B.* **2008,** *112* (10), 3222–3230

Chapter V

5.1. General conclusions

1) PEDOT/Al_2O_3 composites have been successfully synthesized in aqueous solution considering different monomer:alumina ratios in the reaction medium, pHs ranging from 2.3 to 10.8, and both continuous and multi-step *in situ* polymerization strategies.

2) The electrochemical properties for energy storage of PEDOT/Al_2O_3 are better than those of pure PEDOT, which has been attributed to the additional sites for the migration of charges provided by the alumina particles.

3) The best properties of PEDOT/Al_2O_3 composites are obtained applying a multi-step polymerization strategy, a 4:1 EDOT:alumina ratio and a pH of 8.8.

4) The above mentioned conditions (Conclusion 3) are supported by the following observations: (i) 4:1 EDOT:alumina suspensions are stable at pH 8.8 despite it is very close to the isoelectric point of alumina; (ii) the OH^- groups associated to basic pHs participate as dopant agents giving an extra activation to PEDOT; (*iii*) polymeric matrix does not undergo degradation at such moderately high pH; and (*iv*) the interfaces generated by the multi-step polymerization act as a dielectric placed between two polymeric layers.

5) Highly flexible and lightweight free-standing electrodes have been synthesized by functionalizing γ-PGA hydrogels with PEDOT particles, which were subsequently used as polymerization nuclei for the anodic polymerization of PHMeDOT.

6) The γ-PGA hydrogel provides a support with consistency, robustness and open internal structure, which is crucial to permit the ion diffusion process. PEDOT particles play a key role in the

electropolymerization of HMeDOT monomer, favoring the homogeneous distribution of PHMeDOT chains across the hydrogel.

7) The [PEDOT/γ-PGA]PHMeDOT(θ= 7 h) composite presents a great potential in supercapacitors with specific capacitance hitting 45-47 mF cm^{-2}, as obtained by CV and GCD, and excellent cycle durability.

8) The effectiveness of the [PEDOT/γ-PGA]PHMeDOT(θ= 7 h) electrode has been proved through a simple application based on power a red LED. Results show that the as-made [PEDOT/γ-PGA]PHMeDOT(θ= 7 h) electrode can be potentially used in various fields, as for example textiles (*e.g.* wearable electronics) and biomedical, where robustness and flexibility is required.

9) A flexible, compact, lightweight and biocompatible symmetric supercapacitor prototype has been developed by assembling two identical electrodes, constituted by CPs- and alumina-containing electroactive hydrogels, through a γ-PGA biohydrogel doped with $NaHCO_3$, which act as a solid electrolyte.

10) After optimization of the supercapacitor prototype, the best configuration of the prototype exhibits the following characteristics: 4 mm as width of the electrodes, 4 mm as width of the solid electrolyte, working potential window that expands from -0.50 V to 0.50 V at a scan rate of 100 mV s^{-1}.

11) The prepared supercapacitor shows a *SC* of around 13 mF g^{-1}, a good *E* ($4.6 \cdot 10^{-4}$ mWh g^{-1}) and excellent cyclability (92% of retention of the specific capacitance after after 2000 GCD cycles).

12) The excellent electrochemical properties of PEDOT and PHMeDOT, which are enhanced in presence of alumina, in combination with the mechanical strength and flexibility of the γ-PGA biohydrogel, suggest the supercapacitor prototype prepared in this work is a promising small-size and lightweight energy storage devices.

13) We have prepared novel n-doped PEDOT:ionene modified electrodes by electro-oxidative polymerization of EDOT in acetonitrile with $LiClO_4$. The obtained p-doped films are dedoped in aqueous medium and subsequently redoped in presence of ionene aqueous solutions by applying a reduction potential.

14) Ionenes can be successfully used as n-dopant agents of PEDOT, offering an important alternative to conventional TMA and its, also small, derivatives. Thus, redoping with ionenes is a successful strategy to produce n-doped PEDOT electrodes with properties very different from those achieved using small organic cations.

15) Three isomeric ionene polymers containing DABCO and *N*,*N*'-(*x*-phenylene)dibezamide (*x*= *ortho*- / *meta*- / *para*-) linkages have been successfully used as dopant agents to produce n-doped poly(3,4-ethylenedioxythiophene) (PEDOT) electrodes by reducing already dedoped conducting polymer (CP) films.

16) SEM and AFM analyses on PEDOT:**2** reveal some segregation between the PEDOT matrix, which retain the typical globular and porous morphology, and the ionene that organization into nanospheres and ultrathin sheets.

17) The doping levels achieved for PEDOT films n-doped with ionenes are similar to that obtained using TMA, even though properties of the materials are significantly different.

18) The incorporation of ionenes results in a significant increment of the hydrophilicity and the thermal stability in comparison to p-doped and dedoped PEDOT, respectively.

19) The *SC*s, electrochemical stability and wettability of n-doped PEDOT:ionene electrodes are relatively independent of the polycation topology. In contrast, the thermal stability provided by the ionene dopants to the CP increases with the strength of PEDOT⋯ionene interactions, which are stronger for the *meta*-topomer than for the *ortho*- and *para*-ones.

20) The ionene topology has a pronounced effect on the surface topography and microstructure of n-doped PEDOT:ionene films, even though such two properties are also affected by the reduction potential.

21) PEDOT:**1** and PEDOT:**3** films experience *in situ* thermally-induced hydrogelation, forming ionene micro/nano-hydrogels at the surface and inside the CP matrix. After gelation, PEDOT:**1** and PEDOT:**3** exhibit a noticeable improvement of the mechanical response and a significant enhancement of the *SC* increases, evidencing that ionene hydrogels act as a cement and facilitate the charge movement.

Annex

List of Publications

(1) Saborío, M. C. G.; Estrany, F.; Alemán, C. Properties of In Situ Polymerized Poly(3,4-ethylenedioxythiophene)/Alumina Composites for Energy Storage Applications. *J. Polym. Sci., Part B: Polym. Phys.* **2017**, *55* (15), 1131–1141.

(2) Saborío, M. C. G.; Lanzalaco, S.; Fabregat, G.; Puiggali, J.; Estrany, F.; Aleman, C. Flexible Electrodes for Supercapacitors Based on the Supramolecular Assembly of Biohydrogel and Conducting Polymer. *J. Phys. Chem. C* **2018**, *122* (2), 1078–1090.

(3) Saborío, M. C. G.; Bertran, O.; Lanzalaco, S.; Häring, M.; Díaz-Díaz, D.; Estrany, F.; Alemán, C. Cationic Ionene as n-Dopant Agent of Poly(3,4-ethylenedioxythiophene). *Physc. Chem. Chem. Phys.* **2018**, in press.

(4) Saborío, M. C. G.; Bertran, O.; Lanzalaco, S.; Haering, M.; Díaz Díaz, D.; Estrany, F.; Aleman, C. Isomeric Cationic Ionene as n-Dopant Agents of Poly(3,4-ethylenedioxythiophene) for In Situ Gelation. *Phys. Chem. Chem. Phys* ID: CP-ART-11-2017-007878.R1

(5) Saborío, M. C. G.; Zukić, S.; Lanzalaco, S.; Estrany, F.; Aleman, C Prototype Flexible Supercapacitor based on Biohydrogel. *In process of submission.*

BARCELONA TECH

-2018-